PROBING FLOWS IN THE
UPPER SOLAR CONVECTION ZONE

A DISSERTATION
SUBMITTED TO THE DEPARTMENT OF PHYSICS
AND THE COMMITTEE ON GRADUATE STUDIES
OF STANFORD UNIVERSITY
IN PARTIAL FULFILLMENT OF THE REQUIREMENTS
FOR THE DEGREE OF
DOCTOR OF PHILOSOPHY

Laurent Gizon
May 2003

I certify that I have read this dissertation and that in my opinion it is fully adequate, in scope and quality, as a dissertation for the degree of Doctor of Philosophy.

_____
Philip H. Scherrer
(Principal Adviser)

I certify that I have read this dissertation and that in my opinion it is fully adequate, in scope and quality, as a dissertation for the degree of Doctor of Philosophy.

_____
Vahé Petrosian

I certify that I have read this dissertation and that in my opinion it is fully adequate, in scope and quality, as a dissertation for the degree of Doctor of Philosophy.

_____
Thomas L. Duvall, Jr.

Approved for the University Committee on Graduate Studies.

Abstract

In order to better understand the origin and variability of stellar magnetic fields it is necessary to understand mass flows inside stars. With time-distance helioseismology local flows can be inferred in the Sun by measuring the time it takes for seismic waves to propagate between any two points on the solar surface. This dissertation contains new observations of solar plasma flows and a model for the interpretation of time-distance data. It also discusses the prospects for stellar seismology.

First, we present new observations of the solar velocity field in the upper convection zone. Using surface-gravity waves, we discover that supergranulation exhibits wave-like properties, undergoing oscillations with periods of 6-9 days. This points to a mechanism involving traveling-wave convection and explains the observations of anomalously fast rotation of the supergranulation pattern. Near the solar surface we detect a large-scale 50 m/s flow converging toward active regions. Deeper inside the convection zone, we detect, using acoustic waves, bands of slower and faster meridional motion with a period of eleven years.

Second, we present a new and physically motivated general framework for calculations of the sensitivity of travel times to small local perturbations to a solar model, taking into account the fact that the sources of solar oscillations are spatially distributed. We employ the first Born approximation to model scattering from local inhomogeneities and we use a clear and practical definition of travel-time perturbation which allows a connection between observations and theory. After developing the general theory we compute the sensitivity of surface-gravity-wave travel times to local perturbations in the wave excitation and damping rates. We show that the simple single-source picture, employed in most time-distance analyses, is not correct as it does not reproduce all of the features seen in the distributed-source sensitivity kernels.

Last, we show that future observations of stellar pulsations will provide us with the possibility of determining the angular velocity of a Sun-like star and the inclination angle between the direction of the rotation axis and the line of sight. Measuring the inclination angle is useful to determine the true masses of extra-solar planets detected from the radial velocity shifts of their central star.

Acknowledgments

I would like to thank Phil Scherrer for his advice and continuous support. I am very grateful to Tom Duvall and Aaron Birch for teaching me most of what I know. Many people have contributed, in some form or another, to the work presented in this thesis: Thierry Appourchaux, John Beck, Aaron Birch, Tom Duvall, Peter Giles, Douglas Gough, Brad Hindman, Sasha Kosovichev, Rasmus Larsen, Jesper Schou, and Sami Solanki. Margie Stehle, Brian Roberts, and Keh-Cheng Chu are thanked for technical support. Various discussions with Joel Franklin, Claus Fröhlich, Frank Hill, Jesper Jensen, Charlie Lyndsey, Mark Rast, Manfred Schüssler, Takashi Sekii, Peter Sturrock, Juri Toomre, Nigel Weiss, and Junwei Zhao are gratefully acknowledged. I thank Prof. Joe Keller for accepting to chair my oral exam committee. This thesis is dedicated to my wife Катя for her love and patience, to my parents, and to the memory of Prof. Roger Tayler.

Contents

List of Figures

Chapter 1

Introduction

1.1 Perspective

The most important unsolved problem in stellar physics concerns the origin and variability of magnetic fields. Solar variability is most easily seen in the 11-year periodicity of the number of sunspots and their migration in latitude as the cycle develops, the butterfly diagram. The magnetic field polarity reverses within sunspots groups each 11-yr to produce the 22-yr Hale magnetic cycle. Flares and coronal mass ejections are violent magnetic eruptions that occur mostly during periods of maximum activity and can affect space weather and geomagnetic activity. On longer time scales, solar magnetic activity and irradiance variations must have profound implications for the Earth climate.

The general belief is that a dynamo process operating in the solar convection zone is the origin of the solar magnetic cycle. This process whereby poloidal and toroidal magnetic fields generate and maintain each other invokes differential rotation, magnetic buoyancy and cyclonic convection. The toroidal field is driven by rotational shear at the base of the convection zone, while a large-scale poloidal field is generated from the toroidal field by helical turbulence as it rises through the convection zone. Since the dynamo is a dynamical process, it is important to understand mass flows in the solar interior, such as rotation and convective flows. Motion in meridional planes may also play an important role in redistributing the fields into the observed patterns.

Helioseismology is a tool to learn about the internal structure and dynamics of the Sun. Global helioseimology uses the eigenfrequencies of the global modes of acoustic oscillations to infer rotation and sound speed versus latitude and depth. New techniques of local helioseismology aim to produce three dimensional maps of the flows, temperature inhomogeneities, and possibly magnetic field, inside the Sun. In chapter 2 we use a local technique, known as time-distance helioseismology, to reveal new properties of near-surface horizontal flows and their connection to surface magnetic activity. Chapter 3 is an attempt to develop a firm theoretical basis for the interpretation of time-distance data, which is needed to lead time-distance helioseismology to its full potential, in particular at the smallest spatial scales. Asteroseismology, i.e. global helioseimology on stars other than the Sun, will soon become an important tool to study stellar activity cycles. As several asteroseismology space missions are planned, chapter 4 discusses some of the prospects for detecting rotation in distant stars and other stellar parameters.

1.2   Global Helioseismology

The five-minute solar oscillations were first discovered by Leighton et al. (1962) and interpreted as standing acoustic waves by Ulrich (1970). Deubner (1975) then confirmed that the power in the oscillations is concentrated at discrete frequencies for any given horizontal wavenumber, as predicted by Ulrich's theory. The driving mechanism of the global oscillations of the Sun is believed to be near-surface turbulent convection (e.g. Stein & Nordlund, 2001). The purpose of global helioseismology is to observe and invert the frequencies of the normal modes to infer solar internal properties. Today, millions of global modes have been identified.

The small oscillations of a sphere are represented by a linear superposition of eigenmodes, each characterized by a set of three indices: the radial order, n, the spherical harmonic degree, l, and the azimuthal order, m. For instance, the radial perturbation of the fluid displacement can be written

$$\delta r(r, \theta, \phi, t) = \sum_{n,l} \sum_{m=-l}^{l} a_{nlm} \, \xi_{nl}(r) \, Y_l^m(\theta, \phi) \, e^{\mathrm{i}\omega_{nlm}t} \, , \qquad (1.1)$$

where r is the radius, θ and ϕ are spherical-polar coordinates (colatitude and longitude), and t is time. The Y_l^m are spherical harmonics, a_{nlm} is a complex mode amplitude, and $\xi_{nl}(r)$ is the radial eigenfunction of the mode with frequency ω_{nlm}. For a spherically symmetric star, ω_{nlm} does not depend on m. Rotation, however, removes the $(2l + 1)$-fold azimuthal degeneracy of the frequency of the nonradial mode (n, l). The radial order, n, corresponds to the number of nodes of the radial eigenfunction ξ_{nl}.

The m-averaged power spectrum shown in Fig. 1.1 was obtained with the Michelson Doppler Imager (MDI, Scherrer et al., 1995) onboard the SOlar and Heliospheric Observatory (SOHO). Each ridge in the power spectrum corresponds to a different radial order, n. The lowest frequency ridge ($n = 0$) is for the fundamental (f) modes. The f modes are identified as surface gravity waves, with nearly the dispersion relation for deep water waves, $\omega^2 = gk$, where ω is the angular temporal frequency, $g = 274$ m s^{-2} is the gravitational acceleration at the Sun's surface, $k \simeq l/R_\odot$ is the horizontal wavenumber, and $R_\odot = 696$ Mm is the solar radius. The f modes propagate horizontally. All other ridges, denoted p$_n$, correspond to acoustic modes, or p modes. The restoring force for p modes is pressure. The ridge immediately above the f mode in Fig. 1.1 is known as p$_1$, the next one p$_2$, and so forth. Low-l and high-n modes penetrate deeper inside the Sun. For frequencies above the acoustic cutoff frequency (5.3 mHz), acoustic waves are not trapped inside the Sun. For degrees larger than about 150, wave damping becomes significant and modes are not resolved in l (continuous ridges). Acoustic modes with similar values of ω_{nlm}/l propagate to similar depths inside the Sun.

Perhaps the greatest achievement of helioseismology is to have confirmed the basic standard model of stellar structure by measuring the sound speed as a function of depth with great accuracy. Because rotation breaks the azimuthal symmetry between modes propagating around the sun in opposite directions, it has also been possible to map the internal angular velocity versus depth and latitude, with great detail. The current research, however, focuses on small temporal variations connected to the solar cycle that are likely to be related to the magnetic dynamo. Figure 1.2 shows bands of faster and slower rotation beneath the Sun's surface that migrate in latitude as the present activity cycle unfolds (Schou, 1999). These bands,
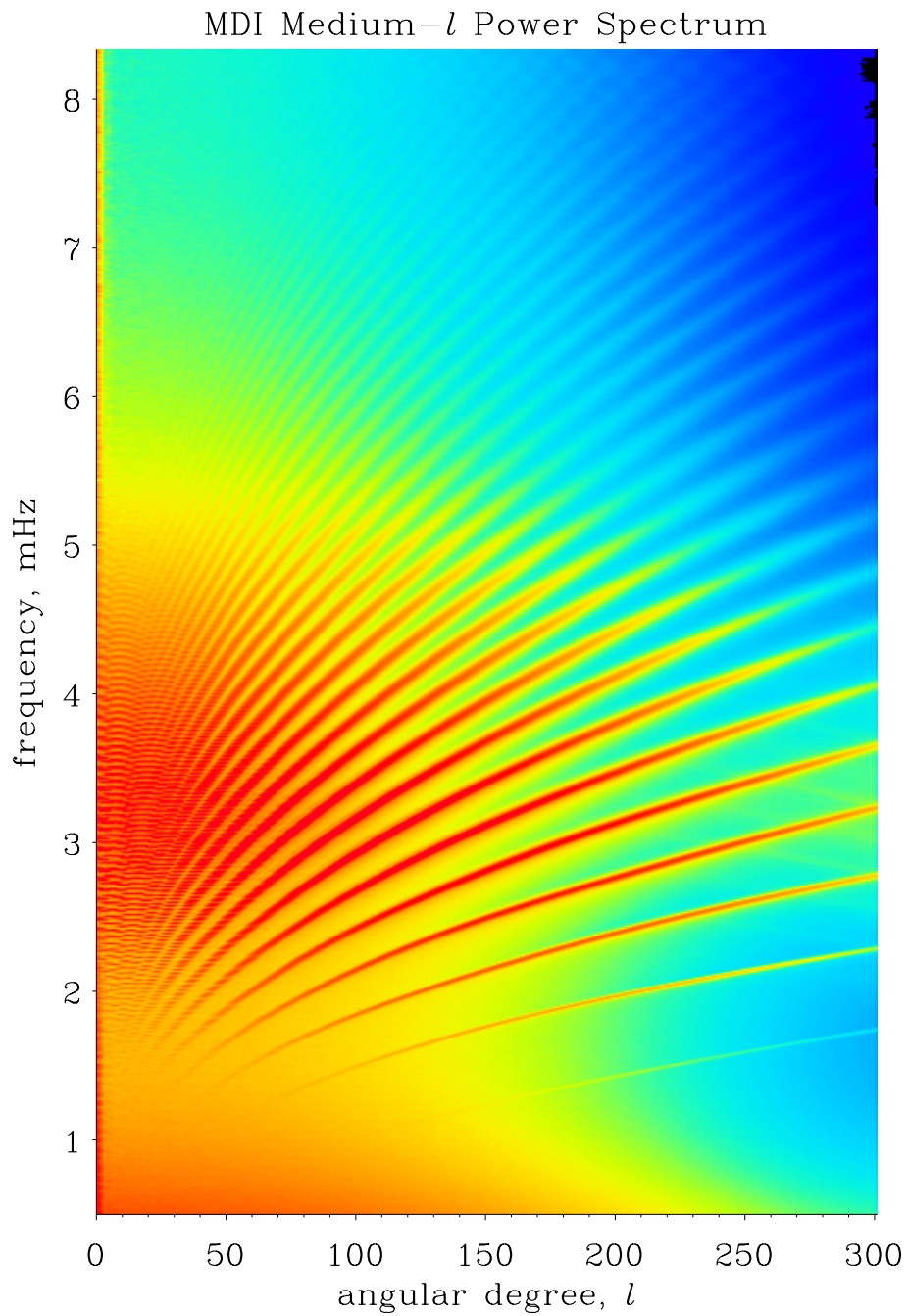
Figure 1.1: m-averaged power spectrum of the five-minute solar oscillations observed in velocity with the MDI instrument.

Zonal flows from MDI f modes
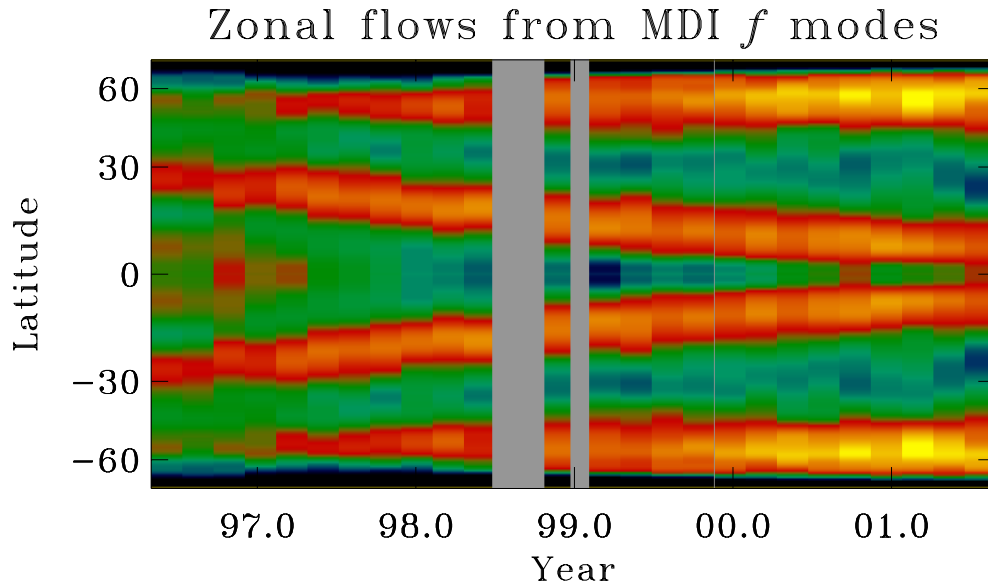
Figure 1.2: Torsional oscillations are bands of slower (blue) and faster (red) rotation with an amplitude of ± 10 m/s that migrate equatorward at low latitudes. This plot was derived from the frequencies of the global f modes in the range $150 < l < 250$. (Courtesy: J. Schou)

called "torsional oscillations", may be driven by the Lorentz force due to a migrating dynamo wave (Schüssler, 1981) or caused by a thermal effect due to surface magnetic fields (Spruit, 2003). Another exciting result concerns the detection of temporal variations in the Sun's asphericity (Antia et al., 2001).

Global mode helioseismology has, however, fundamental limitations: inversions of normal mode frequencies have no resolution in longitude and are unable to distinguish the northern from the southern hemisphere. Also, global helioseismology is not appropriate for measuring flows in meridional planes (meridional circulation). To complement global helioseismology, recent techniques of *local* helioseismology are being developed. Local techniques include ring diagrams (Hill, 1988), acoustic imaging (Chou, 2000), acoustic holography (Lindsey & Braun, 2000) and, the subject of this thesis, time-distance helioseismology.

1.3 Time-Distance Helioseismology

1.3.1 Principle

Time-distance helioseismology (Duvall et al., 1993b) aims at producing three-dimensional maps of the subphotospheric flows, temperature inhomogeneities, and possibly magnetic field. This technique proposes to measure the time it takes for a wavepacket to travel between any two points on the solar surface, in either direction. An acoustic wave packet will reach deeper layers as the horizontal separation between the two points is increased. Surface gravity waves, which propagate horizontally, can be used to probe the near surface. Although the wavefield observed at a given point is due to a random superposition of waves generated by distant source events, the travel time between two locations can be determined from the temporal cross-correlation function of the oscillation signal.

Figure 1.3 shows a theoretical cross-correlation as a function of the distance between two points and the correlation time lag (calculated for a spherically symmetric solar model). The first ridge corresponds to acoustic waves propagating in between the two points without additional reflection from the solar surface. The next ridge corresponds to waves which arrive after one reflection from the surface, and the ridges at greater time delays result from waves arriving after multiple bounces. The backward branch associated with the second ridge corresponds to waves reflected on the far side of the Sun. In most applications, only the direct (first-bounce) travel times are measured.

Local inhomogeneities in the Sun will affect travel times differently depending on the type of perturbation. For example, temperature perturbations and flow perturbations have very different signatures. Given two points on the solar surface, **1** and **2**, the travel time perturbation due to a temperature perturbation is, in general, independent of the direction of propagation between **1** and **2**. However a flow with a component directed along the direction **1** → **2** will break the symmetry in travel time for waves propagating in opposite directions: waves move faster along the flow than against it. Magnetic fields introduce a wave speed anisotropy and will have yet another travel-time signature (this has not been detected yet).
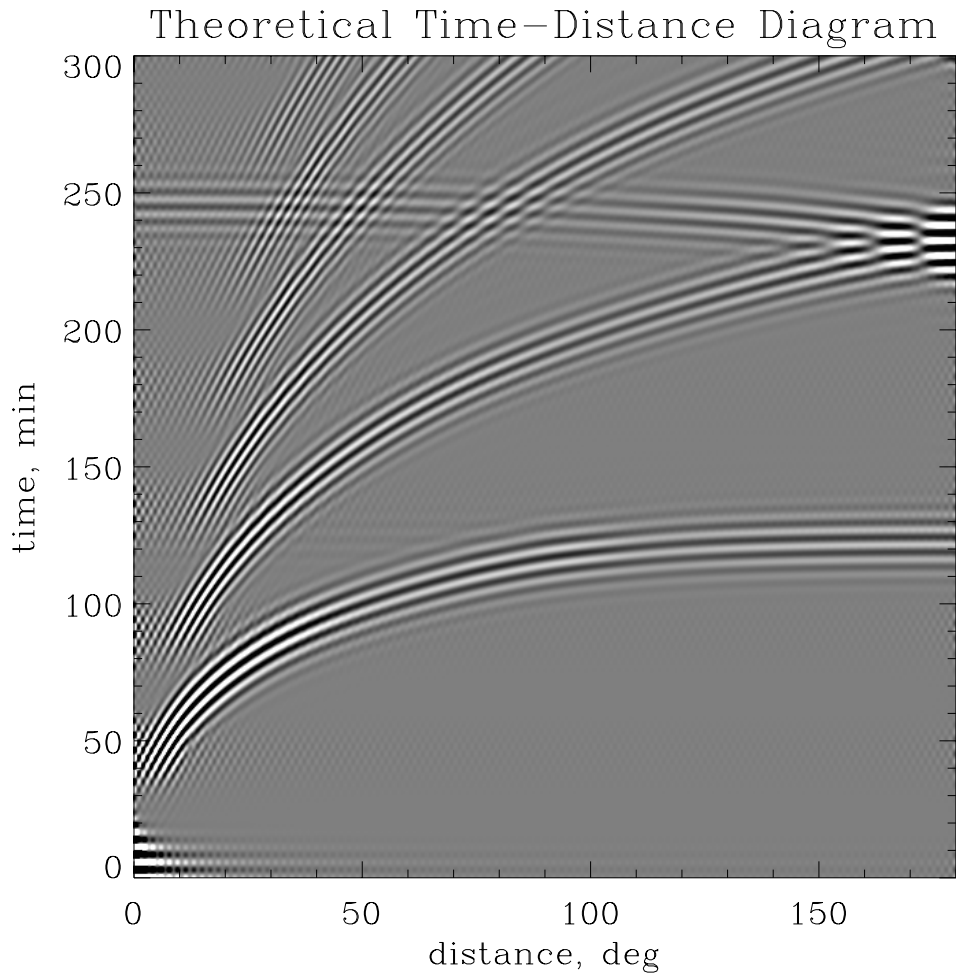
Figure 1.3: Theoretical cross-correlation function for p modes as a function of time lag and arc distance, also called the time-distance diagram. The temporal cross-correlation function between the signal, ϕ, measured at points **1** and **2** is defined by $C(\mathbf{1}, \mathbf{2}, t) = \int \phi(\mathbf{1}, t')\, \phi(\mathbf{2}, t' + t)\, dt'$. In this calculation the solar model is spherically symmetric, and $C(\mathbf{1}, \mathbf{2}, t)$ only depends on the arc distance between **1** and **2** and is symmetric with respect to the correlation time lag, t. (Courtesy: A.G. Kosovichev)

1.3.2   Recent Results

The observational technique for time-distance helioseismology, the measurement of travel times, is rather well established. The interpretation of the travel-time perturbations has not been developed to the same degree. The interpretation of travel times is a two step procedure: the forward problem and the inverse problem. The forward problem of time-distance helioseismology is to compute the sensitivity of travel-time perturbations to local perturbations in a reference solar model, i.e. sensitivity kernels. Traditionally, the observations have been modeled in the ray approximation Kosovichev (1996). The ray approximation is essentially valid when inhomogeneities vary smoothly on a scale larger than the central wavelength of the wave packet. Recently Jensen et al. (2000) and Birch & Kosovichev (2000) computed wave-based kernels in the single source approximation, where waves at one point are assumed to have been generated by a causal source at the other point. We argue in chapter 3 that travel-time sensitivity kernels must include two essential ingredients: (i) a physical description of the wavefield generated by distributed random sources and (ii) the details of the travel-time measurement procedure.

The inverse problem, i.e. using travel-times to learn about how the Sun differs from a model, is a separate issue. Techniques for the 3D inversion of time-distance data have been developed by Kosovichev (1996) and Jensen et al. (1998). The errors in the travel-time measurements, which are essential to solving the inverse problem, are mainly due to realization noise. An important unsolved problem is how to estimate these errors. Notice also that the inverse problem is more or less difficult to solve depending on what data are to be inverted. In a commonly used scheme the travel-time is measured between a central point and a set of surrounding annuli or quadrants. These measurements are mostly sensitive to a region close to the central point. Duvall has implemented a different averaging scheme which would enhance the sensitivity at a target location in the solar interior, by considering all rays which intersect at that location (deep-focusing technique: Duvall, 1995).

Most inversions of travel-time data have been done in the ray approximation. Some of the main results concern large-scale subsurface zonal and meridional flows, convective structures, and flows and sound-speed perturbations below sunspots. Meridional flows, from the equator toward the poles, were first observed in surface

Doppler images with an amplitude of 10-20 m/s (e.g. Howard & LaBonte, 1980; Duvall, 1979). With time-distance helioseismology, Giles et al. (1997) and Giles (2000) showed that these flows persist in depth over a significant fraction of the convection zone. The data are consistent with a small return flow at the base of the convection zone (3 m/s, equatorward). The meridional circulation may play an important role in the transport of magnetic flux and the cyclic polar field reversal. Giles (2000) also confirmed the torsional oscillations.

Convective structures at the supergranular scale (30 Mm) were investigated by Duvall et al. (1997) and Kosovichev & Duvall (1997). In the upper layers (2-3 Mm) horizontal outflows were detected from the center of supergranules. The supergranulation flow pattern becomes very weak below 5 Mm. It is estimated that the correlation between internal flows and surface flows switches sign at depths of 5-10 Mm (Duvall, 1998; Zhao, 2003; Braun & Lindsey, 2003), suggesting the existence of a "return flow" below these depths. The vertical flows of supergranules have been very difficult to measure. A more extensive review of what is known about supergranulation is presented in Sect. 2.2.

One of the exciting areas of time-distance helioseismology concerns sunspots. Downflows were detected below sunspots (Duvall et al., 1996) as well as wave speed perturbations (e.g. Kosovichev et al., 2002). Recently, Zhao et al. (2001) inferred mass flows around a sunspot below the solar surface. Powerful converging and downward directed flows were detected below the sunspot at a depth of 1.5 to 5 Mm, which may provide further evidence for downdrafts and vortex flows suggested for a cluster model of sunspots (Parker, 1979). The sunspot appears to be a relatively shallow phenomenon with a depth of 5-6 Mm. A strong mass flow across the sunspot is found at a depth of 9–12 Mm. In a complementary study, Gizon et al. (2000) used f modes to probe horizontal flows around sunspots in the first 2 Mm beneath the surface. The sunspots are surrounded by outflows (moat flows) with velocities peaking at the outer edge of the penumbra. Moat flows have a fairly well defined boundary, despite azimuthal variations. There is a counter flow at the moat boundary, suggesting the existence of a downflow around the moat. In the penumbra, the subsurface outflow is much smaller than the surface Evershed flow observed in Dopplergrams. The Evershed effect may therefore be a very shallow phenomenon,

as suggested by current theories (Schlichenmaier et al., 1998).

1.3.3 Basic Procedure

Data Requirements

The fundamental data of modern helioseismology are high-resolution Doppler images of the Sun's surface. In order to assess the science that can be extracted from these data by means of local helioseismology, one needs to take into consideration the field of view, the temporal and spatial resolutions, the observation duration, and the overall quality, durability and continuity of the data.

Travel-times are sensitive to inhomogeneities in the vicinity of the geometrical ray path connecting two surface locations. The maximum depth that can be reached is a function of separation distance. For example, distances greater than 45° are required in order to reach the base of the convection zone with p modes. The outer layers of the convection zone are best probed with high-degree f modes.

A cadence of one image per minute is the norm in helioseismology. There is no obvious need for a higher cadence since high-frequency traveling waves have small amplitudes above the Nyquist frequency at 8.33 mHz. A spatial sampling, d, on the Sun's surface gives access to angular degrees up to $l = \pi R_\odot/d$ near disk center. Since there is little mode power beyond $l = 2500$, no better sampling than $d = 0.9$ Mm is required. The study of near-surface phenomena requires high degree modes. Lower degree modes are essential as we probe deeper into the Sun, in combination with high degree modes to evaluate the surface contribution to the total travel-time perturbations.

The level at which a buried localized perturbation is detectable depends on the depth, size and type of the perturbation, and on the observation duration, T. The noise level is expected to go down like $T^{-1/2}$. Duvall recently made an estimate of the magnitude of a flow perturbation that can be detected in one solar rotation as a function of depth in the solar interior (see Gizon et al., 2001a). He constructed travel-time maps using rays that intersect at various target depths (deep-focusing technique). The standard deviation of the inferred velocity values gives an estimate of the "noise" level. Over one solar rotation it should be possible to obtain valuable flow maps (10° resolution) in the upper 100 Mm of the convection zone. It might

however be very challenging to resolve flows near the bottom of the convection zone (Birch, 2002). As will be shown in chapter 2, local flows can be measured with very high precision near the solar surface.

MDI Dopplergrams

The Michelson Doppler Imager has provided line-of-sight Doppler velocity images of the Sun's surface since 1996 with an excellent duty cycle (SOHO is in a halo orbit around the Sun-Earth Lagrange point L_1). MDI Dopplergrams are obtained by combining 4 filtergrams on the wings and core of the Ni 6788 Å absorption line, formed just above the photosphere. Dopplergrams are available at a one minute cadence.

MDI operates under several observing modes. The Dynamics Program runs for 2 to 3 months each year and provides 1024^2 full-disk Doppler images. The plate scale is 2" per pixel, or 0.12 heliographic degrees at disk center ($d = 1.45$ Mm). The orientation is usually parallel to the solar rotation axis. The Structure Program provides continuous coverage: full-disk images are binned onboard into a set of about $20,000$ regions of roughly similar projected areas on the Sun to make use of the narrow telemetry channel. The Structure Program data are used to measure mode frequencies up to $l = 250$ (global helioseismology, Fig. 1.1). MDI can also operate in High-Resolution mode by zooming on a 11' square field of the Sun with a plate scale of 0.625" per pixel and a diffraction-limited resolution of 1.25". A high resolution power spectrum is shown in Fig. 1.4.

Filtering

In general, the first operation in time-distance helioseismology is to track Doppler images at a constant angular velocity, Ω_{track}, to remove the main component of solar rotation (period around 27 days). In this process, images are remapped onto different projection grids, such as the cylindrical equal-area projection or Postel's azimuthal equidistant projection. A series of tracked images form a datacube, i.e. the surface Doppler velocity as a function of the two spatial coordinates and time. Usually, the temporal mean of the images is subtracted from each image in order to remove the latitudinal gradient in rotation, but waves are still advected by flows
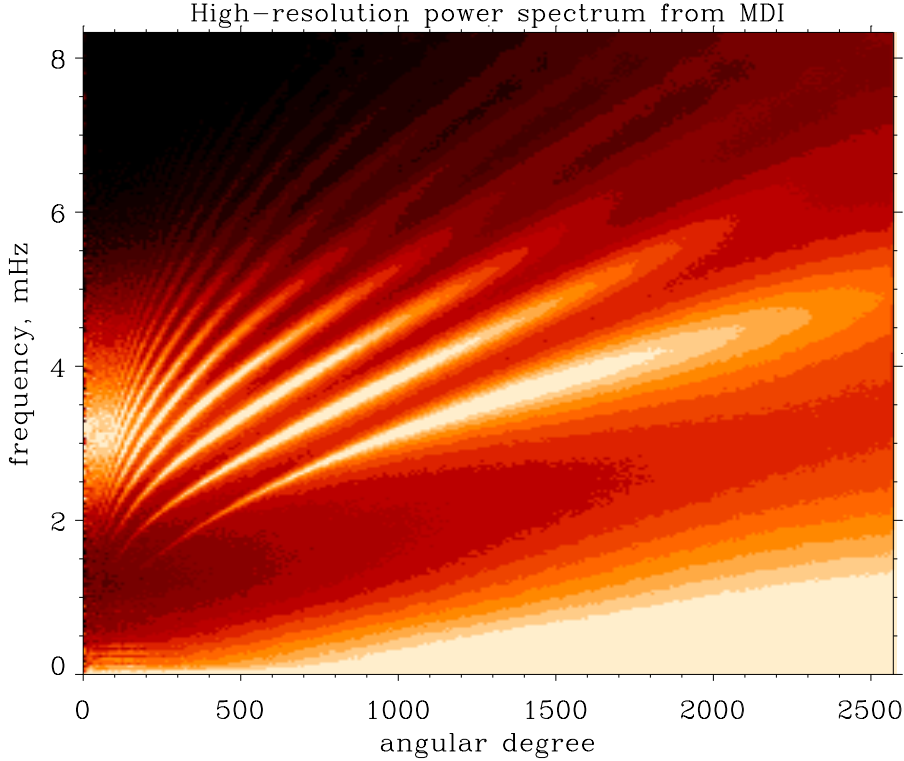
Figure 1.4: Power spectrum from an 8-hour campaign of high-resolution MDI Doppler images. The ridges are visible to very high l values. The power close to zero frequency is due to solar convection, granulation and supergranulation. The lowest frequency ridge corresponds to the surface gravity waves.

measured in a frame co-rotating with the Sun at the angular velocity Ω_{track}.

A filtering procedure is then applied to the datacube in Fourier space (horizontal wavevector $\boldsymbol{k}$ and angular frequency ω). In order to remove granulation and super-granulation noise, frequencies below 1.5 mHz are filtered out. The data are further filtered in Fourier space to select parts of the wave propagation diagram.

For example, in chapter 2, we will use f modes to probe near-surface flows. In this case, all p modes are removed by applying a filter function that only depends on the wavenumber $k = \|\boldsymbol{k}\|$. This function is 1 if, for a given $\boldsymbol{k}$, ω is such that

$$|\omega \pm \sqrt{gk}| < kU_{\text{cut}} \; , \tag{1.2}$$

and 0 otherwise. The parameter U_{cut} selects a region around the f-mode dispersion relation, $\omega^2 = gk$. A reasonable choice is $U_{\text{cut}} = 1$ km/s. This value allows for large

Doppler frequency shifts introduced by flows, and does not let the p_1 ridge through.

In the case of p modes (sect. 2.6) a different filtering is used. The f-mode is filtered out and a phase speed filter is applied. Acoustic waves with the same horizontal phase speed, $v_p = \omega/k$, travel the same horizontal distance Δ (Bogdan, 1997). If we want to measure the travel time for acoustic waves propagating between two surface points separated by Δ, it is appropriate to consider only those waves with the same phase speed v_p. Thus, the choice of the phase speed depends on the travel distance. Standard codes for tracking, remapping, and filtering the data have been developed by Rick Bogart, Tom Duvall, and Peter Giles (see Giles, 2000).

In all cases, the filtered signal, ϕ, can be written as

$$\phi = \mathcal{F}\left\{\hat{\boldsymbol{\ell}} \cdot \boldsymbol{v}\right\}, \tag{1.3}$$

where $\boldsymbol{v}$ is the Eulerian surface velocity and $\hat{\boldsymbol{\ell}}$ is a unit vector in the direction of the line of sight. The operator $\mathcal{F}$ describes the filter used in the data analysis, which includes the time window (time duration T), instrumental effects, and other filtering. Systematic errors in helioseismic analyses can be introduced by imperfections in the Dopplergrams due to focus changes, plate scale, detector misalignment, and point-spread function. These imperfections are symbolically included in the operator $\mathcal{F}$.

Cross-Correlations

The main computation in time-distance helioseismology is the temporal cross-correlation, $C(\mathbf{1}, \mathbf{2}, t)$, between the signal, ϕ, measured at two points, $\mathbf{1}$ and $\mathbf{2}$, on the solar surface,

$$C(\mathbf{1}, \mathbf{2}, t) = \frac{1}{T} \int_{-\infty}^{\infty} \mathrm{d}t' \, \phi(\mathbf{1}, t') \, \phi(\mathbf{2}, t' + t), \tag{1.4}$$

where T is the time duration of the observation. The cross-correlation is useful as it is a phase-coherent average of inherently random oscillations. It can be seen as a solar seismogram, providing information about travel times, amplitudes, and the shape of the wave packets traveling between any two points on the solar surface. For surface gravity waves, the cross-correlation displays two branches (Fig. 1.5). The positive-time branch corresponds to waves moving from $\mathbf{1}$ to $\mathbf{2}$, and the negative-time branch represents waves moving in the opposite direction. For acoustic waves
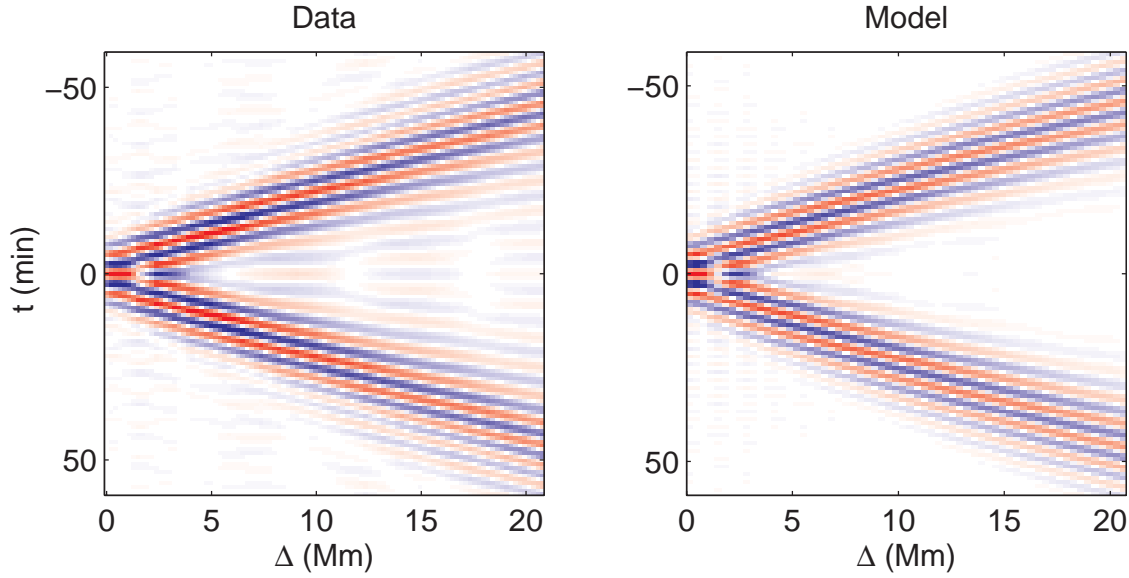
Figure 1.5: Surface gravity wave cross-correlations. The left panel shows an example of an observed cross-correlation $C(\mathbf{1}, \mathbf{2}, t)$ averaged over all possible pairs of points ($\mathbf{1},\mathbf{2}$), as a function of distance $\Delta = \|\mathbf{2} - \mathbf{1}\|$ and time t. Red refers to positive values and blue to negative values. The observations are 8-hr time series from the MDI high-resolution field of view. The filter $\mathcal{F}$ is chosen to isolate surface gravity waves. The right panel shows the theoretical cross-correlation from the model which we discuss in § 3.3.

there are additional branches, at larger absolute time, corresponding to multiple bounces off the surface in between $\mathbf{1}$ and $\mathbf{2}$ (Fig. 1.3).

Spatial Averaging

Since solar oscillations are driven by a stochastic process, the line-of-sight velocity is a sample function of space and time drawn from some probability distribution. The cross-correlations have a significant amount of "realization noise", and it has proved difficult to measure wave travel times between two individual pixels on the solar surface for $T < 1$ day. In order to enhance the signal-to-noise ratio, we construct various spatial averages of the cross-correlations before measuring the travel times.

In chapter 2 we will essentially be interested in measuring flows. To measure separately flows in the west direction and in the north direction, the cross-correlations

are averaged over quadrants:

$$C^{\mathrm{we}}(\boldsymbol{x},\Delta,t) = \iint_{W(\Delta)} C(\boldsymbol{x},\boldsymbol{2},t)\,\mathrm{d}\boldsymbol{2} + \iint_{E(\Delta)} C(\boldsymbol{1},\boldsymbol{x},t)\,\mathrm{d}\boldsymbol{1} \,, \qquad (1.5)$$

$$C^{\mathrm{ns}}(\boldsymbol{x},\Delta,t) = \iint_{N(\Delta)} C(\boldsymbol{x},\boldsymbol{2},t)\,\mathrm{d}\boldsymbol{2} + \iint_{S(\Delta)} C(\boldsymbol{1},\boldsymbol{x},t)\,\mathrm{d}\boldsymbol{1} \,, \qquad (1.6)$$

where W, E, N, and S are four quadrants of an annulus of radius Δ centered on the spatial pixel $\boldsymbol{x}$. The annulus is one pixel thick. These quadrants correspond to the cardinal directions west, east, north, and south (by convention, the direction of solar rotation is west). In practice, the average cross-correlation for each quadrant is obtained by cross-correlating the signal at the central pixel, $\boldsymbol{x}$, with the signal averaged over the quadrant. A third cross-correlation, C^{oi}, is obtained by averaging over the whole annulus:

$$C^{\mathrm{oi}}(\boldsymbol{x},\Delta,t) = \iint_{T(\Delta)} C(\boldsymbol{x},\boldsymbol{2},t)\,\mathrm{d}\boldsymbol{2} \qquad (1.7)$$

where T is the total area of the annulus. The positive-time part of C^{oi} contains information about outgoing waves from $\boldsymbol{x}$, and the negative-time part about waves converging toward the center of the annulus. In the case of the f modes, which propagate horizontally, C^{oi} can be used to provide a proxy for the horizontal divergence of the flow field.

Travel Times

At fixed $\boldsymbol{x}$ and Δ, a cross-correlation oscillates around two characteristic (first-bounce) times $t = \pm t_{\mathrm{g}}$. Duvall et al. (1997) measure travel times by fitting a Gaussian wavelet to the cross-correlation. This procedure distinguishes between group and phase travel times, by allowing both the envelope and the phase of the wavelet to vary independently. The positive-time part of the cross-correlation is fitted with a function of the form

$$w_{+}(t) = A\,\exp[-\gamma^2(t - t_{\mathrm{g}})^2]\,\cos[\omega_0(t - \tau_{+})] \,, \qquad (1.8)$$

where all parameters are free, and the negative-time part of the cross-correlation is fitted separately with

$$w_-(t) = A \, \exp[-\gamma^2(t + t_{\mathrm{g}})^2] \, \cos[\omega_0(t + \tau_-)] \, . \tag{1.9}$$

The times τ_+ and τ_- are the so-called phase travel times. The basic observations in time-distance helioseismology are the travel-time maps $\tau_+(\boldsymbol{x}, \Delta)$ and $\tau_-(\boldsymbol{x}, \Delta)$, measured for each of the three averaged cross-correlations, $C^{\mathrm{we}}(\boldsymbol{x}, \Delta, t)$, $C^{\mathrm{ns}}(\boldsymbol{x}, \Delta, t)$, and $C^{\mathrm{oi}}(\boldsymbol{x}, \Delta, t)$.

Let us consider the cross-correlation C^{we}. The phase travel time τ_+ is for waves that propagate westward, and τ_- is for waves that propagate eastward. For f-modes, which propagate horizontally, the travel time difference $\tau_- - \tau_+$ is proportional to the westward component of the flow in the neighborhood of $\boldsymbol{x}$. The northward flow is related to the south-north travel-time difference. This interpretation is valid for flows that vary smoothly within a distance Δ from $\boldsymbol{x}$. In Sect. 2.1, we determine a simple calibration constant that enables to convert the f-mode travel-time differences into horizontal flow velocities (in m/s). In the case of the cross-correlation C^{oi}, the difference $\tau_- - \tau_+$ is a proxy of the horizontal divergence of the local flow, while the mean travel $(\tau_- + \tau_-)/2$ is connected to local wave-speed perturbations.

A fundamental question is how a general perturbation in internal solar properties affects travel times (the forward problem). This question is addressed in detail in chapter 3.

1.4   Results Contained in this Work

In chapter 2 we present new observations of the solar velocity field in the upper convection zone. To achieve this we employ the technique of time-distance helioseismology which consists in measuring the time it takes for seismic waves to propagate between different points on the solar surface.

Surface-gravity waves (f modes) are used to map the near-surface horizontal flows with a high spatial resolution. We discover that supergranulation exhibits wave-like properties, undergoing oscillations with periods of 6-9 days. This points to a mechanism involving traveling-wave convection, and explains the observations

of anomalously fast rotation of the supergranulation pattern. In addition, the effect of the Coriolis force on supergranular flows is observed for the first time.

We also study flows near regions of magnetic activity. Near the solar surface, we detect a large-scale 50 m/s flow converging toward active regions, whose origin is unknown. Deeper inside the convection zone, and using acoustic waves (p modes), we detect a new component of the solar dynamics: the north-south component of the "torsional oscillations", i.e. bands of slower and faster meridional motion with an 11-yr period.

In chapter 3, we discuss the general forward problem of time-distance helioseismology, i.e. the computation of travel-time perturbations which result from perturbations to a solar model. We present a new and physically motivated general framework for calculations of the sensitivity of travel times to small local perturbations to solar properties, taking into account the fact that the sources of solar oscillations are spatially distributed. In addition to perturbations in sound speed and flows, this theory can also be applied to perturbations in the wave excitation and damping mechanisms.

Our starting point is a description of the wave field excited by distributed random sources in the upper convection zone. We employ the first Born approximation to model scattering from local inhomogeneities. We use a clear and practical definition of travel-time perturbation, which allows a connection between observations and theory. In this framework, travel-time sensitivity kernels depend explicitly on the details of the measurement procedure.

After developing the general theory we consider the example of the sensitivity of surface gravity wave travel times to local perturbations in the wave excitation and damping rates. We derive explicit expressions for the two corresponding sensitivity kernels. We show that the simple single-source picture, employed in most time-distance analyses, does not reproduce all of the features seen in the distributed-source kernels developed in this chapter.

In chapter 4 we address prospects for asteroseismology. Long and continuous space-based observations of stellar pulsations will be made available in a few years.

Asteroseismology provides us with the possibility of determining the angular velocity of a pulsating Sun-like star, Ω, and the angle, i, between the direction of the rotation axis of the star and the line of sight. A knowledge of i is important not just for obtaining improved stellar parameters, but also in order to determine the true masses of extra-solar planets detected from the radial velocity shifts of their central stars. By means of Monte-Carlo simulations, we estimate the precision on the measurement of i and other stellar parameters. We find that the inclination angle can be retrieved accurately when $i \gtrsim 30°$ for stars that rotate at least twice faster than the Sun.

We also investigate the signature of localized magnetic activity in the spectrum of the global modes of oscillation of a Sun-like star. We estimate the measurement precision of the even splitting coefficient a_2 (a measure of asphericity). It is found that, under certain conditions, some information can be retrieved about the surface distribution of stellar activity.

Chapter 2

Time-Distance Helioseismology: Observations [1]

2.1   Time-Distance Helioseismology with f Modes

In this introductory section, we demonstrate the utility of f-mode time-distance helioseismology. Travel times measured for the f mode have been used to study flows near the solar surface in conjunction with simultaneous measurements of the magnetic field. We measure the spatial and temporal power spectra of the supergranular flows for a six-day observing sequence. Previous measurements of Doppler surface rotation, small magnetic feature rotation, supergranular pattern rotation, and surface meridional circulation are confirmed and compared to the f-mode measurements.

2.1.1   Introduction

The fundamental, or f, modes are classified as surface gravity waves with very nearly the classical water-wave dispersion relation, $\omega^2 = gk$, where ω is the angular frequency, $g = 274$ m s^{-2} is the gravitational acceleration at the Sun's surface, and $k = l/R_\odot$ is the horizontal spatial wavenumber expressed in terms of the spherical harmonic degree l and the solar radius $R_\odot$. High-degree f modes propagate horizontally. MDI full-disk data show that f modes are excited with a similar frequency envelope to the acoustic p modes, peaking near circular frequency $\nu = \omega/2\pi = 3$ mHz with a full width at half maximum of 1 mHz. The envelope peak occurs near $l = 880$ and the full power width covers the degree range 600-1200. In this range the f mode kinetic energy is concentrated within 2 Mm of the solar photosphere.

There are several advantages to using the f mode as a tracer of flows near the solar surface. Using the time-distance technique, there is direct sensitivity to both horizontal components of the flow. Already this is much better than direct Doppler measurements, which see only the line-of-sight component. In this respect the f-mode time-distance technique is similar to correlation tracking of granulation (DeRosa et al., 2000). Other techniques for measuring vector flows include ring diagrams (Hill, 1988), p-mode time-distance helioseismology (Duvall et al., 1996) and knife-edge diagnostics (Lindsey et al., 1996). With f modes, there is no direct sensitivity to vertical motion, although by examining the horizontal divergence it may be possible to estimate the vertical motion. Because we know the f-mode eigenfunctions,

the depth over which we are averaging is well defined (Fig. 2.1a).

As f modes have not been been used in time-distance helioseismology before, the purpose of this section is to test the utility of the technique by first observing well-known phenomena. To this end, we simultaneously measure three tracers of solar rotation that in the past have given similar yet consistently different rotation rates (Beck, 2000). By using the same instrument with simultaneous observations, we expect that some of the possible systematic errors will be common. The first tracer we use is the f-mode advection rate determined from time-distance helioseismology, which we identify as a proxy of the surface rotation. This is compared to the surface Doppler rate averaged over 18 years by Snodgrass & Ulrich (1990). The tracer that gives the highest apparent rotation rates is the supergranulation pattern (Duvall, 1980; Snodgrass & Ulrich, 1990). The third tracer is obtained by tracking the small magnetic features (Komm et al., 1993b).

2.1.2   Observations

MDI full-disk Dopplergrams (Scherrer et al., 1995) were used to study flows for the time period 1999 April 14, 16h UT to 1999 April 20, 16h UT, or a total of six days. The region studied was centered at Carrington longitude $180°$. This particular region was picked because it was quiet and the data coverage was very good as it was during MDI's three months of continuous coverage for 1999 (97.3% of the minutes had usable data during the six days). Three separate regions were studied, with all three of size $45°$ in longitude and in latitude, with one centered on the equator, one centered at $40°$ North and the other at $40°$ South. There is some overlap between the regions, and as the equatorial and higher latitude areas were tracked at different rotation rates, this difference was used to calibrate one of the signals, as described below. The B_0 angle was $-5°$ during the observations, and we estimate that latitudes ranging from $-55°$ to $+45°$ can be analyzed safely.

Doppler images were calibrated and located in the CCD frame using the normal MDI pipeline routines. The first step in the analysis is the tracking of the regions to be studied. Images were interpolated onto Postel's azimuthal equidistant projection (Pearson, 1990) centered on a point in latitude $0°$, $+40°$, $-40°$ and at longitude
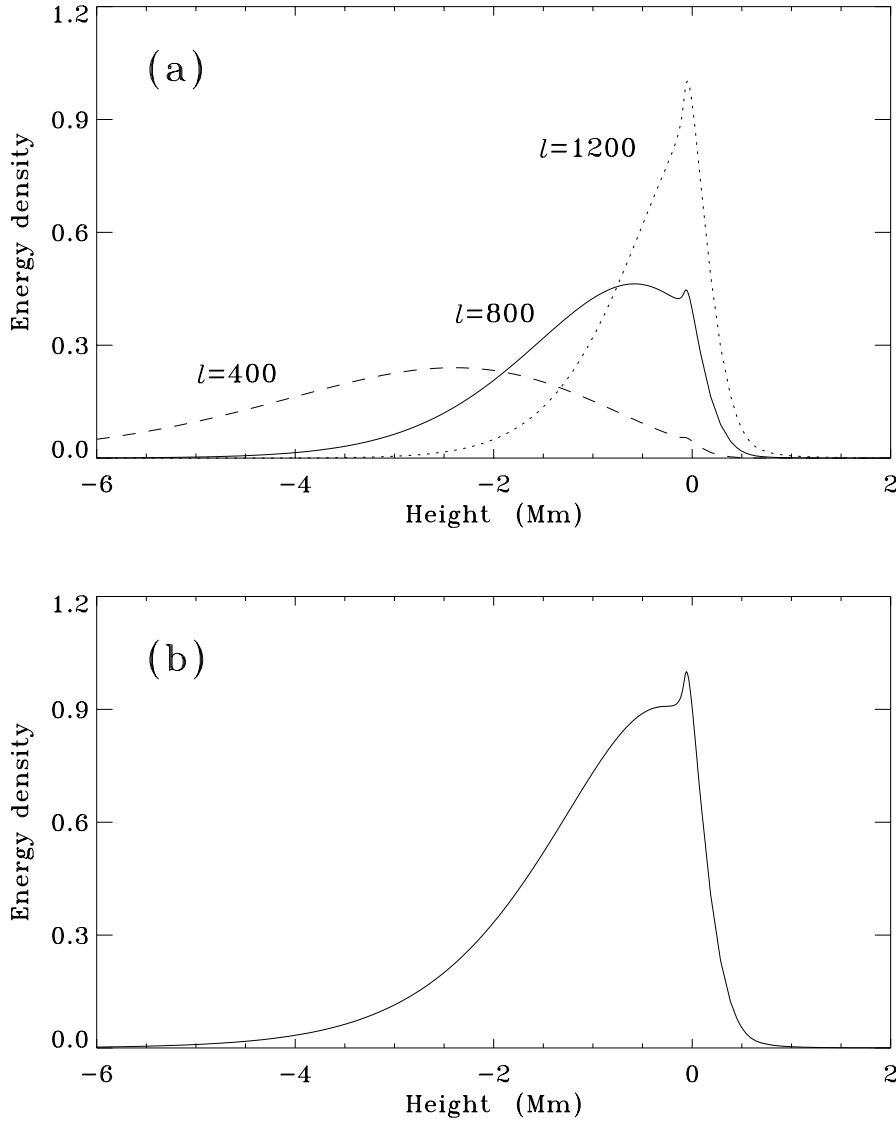
Figure 2.1: F-mode kinetic energy density versus height z, defined by $\rho(z)e^{2kz}$ where ρ is the density and k the wavenumber. **(a)** Kinetic energy density for f modes with degrees 400, 800 and 1200. Calculations are for a plane-parallel atmosphere with constant gravity. The height is measured from the photosphere (radius 695.99 Mm). A free surface is placed 2 Mm above the photosphere. The internal density is taken from the standard solar model of Christensen-Dalsgaard et al. (1993). Above the temperature minimum, density is from the chromospheric model C of Vernazza et al. (1981). Curves are normalized to the same arbitrary constant. **(b)** Average kinetic energy density versus height for the f modes used in this study. The mean and standard deviation of this distribution are respectively -1.05 Mm and 1.01 Mm. The location of the absolute maximum coincides with the highly superadiabatic layer.

180°. The azimuthal equidistant projection is linear in great-circle distance measured from the central point of the projection to outlying points. This projection is used rather than a longitude-sin(latitude) projection so that three-dimensional Fourier filtering can be used on the data more effectively. The regions were followed at a rate appropriate for the central latitude and consistent with the supergranule pattern rate measured by Snodgrass & Ulrich (1990). During the time period of the observations MDI was observing both full-disk Dopplergrams and magnetograms with one-minute cadence. Both Dopplergrams and magnetograms were processed by the above procedure so that detailed comparisons between the two could be made. A smooth background image (spatial scale $0.2\,R_\odot$) was subtracted from each Dopplergram before the projection.

The magnetograms were also processed to remove cosmic rays and smoothed in time. To remove the effect of cosmic rays striking the CCD during the exposure/readout, the temporal pixel-by-pixel median of three successive images was taken and the resultant median replaced the middle image. The cosmic rays commonly affect pixels in a small neighborhood but only for a single image and so are generally removed by the median procedure. This procedure also smooths the field on a three-minute time scale. After the median procedure, images over a ten-minute interval are averaged and a new time series is constructed of these ten-minute means.

To obtain travel times, a similar procedure is used as for p modes (Duvall et al., 1997), except that the filtering is a little different. For each 8-hour interval, the datacube goes through a three-dimensional Fourier filter that cuts off power below 2 mHz (mostly supergranulation) and isolates the f mode ridge. The resultant power spectrum peaks near $\nu = 2.9$ mHz and spherical harmonic degree $l = 800$. The full widths at half maximum are $\Delta\nu = 0.7$ mHz and $\Delta l = 400$. Figure 2.1b displays the average kinetic energy density versus depth for the average wave packet. We see that we can probe the first 2 Mm below the solar surface, with maximum sensitivity at a depth of 1 Mm.

The temporal signal at a central pixel is cross-correlated with the signals in the four quadrants of an annulus centered in arc distance, as described in chapter 1. These quadrants are centered on the cardinal directions north, south, east, and west. Before measuring the travel times, average cross correlations are made for the

waves propagating in the directions west-east and north-south. Additional averages are made for waves propagating outward from the center and inward toward the center of an annulus. The difference between outward and inward travel times is expected to be proportional to the horizontal divergence of the flow. In addition, to make the signal-to-noise acceptable, the cross correlations for a 2×2 grid of origins are averaged, thereby reducing the spatial resolution of the resultant maps by a factor of two below that of the original data.

The thickness of an individual annulus is the same as the spatial sampling of the original images, or $0.12°$. Four of these are combined during the fitting process, and so all pixels from $0.42°$ to $0.9°$ are used in the measurements. The angle $0.9°$ corresponds to a distance of 7.5 pixels in the original spatial sampling and 3.75 in the reduced spatial scale.

The cross correlations were then fit by least squares to a harmonic function multiplied by a gaussian envelope, sometimes called a Gabor wavelet. This functional form has been used for the case of p modes (Kosovichev & Duvall, 1997), and seems to work reasonably well for the f modes. The difference between phase times for counter-propagating waves is proportional to the local horizontal flow velocity (Kosovichev & Duvall, 1997).

2.1.3 Supergranulation Pattern

Supergranulation on the surface of the Sun is a pattern of horizontal outflows with a distinct scale of 30 Mm and an apparent lifetime of 1 day, outlined by a network of small magnetic features. An example of the divergence signal (inward minus outward travel time) for one of the 18 8-hour intervals analyzed is shown in Fig. 2.2 with magnetic field information overlaid. A white, or positive signal, corresponds to an outflow from the center. From the size of the features present, their lifetime, and the presence of the magnetic field in the dark lanes, we identify supergranulation as the main contributor to the signal. This can also be seen by making a spatial power spectrum of the 18 frames covering the 6 days. Averaging over all temporal frequencies, the spatial spectrum is shown in Fig. 2.3. The peak near degree $l = 120$ is characteristic of the supergranulation and has been seen before in the surface Doppler observations (e.g. Hathaway et al., 2000). The histogram of the divergence
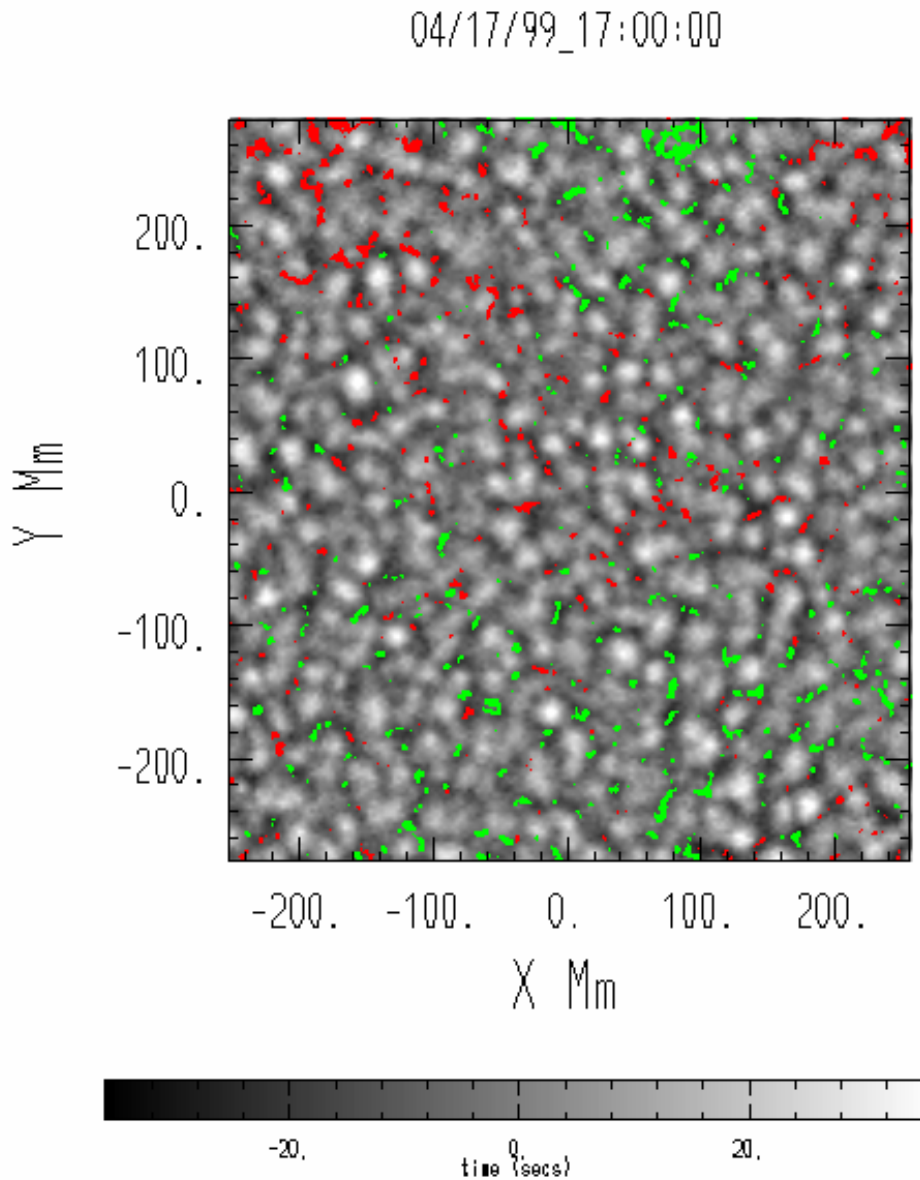
Figure 2.2: Example of the divergence signal (inward travel times minus outward times) with small magnetic features overlaid. Magnetic field is displayed as green and red for the two polarities when the magnitude of the field is larger than 15 Gauss. The gray scale is for the divergence signal with white shades for outflow and dark shades for inflow. The color-bar indicates the travel time difference in seconds. The line Y=0 corresponds to the equator and X=0 corresponds to Carrington longitude 180°. The time-distance data is averaged over 8.5 hours starting at the time shown on top.
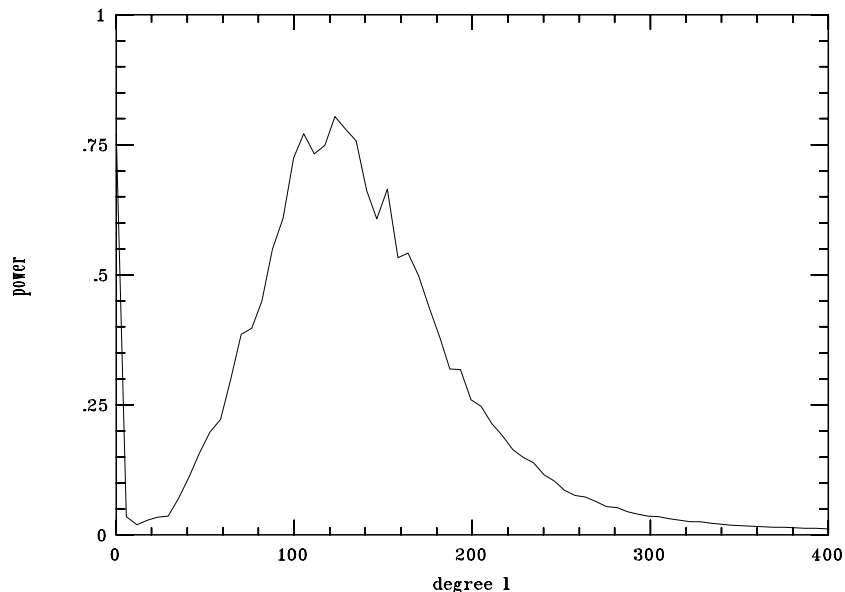
Figure 2.3: Power versus horizontal wavenumber averaged over temporal frequency and azimuth for the divergence signal (inward travel times minus outward times). The power scale is arbitrary.

signal is shown in Fig. 2.4. An asymmetry between the regions of divergent and convergent flows is clearly seen. There are more points associated with a convergent flow than with a divergent one, and the distribution is skewed. It should be noted that both these properties are present in simple models of incompressible hexagonal convection near onset (e.g. Veronis, 1959).

In Fig. 2.5 we show the temporal power spectrum of the divergence signal averaged over all spatial frequencies. We see that much of the power is at very low frequencies, with 85% of the power below 6 μHz. This is reasonably consistent with a Lorentzian-shaped temporal spectrum, as suggested in the Harvey (1985) model, although we note that the power peaks at a non-zero frequency. We also studied the temporal correlation of these images and found that it was significantly negative (-0.1) at a time lag of 3 days, consistent with the observation that new supergranules appear near the boundaries of old supergranules (Shine et al., 2000).
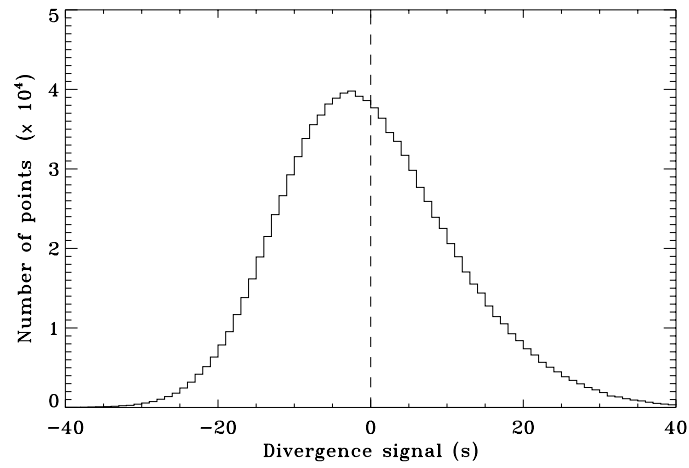
Figure 2.4: Histogram of the divergence signal (inward travel times minus outward times). The maximum of the histogram occurs near -2.5 s and the skewness is 0.42. There are about 20% more points with negative divergence than positive divergence.
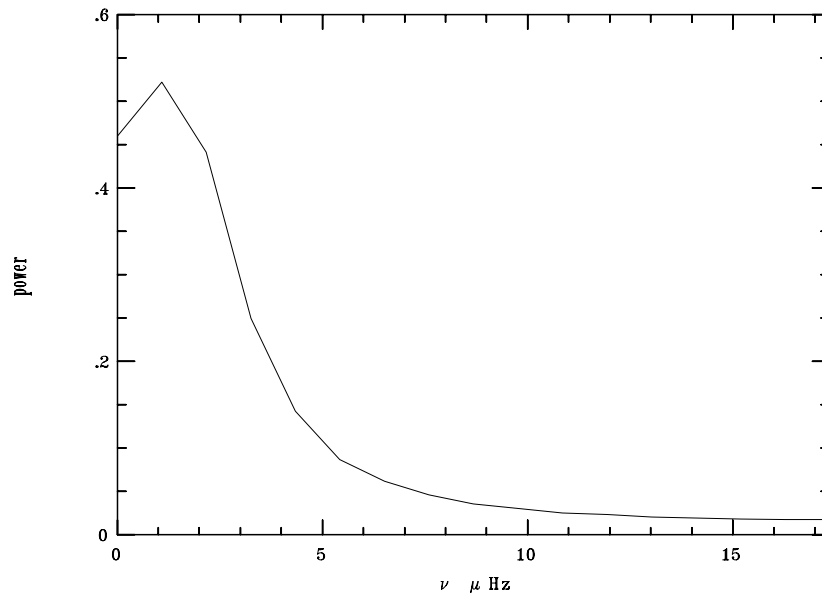
Figure 2.5: Power of the divergence signal versus temporal frequency averaged over horizontal wavenumber. The power scale is arbitrary.

2.1.4   Rotation and Meridional Circulation

To measure differential rotation, we take the difference between the eastward and the westward travel times, $\delta\tau^{\mathrm{ew}}$. After averaging in longitude, we obtain $\delta\tau^{\mathrm{ew}}(\lambda)$ versus latitude, λ. In order to convert the travel-time difference into a westward velocity, v_x, we seek a calibration constant α such that

$$v_x(\lambda) = \alpha\ \delta\tau^{\mathrm{ew}}(\lambda)\ . \tag{2.1}$$

Because the three regions centered at latitude $-40°$, $0°$, and $40°$ were tracked at different known tracking rates and because they overlap in latitude (each is $90°$ wide), it is possible to derive α from the data. We require that the velocity be the same for the equatorial region (eq) and for the northern region (up) where they overlap:

$$V(0°) + \alpha\ \delta\tau^{\mathrm{ew}}(\lambda)\big|_{\mathrm{eq}} \equiv V(40°) + \alpha\ \delta\tau^{\mathrm{ew}}(\lambda)\big|_{\mathrm{up}} \qquad \mathrm{for}\quad 35° < \lambda < 45°\ , \tag{2.2}$$

where $V(\lambda)$ is the differential rotation velocity from Snodgrass & Ulrich (1990). The optimal calibration constant is $\alpha = 7.08$ m s^{-2}. The angular velocity is then given by $\Omega = (v_x + V)/(R_\odot \cos\lambda)$. As a check, we then compare the angular velocity in the overlap region between the equatorial and southern regions and find excellent agreement within 0.3 nHz.

The angular velocity Ω from f modes is compared with the long-term average of the surface Doppler rate in Fig. 2.6a. We see that the two agree rather well. We also measured the near-surface meridional circulation from the south-north travel-time differences using the calibration constant α. The results are shown in Fig. 2.6b, compared with the motion of the magnetic features measured by Meunier (1999). It appears that from six days of data we can make remarkably consistent measurements of rotation and meridional circulation.

To study rotation of the supergranulation pattern we tracked the divergence signal in time, with a time-lag of 8 hour. At each latitude, one-dimensional spatial cross-correlations were computed. The cross-correlations are averaged and then fit to a Gaussian function. The spatial shift at correlation maximum is converted to a longitude, divided by eight hours, and added to the tracking rate to determine
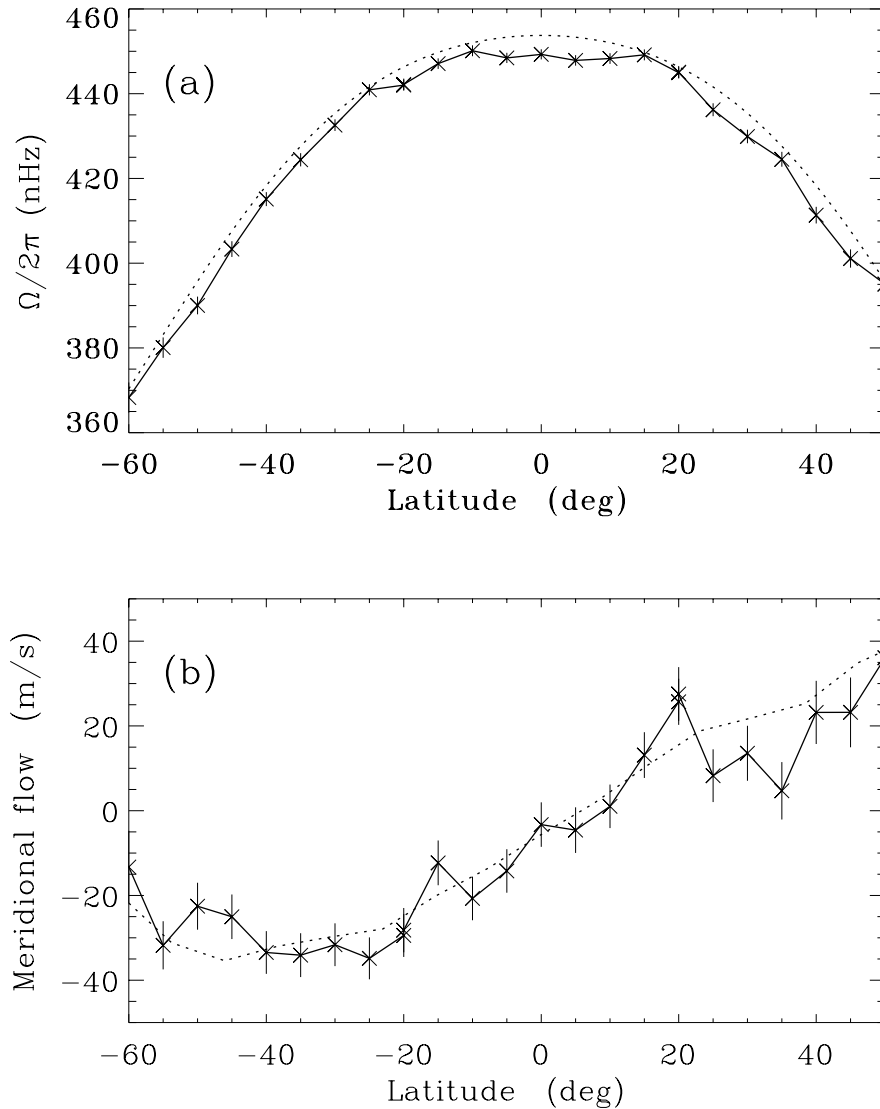
Figure 2.6: (a) f-mode advection rotation rate (solid curve) and surface Doppler rotation (dashed curve) versus latitude. The surface Doppler rate is the average from 1967-84 given by Snodgrass & Ulrich (1990), which is found to be 3.4 nHz higher on average. (b) Meridional circulation versus latitude. The solid curve and crosses are the f-mode measurements. The dashed curve is from the motion of the small magnetic features (Meunier, 1999) for the first year of MDI operation in 1996-97.
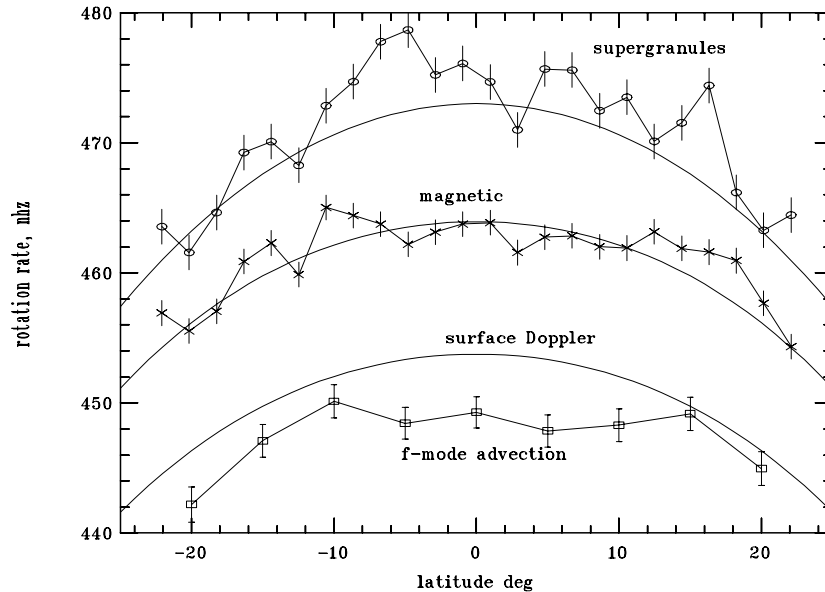
Figure 2.7: Rotation rates measured in this work compared with previous works. From the top, the open circles with error bars are derived from the supergranulation patterns of the divergence signal (this work) and the solid line through the values is the supergranulation feature rate for years 1967-1987 of Snodgrass & Ulrich (1990). In the middle, the crosses with error bars are from the MDI magnetic correlations (this work) and the underlying solid line plots the average over years 1975-1991 of the small magnetic feature rate (Komm et al., 1993b). At the bottom, the open squares with error bars are the f-mode advection measurements from this study and the nearby solid line is from the average surface Doppler rotation rate for years 1967-1984 of Snodgrass & Ulrich (1990).

a pattern rotation rate. The procedure for the small magnetic features is similar except that the time-lag is ten minutes, as this gave the smallest errors.

The three rotation measures are compared with previous work in Fig. 2.7. We find that there is good agreement with earlier data averaged over decades. This figure confirms differences between the rotation rate of the plasma near the solar surface and the apparent rotation rates of supergranulation and magnetic features. It was suggested long ago (Foukal, 1972) that the difference between the rotation of magnetic patterns and the surface Doppler rate may be due to magnetic structures being "rooted" in deeper, more rapidly rotating layers. The high supergranulation rate is more puzzling. An explanation is presented in the next section.

To learn more about the difference between the rotation rates of the supergranulation pattern and the small magnetic features, we examined a movie made from frames similar to Fig. 2.2. After removing differential rotation, the movie confirmed that a small motion of the magnetic features can be seen in the eastward direction (slower rotation) with respect to the supergranulation network. The magnetic features stayed in the dark lanes (convergent flows) as this slow apparent drift took place.

Simultaneous measurements of velocity and magnetic field with MDI is a powerful combination to study the dynamics of the near solar surface. Time-distance helioseismology of the f mode has been shown to be a useful tool to study horizontal flows. In the next section, we focus on the mysterious dynamics of the supergranulation using the same time-distance technique but a much longer MDI data set.

2.2   The Dynamics of Supergranulation

The dynamics of the supergranulation is poorly understood and there is as yet no explanation for the observation that the supergranular pattern appears to rotate faster than the magnetic features. In this section we show that supergranulation undergoes oscillations and supports waves with periods of 6-9 days. The nature of supergranulation appears to be travelling-wave convection. The waves are predominantly prograde, which explains the apparent superrotation of the pattern.

2.2.1   Introduction

Convective-like motion on the solar surface consists of two main components: granulation and supergranulation. Granules, with a typical size of 1.5 Mm, are well understood as a convective phenomenon and can be studied with realistic numerical simulations (Stein & Nordlund, 2000). Supergranules, however, have remained puzzling since the early observations by Hart (1954). Hart (1956) described local variations with a spatial periodicity of 26 Mm and an rms velocity of 0.3 $\mathrm{km\,s^{-1}}$, but rejected a convective instability as an explanation on the basis that the scale of the phenomenon was too "large". In a classic paper, Leighton et al. (1962) reported "large cells of horizontally moving material distributed roughly uniformly over the entire solar surface" that are outlined by the chromospheric network. It is worth citing the physical description of supergranulation given by Simon & Leighton (1964) nearly forty years ago, as it summarizes the current paradigm:

"*The observed cellular flow pattern of the large-scale motions is strongly suggestive of convective motions, and we tentatively propose that we are dealing with a larger scale version of the familiar photospheric granulation – a supergranulation. The observed dimensions of the large cells (32000 km) suggest that they originate in the Sun's convective envelope which extends from the bottom of the photosphere to depths of 5000-100000 km. Although the lifetime (20 h) of the supergranulation appears very long at first glance, if one considers the small velocity and the large dimensions one finds that the matter in all probability does not circulate more than once. This fact, coupled with the very irregular size and shape structure of the cells, suggests that we are observing an example of non-stationary convection, rather than*

the stationary laminar convection of classical Bénard cells. Since we are able to observe the supergranulation only from above, we have no means of determining the geometrical shape of the convection pattern; it may be either a circulating flow or a columnar convection such as a cloud or plume... In view of these considerations it seems proper to ask whether there is a possible mechanism in the Sun which would select cell depths of roughly 5000 km. A possible answer lies in the ionization zones of either neutral He atoms or singly ionized He^+, or perhaps both."

"The observed horizontal motions provide a mechanism for building up relatively strong fields in a narrow network pattern, as is observed. These magnetic channels in turn suggest an explanation for the origin of the Ca^+ emission network... Magnetic fields would tend to be swept to the cell boundaries by the horizontal currents, and concentrate there in strengths several times greater than the average field."

This description makes a lot of sense, although some points still need confirmation. Despite several studies (e.g. Simon & Weiss, 1968) it remains to be shown that a convective instability due to the recombination of ionized Helium is the origin of the distinct supergranular scale. The depth of the supergranulation layer is largely unknown. It has been suggested that the properties of convective motions in a highly stratified atmosphere may imply that supergranules are a deep phenomenon, with depths in excess of their horizontal diameters (Parker, 1973). Local helioseismic studies show that the correlation between internal flows and surface flows appears to switch sign at depths of 5-10 Mm (Duvall, 1998; Zhao, 2003; Braun & Lindsey, 2003), suggesting the existence of a "return flow" below these depths. There have been a number of studies related to the influence of supergranular flows on magnetic fields. It has been shown that a stationary cellular flow tends to expel the magnetic field from the regions of fluid motion and concentrate the flux into ropes at the cell boundaries (Parker, 1963; Galloway et al., 1977; Galloway & Weiss, 1981). For obvious reasons of simplicity, analytical or semi-analytical studies often picture supergranulation as laminar convection, although, as noted above by Simon & Leighton (1964), the flows must be highly turbulent and non-stationary. Recent numerical simulations of stratified convection at high Rayleigh number have revealed a very complex picture. It is now accepted that heat and momentum transport in solar-like turbulent convection is controlled by a network of coherent cyclonic plumes

sinking from the thermal boundary layer (Julien et al., 1996; Brummell et al., 1996). The dynamics of individual plumes is dominated by strong vortex-vortex interactions with neighboring plumes (Julien et al., 1996). Rast (2003) claims that the scale of supergranulation may have its origin in the interaction and merging of individual granular plumes (see also Ploner et al., 2000). A somewhat related model was proposed earlier by Rieutord et al. (2000, 2001) whereby supergranulation is the result of a nonlinear large-scale instability of the granular flow, triggered by exploding granules. In both these models, supergranulation is not a proper scale of thermal convection, and the depth of supergranulation is determined by the depth at which network plumes can remain stable (Rast, 1997). Realistic numerical simulations will be crucial in understanding the nature of supergranulation. Yet, the solar convection zone is so highly turbulent and stratified that numerical modeling at supergranular scales has remained elusive.

On the observational side, the original work of Leighton and coworkers has been refined. A variety of methods have been used to characterize the distribution of the cell sizes. A characteristic scale can be obtained from the spatial autocorrelation function (e.g. Hart, 1956; Simon & Leighton, 1964; Duvall, 1980), the spatial Fourier spectrum (e.g. Hathaway, 1992; Beck, 1997), and segmentation or tessellation algorithms (Hagenaar et al., 1997). Although definitions vary, average cell sizes are in the range 15-30 Mm. The topological properties of the pattern have been studied by Schrijver et al. (1997). It is unclear whether there is a variation of cell sizes with latitude: Rimmele & Schroeter (1989) and Komm et al. (1993a) report a possible decrease with latitude, Berrilli et al. (1999) an increase, and Beck (1997) no significant variation. The typical "lifetime" of the supergranular/chromospheric network, obtained by fitting an exponential decay to the correlation function, is found to be about 1 day (e.g Rogers, 1970; Worden & Simon, 1976; Duvall, 1980; Wang & Zirin, 1989). An important observation by Beck & Duvall (2001) shows that the temporal autocorrelation of the supergranulation pattern does not follow a simple exponential decay with time but becomes negative after a few days. Thus e-folding lifetimes may be misleading (we will come back to this point later). The typical rms horizontal velocity of supergranular flows is known to be about 0.3 km s^{-1}(e.g. Hathaway et al., 2000). However, the vertical component of the flows has been extremely

difficult to measure (e.g. Giovanelli, 1980) or infer (November, 1989). Miller et al. (1984) cautioned that Doppler velocity measurements at the cell boundaries may be polluted by the network field. The best estimate is perhaps due to Hathaway et al. (2002) who find that the vertical flows have speeds of about 10% of their associated horizontal flows or about 30 m s^{-1}, although the topology of the vertical flows is largely unknown. Perhaps even more difficult to measure are the related temperature fluctuations. Observers have searched for the thermal signature of a convective process, i.e. rising hot material at the cell centers and sinking cool material at the cell boundaries. Unfortunately, answers vary too widely (see Lin & Kuhn, 1992, and references therein).

2.2.2   Anomalous Motion of the Pattern

Duvall (1980) showed that the rotation of the supergranular pattern is faster than the photospheric plasma by approximately 5%. This anomaly has since been confirmed by Snodgrass & Ulrich (1990) who used a local correlation tracking method with a time-lag of $\Delta t = 24$ hr (see Fig. 2.7). In order to study this point in more detail, we constructed a series of f-mode divergence maps of size $90° \times 90°$ for the whole 1996 dynamics period (2 months) following the same method as described in the previous section. To quantify the apparent motion of supergranules in the divergence maps we used a local correlation tracking method (e.g. DeRosa, 2001) with various time-lags Δt between frames. Around each point, we consider a small region apodized by a Gaussian surface with a full width at half maximum of 3.84°, i.e. about twice the supergranulation scale (see Fig. 2.8). At fixed Carrington longitude, small regions separated by Δt are spatially cross-correlated. The spatial displacement at correlation maximum, $\Delta \boldsymbol{x}$, is obtained by fitting a parametric surface to the cross-correlation. Three different parametric models were used for the fits (product of Gaussian functions, cylindrical Bessel function $J_1(r)/r$, product of sinc functions). On average, we did not find a significant model-dependent bias. The accuracy of the feature tracking algorithm was successfully tested on divergence maps locally shifted by known amounts. The apparent velocity of the pattern is then given by $\boldsymbol{u}_{\mathrm{LCT}} = \Delta \boldsymbol{x}/\Delta t$.
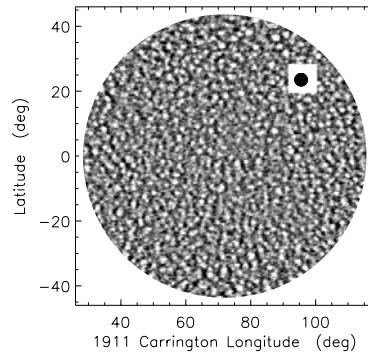
Figure 2.8: An individual map (8 hr average, 1996 MDI Dynamics run) of the horizontal divergence of the flow field. White shades indicate a positive divergence. Around each point, we consider a small region apodized by a Gaussian surface with a full width at half maximum of 3.84° (black disk). Small regions separated by a time-lag Δt are spatially cross-correlated. The spatial displacement at correlation maximum, $\Delta \boldsymbol{x}$, corresponds to the apparent velocity $\boldsymbol{u}_{\mathrm{LCT}} = \Delta \boldsymbol{x}/\Delta t$.
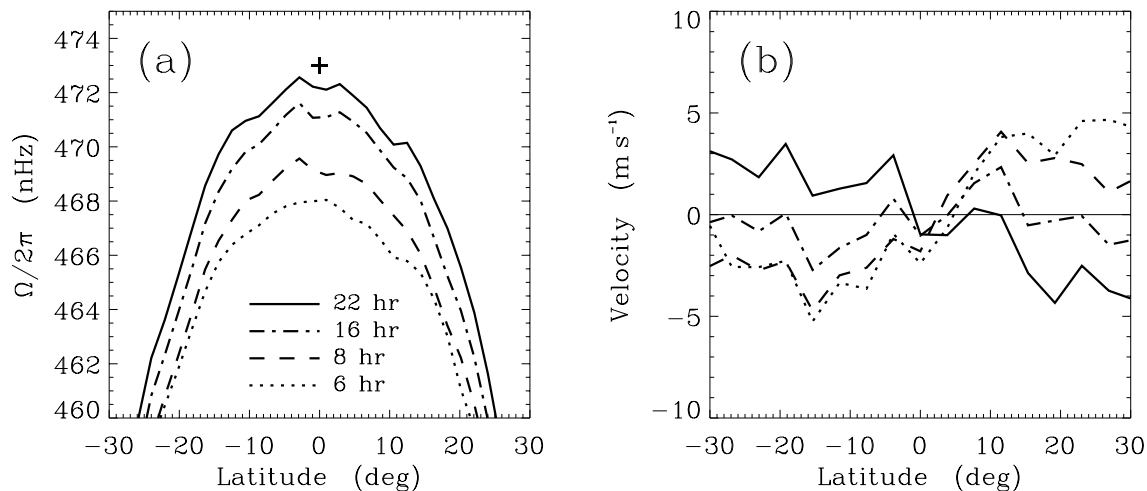
Figure 2.9: Anomalous flows derived from the temporal evolution of the supergranulation pattern, using a local correlation tracking method. **(a)** Apparent rotation of the supergranulation pattern for $\Delta t = 6$, 8, 16, and 22 hr. For comparison, the cross shows the equatorial rotation obtained by Snodgrass & Ulrich (1990) for $\Delta t = 24$ hr. **(b)** Apparent meridional circulation as a function of time-lag, Δt. The meridional motion appears to be equatorward for $\Delta t > 20$ hr. A P-angle correction was applied to the data.

Figure 2.9 shows the apparent rotation and meridional circulation that we obtained as a function of Δt. The meridional circulation is very small and even equatorward for large Δt. The rotation rate increases rapidly with Δt. It has been speculated (e.g. Corbard & Thompson, 2002) that the fast rotation of the pattern may be a consequence of convective cells deeply rooted in the shear layer below the surface (rotation increases inward at low latitudes). However, Beck & Schou (2000) point out that rotation measured from correlation tracking ($\Delta t = 24$ hr) is faster than the rotation of the solar plasma measured at *any* depth in the interior. It is especialy puzzling that the rotation of the magnetic network (Komm et al., 1993b) is also less than that of the supergranular pattern, since magnetic fields are expected to be strongly advected by supergranular flows. To date, a definitive explanation of the excess rotation speed of the supergranular pattern has not been presented.

In the following, we study yet another time series of flow maps of the solar supergranulation, obtained from f-mode time-distance helioseismology. These data of even larger size ($120° \times 120°$) cover the whole 1996 Dynamics run and enable us to characterize, for the first time, the true dynamics of the supergranulation. We find that the power spectrum appears to be consistent with a spectrum of traveling waves (Gizon et al., 2003).

2.2.3   Supergranulation Supports Waves

Turbulent solar convection is commonly characterized by an autocorrelation function that exhibits an exponential decay in time (Harvey, 1985; Kuhn et al., 2000), leading to a power spectrum that is a decreasing function of temporal frequency. That supergranulation may not follow such a simple model has been hinted at previously. For example, the observed autocorrelation function becomes negative after 60 hr (Beck & Duvall, 2001) and new supergranular cells appear to form near the boundaries of decaying cells (Shine et al., 2000). The negative excursion of the autocorrelation function leads to a power spectrum peaked at a low non-zero frequency (Duvall & Gizon, 2000, and previous section), suggesting an underlying long-range order.

To study supergranulation, we use a 60-day sequence of Doppler velocity images obtained in 1996 by the Michelson Doppler Imager (Scherrer et al., 1995) on board

SOHO. MDI full-disk Dopplergrams are observed at a one-minute cadence with a spatial sampling of 0.12° at disk center. Images are tracked at the Carrington angular velocity ($\Omega_C = 2.87$ μrad s^{-1}) to remove the main component of solar rotation. We apply the techniques of time-distance helioseismology (Duvall et al., 1993b) to obtain every 12 hr a 120° × 120° map of the horizontal divergence of the flows in a 1 Mm-deep layer beneath the surface (Duvall & Gizon, 2000). Unlike raw Doppler images, the divergence signal has uniform sensitivity across the solar disk and is subject to few systematic errors. Supergranules appear as cellular patterns of horizontal outward flow in the divergence maps.

The divergence maps are obtained by measuring the time it takes for solar f modes to propagate from any given point on the solar surface to a concentric annulus around that point. The difference in travel times between inward and outward propagating waves is a proxy for the local horizontal divergence of the flow field. Images were interpolated onto Postel's azimuthal equidistant projection (Pearson, 1990) centered on latitude 0° and Carrington longitude at image center. Data cubes go through a three-dimensional Fourier filter to isolate the f-mode ridge and cut off the power below 2 mHz (supergranulation noise). The temporal signal at a given pixel is cross-correlated with the signal in a concentric annulus of thickness 0.12°. The cross-correlation function contains information about waves propagating outward and inward from the central pixel depending on the sign of the correlation time lag. To enhance the signal, cross-correlations are averaged on a 2 × 2 grid of origins, corresponding to a spatial sampling of 0.24° at image center. Travel times for inward and outward propagating waves are measured by fitting a Gaussian wavelet to the cross-correlations. Travel-time differences are then averaged for a range of annuli (mean radius 15 Mm). The divergence maps are finally interpolated onto a Carrington longitude-latitude grid with a resolution of 0.24° in both coordinates.

For any given target latitude, λ, we extract a longitudinal section of the data 10° wide in latitude centered about λ. The divergence signal is Fourier transformed in three dimensions to make power spectra as a function of frequency, ν, and horizontal wavevector, $\boldsymbol{k} = (k_x, k_y)$, where k_x and k_y are in the East-West and South-North directions respectively. In cylindrical coordinates, $\boldsymbol{k}$ is uniquely specified by its
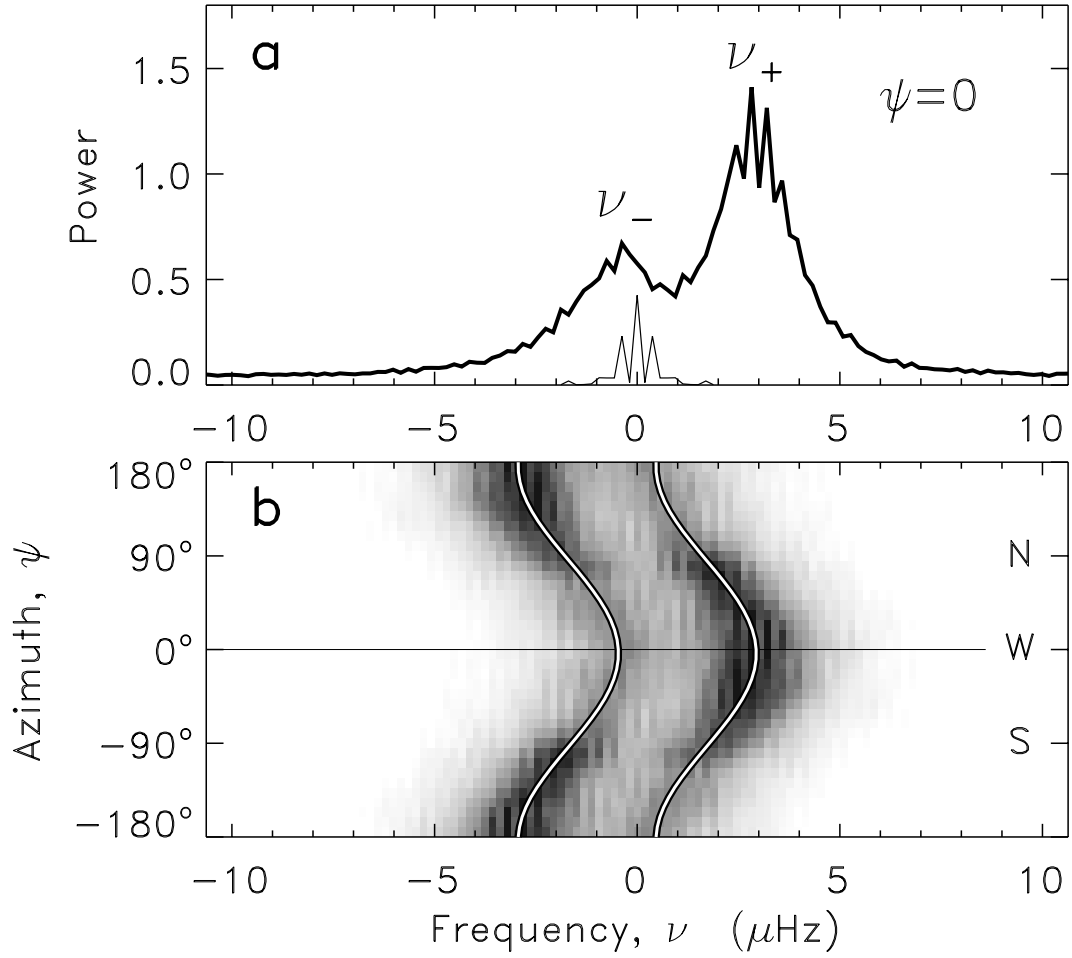
Figure 2.10: Power spectrum of the supergranulation signal near the equator ($\lambda = 0°$). Cuts are shown at constant wavenumber $k = 120/R$ where R is the solar radius. **(a)** The thick line is the power spectrum versus frequency, ν, for $\boldsymbol{k} = (k, 0)$ pointing in the direction of solar rotation, $\psi = 0$ (West). There are two peaks at frequencies ν_- and ν_+. The frequency resolution is given by the power spectrum of the temporal window function (thin line). **(b)** Cylindrical cut, $P_k(\nu, \psi)$, in the power spectrum at constant k versus ν and the direction of $\boldsymbol{k}$, ψ. By construction, $P_k(\nu, \psi) = P_k(-\nu, \psi - \pi)$. Power peaks in two ridges at frequencies $\nu_-(\psi)$ and $\nu_+(\psi)$. For each ψ, we measure $\nu_\pm$ by fitting the sum of two independent Lorentzian functions to the power. The fits take into account the convolution by the window function. The sinusoidal variation of $\nu_\pm$ with ψ is due to advection by a background flow $\boldsymbol{u} = (u_x, u_y)$. The double lines show the fit $\nu = \pm\nu_0 + (ku_x \cos\psi + ku_y \sin\psi)/2\pi$ to $\nu_\pm(\psi)$, where ν_0 is a constant frequency. At the equator we find $\boldsymbol{u} = (43, 0)\,\mathrm{m\,s^{-1}}$. The velocity u_x is measured in a frame co-rotating with the Sun at the Carrington rotation rate. (Gizon et al., 2003)

magnitude, k, and its direction, ψ, such that

$$k_x = k \cos \psi \tag{2.3}$$
$$k_y = k \sin \psi . \tag{2.4}$$

Figure 2.10 shows cuts in the equatorial power spectrum at a constant k typical of the supergranulation. For each azimuth ψ, the power has two broad peaks at frequencies ν_+ and ν_- (Fig. 2.10a). No Galilean transformation can cause these peaks to coalesce, at zero frequency or otherwise. This implies that the supergranulation undergoes oscillations.

For each azimuth, we measure the frequencies ν_+ and ν_- by fitting the sum of two Lorentzian functions to the power (Fig. 2.10b). Observations show that the difference $\nu_+ - \nu_-$ is essentially independent of azimuth, and $\nu_\pm$ have a sinusoidal dependence with ψ of the form:

$$\nu_\pm = \pm\nu_0 + \nu_1 \cos(\psi - \psi_0) . \tag{2.5}$$

We interpret ν_1 to be a Doppler frequency shift,

$$\nu_1 = k\|\boldsymbol{u}\|/2\pi , \tag{2.6}$$

produced by a horizontal background flow $\boldsymbol{u}$ pointing in the direction ψ_0, as one does in helioseismological ring analysis (Schou & Bogart, 1998). The nearly linear relationship measured between ν_1 and k in the range $40 < l < 180$ ($l = kR_\odot$) is consistent with this interpretation. The latitudinal dependence of $\boldsymbol{u}$ is shown in Figure 2.11. The inferred rotation (Fig. 2.11a) and meridional circulation (Fig. 2.11b) are both remarkably similar to that of the small magnetic features (Komm et al., 1993b,c). This property is consistent with the view that magnetic fields are advected by supergranular flows.

The dynamics of the supergranulation are best studied once the background flow, $\boldsymbol{u}$, has been removed. In a co-moving frame, each spatial component oscillates at a characteristic frequency ν_0. We find a clear relationship between ν_0 and the wavenumber k, well described by a power law (Fig. 2.12a). This is a fundamental
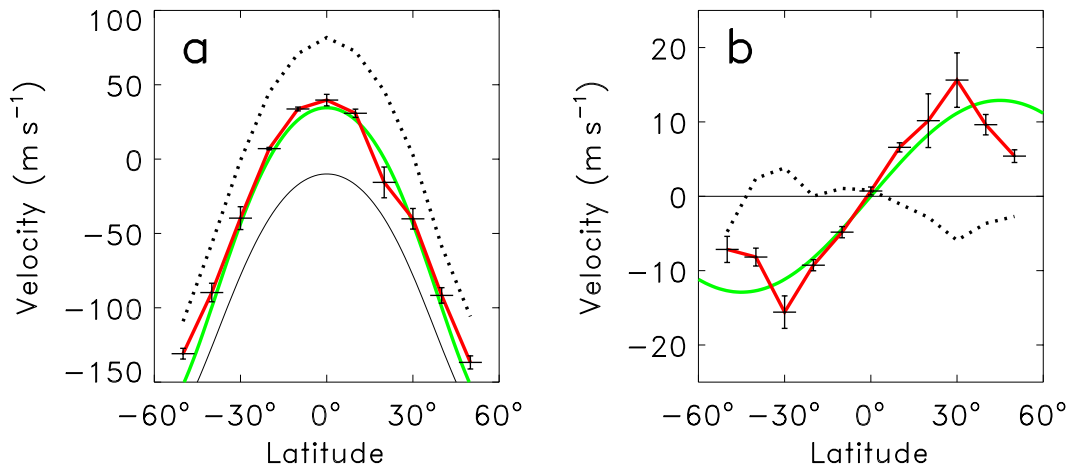
Figure 2.11: Flows, $\boldsymbol{u}$, inferred from the advection of the supergranulation spectrum versus latitude, λ. **(a)** Flow in the direction of solar rotation, u_x (red line and error bars). The green line shows the rotation of the small magnetic features (Komm et al., 1993b) and the black line is for the photospheric rotation (Snodgrass & Ulrich, 1990). The dotted line shows the pattern rotation obtained by tracking supergranular features with a 24 hr delay, in agreement with an earlier measurement (Snodgrass & Ulrich, 1990). **(b)** Northward meridional flow, u_y (red line and error bars). The meridional flow of the magnetic features from Komm et al. (1993c) (green) is again similar. The dotted line shows the anomalous results obtained by tracking the supergranulation pattern with a 24 hr delay. (Gizon et al., 2003)

relationship as it is measured to be independent of both ψ and λ. The data are consistent with a spectrum of travelling waves with a dispersion relation $\nu = \nu_0(k)$. The waves have a rather low quality factor, as can be seen in the azimuthally averaged power spectrum (Fig. 2.12b). The shape of the power spectrum is described accurately by the sum of two Lorentzian functions. From the measured line widths (Fig. 2.12a) we find that the lifetime of supergranules is about 2 days at $l = 100$.[2]

Since ν_0 and the dominant size of supergranules are observed to be essentially independent of latitude, the general dynamics determining the time scale and the spatial scale of supergranulation is not affected by the Coriolis force associated with the large scale vorticity (rotation). We observe, however, a pronounced anisotropy in the azimuthal distribution of wave power at fixed k (Fig. 2.13a). The power is maximum in the direction of rotation and toward the equator in both hemispheres (Fig. 2.13b). The pattern therefore senses the effect of rotation. A snapshot of the

---

[2]The lifetime is given by $(2\pi \, \mathrm{HWHM})^{-1}$ where the HWHM is measured in Hz.
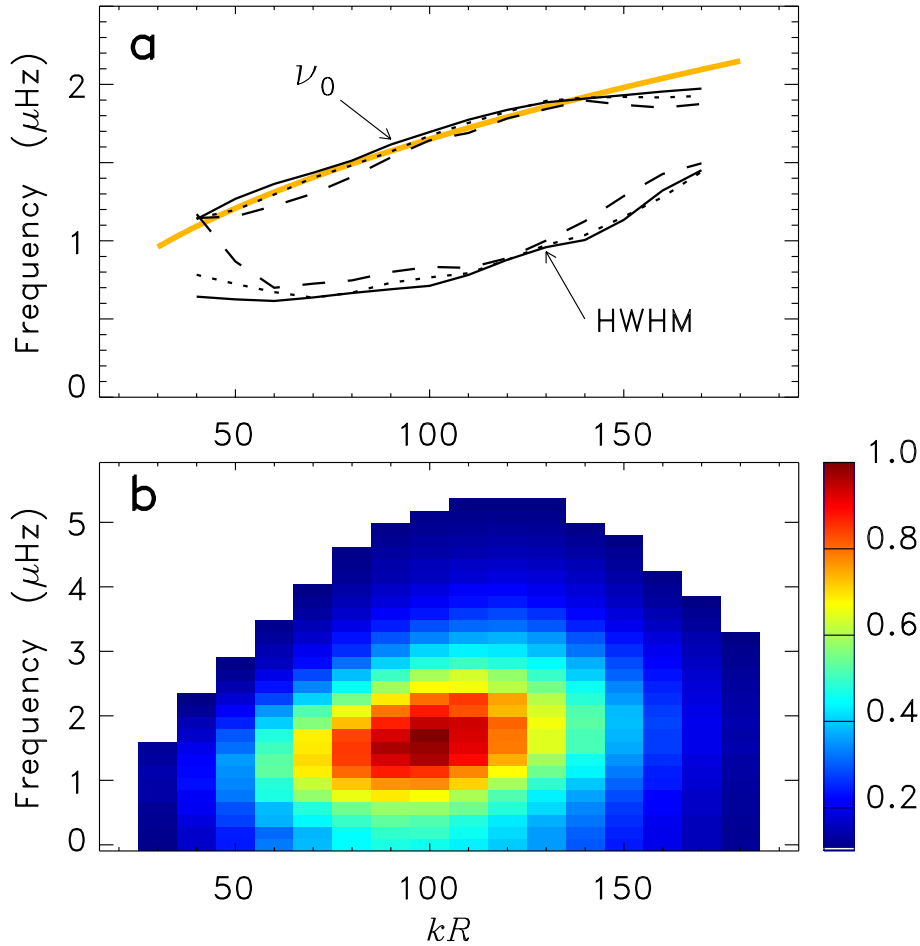
Figure 2.12: Average dynamical properties in a co-moving frame. **(a)** Oscillation frequency ν_0 versus l at latitudes $\lambda = 0°$ (solid), $\lambda = \pm25°$ (dotted) and $\lambda = \pm50°$ (dashed). For reference, we plot the approximate dispersion relation $\nu = 1.65(l/100)^{0.45}$ μHz (orange). Also shown is the half width at half maximum (HWHM) of the Lorentzian profiles for the same latitudes, implying an e-folding lifetime of 1-3 days. The quality factor, $\nu_0/$HWHM, does not exceed 2. **(b)** Power spectrum corrected for rotation and meridional circulation and averaged over azimuth and latitude. We note that the distribution of power as a function of frequency is affected only by the known temporal window function, while the wavenumber dependence includes effects of the telescope optics and of the time-distance analysis which are not fully understood. (Gizon et al., 2003)
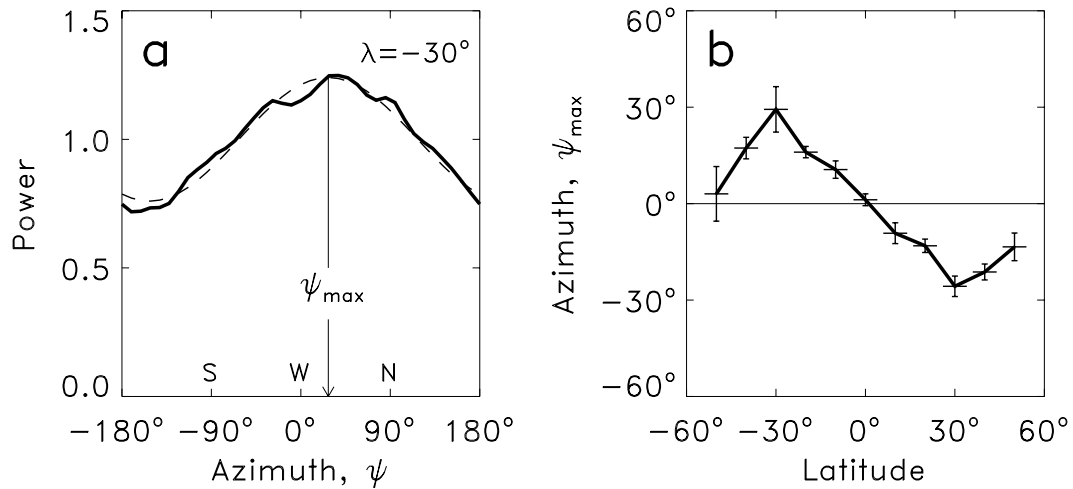
Figure 2.13: Wave power as a function of azimuth and latitude. **(a)** Directional distribution of power at latitude $\lambda = -30°$ (solid line), obtained by integrating $P_k(\nu, \psi)$ over frequencies $\nu > \boldsymbol{k} \cdot \boldsymbol{u}/2\pi$ and then averaging over k. We applied an MTF correction estimated from the data. The azimuth of maximum power, $\psi_{\max}$, is measured by fitting a sinusoidal function (dashed line). **(b)** Plot of $\psi_{\max}$ versus latitude. There is excess power in the direction of solar rotation and toward the equator in both hemispheres. (Gizon et al., 2003)

divergence field would not reveal this as the sum of the powers measured in opposite directions is nearly isotropic (Fig. 2.13a); the vorticity field, on the other hand, is slightly sensitive to the effect of the Coriolis force as we will show later.

As already mentioned, earlier estimates of supergranulation rotation (Duvall, 1980; Snodgrass & Ulrich, 1990), obtained by tracking the supergranulation pattern from one image to the next, were systematically found to be higher than the rotation of the magnetic network (Fig. 4a). This apparent super-rotation of the pattern can now be understood since waves are predominantly prograde. The East-West motion of the pattern is effectively a power-weighted average of the true rotation and the non-advective phase speed $u_{\mathrm{w}} = 2\pi\nu_0/k \sim 65~\mathrm{m\,s^{-1}}$. Similarly, the excess of wave power toward the equator is reflected in the meridional motion of the pattern (Fig. 4b).

We have shown that supergranulation displays a high level of organization in space and time. Perhaps this order has its origin in the network of coherent cyclonic plumes that controls solar-like turbulent convection. The prograde excess of wave

power is most likely due to the influence of rotation that breaks the East-West symmetry, allowing for new instabilities to propagate. Recent numerical simulations of solar convection (Miesch et al., 2000) show patterns that move prograde relative to the local rotation at low latitudes, and may help explain the observations. Convection in oblique magnetic fields (Hurlburt et al., 1996) also exhibits solutions that take the form of travelling waves, where the tilt of the convection cells, their wave speed, and direction depend on the strength and obliquity of the field. Supergranulation would appear to be a rare known example of travelling-wave convection in a very highly turbulent fluid.

2.3 Effect of the Coriolis Force on Supergranulation

An interesting effect that can be studied with both horizontal components of the flows is the effect of the Coriolis force on convection. This was studied theoretically for a simplified solar convection model by Hathaway (1982). Cellular convection in a rotating incompressible fluid was also studied by Veronis (1959). In these models, the Coriolis force causes divergent and convergent horizontal flows to be associated with vertical components of vorticity of opposite signs. In the northern hemisphere, the cell rotates clockwise where the horizontal divergence is positive, while it rotates counterclockwise in the convergent flow towards the sinks. A corresponding pattern of streamlines is shown in Fig. 2.14. The sense of circulation is reversed in the southern hemisphere and the amplitude is proportional to the radial component of rotation. The vorticity associated with supergranular flows was apparently detected by Kubičela (1973), which is quite remarkable considering the state of technology at that time. The first unambiguous detection of the Coriolis effect is due to Duvall & Gizon (2000). Here we present a more detailled study (Gizon & Duvall, 2003), using the data from the previous section.

As we have seen earlier, f-mode time-distance helioseismology not only provides maps of the horizontal divergence of the flows, but it also provides information about the two individual components of the horizontal velocity (Duvall & Gizon, 2000). We use the data from the previous section to estimate the horizontal vector flow, $\boldsymbol{v} = (v_x, v_y)$, by measuring the difference in travel time for f modes propagating in opposite directions. From each 12 hr vector flow image we subtract the mean image, to remove rotation and field effects. Like before, we consider longitudinal strips centered at latitude λ and $10°$ wide in latitude. The vertical component of the vorticity is given by

$$\text{curl} = \partial_x v_y - \partial_y v_x \,, \tag{2.7}$$

where spatial derivatives are approximated by a first-order centered difference. Note that differential rotation does not contribute to the vorticity as it has been removed. The horizontal divergence of the flow field, denoted by div, can either be obtained
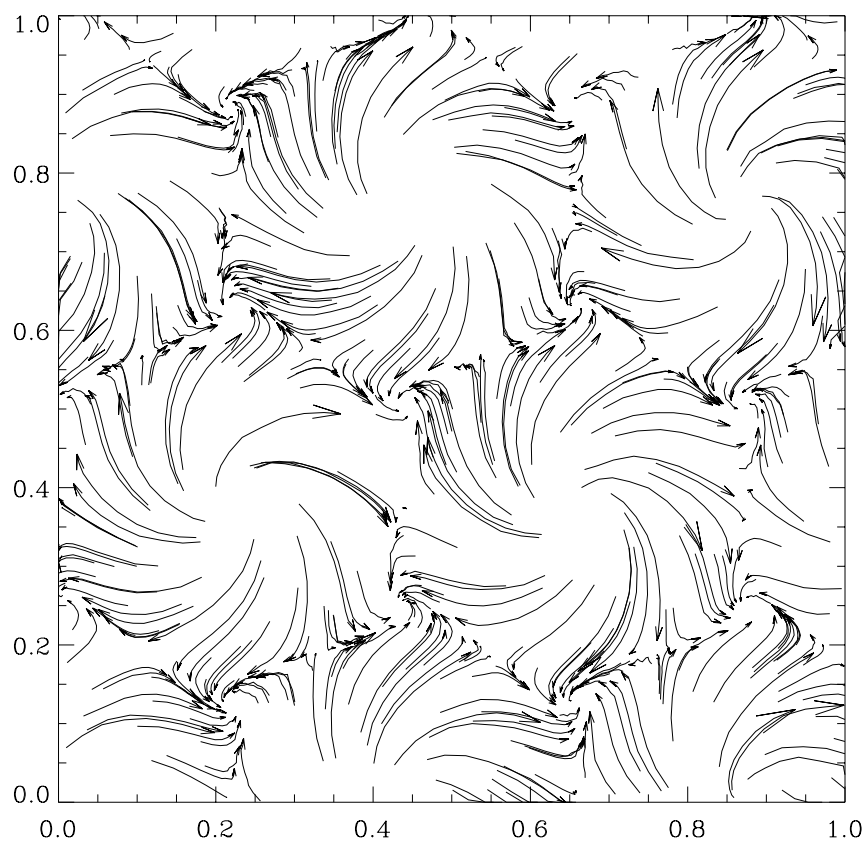
Figure 2.14: A sketch of horizontal streamlines in rotating hexagonal convection cells (Veronis, 1959). The rotation vector is coming out of the page.

by calculating $\partial_x v_x + \partial_y v_y$, or by using the "divergence signal" (difference in travel-times for f modes propagating between a central point and an annulus). In general the second method is preferable as it is less noisy; although both methods compare favorably.

It is not straightforward to predict the statistical properties of the vorticity in rotating turbulent convection (cf. Hathaway, 1982). Vorticity production is due to the effect of the Coriolis force and to vortex stretching and tilting mechanisms. The importance of the Coriolis force is characterized by an inverse Rossby number, or Coriolis number, defined by

$$\mathrm{Co} = 2\tau_{\mathrm{c}}\,\boldsymbol{\Omega}\cdot\hat{\boldsymbol{g}}\;, \tag{2.8}$$

were $\hat{\boldsymbol{g}}$ is a unit vector in the downward direction and τ_{c} is a characteristic correlation time of the turbulence. Linear theory predicts curl $\sim$ Co div (order of magnitude), and we expect the latitudinal variations of the Coriolis effect to go like

$$f(\lambda) = \frac{\Omega(\lambda)\sin\lambda}{\Omega_{\mathrm{eq}}}\;, \tag{2.9}$$

where Ω_{eq} is the equatorial solar angular velocity. Away from the equator, the magnitude of Co is greater than unity in most on the convection zone, except near the surface where it can be very small. Taking $\tau_{\mathrm{c}} = 2$ day we find that Co $\simeq -0.98\sin\lambda$ for supergranulation.

Despite the fact that the vorticity field is very noisy, we detect a significant correlation of a few percent between the vertical vorticity and the horizontal divergence (Fig. 2.15a). The correlation coefficient at latitude λ is defined by

$$\mathcal{C}(\lambda) = \frac{\langle\mathrm{div\ curl}\rangle}{\sqrt{\langle\mathrm{div}^2\rangle\langle\mathrm{curl}^2\rangle}}\;, \tag{2.10}$$

where the angle brackets denote the spatial average over the area of a 10° band centered around λ. In the North, positive (negative) divergence is correlated with clockwise (anticlockwise) vorticity. The correlation changes sign in the South. The sign and the latitudinal variation of $\mathcal{C}(\lambda)$ are both characteristic of the effect of the Coriolis force on the flows. Away from the equator, the number of right-handed cyclones is not equal to the number of left-handed cyclones.
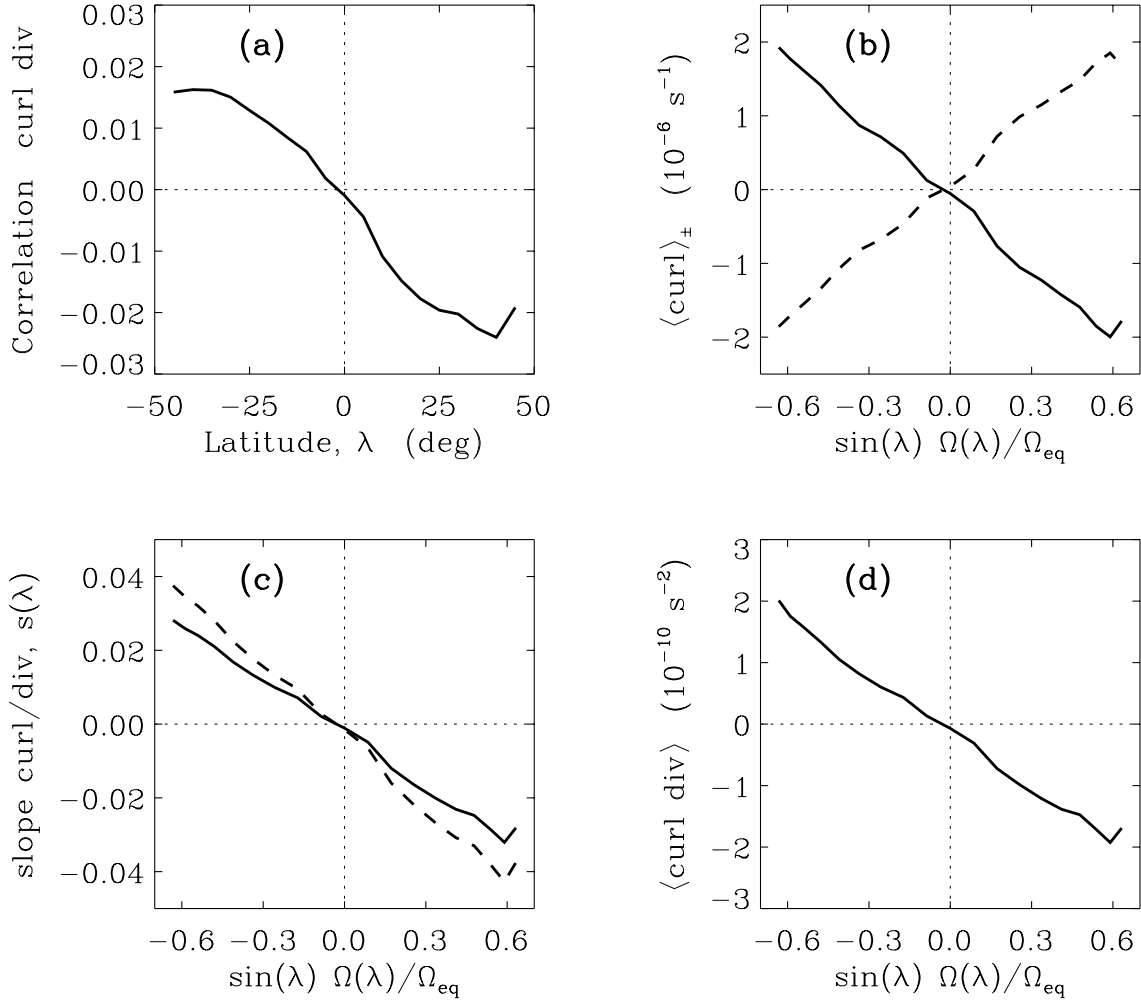
Figure 2.15: Effect of the Coriolis force on supergranular flows. **(a)** Plot of the correlation coefficient, $\mathcal{C}(\lambda)$, between the vertical vorticity, curl, and the horizontal divergence, div. **(b)** Horizontal averages of the vorticity, $\langle\text{curl}\rangle_+$ (solid) and $\langle\text{curl}\rangle_-$ (dashed), over regions with div > 0 and div < 0 respectively. A vorticity of 1 Ms^{-1} corresponds to an angular velocity of $2.5°$ day^{-1} or a typical circular velocity of 10 m s^{-1}. **(c)** Estimate of the slope, s, in the linear fit curl $= s$ div. The solid line shows $s(\lambda)$ versus $f(\lambda)$ in the case when the ratio of errors $r = \sigma_{\text{div}}/\sigma_{\text{curl}}$ is assumed to be zero. The dashed line is for the case $r = 2$. **(d)** Plot of $\langle\text{curl div}\rangle$ versus $f(\lambda)$.

Figure 2.15b shows horizontal averages of the vertical vorticity, $\langle \text{curl} \rangle_{\pm}$, versus $f(\lambda)$, where the averages $\langle \cdot \rangle_{+}$ and $\langle \cdot \rangle_{-}$ are restricted to the regions of positive and negative divergence respectively. We observe a nearly perfect linear relationship between $\langle \text{curl} \rangle_{\pm}$ and $\mp f(\lambda)$, given by $\langle \text{curl} \rangle_{\pm} \simeq \mp 3 f(\lambda)$ Ms^{-1}. This is again consistent with the interpretation as a Coriolis effect. In principle, a linear fit of the form

$$\text{curl}(\lambda) = s(\lambda) \, \text{div}(\lambda) \tag{2.11}$$

can be extracted from the data at each latitude, λ. This operation is not trivial as it requires a knowledge of the errors in the observations, σ_{curl} and σ_{div}. A first approximation is to assume that div is mostly signal, and curl is mostly noise:

$$s \rightarrow \frac{\langle \text{div} \, \text{curl} \rangle}{\langle \text{div}^2 \rangle} \qquad \text{as} \quad r = \frac{\sigma_{\text{div}}}{\sigma_{\text{curl}}} \rightarrow 0 \ . \tag{2.12}$$

In this limit we find $s(\lambda) \simeq -0.048 \, f(\lambda)$ (Fig. 2.15c), or $s(\lambda) \sim \text{Co}(\lambda)/20$ in terms of the Coriolis number quoted above.

Figure 2.15d shows that the latitudinal variations of the horizontal average $\langle \text{div} \, \text{curl} \rangle$ are well described by $\langle \text{div} \, \text{curl} \rangle \simeq -3 f(\lambda) \times 10^{-10}$ s^{-2}. This observation may be compared directly to a prediction by Rüdiger et al. (1999), who used the mixing length theory to estimate the effect of rotation on convection:

$$\langle \text{div} \, \text{curl} \rangle \sim -\frac{8\alpha^2}{35\gamma^2} \frac{\Omega_{\text{eq}}}{\tau_{\text{c}}} \, f(\lambda) \ , \tag{2.13}$$

where α is the mixing length parameter and γ is the ratio of specific heats. For $\alpha = 1.5$, $\gamma = 5/3$, and $\tau_{\text{c}} = 2$ day, the prediction is $\langle \text{div} \, \text{curl} \rangle = -3 f(\lambda) \times 10^{-12}$ s^{-2} for supergranulation, i.e. two orders of magnitude smaller that the measured value. This disagreement is perhaps not too surprising as there is some freedom in choosing α and τ in Eq. (2.13) and the mixing length theory may oversimplify the problem. On the other hand, the measurement errors are not well understood either.

2.4   Large-Scale Flows Around Active Regions

2.4.1   Data Analysis

In this section we use an extensive set of Dopplergrams from the MDI Dynamics Program to construct synoptic maps of the near-surface horizontal flows from measurements of f-mode travel times. The data sets we considered include up to three months of continuous Dopplergrams for each of the years 1996, 1998, and 1999. We recall that in 1996 the sunspot cycle was at a minimum of activity. Regions of size 90° in longitude and 90° in latitude were tracked at the Carrington rotation rate for 24 hr. Images were interpolated onto Postel's azimuthal equidistant projection centered on latitude 0° and Carrington longitude at image center. The tracking procedure is repeated every 20.3 hr so that the Carrington longitude at image center decreases by 12° at each step. Each 24-hr tracked region was then split into three 8-hr data cubes. For each Dynamics period, we thus obtained a sequence of 8-hr data cubes covering two to three months each year. Data cubes go through a three-dimensional Fourier filter to isolate the f-mode ridge and cut off the power below 2 mHz. The temporal signal at a given pixel is cross-correlated with the signal in concentric quadrants of thickness 0.12°. To enhance the signal, cross-correlations are averaged on a 2×2 grid of origins, corresponding to a spatial resolution of 0.24° at image center. West-east and north-south travel time differences are measured by fitting a Gaussian wavelet to the cross-correlations. Travel-times are averaged over a range of annuli with radii ranging from 0.42° to 0.90°. The travel-time perturbations are converted into velocity by using the calibration from section 2.1. In addition, we measure in-out mean travel times. Travel-time maps are then interpolated onto a Carrington longitude-latitude grid with 0.24° resolution in both coordinates.

In order to examine field effects as a source of systematic errors, we construct averages of the flow maps without shifting images with respect to the central meridian longitude. These averages are shown in Fig. 2.16 for rotation and meridional circulation. The small scale fluctuations in theses maps are essentially due to supergranulation. However, at fixed longitude, there are smooth variations as a function of central meridian longitude which cannot be of solar origin. In 1996, the equatorial rotation can vary by as much as ~50 m/s across the 90° longitudinal range (the west
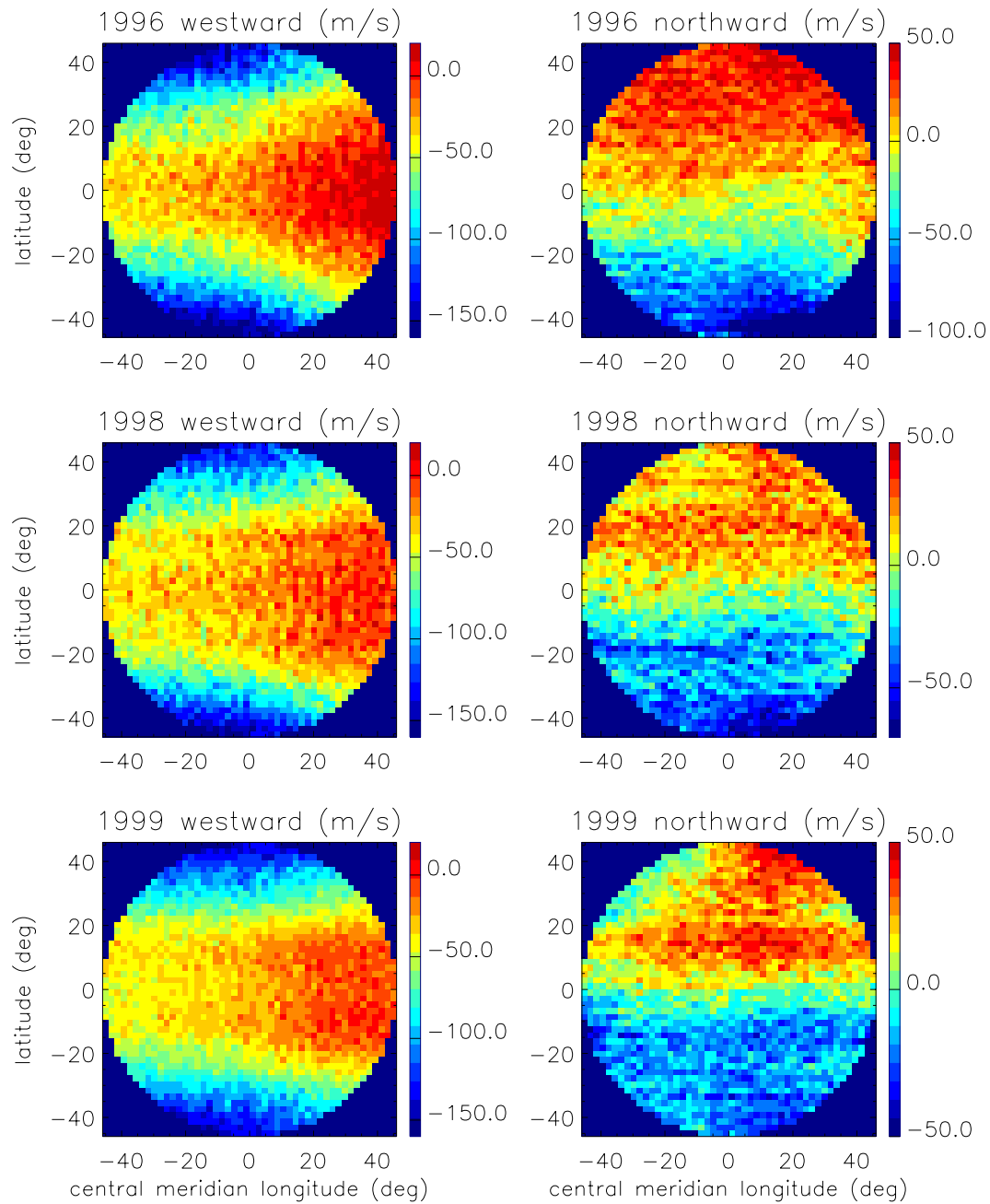
Figure 2.16: Field effects. Average of the maps obtained for the 1999 Dynamics period. The figures on the left are for rotation (measured in a frame corotating at the Carrington angular velocity) and the figures on the right are for meridional circulation. The upper figures are for the 1996 MDI Dynamics run, the middle figures for 1998, and the lower figures for 1999.

limb appears to rotate faster than the east limb). We note that the systematic errors do not appear to be as severe in 1998 and 1999. Field effects can have many possible causes (e.g. point spread function, solar radius error, cubic distorsion, tilt of ccd, plate scale, remapping errors, etc.) and do vary with time (the MDI telescope was, by design, out of focus in 1996 and mostly in focus during 1999). The main causes have not been identified.

2.4.2   Longitudinal Averages

The longitudinal averages of rotation and meridional circulation are plotted in Fig 2.17 for the three dynamics periods. Small offsets were subtracted from the meridional circulation curves to correct for a $0.2°$ P-angle error in the orientation of MDI images (Toner, 2001) and a $0.1°$ error in Carrington's measurement of the inclination of the solar equator to the ecliptic (Giles, 2000).[3] These errors cause solar rotation to leak into the meridional circulation signal with a one year periodicity.

We observe in Fig 2.17 that both rotation and meridional circulation seem to change with time, although we need to keep in mind that there is a time dependence in the systematic errors. Note that poleward meridional motion is not a monotonic function of latitude during periods of magnetic activity (1998 and 1999). In 1998 (resp. 1999) meridional circulation reaches a maximum at latitude $20°$ (resp. $16°$). Other studies reveal a similar behavior (Giles, 2000; Meunier, 1999). As for rotation, it is known from surface Doppler measurements (Howard, 1996) and inversions of global-mode frequency splittings (Schou, 1999) that there are small solar-cycle variations in the rotation rate, known as torsional oscillations or zonal flows. To measure the zonal flows for each dynamics period, we subtract a smooth fit to the angular velocity of the form $\Omega(\lambda) = \Omega_0 + \Omega_1 \sin^2 \lambda + \Omega_2 \sin^4 \lambda$, where λ is the latitude. The north-south symmetric component of the zonal flows is shown in Fig 2.18 (dashed line). The thin solid line shows a previous measurement obtained by Schou (1999) for the same time periods (global modes). The thick solid line shows the zonal flows measured by tracking the superganulation pattern with a correlation tracking technique with $\Delta t = 8$ hr (see Fig 2.9). Figure 2.18 shows a very good

---

[3]P denotes the position angle of the northern extremity of the axis of rotation, measured eastward from the north point of the disk. The $0.2°$ P-angle error in the pointing of MDI is within specifications.
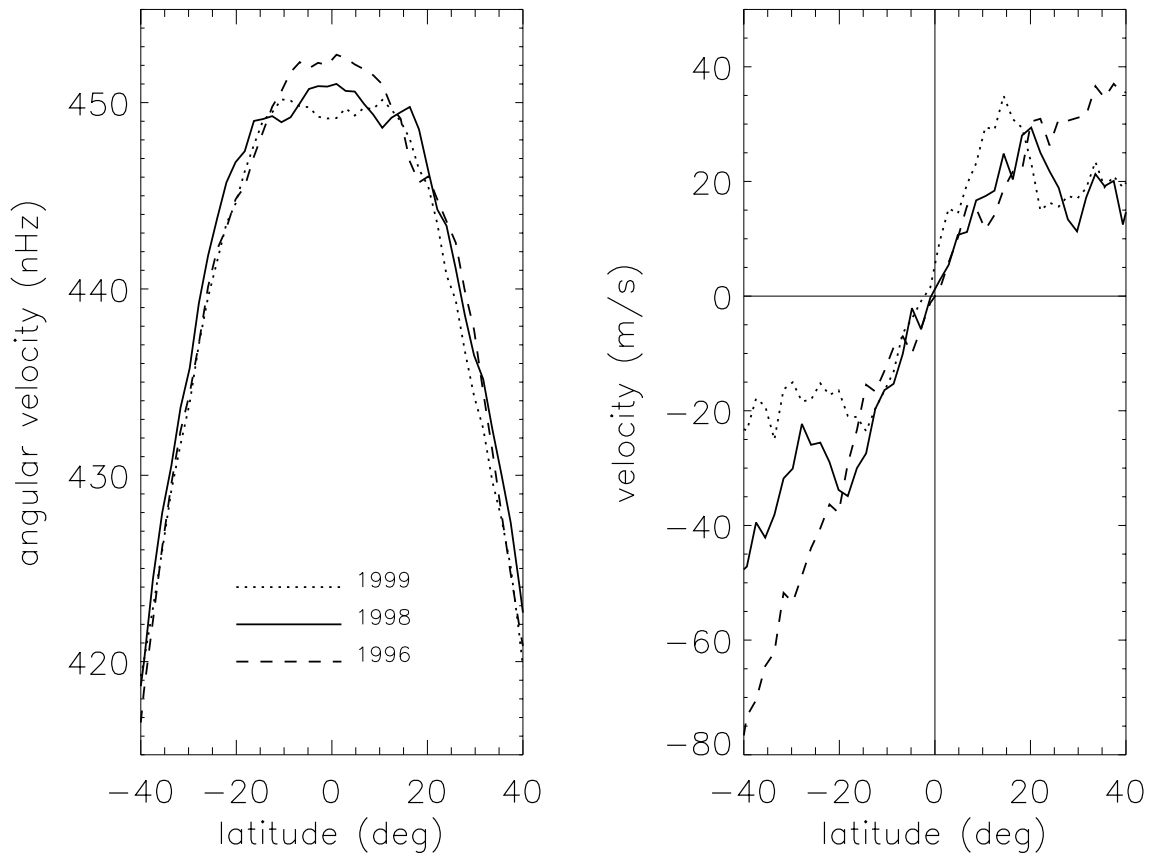
Figure 2.17: Rotation and meridional circulation for the three MDI Dynamics runs of 1996, 1998, and 1999.
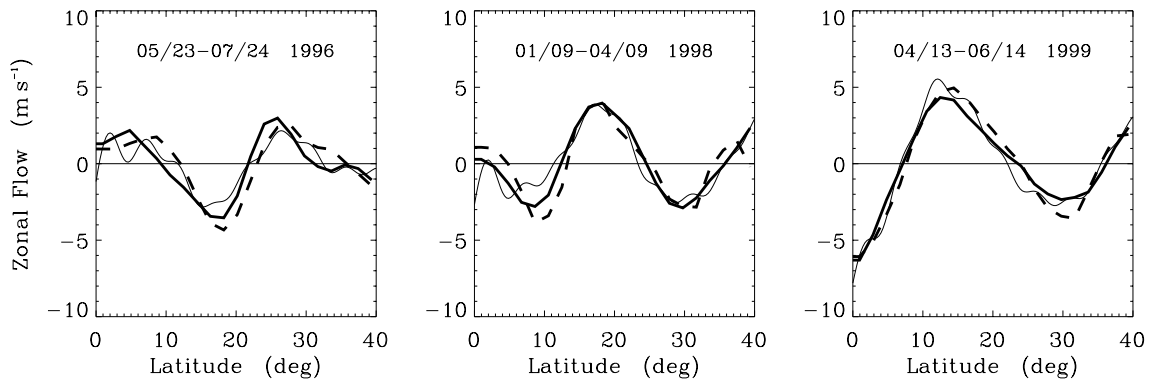
Figure 2.18: North-South symmetric component of the zonal flows obtained after subtraction of smooth rotation curves (thick dashed line, see Fig 2.17). The thick solid line is from correlation tracking of the supergranulation pattern ($\Delta t = 8$ hr, see Fig 2.9). The thin line shows the zonal flows obtained from f-mode frequency splittings (Schou, 1999) for the same time periods.

agreement, in both phase and amplitude, between these three independent methods. This suggests that we are able to measure zonal flows with a very high level of precision, of the order of 1 m/s, and that time-distance helioseismology does work. Because the torsional oscillations vary much faster with latitude ($\sim 20°$ period) than the systematic field effects, we were able to separate the two.

2.4.3   Local Flows

We now investigate the structure of the local flows and their relation to magnetic activity. For a given Dynamics run, we subtract the average flow map (Fig. 2.16) from each individual 8-hr flow map. This enables us to remove all unwanted field effects, and to study residual flows. We then construct synoptic maps by averaging the flows at fixed Carrington longitude. In other words, the maps are averaged in a frame that is corrotating with the Sun at the Carrington rotation rate. This procedure implies that the flows are effectively averaged in time over 7.5 days near the equator; there is less temporal averaging at higher latitudes because individual maps are disks ($45°$ radius, see Fig. 2.16).

Each solar rotation is denoted with a Carrington number. The synoptic residual flow maps are plotted in Fig. 2.19 for Carrington rotation number 1911 in 1996, Fig. 2.20 for Carrington rotation 1948 in 1999, and Fig. 2.21 for Carrington rotation 1949 in 1999. Arrows are plotted every $3.84°$. We remind the reader that horizontal flows obtained by f-mode time-distance helioseismology are averaged over the first 2 Mm beneath the photosphere. Also plotted for comparison are MDI synoptic magnetic maps (photospheric magnetic field strength). In addition, we constructed synoptic maps of the mean travel-time perturbations. Mean travel times are obtained by measuring the average travel time for f-modes traveling the distance between a central point and an annulus (inward and outward). Like for the flow maps, we subtracted a background mean travel-time map from each 8-hr map before making the synoptic maps. The mean travel-time perturbations are overlaid on the flow maps.

It is quite clear from the synoptic maps that we detect large-scale flows converging toward active regions. The convergent flows have a magnitude of the order of 30 to 50 m/s and can be detected as far as $\sim 15°$ from a large active center (see
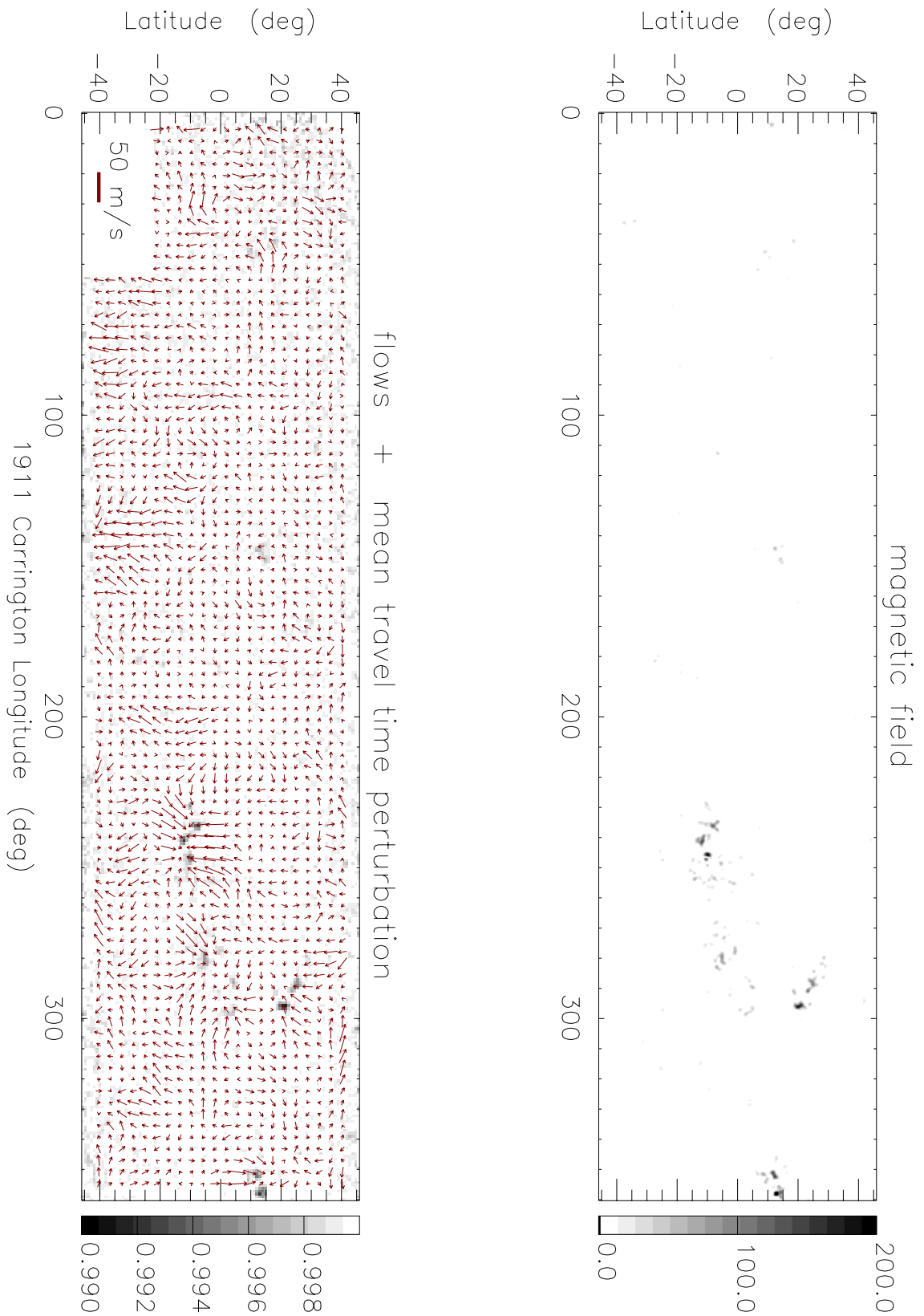
Figure 2.19: Carrington Rotation 1911 (1996). Continuum intensity, magnetic field (Gauss), mean travel time perturbation (normalized), and flow field (absolute magnetic field in the background).
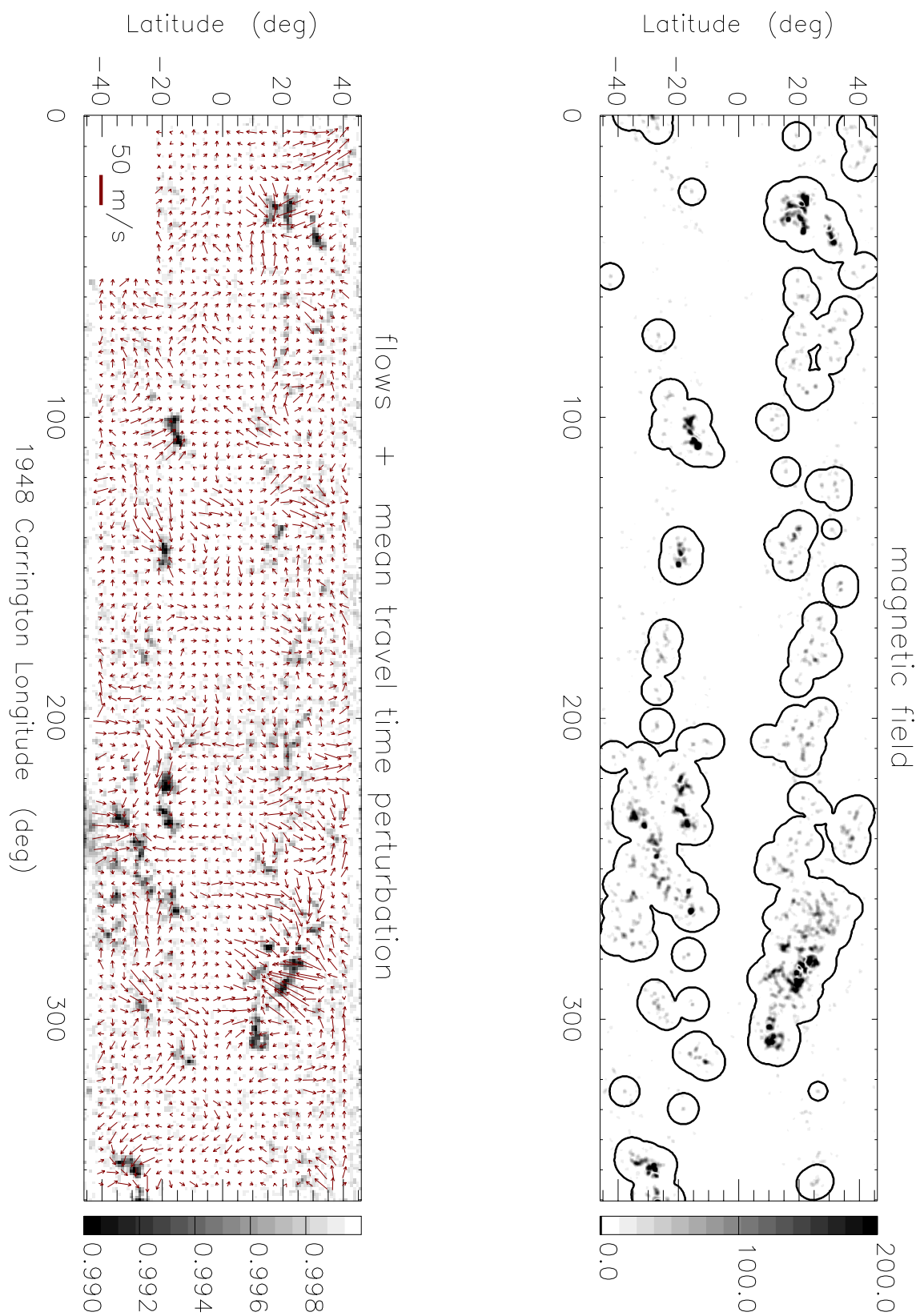
Figure 2.20: Carrington Rotation 1948 (1999)
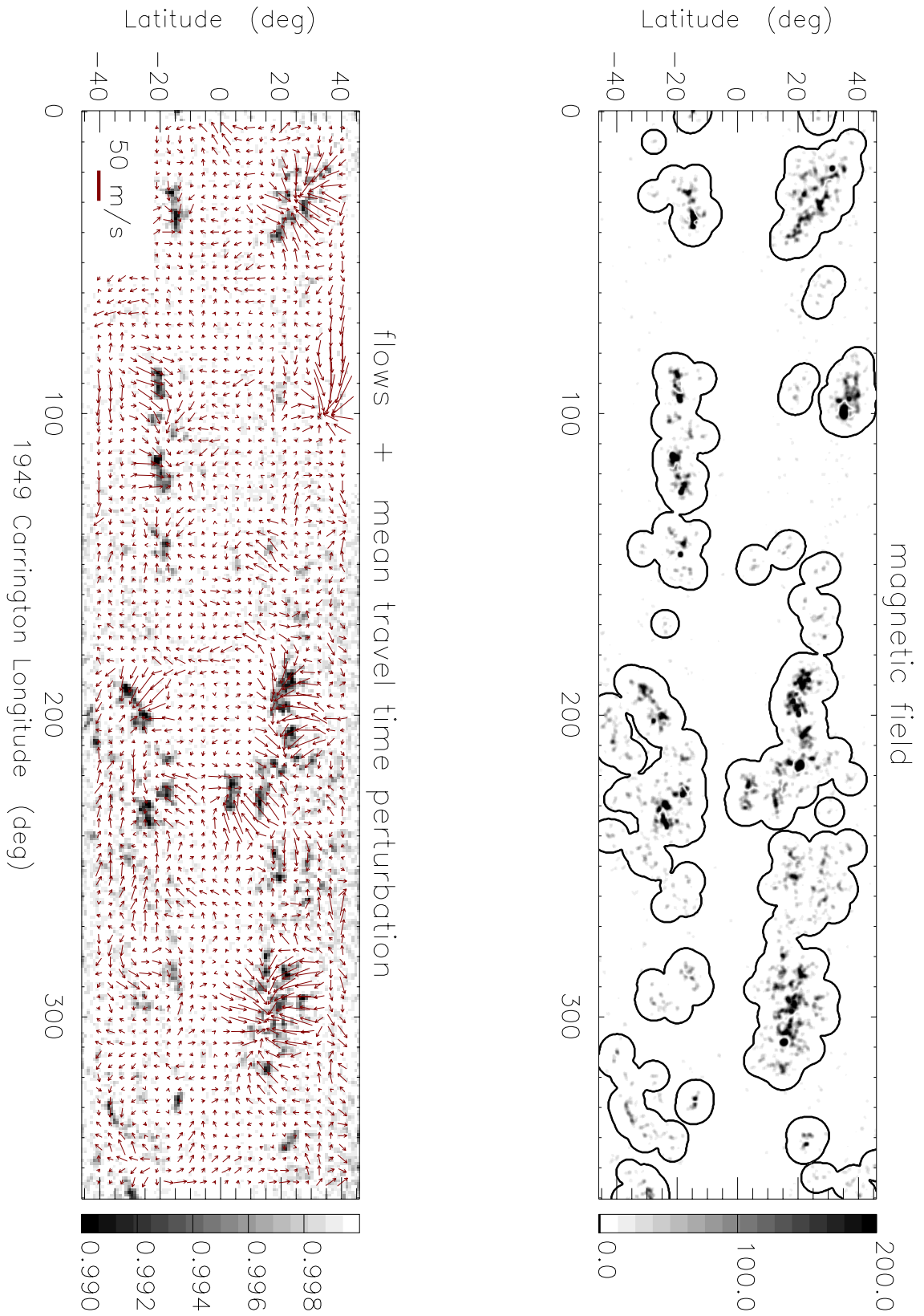
Figure 2.21: Carrington Rotation 1949 (1999)
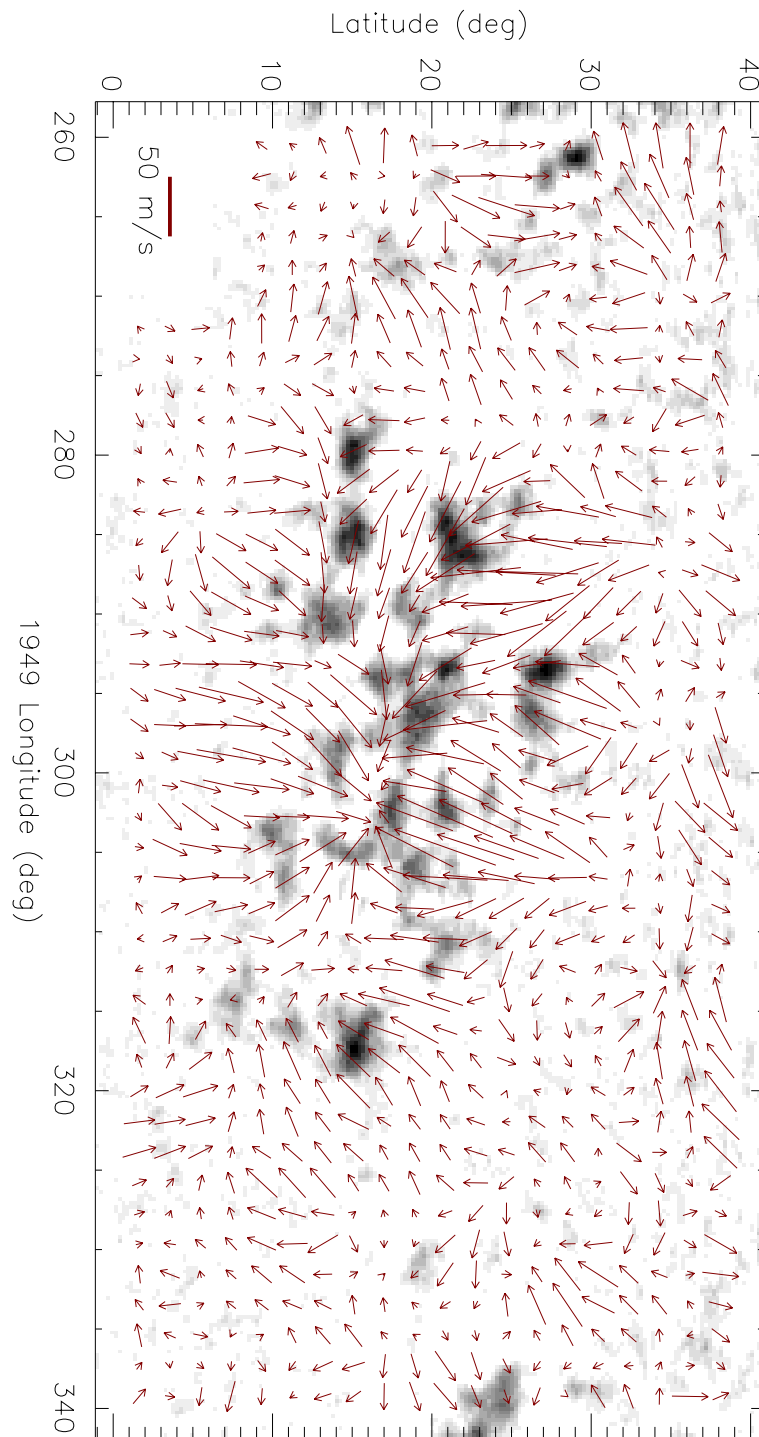
Figure 2.22: Zoom on part of Carrington Rotation 1949 (1999)

Fig. 2.22 for a zoom). Because these flows are small it is important to ask if they are real. Could the travel-time differences be caused by other types of perturbations? This question was first raised by Woodard (1997) who suggested that increased wave damping in active regions could introduce a travel-time difference and therefore mimic a flow. However, both Woodard's analysis and the work presented in chapter 3 imply that travel times should be slightly smaller for waves propagating away from a region of increased damping. Hence this effect cannot be dominant, or we would observe a divergent flow around active regions.

The synoptic maps also reveal that the mean travel-time perturbations are highly correlated with the magnetic field strength: mean travel times are reduced in active regions. This may imply that f-modes travel faster in active regions. Other effects may contribute as well. For instance, if the power spectrum is affected in such a way that high frequency waves have decreased power in active regions then the central frequency of the wave packet would decrease, and the travel-time would decrease as well. The effect of magnetic fields on travel times remains to be studied.

We now come back to the zonal and meridional flows. We have already seen that the longitudinal averages of these flows vary with the solar cycle. An important question is how local flows around large complexes of activity contribute to the longitudinal averages. In order to answer it, we separate the regions of magnetic activity from the quiet regions in Carrington maps 1948 and 1949 (as shown by the contours in Figs. 2.20 and 2.21). Figure 2.23 shows the torsional oscillations and the meridional flows when magnetic regions are excluded from the longitudinal average (thick lines) and when all data are taken into account (thin line). We find that in 1999 the zonal flows are only slightly affected when active regions are excluded from the average. It appears that regions of magnetic activity rotate a little faster. This result was already known (active regions may be rooted beneath the surface where rotation is larger). The active regions are affecting the mean meridional circulation by no more than ± 5 m/s, producing a little kink around the latitude of mean activity. Thus the converging flows around active regions produce a longitudinal modulation in the torsional oscillation. We will come back to this observation later.
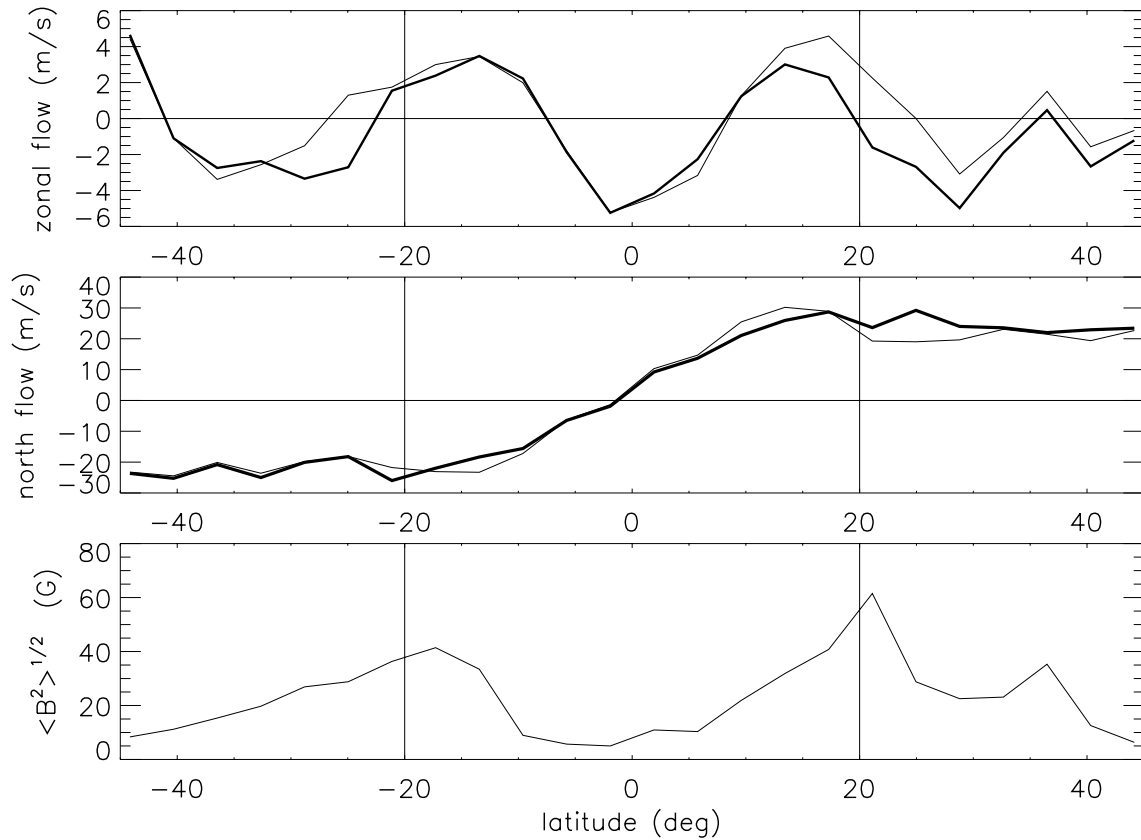
Figure 2.23: Zonal and meridional flows for Carrington rotations 1948 and 1949 in 1999. The thick lines correspond to the longitudinal averages when active regions are excluded from the calculation. The thin lines are averages over the whole maps (quiet and active regions). The bottom panel shows the latitudinal distribution of the magnetic field strength.

2.5 Comparison with Ring-Diagram Flow Maps

In the local helioseismic technique of ring-diagram analysis, a $15° \times 15°$ region of a Doppler image of the Sun is tracked and Fourier transformed in 3 dimensions to obtain a power spectrum. In the presence of flows, waves with the same wavenumber propagating in opposite directions have their frequency split by the Doppler effect. Such frequency splittings are used in ring analysis to measure flow velocities averaged over the depths where the p or f modes have significant amplitudes.

The resulting flow fields display complex and dynamic behavior. At the smallest scales, time-distance has successfully measured supergranular flows (Duvall & Gizon, 2000) and the moat flow around sunspots (Gizon et al., 2000). At larger scales, likely connected to giant cell convection, both the time-distance and ring analysis techniques have now detected strong correlations with magnetic features and near-surface converging flows around active regions. Finally, on global scales, the local techniques have confirmed the presence of the migrating torsional oscillations (e.g. Hathaway et al., 1996; Schou, 1999) and have shown that meridional circulation evolves with the solar cycle (Giles, 2000; Haber et al., 2000; Haber et al., 2002; Beck et al., 2002). Most of this work has been performed independently with little validation of the measurements through comparisons with other techniques. Before, we can fully trust the exciting discoveries of local helioseismology, we must verify that the different local helioseismic techniques are reliable and robust. In this section we make the first direct comparison of flows obtained through ring and time-distance analyses.

Ring analysis assesses the speed and direction of horizontal flows below the solar surface by measuring the Doppler shift of ambient acoustic waves that are advected by the flows. Using the procedures detailed in Haber et al. (2002), the Doppler shifts are measured by careful fitting of the peaks within a 3-D power spectra. Through 1-D RLS inversion of the integral equation which relates the frequency splittings to the flow properties, the horizontal velocity is computed as a function of depth below the photosphere (Hill, 1988; Thompson et al., 1996; Haber et al., 2002). Using Dynamics Program data from MDI, this mode fitting and inversion procedure was applied to different patches on the solar surface on a daily basis to build maps of the local flow field as a function of time and position on the solar disk. Typically, each

region consists of a 15° diameter disk. A mosaic of such tiles fills the solar disk out to 60° from the center, with tile centers separated by 7.5° in longitude and latitude. Before analysis, each tile is tracked at the surface rotation rate (Snodgrass, 1984) to remove the effects of differential rotation. The end result is a measurement of the flow field as a function of time, depth, and position on the solar disk. The horizontal resolution is roughly 15° and the vertical resolution is a few Mm near the surface.

Time-distance helioseismology applied to f modes provides information about the two components of the horizontal flows in a 1 Mm-deep layer beneath the surface (§ 2.4). These time-distance flow maps are sampled every 0.24°. For comparison with the ring analyses which have far coarser resolution, the resolution of the time-distance measurements has been degraded by spatial averaging. The averaging was performed over each of the 15° diameter tiles in the ring-analysis mosaic, and the flows were weighted by the spatial apodization function used to generate the 3–D spectra employed in the ring analysis. The end result is a set of measurements with the same coverage and horizontal resolution as the ring-analysis. Figure 2.24 shows synoptic maps of the residual flow field that remain after the longitudinal mean has been removed from both the time-distance and ring-analysis flows. Figure 2.25 shows the longitudinal means of the zonal and meridional flows for both techniques. The data are for the Carrington rotation 1948 (1999).

The residual flows obtained using the time-distance and ring analysis methods agree remarkably well. Subtle differences do appear in the flow details. However, centers of outflow and inflow as well as flow directions are largely identical in the synoptic maps obtained using either technique. In particular, the inflows located around magnetic active regions are captured by both methods. The Spearman rank correlation coefficient between the two sets of residual flows is roughly 0.8 for the Carrington rotation shown in Fig. 2.24. In comparison, correlations made between the time-distance measurements for one Carrington rotation and the ring analysis measurements for a different rotation generally produce a coefficient with a modulus less than 0.1. The correlation is highest when the depth used for the ring analysis is roughly 1 Mm, the height best sampled by the f modes used in the time-distance analyses. The correlation begins to drop precipitously as the depth increases beyond 2 Mm, dropping to as low as 0.4 at a depth of 16 Mm.
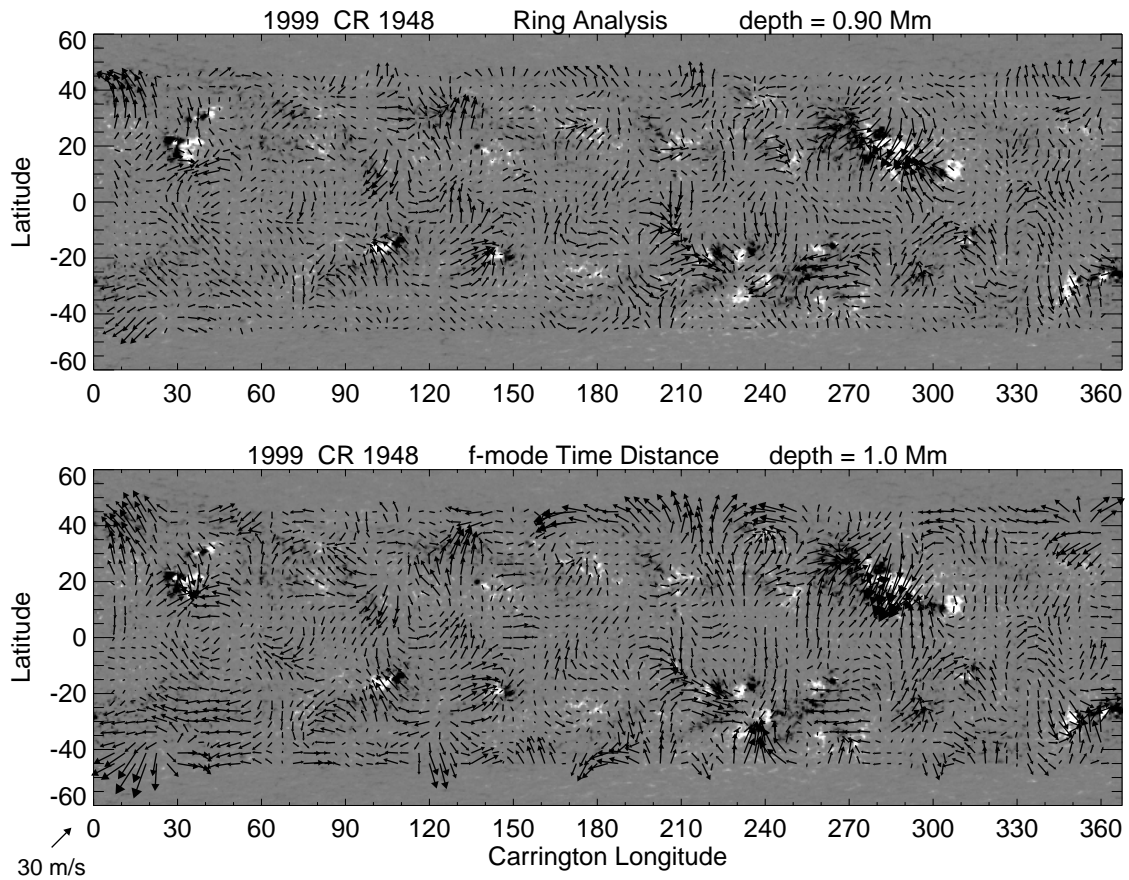
Figure 2.24: Synoptic maps of near-surface flows for Carrington rotation 1948 spanning 3 Apr − 29 Apr 1999. The flow field shown is the residual that remains after the mean meridional and zonal flows have been subtracted. The upper map was obtained using ring analyses with RLS inversion. The lower map was generated from time-distance analyses of f-mode data without depth inversion. The time-distance measurements have been averaged spatially such that the two analysis schemes have the same horizontal resolution of 15°. The tiles used in the ring analyses overlap by 7.5°, and the resulting flow field has been interpolated twofold to generate arrows with a spacing of 3.75°.
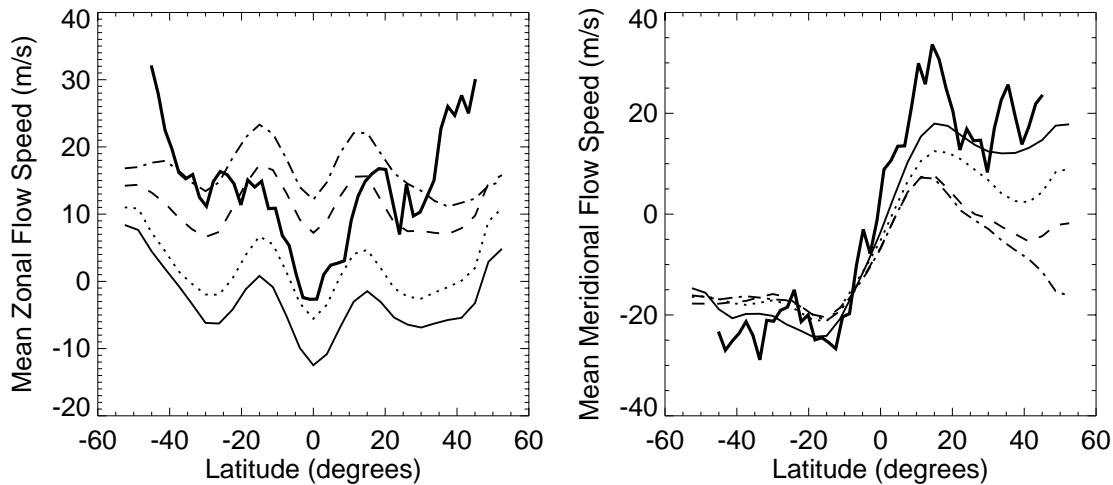
Figure 2.25: The mean zonal flows (left panel) and meridional flows (right panel) as a function of latitude obtained using ring analysis and time-distance f-mode analysis of Dynamics Program data from Carrington rotation 1948 (in 1999). The zonal flow is measured relative to the surface differential rotation rate of Snodgrass (1984). The thick solid curve is the flow obtained with time-distance analysis. The other curves were obtained using ring analysis, and correspond to the flow at different depths: solid 0.9 Mm, dotted 2.0 Mm, dashed 4.4 Mm, and dot-dashed 7.1 Mm. These flows were removed from the full flow field to obtain the synoptic map shown in Fig. 2.24.

In contrast, the mean flows display less similarity. Both techniques generate zonal flows that have consistent shape as a function of latitude. However, there appears to be a substantial constant offset of 15 m/s between the rotation rates. This offset represents about 0.8% of the sun's equatorial rotation rate. We do not fully understand the source of this offset, although we suspect that it is due to the different tracking and remapping methods used to remove rotation and sphericity. The time-distance analyses for a given day are performed on a single region, 90° square, that is tracked at the Carrington rate and remapped using an equal area projection. The ring analysis is executed on many different regions each 15° in diameter, each tracked at the local surface differential rotation rate and remapped using Postel's projection. The mean meridional flows obtained by both techniques and shown in Fig. 2.25 are roughly consistent when the time-distance results are compared to the 0.9 Mm depth of the ring analysis measurements.

The similarities between the residual flows obtained with f-mode time-distance

and ring analysis are heartening. Both techniques appear to provide reliable measurements of large scale flows just beneath the solar surface.

2.6   Solar-Cycle Variation of the Meridional Flows

We construct maps of rotation and meridional flows using time-distance helioseismology applied to p modes from the MDI Structure Program. The mean travel distance is $17°$ corresponding to a maximum depth of 65 Mm below the surface (no depth inversion is done). Meridional flow maps show a time-varying component that has a banded structure with an equatorward migration over the solar cycle. The time-varying component of meridional flow consists of a flow diverging from the dominant latitude of magnetic activity. This map is compared with torsional oscillation maps and with magnetic strength maps, showing a correlation with active latitudes and a strong link between the time-varying component of the meridional flow and the east-west torsional oscillations.

2.6.1   Introduction

Torsional oscillations and meridional flows have been studied for over two decades (e.g. Howard & LaBonte, 1980; Duvall, 1979; Ulrich, 1988). The surface meridional flow is generally agreed to be poleward in both hemispheres with an amplitude of 10-20 $m\,s^{-1}$. The torsional oscillations (also termed 'zonal flows') consist of latitudinal bands of alternating faster and slower rotation which migrate toward the equator over the solar cycle and are superimposed on top of the differential rotation. The zonal flows can be seen at depths of 56 Mm (Howe et al., 2000) with global helioseismology.

Meridional flows have been difficult to measure by direct Doppler observation due to their small amplitude compared to the large amplitude velocity patterns such as convective limb shift and rotation. However, Nesme-Ribes et al. (1997) have studied meridional flows using sunspots as tracers and have identified a correlation of east-west and north-south motions consistent with angular momentum transport which would sustain differential rotation. Time variations of the meridional flow were noticed by Ulrich (1988) and Hathaway (1996).

The p-mode time-distance helioseismology studies of the meridional circulation conducted by Giles et al. (1997) and Giles (2000) showed that it extends through the convection zone. Haber et al. (2002) studied meridional flows using ring-diagram

analysis and found indications of a second meridional cell during the years 1998 through 2001 in the outer 7 Mm; additionally, they found an asymmetry in the meridional flows between the northern and southern hemispheres which would have impact on angular momentum transport. Chou & Dai (2001) studied subsurface meridional flows using time-distance helioseismology and found a time-varying component which extends down to 70 Mm. They suggested that the varying flow could be linked to magnetic activity. Furthermore we showed in Sec. 2.4 that, near the surface, meridional circulation is affected by large-scale convergent flows around active regions.

2.6.2   Analysis and Results

The data reduction followed the description by Giles (2000). The data spanned from May 1996 through July 2001 and consist of medium-resolution MDI dopplergrams. The data gap from June 1998 until March 1999 corresponds to the period of broken contact with SOHO. Images were grouped into 72-hour periods for detrending of solar rotation and supergranulation. Regions, spanning 100° in latitude and longitude, were tracked at the solar rotation rate. These tracked regions were 'stacked' into a data cube for further processing, which consisted of applying a high-pass filter (cutoff at 1.7 mHz) to remove supergranulation and applying a phase-speed filter to select acoustic modes. Temporal cross-correlations were obtained using code developed by Giles (2000). To measure meridional flows, cross-correlations are computed between pairs of points separated in latitude by amounts ranging from 3° to 45°. To improve the signal-to-noise ratio, the cross-correlation functions for each latitude were averaged over three-month periods. Further averaging was done keeping the mid-point constant, and producing 61 latitude bins ($\sim 3°$ sampling). This was repeated for 21 three-month epochs. This procedure was also performed in an east-west direction to measure rotation.

Wave travel times were measured by fitting to the cross-correlation function. A positive time delay corresponds to a flow to the north in the case of meridional circulation or a flow to the west for rotation. The measurement of the travel-time shifts follows closely the method discussed by Gizon & Birch (2002). At each distance, a mean reference cross-correlation symmetric for the two senses of time
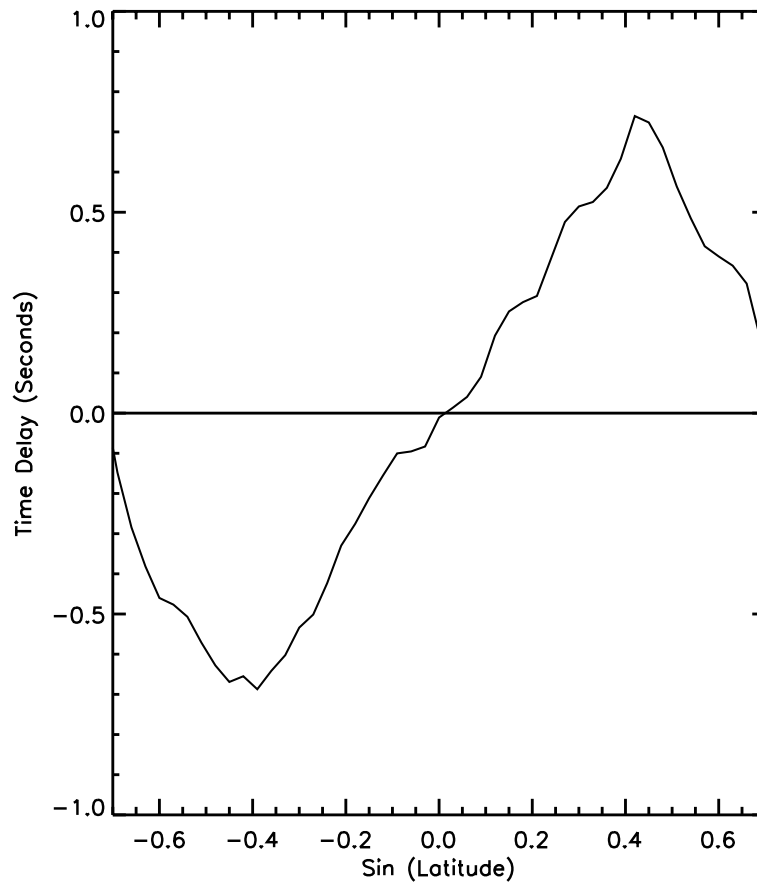
Figure 2.26: Mean meridional flow. The mean signal of meridional flows is shown here for the interval May 1996-July 2001. A northward flow corresponds to a positive travel-time shift. From a simple meridional flow model (Giles, 2000), we estimate that a 1 s time shift corresponds to ~ 20 m s^{-1} .

lag was derived. This reference function was cross-correlated with an individual cross-correlation to yield an approximately zero-centered result except for the shift away from zero due to the flow. A weighted average over distances was derived with the contribution peaked near a distance of 17° with a width of 4°. A ray connecting points separated by 17° extends to a depth of 65 Mm. The time shift was measured as twice the shift of the maximum of this correlation away from zero lag by forcing a parabola through the three closest points to the peak. The factor of two is necessary to match earlier definitions of time shift which involved measuring the shift of positive time lags and negative time lags separately and taking the difference, effectively doubling the signal.

As shown in Fig. 2.26, the meridional flow averaged over time is strongly antisymmetric as a function of latitude, with positive values indicating a northward flow. The peak velocity is about $15 \mathrm{~m\,s}^{-1}$ toward the poles at mid-latitudes. Small errors in the pointing of the MDI telescope can cause solar rotation to contaminate meridional velocity measurements. Taking the antisymmetric component removes this error. The time-varying component of the meridional flow was obtained by subtracting a smooth fit to the 5-year average from the measurement at each epoch. Figure 2.27a shows the residuals, with red indicating poleward motion in both hemispheres. The east-west flow was similarly analyzed, with the exception that a smooth rotation curve was subtracted to produce the torsional oscillation pattern shown in Fig. 2.27b. Torsional oscillations obtained from f-mode frequency splittings by Schou (1999) are shown for comparison in Fig. 2.27c.

A map of magnetic field strength is included in Figure 2.27d to indicate the active latitudes over the period of interest. To compare with the flow maps, a mean latitude of magnetic activity was derived by taking the absolute value of the magnetic field (from MDI synoptic charts), re-binning in latitude and longitude, symmetrizing in latitude, squaring, and fitting a Gaussian function in latitude at each longitude. The mean latitude of activity, given by the location of the peak of the Gaussian, is plotted on top of the velocity maps in Figure 2.27 to indicate the strong connection between the magnetic cycle and the equatorward propagating flow patterns.

The flows are organized about the mean latitude of magnetic activity. The residual meridional flow is away from the latitude of activity. Whether the residual flows cause the magnetic activity to emerge at this latitude or is a result of rising magnetic flux is unknown. The zonal flow is faster equatorward of the mean latitude of activity and slower poleward, as noted previously by LaBonte & Howard (1982). The time-varying component of the meridional flow correlates very well with the zonal flows, with a more strongly poleward flow corresponding to a slower rotation. Although we have not derived the depth dependence of the flows explicitly, the north-south component of the "torsional oscillation" that we detect is tens of megameters beneath the surface (65 Mm maximum). What is not known yet is the longitudinal structure of the residual flows.
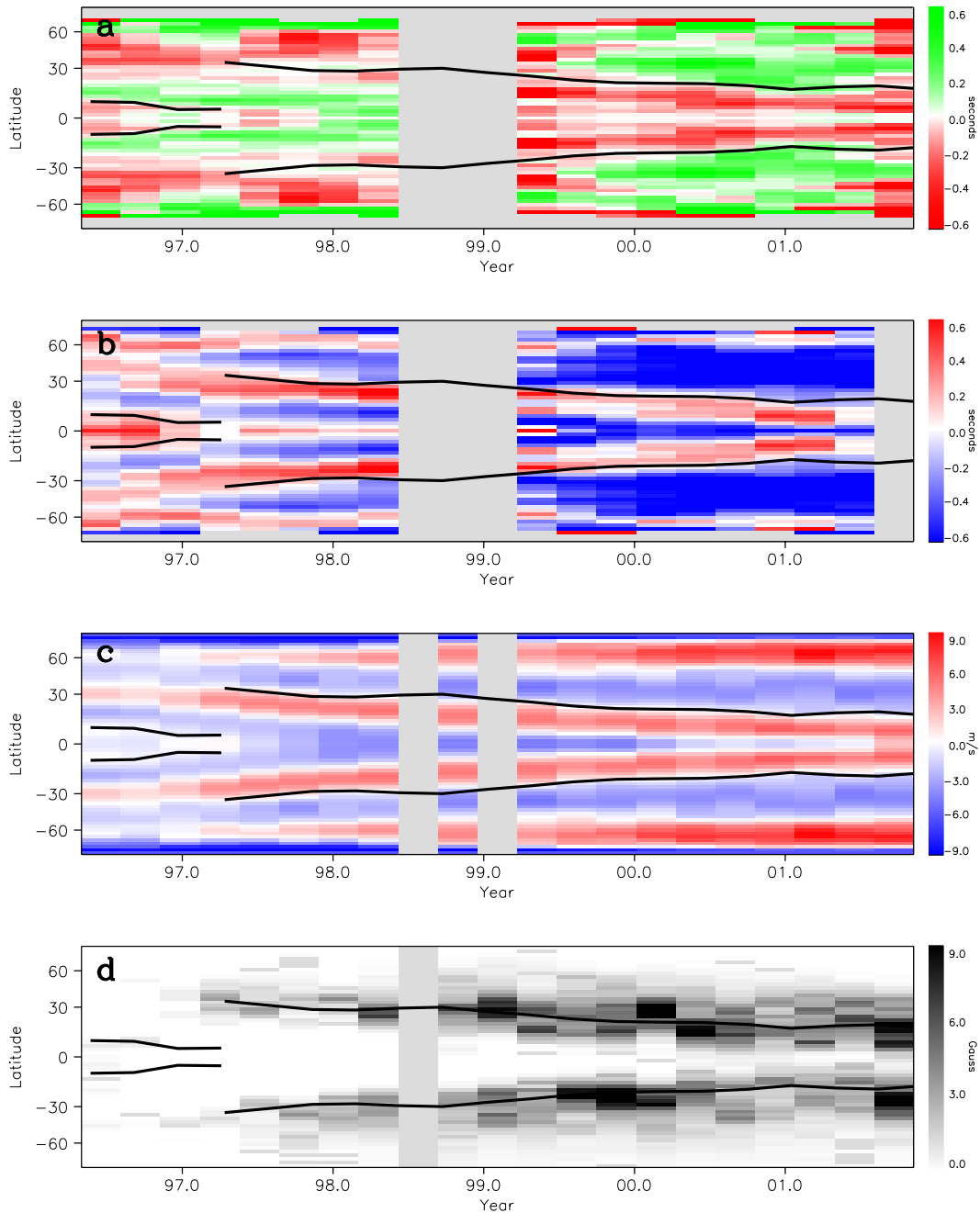
Figure 2.27: Residual meridional flow and torsional oscillation maps from time-distance helioseismology compared with a torsional oscillation map from global modes and a butterfly diagram of magnetic fields. The heavy black line over-plotted is the mean latitude of activity. a) The poleward flow, obtained from subtracting a fit to the mean meridional flow and symmetrizing the residuals. A positive time delay indicates a poleward flow in both hemispheres. b) The torsional oscillations obtained from time-distance helioseismology. Red is prograde. c) Torsional oscillations obtained from f-mode frequency splittings (Schou, 1999). d) Magnetic field strength derived from MDI synoptic charts.

Chapter 3

Time-Distance Helioseismology: Interpretation of Travel Times [1]

---

[1] This chapter is from a paper published in the Astrophysical Journal (Gizon & Birch, 2002). The basic theory presented here was developed independently and in parallel by the authors.

3.1 Introduction

Time-distance helioseismology, introduced by Duvall et al. (1993b), has yielded numerous exciting insights into the interior of the Sun. This technique, which gives information about travel times for wave packets moving between any two points on the solar surface, is an important complement to global-mode helioseismology as it is able to probe subsurface structure and dynamics in three dimensions. Some of the main results concern flows and wave-speed perturbations underneath sunspots (Duvall et al., 1996; Kosovichev et al., 2000; Zhao et al., 2001), large-scale subsurface poleward flows (Giles et al., 1997), and supergranulation flows (Duvall & Gizon, 2000).

The interpretation of time-distance data can be divided into a forward and an inverse problem. The forward problem is to determine the relationship between the observational data (travel times $\delta\tau$) and internal properties (q_α). Generally, this relationship is sought in the form of a linear integral equation,

$$\delta\tau = \sum_\alpha \int_\odot \mathrm{d}\boldsymbol{r}\, \delta q_\alpha(\boldsymbol{r})\, K^\alpha(\boldsymbol{r})\,, \tag{3.1}$$

where the $\delta q_\alpha(\boldsymbol{r})$ represent the deviations in internal solar properties from a theoretical reference model. The index α refers to all relevant types of independent perturbations, such as sound speed, flows, or magnetic field. The integral $\int_\odot \mathrm{d}\boldsymbol{r}$ denotes spatial integration over the volume of the Sun. The kernels of the integrals, $K^\alpha(\boldsymbol{r})$, give the sensitivity of travel times to the perturbations to the solar model. The inverse problem is to invert the above equation, i.e. to estimate δq_α, as a function of position $\boldsymbol{r}$, from the observed $\delta\tau$. In this chapter we consider only the forward problem.

An accurate solution to the forward problem is necessary for making quantitative inferences about the Sun from time-distance data. There have been a number of previous efforts to understand the effect of local perturbations on travel times. D'Silva et al. (1996), Kosovichev (1996), and Zhao et al. (2001) used geometrical acoustics to describe the interaction of acoustic waves with sound-speed perturbations and flows. Bogdan (1997) argued that a finite-wavelength theory is needed.

Birch & Kosovichev (2000) solved the linear forward problem for sound-speed perturbations, in the single-source approximation. Jensen et al. (2000) solved a weakly nonlinear forward problem for sound-speed perturbations, in the single-source approximation, and proposed the use of Fresnel-zone based travel-time kernels. Bogdan et al. (1998) used a normal mode approach to compute travel-time perturbations in a model sunspot. Woodard (1997) estimated the effect of wave absorption by sunspots on travel times. This important work, which required a model for random distributed wave sources, is one of the primary motivations for obtaining a general theory for travel-time sensitivity kernels. The model developed by Woodard (1997) employs, however, the approximation that wave damping affects only the amplitude of transmitted waves, ignoring scattering. Birch et al. (2001) tested the accuracy of travel times obtained in the Born approximation, which models single scattering from local inhomogeneities. Although the above mentioned efforts represent substantial progress, there is not yet a general procedure for relating actual travel-time measurements to perturbations to a solar model that takes into account random distributed sources for solar oscillations, despite a preliminary study by Gizon & Birch (2001).

The first part of this chapter (§ 3.2) is an attempt to synthesize and extend the current knowledge into a flexible framework for the computation of the linear sensitivity of travel times to local inhomogeneities. We start from a physical description of the wave field, including wave excitation and damping. We incorporate the details of the measurement procedure. Two other key ingredients of our approach are the single-scattering Born approximation and a clear observational definition of travel time, both taken from the geophysics literature (e.g. Tong et al., 1998; Zhao & Jordan, 1998; Marquering et al., 1999). The main difference between the geophysics and helioseismology problems is that helioseismology deals with multiple random wave sources as opposed to a single isolated source.

The second part of this chapter (§ 3.3) is an example calculation of travel time kernels for surface gravity waves. The purpose is to demonstrate the application of the general theory described in Section 3.2. We compute travel-time kernels for local perturbations in source strength and damping rate. In our model, these perturbations are confined to the surface and therefore are computationally convenient as we

obtain two-dimensional kernels. Localized source and damping perturbations are interesting and not yet well understood. For this example, we also compare these kernels with kernels calculated in the single-source picture (Birch & Kosovichev, 2000; Jensen et al., 2000), in which distributed random sources are replaced by an artificial causal source placed at one of the observation points. We show that the single-source kernels do not reproduce all the features seen in the distributed-source kernels.

3.2   The General Forward Problem for Random Distributed Sources

3.2.1   Definition of Travel Times

The fundamental data of modern helioseismology are high-resolution Doppler images of the Sun's surface. In general, the filtered line-of-sight projection of the velocity field can be written as

$$\phi = \mathcal{F}\left\{\hat{\boldsymbol{\ell}} \cdot \boldsymbol{v}\right\},\tag{3.2}$$

where $\boldsymbol{v}$ is the Eulerian velocity and $\hat{\boldsymbol{\ell}}$ is a unit vector in the direction of the line of sight. The operator $\mathcal{F}$ describes the filter used in the data analysis, which includes the time window (time duration T), instrumental effects, and other filtering.

The basic computation in time-distance helioseismology is the temporal cross-correlation, $C(\mathbf{1}, \mathbf{2}, t)$, between the signal, ϕ, measured at two points, $\mathbf{1}$ and $\mathbf{2}$, on the solar surface,

$$C(\mathbf{1}, \mathbf{2}, t) = \frac{1}{T} \int_{-\infty}^{\infty} \mathrm{d}t' \, \phi(\mathbf{1}, t') \, \phi(\mathbf{2}, t' + t),\tag{3.3}$$

where T is the time duration of the observation. The cross-correlation is useful as it is a phase-coherent average of inherently random oscillations. It can be seen as a solar seismogram, providing information about travel times, amplitudes, and the shape of the wave packets traveling between any two points on the solar surface. Figure 1.5 shows an example of a surface gravity wave cross-correlation. The positive-time branch corresponds to waves moving from $\mathbf{1}$ to $\mathbf{2}$, and the negative-time branch

represents waves moving in the opposite direction. For acoustic waves there are additional branches, at larger absolute time, corresponding to multiple bounces off the surface in between **1** and **2**.

We define the "travel time" for each branch to be the time lag that minimizes the difference between the measured cross-correlation, C, and a sliding reference wavelet, C^{ref}. Depending on the choice of reference wavelet the term "travel time" may be an abuse of language; this issue will be clarified later. The travel time for waves going from **1** to **2** is denoted by $\tau_+(\mathbf{1}, \mathbf{2})$ and the travel time for waves going from **2** to **1** by $\tau_-(\mathbf{1}, \mathbf{2})$. The difference (in the least squares sense) between the observed cross-correlation and the reference wavelet is

$$
\begin{aligned}
X_\pm(\mathbf{1}, \mathbf{2}, t) &= \int_{-\infty}^{\infty} \mathrm{d}t'\, f(\pm t') \\
&\quad \times \left[C(\mathbf{1}, \mathbf{2}, t') - C^{\text{ref}}(\mathbf{1}, \mathbf{2}, t' \mp t) \right]^2 .
\end{aligned} \tag{3.4}
$$

The window function, $f(t')$, is a one-sided function (zero for t' negative) used to separately examine the positive- and negative-time parts of the cross-correlation. The window $f(t')$ is used to measure τ_+, and $f(-t')$ is used to measure τ_-. One possible choice is a window that isolates the first-skip branch of the cross-correlation. Other window functions could be chosen to, for example, isolate the second bounce branch of a cross-correlation in the case of acoustic modes.

By definition the travel times $\tau_\pm$ are the time lags that minimize $X_\pm$:

$$
\tau_\pm(\mathbf{1}, \mathbf{2}) = \operatorname*{argmin}_t \{\, X_\pm(\mathbf{1}, \mathbf{2}, t) \,\} . \tag{3.5}
$$

Minimizing $X_\pm$ is equivalent to fitting $C^{\text{ref}}(t' \mp t)$ to $C(t')$ with a weighting in time given by $f(\pm t')$, varying the time lag t only. An example of measuring the travel times $\tau_\pm$ from a cross-correlation is shown in Figure 3.1.

The choice of reference wavelet $C^{\text{ref}}(\mathbf{1}, \mathbf{2}, t)$ is left to the observer. For most applications the reference wavelet needs only be a function of distance $\Delta = \|\mathbf{2} - \mathbf{1}\|$ and time t. As was done in Figure 3.1, one possible choice is to take C^{ref} to look like a cross-correlation. In this case τ_+ and τ_- are small and the term "travel time" should
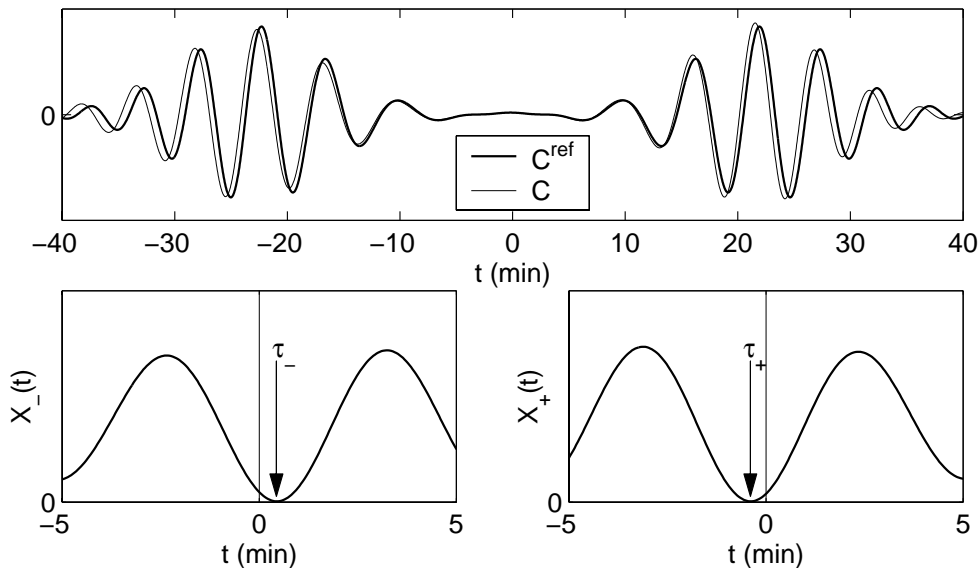
Figure 3.1: An example showing how to measure the travel times $\tau_\pm$ from a cross-correlation $C(\mathbf{1}, \mathbf{2}, t)$. In this figure we choose the reference wavelet C^{ref} (heavy line in top panel) to be the zero-order cross-correlation, for the distance $\Delta = 10$ Mm, from the surface gravity wave example discussed in Section 3.3. In general, the observer is free to choose any reference wavelet. This function C^{ref} is even in time. The light line (top panel) shows an example cross-correlation, C, which in this particular case was computed from a model including a uniform horizontal flow of 400 m s^{-1} in the direction $\mathbf{1} \to \mathbf{2}$. To measure the travel times $\delta\tau_\pm$ from C we need to minimize the functions $X_\pm$. The lower panels show the functions $X_-(t)$ and $X_+(t)$, constructed using equation (3.4). The window function f was chosen to be the Heaviside step function. For the positive-time branch of C, the best fit is obtained by shifting C^{ref} toward $t = 0$ (to the left). The minimum of $X_+(t)$ occurs at a negative time τ_+, as can be seen in the right bottom panel. For the negative-time branch of C, the minimum of the function $X_-(t)$ occurs at a positive time τ_- (see bottom left panel). The locations, τ_- and τ_+, of the minima of the functions $X_-(t)$ and $X_+(t)$ are, by definition, the measured travel times. In this particular example the signs $\tau_+ < 0$ and $\tau_- > 0$ make sense as waves travel faster with the flow than against it.

be understood to mean "time lag". A reference wavelet that resembles a cross-correlation can be constructed by either averaging the observed cross-correlations over all possible pairs of points $(\mathbf{1}, \mathbf{2})$ for each distance Δ (see Fig. 1.5), or by computing a theoretical cross-correlation from a solar model (see § 3.3). Another possible choice is to take $C^{\text{ref}}(\mathbf{1}, \mathbf{2}, t)$ to look like a single wavelet centered about $t = 0$. In this case τ_+ and τ_- will essentially represent the time it takes for wavepackets to travel between the observation points, and the denomination "travel times" for $\tau_\pm$ is appropriate.

The definition of travel time presented here is analogous to the typical definition of travel time used in the geophysics literature (e.g. Zhao & Jordan, 1998). In time-distance helioseismology Duvall et al. (1997) measure travel times by fitting a Gaussian wavelet to cross-correlations. This procedure distinguishes between group and phase travel times, by allowing both the envelope and phase of the wavelet to vary independently. Our definition is a simplification of this procedure as it contains only one travel-time parameter per branch. The travel time defined here is neither a pure group or phase time; it is, however, perfectly well defined and has already been used in a time-distance study with real data (Gizon et al., 2000). Without significant difficulty, the fitting presented here could be extended to include more parameters, for example amplitude and central frequency, as is done by Duvall et al. (1997).

Traditionally, mean and difference travel times have been used in place of the one-way travel times. The mean and difference travel times are obtained from the one-way travel times by

$$\tau_{\text{mean}} \;\; = \;\; \frac{1}{2}(\tau_+ + \tau_-)\,, \tag{3.6}$$

$$\tau_{\text{diff}} \;\; = \;\; \tau_+ - \tau_- \,. \tag{3.7}$$

The motivation behind using τ_{mean} and τ_{diff} is that sound-speed perturbations are expected to contribute mostly to the mean travel time and flows to the travel-time difference (e.g. Kosovichev & Duvall, 1997).

The definition of travel-time perturbations described here leaves observers free to measure without reference to a solar model. We note, however, that in order for a proper interpretation of measured travel-time perturbations to be made it

is essential for observers to report their choices of reference wavelet C^{ref}, window function f, and filter $\mathcal{F}$. A solar model is only necessary for the next step, the interpretation of travel-time perturbations in terms of local perturbations to a solar model, to which we now turn.

3.2.2   Interpretation of Travel Times

The goal of time-distance helioseismology is to estimate the internal solar properties which produce model travel times that best match observed travel times. To achieve this, we need to know how to compute the travel times for a particular solar model. In order to make the inverse problem feasible we also need to linearize the forward problem around a background state that is close to the Sun.

A background solar model is fully specified by a set of internal properties (density, pressure, etc.) which we denote by $q_\alpha(\boldsymbol{r})$ for short. Standard solar models provide a reasonable background state. In the background state the cross-correlation and the travel times are C^0 and $\tau_\pm^0$ respectively. We then consider small perturbations, $\delta q_\alpha(\boldsymbol{r})$, to the solar properties. These perturbations could include, for example, local changes in density, sound speed, or flows. The difference between the resulting cross-correlation, C, and the background cross-correlation we denote by δC,

$$\delta C(\boldsymbol{1}, \boldsymbol{2}, t) = C(\boldsymbol{1}, \boldsymbol{2}, t) - C^0(\boldsymbol{1}, \boldsymbol{2}, t) \,. \tag{3.8}$$

Likewise, the perturbed travel times $\delta\tau_\pm$ are

$$\delta\tau_\pm(\boldsymbol{1}, \boldsymbol{2}) = \tau_\pm(\boldsymbol{1}, \boldsymbol{2}) - \tau_\pm^0(\boldsymbol{1}, \boldsymbol{2}) \,. \tag{3.9}$$

The travel times $\tau_\pm(\boldsymbol{1}, 2)$ are measured from the cross-correlation $C(\boldsymbol{1}, \boldsymbol{2}, t)$. The reference times $\tau_\pm^0$ are the travel times which would be measured if the Sun and the background model were identical.

As we are considering small changes in the solar model, the correction to the model cross-correlation, δC, will also be small. As a result we can linearize the dependence of the travel-time perturbations $\delta\tau_\pm$ on δC. The algebra is detailed in

Appendix A. The result of this calculation can be written as

$$\delta\tau_{\pm}(\mathbf{1}, \mathbf{2}) = \int_{-\infty}^{\infty} \mathrm{d}t \, W_{\pm}(\mathbf{1}, \mathbf{2}, t) \, \delta C(\mathbf{1}, \mathbf{2}, t) \,. \tag{3.10}$$

The functions $W_{\pm}$ depend on the zero-order cross-correlation C^0, the reference wavelet C^{ref}, and the window function f, and are given in equation (A.7). The sensitivity of $\delta\tau_{\pm}$ to δC is given by the weight functions $W_{\pm}$. We emphasize that the travel-time perturbations $\delta\tau_{\pm}$ are proportional to δC, which is a first-order perturbation to the background solar model. We interpret the right-hand side of equation (3.10) as a model for the difference between the observed travel times and the theoretical travel times in the background solar model.

The source of solar oscillations is turbulent convection near the solar surface (e.g. Stein, 1967). As a result the signal ϕ and the cross-correlation C are realizations of a random process. In general, a random variable is fully characterized by its expectation value and all of its higher-order moments. As a result, to describe a travel time perturbation $\delta\tau$ we need its expectation value (ensemble average) as well as its variance, etc. In this chapter we consider only the expectation value. A calculation of the variance of the travel times would be essential to characterize the realization noise in travel time measurements. An accurate estimate of the noise in travel time measurements is important for solving the inverse problem.

In this chapter we only compute the expectation values of travel time perturbations and cross-correlations. This represents a first and necessary step. Notice in addition that under the assumptions of the Ergodic theorem (e.g. Yaglom, 1962) the cross-correlations (hence travel times) tend to their expectation values as the observational time interval increases.

3.2.3   Modeling The Observed Signal

In order to obtain the cross-correlation, C^0, and its first-order perturbation, δC, we need to compute the observable, ϕ, defined in equation (3.2), and therefore the wave velocity $\boldsymbol{v}$. Linear oscillations are governed by an equation of the form (e.g. Gough, 1993)

$$\boldsymbol{\mathcal{L}}\boldsymbol{v} = \boldsymbol{S} \,. \tag{3.11}$$

The vector $\boldsymbol{S}$ denotes the source of excitation for the waves. The linear operator $\boldsymbol{\mathcal{L}}$, acting on $\boldsymbol{v}$, should encompass all the physics of wave propagation in an inhomogeneous stratified medium permeated by flows and magnetic fields. Damping processes should also be accounted for in $\boldsymbol{\mathcal{L}}$. An explicit expression for the operator $\boldsymbol{\mathcal{L}}$ including steady flows is provided by Lynden-Bell & Ostriker (1967). Bogdan (2000) includes magnetic field.

We now expand $\boldsymbol{\mathcal{L}}$, $\boldsymbol{v}$, and $\boldsymbol{S}$ into zero- and first-order contributions, which refer to the background solar model and to the lowest-order perturbation to that model:

$$\boldsymbol{\mathcal{L}} = \boldsymbol{\mathcal{L}}^0 + \delta\boldsymbol{\mathcal{L}}\,, \tag{3.12}$$

$$\boldsymbol{v} = \boldsymbol{v}^0 + \delta\boldsymbol{v}\,, \tag{3.13}$$

$$\boldsymbol{S} = \boldsymbol{S}^0 + \delta\boldsymbol{S}\,. \tag{3.14}$$

The operator $\delta\boldsymbol{\mathcal{L}}$ depends on first-order quantities such as local perturbations in density, sound speed, damping rate, as well as flows and magnetic field. In general, one may contemplate time-dependent perturbations. There are, however, many interesting structures on the Sun (e.g. supergranules, meridional flow, moat flows) which are approximately time independent on the time scale on which time-distance measurements are made (at least several hours). As a result, for the sake of simplicity, we only consider time-independent perturbations. These perturbations, which we denoted by $\delta q_\alpha(\boldsymbol{r})$ for short, are thus only functions of position $\boldsymbol{r}$ in the solar interior.

To lowest order, equation (3.11) reduces to

$$\boldsymbol{\mathcal{L}}^0\boldsymbol{v}^0 = \boldsymbol{S}^0\,. \tag{3.15}$$

In order to solve this equation, we introduce a set of causal Green's vectors $\boldsymbol{G}^i$ defined by

$$\boldsymbol{\mathcal{L}}^0\boldsymbol{G}^i(\boldsymbol{x},t;\boldsymbol{s},t_{\rm s}) = \hat{\boldsymbol{e}}_i(\boldsymbol{s})\,\delta_{\rm D}(\boldsymbol{x}-\boldsymbol{s})\,\delta_{\rm D}(t-t_{\rm s})\,, \tag{3.16}$$

where the $\hat{\boldsymbol{e}}_i(\boldsymbol{s})$ are three orthogonal basis vectors at the point $\boldsymbol{s}$ and $\delta_{\rm D}$ is the Dirac delta function. The vector $\boldsymbol{G}^i(\boldsymbol{x},t;\boldsymbol{s},t_{\rm s})$ is the velocity at location $\boldsymbol{x}$ and time t which results from a unit impulsive source in the $\hat{\boldsymbol{e}}_i$ direction at time $t_{\rm s}$ and location

s. Note that the vector $\boldsymbol{G}^i$ does not in general point in the direction of $\hat{\boldsymbol{e}}_i$. Guided by equation (3.2), we define the zero-order Green's functions for the observable ϕ:

$$\mathcal{G}^i(\boldsymbol{x}, t; \boldsymbol{s}, t_{\mathrm{s}}) = \mathcal{F}\left\{\hat{\boldsymbol{\ell}}(\boldsymbol{x}) \cdot \boldsymbol{G}^i(\boldsymbol{x}, t; \boldsymbol{s}, t_{\mathrm{s}})\right\}. \tag{3.17}$$

In terms of $\mathcal{G}^i$, the unperturbed signal reads:

$$\phi^0(\boldsymbol{x}, t) = \int_\odot \mathrm{d}\boldsymbol{s} \int_{-\infty}^{\infty} \mathrm{d}t_{\mathrm{s}} \, \mathcal{G}^i(\boldsymbol{x}, t; \boldsymbol{s}, t_{\mathrm{s}}) \, S_i^0(\boldsymbol{s}, t_{\mathrm{s}}). \tag{3.18}$$

The sum is taken over the repeated index i, as is done for all repeated indexes throughout this chapter.

To the next order of approximation, equation (3.11) gives

$$\boldsymbol{\mathcal{L}}^0 \, \delta\boldsymbol{v} = -\delta\boldsymbol{\mathcal{L}} \, \boldsymbol{v}^0 + \delta\boldsymbol{S}. \tag{3.19}$$

This is the single-scattering Born approximation (e.g. Sakurai, 1995). The first-order Born approximation has been shown to work for small perturbations (e.g. Hung et al., 2000; Birch et al., 2001). We note that equation (3.19) is of the same form as equation (3.15): the term $-\delta\boldsymbol{\mathcal{L}} \, \boldsymbol{v}^0 + \delta\boldsymbol{S}$ appears as a source for the scattered wave velocity $\delta\boldsymbol{v}$. The solution to equation (3.19) is thus

$$\begin{aligned}
\delta\boldsymbol{v}(\boldsymbol{x}, t) &= \int_\odot \mathrm{d}\boldsymbol{s} \int_{-\infty}^{\infty} \mathrm{d}t_s \, \boldsymbol{G}^i(\boldsymbol{x}, t; \boldsymbol{s}, t_s) \\
&\quad \times \left\{-\delta\boldsymbol{\mathcal{L}}\boldsymbol{v}^0(\boldsymbol{s}, t_s) + \delta\boldsymbol{S}(\boldsymbol{s}, t_s)\right\}_i,
\end{aligned} \tag{3.20}$$

where $\{\cdot\}_i$ denotes the i-th component of the vector inside the curly braces.

By expressing the zero-order velocity $\boldsymbol{v}^0$ in terms of the Green's function and the source, and using equations (3.20) and $\delta\phi = \mathcal{F}\{\hat{\boldsymbol{\ell}} \cdot \delta\boldsymbol{v}\}$, the perturbed signal can be written as

$$\begin{aligned}
\delta\phi(\boldsymbol{x}, t) &= \Bigg[\int_\odot \mathrm{d}\boldsymbol{r} \int_{-\infty}^{\infty} \mathrm{d}t' \int_\odot \mathrm{d}\boldsymbol{s} \int_{-\infty}^{\infty} \mathrm{d}t_{\mathrm{s}} \, \mathcal{G}^i(\boldsymbol{x}, t; \boldsymbol{r}, t') \\
&\quad \times \left\{-\delta\boldsymbol{\mathcal{L}}\boldsymbol{G}^j(\boldsymbol{r}, t'; \boldsymbol{s}, t_{\mathrm{s}})\right\}_i S_j^0(\boldsymbol{s}, t_{\mathrm{s}})\Bigg] \\
&\quad + \int_\odot \mathrm{d}\boldsymbol{s} \int_{-\infty}^{\infty} \mathrm{d}t_{\mathrm{s}} \, \mathcal{G}^i(\boldsymbol{x}, t; \boldsymbol{s}, t_{\mathrm{s}}) \, \delta S_i(\boldsymbol{s}, t_{\mathrm{s}}).
\end{aligned} \tag{3.21}$$

We recall that the operator $\delta\mathcal{L}$ contains the first-order perturbations to the solar model, $\delta q_\alpha(\boldsymbol{r})$. The first term in the above equation contains two Green's functions; it represents the contribution to $\delta\phi(\boldsymbol{x}, t)$ that comes from a wave that is created by the source at location $\boldsymbol{s}$ at time t_s, is scattered at time t' by the perturbations at location $\boldsymbol{r}$, and then propagates to the location $\boldsymbol{x}$. The details of the scattering process are encoded in the operator $\delta\mathcal{L}$. The second term results from the perturbation to the source function, and involves only a single Green's function, which propagates waves from the location and time of the source to the observation location and time. As we now have ϕ^0 and $\delta\phi$ we can next compute the zero- and first-order cross-correlations, C^0 and δC.

3.2.4   Temporal Cross-Correlation

We remind the reader that we only want to compute the expectation value of the cross-correlation (see § 3.2.2). In the rest of this chapter, cross-correlations stand for their expectation values. From equation (3.3) and the equation for ϕ^0 derived in the previous section (eq. [3.18]) we deduce a general expression for the zero-order cross-correlation:

$$
\begin{aligned}
C^0(\mathbf{1}, \mathbf{2}, t) \;\; = \;\; & \frac{1}{T} \int \mathrm{d}t' \, \mathrm{d}\boldsymbol{s} \, \mathrm{d}t_\mathrm{s} \, \mathrm{d}\boldsymbol{s}' \, \mathrm{d}t'_\mathrm{s} \; M^0_{ij}(\boldsymbol{s}, t_\mathrm{s}; \boldsymbol{s}', t'_\mathrm{s}) \\
& \times \mathcal{G}^i(\mathbf{1}, t'; \boldsymbol{s}, t_\mathrm{s}) \, \mathcal{G}^j(\mathbf{2}, t' + t; \boldsymbol{s}', t'_\mathrm{s}) \,,
\end{aligned}
\tag{3.22}
$$

with

$$
M^0_{ij}(\boldsymbol{s}, t_\mathrm{s}; \boldsymbol{s}', t'_\mathrm{s}) = \mathrm{E}\big[S^0_i(\boldsymbol{s}, t_\mathrm{s}) \, S^0_j(\boldsymbol{s}', t'_\mathrm{s})\big] \,,
\tag{3.23}
$$

where $\mathrm{E}[\cdot]$ denotes the expectation value of the expression in square brackets. For the sake of readibility, we have omitted the limits of integration in equation (3.23). The matrix $\mathbf{M}^0$ gives the correlation between any two components of $\boldsymbol{S}^0$, measured at two possibly different positions.

No assumption has been made about $\mathbf{M}^0$ to obtain equation (3.22). With the assumptions of stationarity in time and homogeneity and isotropy in the horizontal direction, $\mathbf{M}^0$ only depends on the time difference $t_\mathrm{s} - t'_\mathrm{s}$, the horizontal distance between $\boldsymbol{s}$ and $\boldsymbol{s}'$, and their depths. Further assumptions could be made in order to simplify the computation of equation (3.22). In the spirit of Woodard (1997) one

might assume that the sources are spatially uncorrelated or are located only at a particular depth. A better approach might be to obtain the statistical properties of $\boldsymbol{S}^0$ from recent numerical simulations of solar convection (e.g. Stein & Nordlund, 2000) or observations of photospheric convection (e.g. Title et al., 1989; Chou et al., 1991; Strous et al., 2000). Furthermore, a comparison of models and observations of the power spectrum of solar oscillations can be used to constrain the depths and types of sources (e.g. Duvall et al., 1993a).

We now perturb equation (3.3) and take the expectation value to obtain

$$
\begin{aligned}
\delta C(\boldsymbol{1}, \boldsymbol{2}, t) \;=\; & \frac{1}{T} \int_{-\infty}^{\infty} \mathrm{d}t' \, \mathrm{E}\big[\delta\phi(\boldsymbol{1}, t') \, \phi^0(\boldsymbol{2}, t' + t) \\
& + \phi^0(\boldsymbol{1}, t') \, \delta\phi(\boldsymbol{2}, t' + t) \big] \, .
\end{aligned}
\tag{3.24}
$$

The function δC has two contributions, one from the perturbation to the wave operator, $\delta C_{\mathcal{L}}$, and one from the source perturbation, δC_S :

$$
\delta C = \delta C_{\mathcal{L}} + \delta C_S \, .
\tag{3.25}
$$

Using the expressions for ϕ^0 and $\delta\phi$ given by equations (3.18) and (3.21), we obtain the perturbation to the cross-correlation resulting from a change in the wave operator $\mathcal{L}$:

$$
\begin{aligned}
\delta C_{\mathcal{L}}(\boldsymbol{1}, \boldsymbol{2}, t) \;=\; & \frac{1}{T} \int_{\odot} \mathrm{d}\boldsymbol{r} \int \mathrm{d}t' \, \mathrm{d}t'' \, \mathrm{d}\boldsymbol{s} \, \mathrm{d}t_{\mathrm{s}} \, \mathrm{d}\boldsymbol{s}' \, \mathrm{d}t_{\mathrm{s}}' \\
& \times \big\{ -\delta\boldsymbol{\mathcal{L}} \boldsymbol{G}^i(\boldsymbol{r}, t''; \boldsymbol{s}, t_{\mathrm{s}}) \big\}_k M^0_{ij}(\boldsymbol{s}, t_{\mathrm{s}}; \boldsymbol{s}', t_{\mathrm{s}}') \\
& \times \big[\mathcal{G}^j(\boldsymbol{2}, t' + t; \boldsymbol{s}', t_{\mathrm{s}}') \, \mathcal{G}^k(\boldsymbol{1}, t'; \boldsymbol{r}, t'') \\
& + \mathcal{G}^j(\boldsymbol{1}, t'; \boldsymbol{s}', t_{\mathrm{s}}') \, \mathcal{G}^k(\boldsymbol{2}, t' + t; \boldsymbol{r}, t'') \big] \, .
\end{aligned}
\tag{3.26}
$$

The above equation, which gives the perturbation to the cross-correlation due to scattering, has two components, illustrated in Figure 3.2a. The first component comes from the correlation of the scattered wave at $\boldsymbol{1}$ with the direct wave at $\boldsymbol{2}$, i.e. $\delta\phi(\boldsymbol{1}, t')\phi^0(\boldsymbol{2}, t' + t)$, and the second component comes from $\phi^0(\boldsymbol{1}, t')\delta\phi(\boldsymbol{2}, t' + t)$. Both these components appear in equation (3.26) as the product of three Green's functions. From the term $\delta\phi(\boldsymbol{1}, t')\phi^0(\boldsymbol{2}, t' + t)$ there is one Green's function for

the wave that goes directly from s' to $\mathbf{2}$, which gives $\phi^0(\mathbf{2})$. There is a second Green's function for the wave that is created at s and travels to r, and the third Green's function takes the scattered wave from r to $\mathbf{1}$, which gives $\delta\phi(\mathbf{1})$. The term $\phi^0(\mathbf{1}, t')\delta\phi(\mathbf{2}, t' + t)$ can be understood by switching the roles of $\mathbf{1}$ and $\mathbf{2}$. The scattering process is described by the operator $\delta\mathcal{L}$, which depends on the perturbations $\delta q_\alpha(r)$. The Green's function $\mathcal{G}$ is used for waves that arrive at an observation point as it gives the response of ϕ to a source. The Green's vectors $\boldsymbol{G}^i$ are used to propagate the wave velocity from a source to the scattering point, as the scattered wave depends on the vector velocity of the incoming wave.

The cross-correlation is also sensitive to changes in the source function. The first-order perturbation resulting from a small change in the source function can be written as (from eqs. [3.18] and [3.21])

$$
\begin{aligned}
\delta C_S(\mathbf{1}, \mathbf{2}, t) \;=\; & \frac{1}{T} \int \mathrm{d}t'\, \mathrm{d}\boldsymbol{s}\, \mathrm{d}t_{\mathrm{s}}\, \mathrm{d}\boldsymbol{s}'\, \mathrm{d}t'_{\mathrm{s}}\; \delta M_{ij}(\boldsymbol{s}, t_{\mathrm{s}}; \boldsymbol{s}', t'_{\mathrm{s}}) \\
& \times \mathcal{G}^i(\mathbf{1}, t'; \boldsymbol{s}, t_{\mathrm{s}})\, \mathcal{G}^j(\mathbf{2}, t' + t; \boldsymbol{s}', t'_{\mathrm{s}})\,,
\end{aligned}
\tag{3.27}
$$

where the perturbation to the source covariance is:

$$
\begin{aligned}
\delta M_{ij}(\boldsymbol{s}, t_{\mathrm{s}}; \boldsymbol{s}', t'_{\mathrm{s}}) \;=\; & \mathrm{E}\left[S_i^0(\boldsymbol{s}, t_{\mathrm{s}})\, \delta S_j(\boldsymbol{s}', t'_{\mathrm{s}}) \right. \\
& \left. + \delta S_i(\boldsymbol{s}, t_{\mathrm{s}})\, S_j^0(\boldsymbol{s}', t'_{\mathrm{s}}) \right].
\end{aligned}
\tag{3.28}
$$

Figure 3.2b gives a graphical interpretation of this equation. Unlike the perturbation to the cross-correlation due to scattering, the above equation contains only two Green's functions. One connects the unperturbed source with the unperturbed signal at an observation point, while the second relates the source perturbation to the perturbed signal at the other observation point.

Later in this chapter it will be necessary to express the perturbation to the cross-correlation as a spatial integral over the location, r, of the perturbation to the solar model. In order to be able to write equation (3.27) for δC_S in this form, we introduce the change of variable $\boldsymbol{r} = (\boldsymbol{s} + \boldsymbol{s}')/2$ and $\boldsymbol{u} = \boldsymbol{s} - \boldsymbol{s}'$. This change of variable is also useful because we expect the source covariance $\mathbf{M}$ to be small for large $\boldsymbol{u}$, i.e. for sources that are far apart. In the limit of very small source correlation length, $\mathbf{M}$ is a function only of $\boldsymbol{r}$.
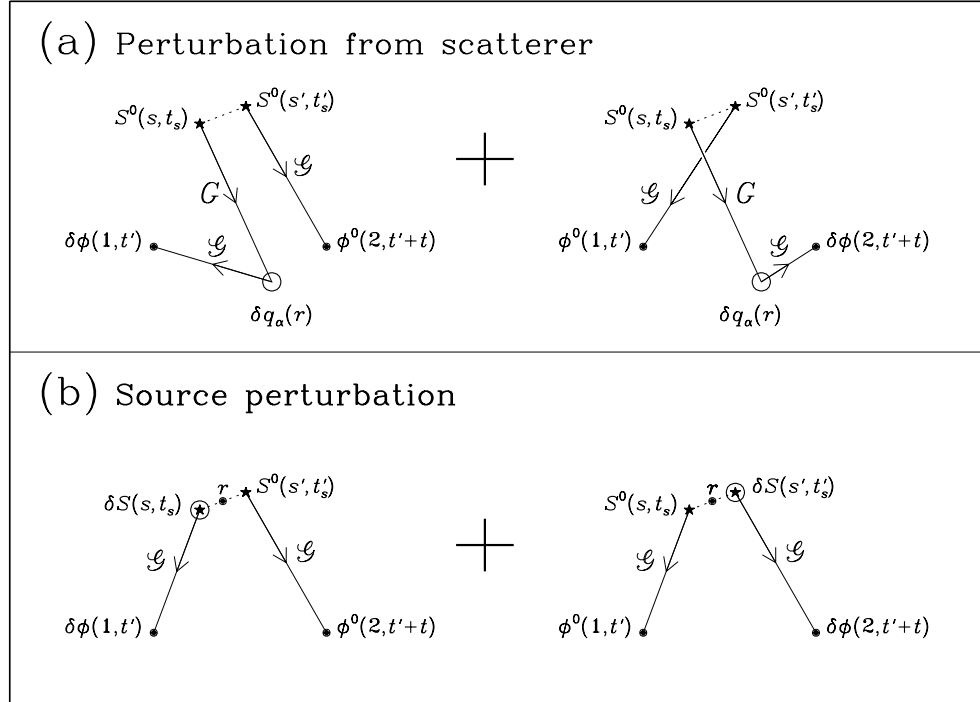
Figure 3.2: A graphical representation of the two types of contributions to the first-order perturbation to the cross-correlation (eqs [3.26] and [3.27]). Panel (a) is for scattering from perturbations $\delta q_\alpha(\boldsymbol{r})$ to the model and panel (b) is for changes $\delta\boldsymbol{S}$ in the source function. Scattering processes contribute to the cross-correlation as the product of three Green's functions: one Green's function to describe the direct wave from the source to an observation point and two Green's functions to obtain the scattered wave at the other observation point, in the Born approximation. The sensitivity of the cross-correlation to a change in the source function only involves two Green's functions, one to propagate waves from the unperturbed source to an observation point and one to give the response, at the other observation point, to the change in the source function. Throughout the diagram, as in the text, the Green's function for the observable is given by $\mathcal{G}$ and the Green's function for the vector velocity is $\boldsymbol{G}$. The dotted line between the source locations, $\boldsymbol{s}$ and $\boldsymbol{s}'$, indicates that the two sources are connected through the source covariance matrix $\mathbf{M}$.

We have shown how to obtain C^0 and δC from an assumed solar model consisting of a background model ($\boldsymbol{\mathcal{L}}^0$ and $\boldsymbol{S}^0$) and small perturbations ($\delta\boldsymbol{\mathcal{L}}$ and $\delta\boldsymbol{S}$). Earlier, in § 3.2.2, we showed how to connect perturbations to the cross-correlation to travel-time perturbations. In the next section we put these pieces together and obtain travel-time kernels, which give the travel-time perturbations resulting from small changes in the solar model.

3.2.5   Travel-Time Sensitivity Kernels

It is useful for the derivation of travel-time kernels to express the perturbation to the cross-correlation δC as an integral over the location $\boldsymbol{r}$ of the perturbations $\delta q_\alpha(\boldsymbol{r})$. In general $\delta\boldsymbol{\mathcal{L}}$ and $\delta\mathbf{M}$ involve spatial derivatives of the perturbations $\delta q_\alpha(\boldsymbol{r})$ to the solar model and so integration by parts on the variable $\boldsymbol{r}$ may be required to obtain, from equations (3.25), (3.26), and (3.27):

$$\delta C(\mathbf{1}, \mathbf{2}, t) = \int_\odot \mathrm{d}\boldsymbol{r}\, \delta q_\alpha(\boldsymbol{r})\, \mathcal{C}^\alpha(\mathbf{1}, \mathbf{2}, t; \boldsymbol{r})\,. \tag{3.29}$$

The index α refers to the different types of perturbations in the solar model, for example perturbations to sound speed or flows. The sum over α is over all relevant types of perturbations. We note that any particular perturbation δq_α may appear in both the operator $\delta\boldsymbol{\mathcal{L}}$ and the perturbation to the source covariance $\delta\mathbf{M}$. For example a flow will both advect waves as well as Doppler shift the sources. For any particular $\delta\mathbf{M}(\delta q)$ it may be helpful to do partial integrations on equation (3.27) before making the change of variable $\boldsymbol{r} = (\boldsymbol{s} + \boldsymbol{s}')/2$ described above. In Section 3.3, we will show a detailed example of the derivation of $\mathcal{C}^\alpha$ for local perturbations to source strength and damping rate for surface gravity waves.

In § 3.2.2 we showed how to relate the travel-time perturbations $\delta\tau_\pm$ to the perturbation to the cross-correlation δC. Using equation (3.29) for δC, and equation (3.10) for $\delta\tau_\pm$, we obtain:

$$\delta\tau_\pm(\mathbf{1}, \mathbf{2}) = \int_\odot \mathrm{d}\boldsymbol{r}\, \delta q_\alpha(\boldsymbol{r}) \int_{-\infty}^\infty \mathrm{d}t\, W_\pm(\mathbf{1}, \mathbf{2}, t)\, \mathcal{C}^\alpha(\mathbf{1}, \mathbf{2}, t; \boldsymbol{r})\,. \tag{3.30}$$

As we want to define sensitivity kernels in the form

$$\delta\tau_{\pm}(\mathbf{1}, \mathbf{2}) = \int_{\odot} \mathrm{d}\mathbf{r}\, \delta q_{\alpha}(\mathbf{r})\, K_{\pm}^{\alpha}(\mathbf{1}, \mathbf{2}; \mathbf{r}),\tag{3.31}$$

we make the identification

$$K_{\pm}^{\alpha}(\mathbf{1}, \mathbf{2}; \mathbf{r}) = \int_{-\infty}^{\infty} \mathrm{d}t\, W_{\pm}(\mathbf{1}, \mathbf{2}, t)\, \mathcal{C}^{\alpha}(\mathbf{1}, \mathbf{2}, t; \mathbf{r}).\tag{3.32}$$

By definition, $K_{\pm}^{\alpha}$ represent the local sensitivity of the travel-time perturbations $\delta\tau_{\pm}$ to perturbations to the model, δq_{α}. From the above equation we can see that the kernels depend on both the definition of travel time, through the functions $W_{\pm}$, as well as on the zero-order problem and the form of the first-order perturbations, through $\mathcal{C}^{\alpha}$. The inputs needed to compute $W_{\pm}$ are the zero-order cross-correlation C^0, and the reference wavelet C^{ref} and the window function $f(t)$ used in the travel-time measurement procedure (eq. [A.7]). The function $\mathcal{C}^{\alpha}$ depends on the source covariance, the Green's function, the filter, and the forms of the wave operator and the source function (eqs. [3.26] and [3.27]).

We have now shown a general procedure for computing travel time kernels for any particular model. In order to demonstrate the utility and feasibility of this procedure we will, in the next section, derive two-dimensional kernels for surface gravity waves.

3.3 An Example: Surface Gravity Waves

3.3.1 Outline

In this section we derive the sensitivity of surface gravity wave travel times to local perturbations to source strength and damping rate. We work in a plane-parallel model with constant density and gravity. In this model, wave excitation and attenuation act only at the fluid surface, and the problem can be reduced to a two-dimensional problem. Our model is a very simplified version of the actual solar f-mode case, yet incorporates most of the basic physics. We will follow the basic recipe outlined in Section 3.2 for deriving kernels.

The example is written in four parts. In § 3.3.2 we fully specify the problem: we derive the equations of motion, encapsulated in the operator $\mathcal{L}$, and describe our models for the source covariance and wave damping. We also describe the filter $\mathcal{F}$ which includes an approximation to the MDI/SOHO point spread function. In § 3.3.3 we compute the zero-order solution to the problem: the Green's function, power spectrum, and zero-order cross-correlation. Travel-time kernels for perturbations in source strength and damping rate are derived in § 3.3.4. We conclude, in § 3.3.5, with a comparison of the kernels from § 3.3.4 with kernels obtained in the single-source picture.

3.3.2   Specification of the Problem

We consider a simple plane-parallel medium appropriate to studying waves with wavelengths small compared to the solar radius. The geometry is shown in Figure 3.3. The height coordinate is z, measured upward, and a horizontal coordinate vector is denoted by $\boldsymbol{x}$. Gravitational acceleration is assumed to be constant, $-g\hat{\boldsymbol{z}}$, where $g = 274$ m s^{-2} is the solar surface value. For $z < 0$ the fluid has a uniform constant density ρ. This assumption simplifies the problem considerably and does not affect the dispersion relation ($\omega^2 = gk$). In addition, acoustic waves are not present in this problem because the medium is incompressible. In the steady background state there is a free surface at $z = 0$. The background pressure distribution, $P(z)$, is hydrostatic, with $P = -\rho gz$.

In the following sections, we develop the equations of motion, encapsulated in the operator $\mathcal{L}$, and describe our models for the source covariance and the wave damping operator. We also describe the filter $\mathcal{F}$ which includes an approximation to the MDI/SOHO point spread function. The measurement procedure is specified by choosing the reference wavelet and the window function.

Equations of Motion

We now derive the equations of motion, which we want in the form of equation (3.11). For an inviscid fluid of constant density, the linearized equations of conservation of
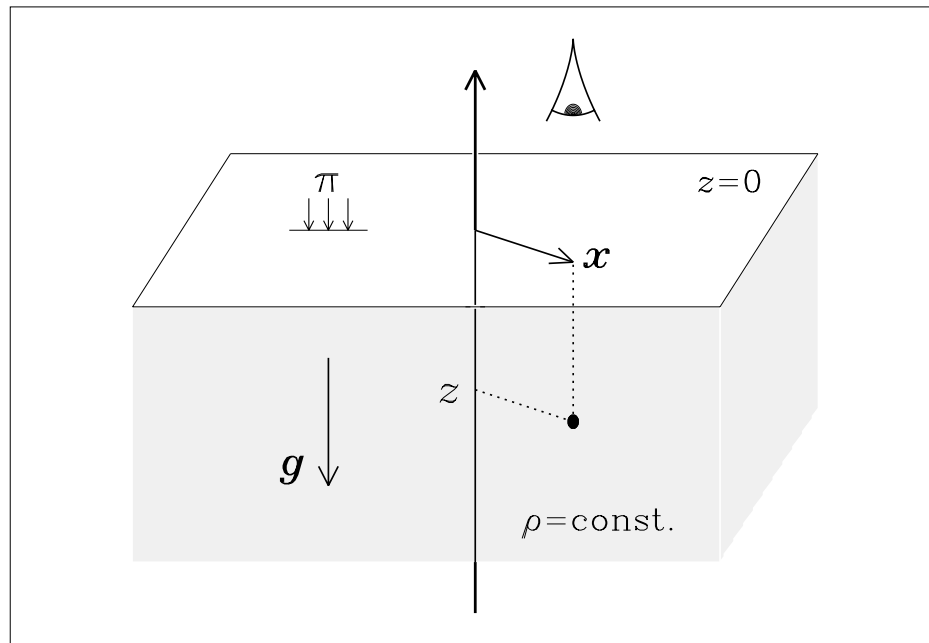
Figure 3.3: The basic setup for the example. The coordinate z denotes height and $\boldsymbol{x}$ is a horizontal coordinate vector. The half space $z < 0$ is filled with an incompressible fluid of density ρ and the space above is empty. The line-of-sight vector is $\hat{\boldsymbol{\ell}} = \hat{\boldsymbol{z}}$, i.e. the observer is looking straight down at the surface. Gravitational acceleration is constant and points in the $-\hat{\boldsymbol{z}}$ direction. Surface gravity waves are excited by a stochastic pressure distribution Π applied at the surface, $z = 0$.

mass and momentum read

$$\boldsymbol{\nabla} \cdot \boldsymbol{v} \;\; = \;\; 0 \,, \tag{3.33}$$

$$\rho \dot{\boldsymbol{v}} + \boldsymbol{\nabla} p \;\; = \;\; \boldsymbol{0} \,, \tag{3.34}$$

where p is the pressure perturbation associated with the waves. Provided that there exists a time at which the velocity field is irrotational, it will remain irrotational for all time. We may imagine a medium free of waves as a starting condition and subsequently switch on the pressure sources at some initial time in the distant past. As a result we assume that

$$\boldsymbol{\nabla} \times \boldsymbol{v} = \boldsymbol{0} \tag{3.35}$$

holds for all times.

In the Sun the wave excitation mechanism is near-surface turbulent convection, with various types of sources distributed with depth (e.g Nigam & Kosovichev, 1999; Kumar & Basu, 2000). Here, we excite surface gravity waves by applying a stochastic pressure source Π at the fluid surface. Thus, the wave pressure perturbation, p, satisfies the linearized dynamic boundary condition

$$p - \rho g \xi = \Pi \,, \quad \text{at } z = 0 \,, \tag{3.36}$$

where ξ is the vertical displacement, which has time derivative equal to the vertical velocity at the surface.

In principle, turbulent convection is also responsible for damping f modes (e.g. Duvall et al., 1998). Turbulent convection can also modify the dispersion relation (Murawski & Roberts, 1993). Here, however, we use a phenomenological model for wave attenuation by including a dissipative term $\rho \Upsilon \boldsymbol{v}$ in the momentum equation at the surface. The operator Υ is a temporal convolution which reproduces the observed damping rates, it will be discussed in detail later. At the surface, the momentum equation thus becomes:

$$\rho \dot{\boldsymbol{v}} + \boldsymbol{\nabla} p = -\rho \Upsilon \boldsymbol{v} \,, \quad \text{at } z = 0 \,. \tag{3.37}$$

Eliminating p from equations (3.37) and (3.36), the surface boundary conditions

reduce to the equation

$$\partial_z \ddot{w} - g \boldsymbol{\nabla}_{\mathrm{h}}^2 w - \partial_t \boldsymbol{\nabla}_{\mathrm{h}} \cdot (\Upsilon \boldsymbol{u}) = \frac{1}{\rho} \boldsymbol{\nabla}_{\mathrm{h}}^2 \dot{\Pi} \,, \tag{3.38}$$

where $\boldsymbol{\nabla}_{\mathrm{h}}$ is the horizontal gradient and $\boldsymbol{u}$ and w are the horizontal and vertical components of the wave velocity,

$$\boldsymbol{v} = \boldsymbol{u} + w\,\hat{\boldsymbol{z}} \,. \tag{3.39}$$

We note that perturbations at the surface do not affect equations (3.33) and (3.35) for $z < 0$. As a result the effect of surface perturbations is contained entirely in equation (3.38). Therefore the problem is completely specified by equation (3.38) on the surface and the auxiliary equations $\boldsymbol{\nabla} \times \boldsymbol{v} = \boldsymbol{0}$ and $\boldsymbol{\nabla} \cdot \boldsymbol{v} = 0$ for $z < 0$. The problem is thus essentially two-dimensional, and equation (3.38) is the relevant equation to put in the form of equation (3.11). So we have

$$\mathcal{L}\boldsymbol{v} \;=\; \partial_z \ddot{w} - g \boldsymbol{\nabla}_{\mathrm{h}}^2 w - \partial_t \boldsymbol{\nabla}_{\mathrm{h}} \cdot (\Upsilon \boldsymbol{u}) \,, \tag{3.40}$$

$$S \;=\; \frac{1}{\rho} \boldsymbol{\nabla}_{\mathrm{h}}^2 \dot{\Pi} \,. \tag{3.41}$$

We notice that the source function S is scalar, unlike in the general theory (§ 3.2). Now that we have specified the operator $\mathcal{L}$ and the source function S it remains only to follow the recipe presented in the theory section.

The first part of the recipe is to write the zero-order problem and the first-order Born approximation. We consider two different types of perturbations to the background state: a change in the damping operator, $\delta\Upsilon$, and a change in the source function, δS. The zero-order problem is

$$\mathcal{L}^0 \boldsymbol{v}^0 = S^0 \,, \tag{3.42}$$

where

$$\mathcal{L}^0 \boldsymbol{v}^0 \;=\; \partial_z \ddot{w}^0 - g \boldsymbol{\nabla}_{\mathrm{h}}^2 w^0 + \partial_t \Upsilon^0 \partial_z w^0 \,, \tag{3.43}$$

$$S^0 \;=\; \frac{1}{\rho} \boldsymbol{\nabla}_{\mathrm{h}}^2 \dot{\Pi}^0 \,. \tag{3.44}$$

Here, S^0 is the zero-order source function, $\mathcal{L}^0$ the zero-order wave operator, and $\boldsymbol{v}^0$ the unperturbed wave velocity. We have used the fact that the zero-order damping operator Υ^0 commutes with spatial derivatives. The first-order approximation gives:

$$\mathcal{L}^0 \, \delta\boldsymbol{v} = -\delta\mathcal{L} \, \boldsymbol{v}^0 + \delta S \,, \tag{3.45}$$

where

$$-\delta\mathcal{L} \, \boldsymbol{v}^0 \;\; = \;\; \partial_t \boldsymbol{\nabla}_{\mathrm{h}} \cdot (\delta\Upsilon \, \boldsymbol{u}^0) \,, \tag{3.46}$$

$$\delta S \;\; = \;\; \frac{1}{\rho} \boldsymbol{\nabla}_{\mathrm{h}}^2 \, \delta\dot{\Pi} \,. \tag{3.47}$$

Here, δS is the perturbation to the source function, $\delta\mathcal{L}$ the perturbation to the wave operator, and $\delta\boldsymbol{v}$ the first Born approximation to the wave velocity. Notice that equation (3.45) has the same operator, $\mathcal{L}^0$, on the left-hand side as the zero-order problem (eq. [3.42]).

Source Covariance

In order to model the zero-order covariance M^0 of the source function S^0, which is necessary to compute the cross-correlation, we introduce the covariance of the applied surface pressure distribution Π^0,

$$\rho^2 m^0(\boldsymbol{x}, t; \boldsymbol{x}', t') = \mathrm{E}\left[\Pi^0(\boldsymbol{x}, t)\, \Pi^0(\boldsymbol{x}', t')\right] \,, \tag{3.48}$$

which is a physical quantity. In terms of m^0, the zero-order source covariance M^0 is given by

$$M^0(\boldsymbol{x}, t; \boldsymbol{x}', t') \;\; = \;\; \boldsymbol{\nabla}_{\boldsymbol{x}}^2 \, \boldsymbol{\nabla}_{\boldsymbol{x}'}^2 \, \partial_t \, \partial_{t'} \, m^0(\boldsymbol{x}, t; \boldsymbol{x}', t') \,, \tag{3.49}$$

where $\boldsymbol{\nabla}_{\boldsymbol{x}}^2$ denotes the horizontal Laplacian with respect to the variable $\boldsymbol{x}$. Guided by the observations of Title et al. (1989) we write m^0 as a product of spatial and temporal decaying exponentials. Under the assumption of translation invariance (in time and space):

$$m^0(\boldsymbol{x}; t; \boldsymbol{x}', t') = a \, \frac{e^{-\|\boldsymbol{x}-\boldsymbol{x}'\|/L_{\mathrm{s}}}}{2\pi L_{\mathrm{s}}^2} \, \frac{e^{-|t-t'|/T_{\mathrm{s}}}}{2T_{\mathrm{s}}} \,. \tag{3.50}$$

Here L_{s} is the correlation length and T_{s} the correlation time of the lowest-order turbulent pressure field Π^0. The constant a is the overall amplitude of m^0. The normalization factors $2\pi L_{\mathrm{s}}^2$ and $2T_{\mathrm{s}}$ are included so that in the limits of $L_{\mathrm{s}} \to 0$ and $T_{\mathrm{s}} \to 0$, m^0 becomes the product of two Dirac delta functions, $\delta_{\mathrm{D}}(\boldsymbol{x} - \boldsymbol{x}')$ and $\delta_{\mathrm{D}}(t - t')$.

Title et al. (1989) computed the covariance function of quiet-sun granulation intensity and found exponential dependence on the temporal and spatial separations, $|t - t'|$ and $\|\boldsymbol{x} - \boldsymbol{x}'\|$, with correlation time 400 s and correlation length 450 km. For this work, we take $T_{\mathrm{s}} = 400$ s and $L_{\mathrm{s}} = 0$. Neglecting the source correlation length, i.e. treating the sources as spatially uncorrelated, is done for the sake of computational simplicity; it is not at all a limitation of the theory. The approximation of zero-correlation length is appropriate because L_s is smaller than a wavelength. For the form of m^0 given by equation (3.50), and the definition of the Fourier transform appropriate for functions that are translation invariant (eq. [B.4]) we obtain

$$m^0(\boldsymbol{k}, \omega) = \frac{a}{(2\pi)^3[1 + (\omega T_{\mathrm{s}})^2]}, \quad \text{as } L_{\mathrm{s}} \to 0, \tag{3.51}$$

which in particular does not depend on $\boldsymbol{k}$ for spatially uncorrelated sources. Here, as in the rest of the chapter, $\boldsymbol{k}$ is the horizontal wave vector and ω is the angular frequency.

We now consider source perturbations. As we have already shown, what matters for the computation of cross-correlations is not the perturbation to the source but rather the perturbed source covariance, δM, which can be obtained from δm through

$$\delta M(\boldsymbol{x}, t; \boldsymbol{x}', t') \;\; = \;\; \boldsymbol{\nabla}_{\boldsymbol{x}}^2 \, \boldsymbol{\nabla}_{\boldsymbol{x}'}^2 \, \partial_t \, \partial_{t'} \, \delta m(\boldsymbol{x}, t; \boldsymbol{x}', t'). \tag{3.52}$$

Three possible types of perturbations to the source covariance are local changes in source correlation time, correlation length, and amplitude. For instance, Title et al. (1989) report different correlation times in quiet Sun and magnetic network. Magnetic fields affect near-surface convection and thus are expected to introduce local changes in the source strength as well. Here we consider only perturbations to the local amplitude, a, of m, i.e. to model regions of increased or decreased f-mode

emission. We choose

$$\delta m(\boldsymbol{x}, t; \boldsymbol{x}', t') = \frac{\delta a(\boldsymbol{r})}{a}\, m^0(\boldsymbol{x}, t; \boldsymbol{x}', t')\,, \qquad (3.53)$$

with

$$\boldsymbol{r} = \frac{1}{2}(\boldsymbol{x} + \boldsymbol{x}')\,. \qquad (3.54)$$

Here $\delta a(\boldsymbol{r})$ gives the local change in the amplitude of the source covariance. We have used the assumption that the source correlation length is small compared to the length scale of the spatial variation of the amplitude of the source function, to write δa as a function of only the central position $\boldsymbol{r}$.

Damping

Theoretical descriptions of the damping of f modes by scattering from near-surface convective turbulence exist (e.g. Duvall et al., 1998), but we elect to use a phenomenological model for the sake of simplicity. It is known from observations that high-frequency waves are damped more strongly than low-frequency waves (e.g. Duvall et al., 1998). As a result we need a frequency-dependent damping rate. The easiest way to implement general frequency dependence is through a temporal convolution (e.g. Dahlen & Tromp, 1998). Thus, we express the zero-order damping operator, Υ^0, as

$$\Upsilon^0 \boldsymbol{v}(\boldsymbol{x}, t) = \frac{1}{2\pi} \int_{-\infty}^{\infty} dt'\, \Gamma^0(t - t')\, \boldsymbol{v}(\boldsymbol{x}, t')\,. \qquad (3.55)$$

We have assumed that damping is acting purely locally. A more sophisticated model would presumably include a spatial convolution in addition to the temporal convolution. With the Fourier convention given in Appendix B, Υ^0 can be written as

$$\Upsilon^0 \boldsymbol{v}(\boldsymbol{k}, \omega) = \Gamma^0(\omega)\, \boldsymbol{v}(\boldsymbol{k}, \omega)\,, \qquad (3.56)$$

where $\Gamma^0(\omega)$ is the temporal Fourier transform of $\Gamma^0(t)$. In addition, we see that the operator $\partial_t + \Upsilon^0$, which appears in equation (3.37), becomes multiplication by $-i\omega + \Gamma^0(\omega)$ in the Fourier domain.

For the sake of simplicity, we choose the function $\Gamma^0(t)$ to be real and even in time. As a result $\Gamma^0(\omega)$ is real and even. A non-physical consequence of this choice

is that the damping operator is not causal. We will see, however, that the Green's function derived using this damping operator is still causal. A treatment of causal frequency-dependent damping can be found in Dahlen & Tromp (1998). In order to damp all frequencies ω the function $\Gamma^0(\omega)$ must be positive. We will see later that $\Gamma^0(\omega)$ is the full frequency width at half maximum of the surface gravity wave power. We obtain a good fit to observed f-mode line widths (Duvall et al., 1998) if we write $\Gamma^0(\omega)$ in the form

$$\Gamma^0(\omega) = \gamma \left| \frac{\omega}{\omega_\star} \right|^\beta , \tag{3.57}$$

with the parameters $\omega_\star/2\pi = 3$ mHz , $\gamma/2\pi = 100\ \mu$Hz, and $\beta = 4.4$. This fit is accurate in the range $1.5\,\mathrm{mHz} < \omega/2\pi < 5\,\mathrm{mHz}$. The frequency dependence of the damping rate is strong.

There are two basic types of perturbations to the local damping rate: a change in the amplitude of the damping rate, γ, and a change in the exponent, β. In this chapter we only consider the former and write the perturbation to the damping operator as

$$\delta \Upsilon \, \boldsymbol{v}(\boldsymbol{x}, t) = \frac{\delta \gamma(\boldsymbol{x})}{\gamma} \, \Upsilon^0 \boldsymbol{v}(\boldsymbol{x}, t) , \tag{3.58}$$

where $\delta\gamma(\boldsymbol{x})/\gamma$ is the local fractional perturbation in the damping rate.

Observational Filter

For this example we take the line-of-sight vector to be vertical and independent of horizontal position, $\hat{\boldsymbol{\ell}} = \hat{\boldsymbol{z}}$. Then in accordance with equation (3.2) the observable is

$$\phi(\boldsymbol{x}, t) = \mathcal{F}\{\boldsymbol{v}(\boldsymbol{x}, t) \cdot \hat{\boldsymbol{z}}\} . \tag{3.59}$$

In this example we consider only the case where there is no spatial or temporal window function in the filter $\mathcal{F}$, i.e. we observe the wavefield over an area A and a time interval T which are both very large. Therefore the filter $\mathcal{F}$ can be represented by multiplication by a function $F(\boldsymbol{k}, \omega)$ in the Fourier domain,

$$\phi(\boldsymbol{k}, \omega) = F(\boldsymbol{k}, \omega) \, w(\boldsymbol{k}, \omega) , \tag{3.60}$$

where $w = \boldsymbol{v} \cdot \hat{\boldsymbol{z}}$. The function F includes the instrumental Optical Transfer Function (OTF), which is the Fourier transform of the point spread function of the telescope optics, as well as the effect of the finite pixel size of the detector. We use an azimuthal average of the OTF estimated by Tarbell et al. (1997) for the MDI/SOHO telescope in its high-resolution mode near disk center. We correct the OTF for the effect of finite pixel size, ϵ, by multiplying by $\mathrm{sinc}(k\epsilon/2)$, with $\epsilon = 0.83$ Mm and $k = \|\boldsymbol{k}\|$.

In general, F also includes the filter used to select the particular waves of interest in the k-ω diagram and to remove low frequency noise from the data. In this example there is only one ridge in the k-ω diagram, corresponding to the surface gravity waves. We choose a filter which is zero for frequencies less than $\omega_{\mathrm{min}}/2\pi = 2$ mHz and more than $\omega_{\mathrm{max}}/2\pi = 4$ mHz, as was done for the data shown in Figure 1.5.

We include an additional factor, R, in the filter to make our unstratified example look more solar. The function $R(k)$ is the ratio of mode inertia in our model to mode inertia in a standard stratified solar model:

$$R(k) = \frac{\rho \int_{-\infty}^{0} e^{2kz} \, \mathrm{d}z}{\int_{-\infty}^{z_\star} \rho_\odot(z) \, e^{2kz} \, \mathrm{d}z} \, . \tag{3.61}$$

Here ρ is the constant density in our model and $\rho_\odot$ is the density as a function of depth in the solar model. We use the solar model of Christensen-Dalsgaard et al. (1993) complemented by the chromospheric model of Vernazza et al. (1981) up to $z_\star = 2$ Mm. In the solar model $z = 0$ is the photosphere. If we had started from the full stratified solar problem we would presumably obtain a solar-like power spectrum without this correction factor.

To summarize, we take the filter F to be:

$$F(\boldsymbol{k}, \omega) = \mathrm{OTF}(k) \, R(k) \, \mathrm{Hea}(\omega - \omega_{\mathrm{min}}) \, \mathrm{Hea}(\omega_{\mathrm{max}} - \omega) \, , \tag{3.62}$$

where Hea is the Heaviside step function. The OTF and the k dependence of the full filter, F, are shown in Figure 3.4. We repeat that we have not included the effect of an observational time window, nor the effect of observing a finite area on the sun. Both of these effects could be included, though the filter could no longer be represented as a simple multiplication in the Fourier domain.
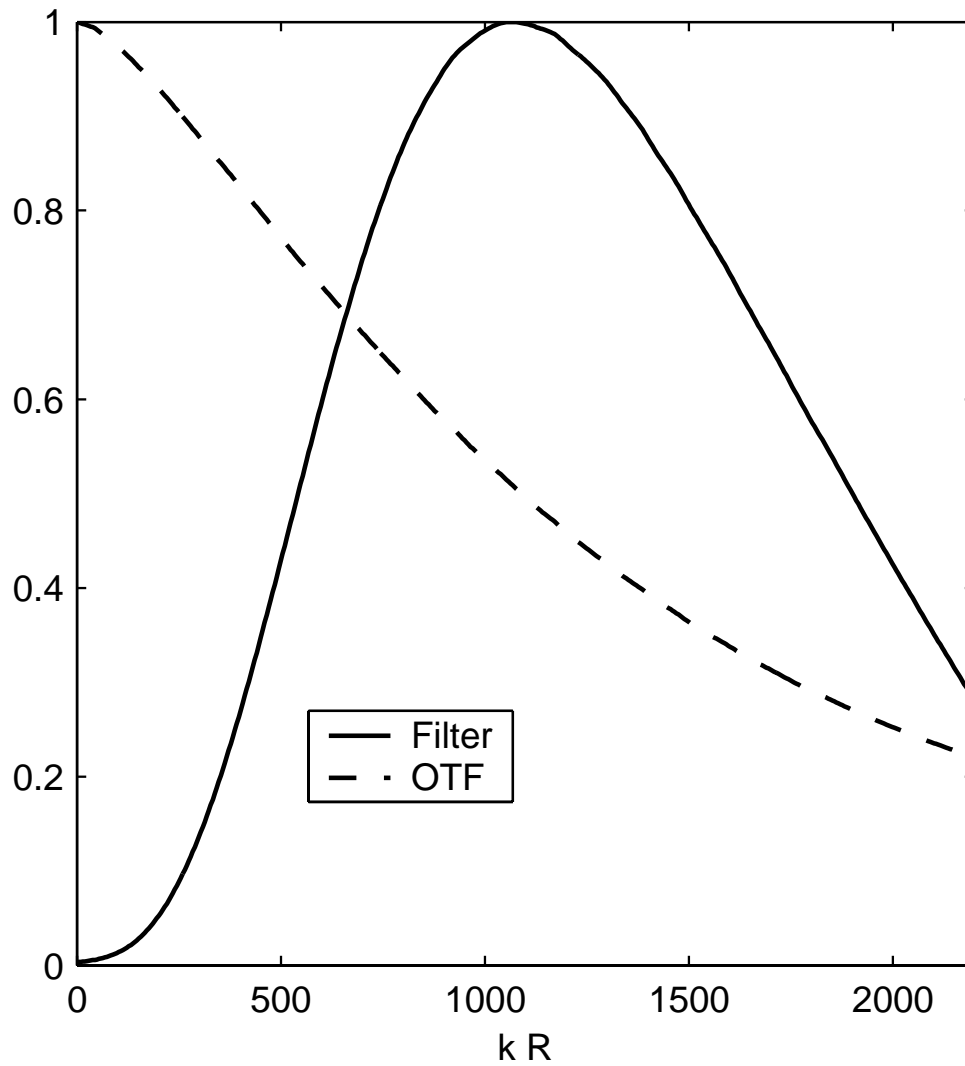
Figure 3.4: The wavenumber dependence of the filter F and of the OTF for the example calculation. The dashed line is the azimuthal average of the OTF estimated by Tarbell et al. (1997) for the MDI/SOHO high-resolution telescope. The filter F is the product of the OTF and the mode-mass correction R given by equation (3.61). Notice that the mode-mass correction suppresses the low-wavenumber part of the spectrum, which gives better agreement between our unstratified model and a stratified solar model, for which low wavenumbers modes are difficult to excite.

Measurement of Travel Times

As explained in § 3.2.1, the observer needs to select the reference wavelet C^{ref} and the window function f in order to make a travel-time measurement. For this example, we choose C^{ref} to be the zero-order cross-correlation of the model,

$$C^{\text{ref}}(\mathbf{1}, \mathbf{2}, t) = C^0(\mathbf{1}, \mathbf{2}, t)\,, \tag{3.63}$$

and the window function f to be the Heaviside step function,

$$f(t) = \text{Hea}(t)\,. \tag{3.64}$$

For this choice of reference wavelet, the zero-order travel times $\tau_{\pm}^0$ are zero (see Appendix A). The window function f is acceptable as we have only a single skip (surface waves). Using equation (A.8), we rewrite the travel-time perturbations $\delta\tau_{\pm}$ in terms of the temporal Fourier transforms of $W_{\pm}$ and δC:

$$\delta\tau_{\pm}(\mathbf{1}, \mathbf{2}) = 4\pi\text{Re}\int_0^{\infty} \mathrm{d}\omega\; W_{\pm}^*(\mathbf{1}, \mathbf{2}, \omega)\,\delta C(\mathbf{1}, \mathbf{2}, \omega)\,, \tag{3.65}$$

where Re selects the real part of the expression. The real and imaginary parts of $W_{\pm}(\omega)$ form a Hilbert transform pair:

$$W_{\pm}^*(\mathbf{1}, \mathbf{2}, \omega) = \frac{-\text{Hilb}[\omega C^0(\mathbf{1}, \mathbf{2}, \omega)] \mp \mathrm{i}\omega C^0(\mathbf{1}, \mathbf{2}, \omega)}{4\pi\int_0^{\infty} \omega'^2 |C^0(\mathbf{1}, \mathbf{2}, \omega')|^2\; \mathrm{d}\omega'}\,, \tag{3.66}$$

where $\text{Hilb}[\cdot]$ denotes the Hilbert transform (Saff & Snider, 1993). Note that we used the fact that $C^0(t)$ is even. We now have an explicit definition of the travel-time perturbations $\delta\tau_+$ and $\delta\tau_-$ for our example.

The mean travel-time perturbation, $\delta\tau_{\text{mean}}$, and the travel-time difference, $\delta\tau_{\text{diff}}$, can be expressed in the form of equation (3.65) with weight functions $W_{\text{mean}}^*(\omega)$ and $W_{\text{diff}}^*(\omega)$ given by

$$W_{\text{mean}}^* = \frac{1}{2}\left(W_+^* + W_-^*\right)\,, \tag{3.67}$$

$$W_{\text{diff}}^* = W_+^* - W_-^*\,. \tag{3.68}$$

From equation (3.66), and because $C^0(\omega)$ is real, we see that $W^*_{\text{mean}}(\omega)$ is real and that $W^*_{\text{diff}}(\omega)$ is imaginary. Thus the real part of the perturbation to the cross-correlation, $\delta C(\omega)$, introduces a mean travel-time perturbation. The imaginary part of $\delta C(\omega)$ causes a travel-time difference.

3.3.3   Zero-Order Solution

Now that the problem has been fully specified, we can compute the Green's function, the power spectrum, and the cross-correlation for the zero-order model. We show that the power spectrum in our example resembles the solar f-mode spectrum. We find that the unperturbed cross-correlation is the inverse Fourier transform of the power spectrum.

Green's Function

Here we derive the Green's function appropriate for solving a problem of the form of equation (3.42). The vector Green's function, $\boldsymbol{G}(\boldsymbol{x}, z, t; \boldsymbol{s}, t_{\text{s}})$, is the velocity response at horizontal coordinate $\boldsymbol{x}$, height z, and time t to an impulsive source in S at surface location $\boldsymbol{s}$ and time t_{s}. In our example S is scalar, so we need only one vector Green's function, and we drop the superscript on the Green's function, which appeared in the general theory (eq [3.16]). By definition $\boldsymbol{G}$ solves the surface boundary condition

$$\mathcal{L}^0 \boldsymbol{G}(\boldsymbol{x}, z, t; \boldsymbol{s}, t_{\text{s}}) = \delta_{\text{D}}(\boldsymbol{x} - \boldsymbol{s})\, \delta_{\text{D}}(t - t_{\text{s}}) \quad \text{at } z = 0, \tag{3.69}$$

with the additional constraints that $\boldsymbol{G}$ must be irrotational and divergenceless in the bulk, as well as vanish as $z \to -\infty$. The Green's function $\boldsymbol{G}$ is only a function of the horizontal spatial separation $\boldsymbol{x} - \boldsymbol{s}$, the time lag $t - t_{\text{s}}$, and the observation height z. Using the Fourier convention given by equation (B.4), the Fourier transform of the Green's function can be written

$$\boldsymbol{G}(\boldsymbol{k}, \omega; z) = \frac{(\mathrm{i}\hat{\boldsymbol{k}} + \hat{\boldsymbol{z}})\, e^{kz}}{(2\pi)^3 k\, [gk - \omega^2 - i\omega\Gamma^0(\omega)]}, \tag{3.70}$$

where $\hat{\boldsymbol{k}} = \boldsymbol{k}/k$. We remind the reader that in this example the wave vector $\boldsymbol{k}$ is horizontal. From the above expression we can see that the horizontal component of $\boldsymbol{G}(\boldsymbol{k}, \omega; z)$ is in the direction of $\boldsymbol{k}$ and that the horizontal and vertical components are of the same magnitude and $\pi/2$ out of phase. The amplitude of the Green's function decays exponentially with depth; the same result would apply for a vertically stratified medium (Lamb, 1932). At fixed wavenumber k, the Green's function has resonant frequencies $\omega \simeq \pm\sqrt{gk} - i\Gamma^0/2$ in the limit of small damping. We recognize the dispersion relation for deep water waves. Since $\Gamma^0(\omega)$ is positive, the imaginary part of the two poles of the Green's function is negative. This ensures that the Green's function is causal (e.g. Saff & Snider, 1993). For later use, we also introduce another Green's function,

$$\mathcal{G}^{\Pi}(\boldsymbol{k}, \omega) = i\omega k^2 F(\boldsymbol{k}, \omega) G_z(\boldsymbol{k}, \omega, z = 0) , \qquad (3.71)$$

which gives the vertical velocity at the surface resulting from an impulsive source in Π/ρ. The Green's function G_z is the $\hat{\boldsymbol{z}}$ component of $\boldsymbol{G}$ given by equation (3.70).

Power

By definition the power spectrum is the square of the modulus of the Fourier transform of the observable. For convenience, we consider the zero-order power spectrum per unit area and per unit time:

$$P(\boldsymbol{k}, \omega) = \frac{(2\pi)^3}{AT} \mathrm{E}\left[|\phi^0(\boldsymbol{k}, \omega)|^2\right] , \qquad (3.72)$$

where A is the area and T the time interval over which the power is computed. After a few simple manipulations, we find that P is given by

$$P(\boldsymbol{k}, \omega) = (2\pi)^6 \, |\mathcal{G}^{\Pi}(\boldsymbol{k}, \omega)|^2 \, m^0(\boldsymbol{k}, \omega) . \qquad (3.73)$$

None of the terms in the above equation depend on the direction of $\boldsymbol{k}$. In particular, $m^0 = m^0(k, \omega)$ because the sources are spatially homogeneous and isotropic in the zero-order problem. In addition the filter F is a function only of the wavenumber k and frequency ω. Therefore the power spectrum is independent of the direction

of $\boldsymbol{k}$. The term $|\mathcal{G}^{\Pi}(\boldsymbol{k}, \omega)|^2$ specifies the shape of the resonance peaks in the power spectrum. For ω near $\sqrt{gk}$ we have approximately

$$P(\boldsymbol{k}, \omega) \sim \frac{k^2 F^2 m^0}{4} \left[\left(\omega - \sqrt{gk} \right)^2 + \left(\Gamma^0 / 2 \right)^2 \right]^{-1}. \qquad (3.74)$$

Thus, at fixed wavenumber, the line shape is Lorentzian with full-width at half-maximum $\Gamma^0(\omega)$.

Figure 3.5 compares the power spectrum for our model, $P(k, \omega)$, with the power spectrum for the solar f-mode ridge observed with the MDI/SOHO high-resolution telescope. The distribution of power with frequency and wavenumber confirms that there is a good agreement between the model and the observations.

Cross-correlation

To obtain the zero-order cross-correlation, we use the definition of C^0 (eq. [3.22]), the expression for the source covariance (eq. [3.49]), and the definition of the Fourier transform to obtain:

$$C^0(\boldsymbol{1}, \boldsymbol{2}, t) = \iint_{-\infty}^{\infty} \mathrm{d}\boldsymbol{k} \int_{-\infty}^{\infty} \mathrm{d}\omega \, e^{\mathrm{i}\boldsymbol{k}\cdot\boldsymbol{\Delta} - \mathrm{i}\omega t} \, P(\boldsymbol{k}, \omega), \qquad (3.75)$$

where $\boldsymbol{\Delta} = \boldsymbol{2} - \boldsymbol{1}$. For the zero-order problem the cross-correlation is therefore the inverse Fourier transform of the power spectrum. This is a consequence of the fact that the problem is translation invariant. Since in our example P does not depend on the direction of $\boldsymbol{k}$ we can perform the integration over the angle between $\boldsymbol{k}$ and $\boldsymbol{\Delta}$ to obtain

$$C^0(\boldsymbol{1}, \boldsymbol{2}, t) = 2\pi \int_0^{\infty} k \, \mathrm{d}k \int_{-\infty}^{\infty} \mathrm{d}\omega \, e^{-\mathrm{i}\omega t} J_0(k\Delta) P(k, \omega), \qquad (3.76)$$

where J_0 is the cylindrical Bessel function of order zero. From the above expression it is clear that the zero-order cross-correlation is only a function of the time lag t and the spatial separation between $\boldsymbol{1}$ and $\boldsymbol{2}$, $\Delta = \|\boldsymbol{\Delta}\|$. Notice that the amplitude of the cross-correlation falls off like $\Delta^{-1/2}$ at large distances as result of the asymptotic form of $J_0(k\Delta)$. This factor accounts for the geometrical spreading of two-dimensional waves, like surface-gravity waves.
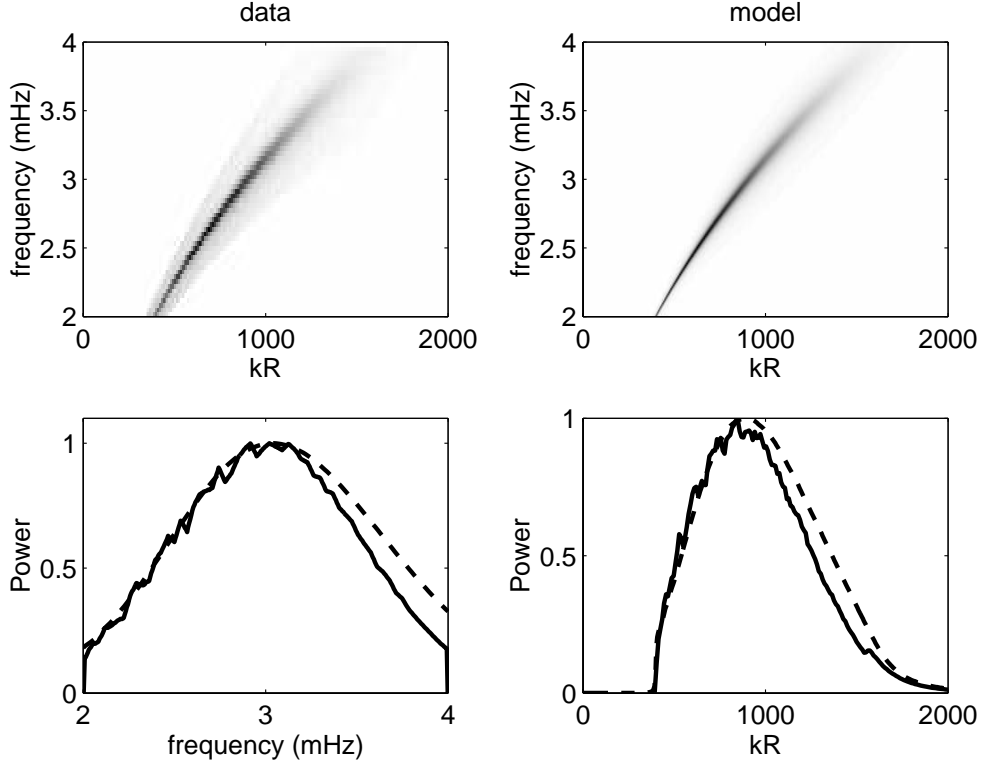
Figure 3.5: A comparison of observed and model power spectra. The upper-right figure shows the zero-order power spectrum in our model, $P(k,\omega)$, defined by equation (3.73). The coordinates are frequency, $\omega/2\pi$, and dimensionless wavenumber, $kR_\odot$, where $R_\odot = 696$ Mm is the solar radius. In the upper-left figure is the azimuthal average of the power observed with the MDI/SOHO high-resolution telescope. The f-mode ridge has been isolated by a simple boxcar filter. The lower-left panel displays the power integrated over wavenumber, as a function of frequency. The dashed and solid lines refer to the model and the observations respectively. The lower-right figure shows the power integrated over frequency, as a function of wavenumber $kR_\odot$. Again the dotted line refers to the model and the solid line to the data. In our model the source correlation length and time are $L_s = 0$ and $T_s = 400$ s. The agreement between the model and the observations could be further improved by considering a non-zero source correlation length, which would reduce the power at high spatial frequencies.

From the power spectrum, we can compute numerically the cross-correlation using equation (3.76). Figure 1.5 provides a comparison between the model cross-correlation C^0 (right panel) and the average MDI cross-correlation for the f-mode (left panel). The two cross-correlations show the same features, including at very short distances. The two branches of the cross-correlation correspond to the propagation of the energy of the wave packets at the group speed, $v_{\rm g} = g/2\omega$, where ω is the central frequency. For a central frequency of 3 mHz the group speed is 7.3 km s^{-1}. The effect of dispersion is also clearly visible: the oscillating fine structure has a different slope than the envelope slope, given by the phase speed $v_{\rm p} = 2v_{\rm g}$. Low-frequency waves propagate faster than high-frequency waves, because the phase speed is inversely proportional to ω. Note that for distances less than about half a wavelength (2.5 Mm) the two branches of the cross-correlation are merged. This implies that travel-time measurements are difficult in the near field. The effect of damping is to strongly suppress high-frequency waves at large distances. Figure 3.1 shows a plot of the zero order cross-correlation, $C^0 = C^{\rm ref}$, at a distance $\Delta = 10$ Mm. As a consequence of the dependence of the phase speed on frequency (dispersion), the instantaneous frequency of the cross-correlation is seen to increase with time lag t.

3.3.4 Kernels for Source Strength and Damping Rate

In this section we derive travel-time kernels, $K_\pm^a$ and $K_\pm^\gamma$, for perturbations to local source strength and damping rate respectively. These kernels connect travel-time perturbations $\delta\tau_\pm$ to fractional perturbations to the model:

$$
\begin{aligned}
\delta\tau_\pm(\mathbf{1}, \mathbf{2}) \;=\; & \int_{(A)} \mathrm{d}\mathbf{r}\, \frac{\delta a(\mathbf{r})}{a}\, K_\pm^a(\mathbf{1}, \mathbf{2}; \mathbf{r}) \\
& + \int_{(A)} \mathrm{d}\mathbf{r}\, \frac{\delta\gamma(\mathbf{r})}{\gamma}\, K_\pm^\gamma(\mathbf{1}, \mathbf{2}; \mathbf{r})\,.
\end{aligned}
\tag{3.77}
$$

Here $\delta a(\mathbf{r})/a$ is the local fractional change in the source strength and $\delta\gamma(\mathbf{r})/\gamma$ the fractional change in damping rate. The two-dimensional integrals are taken over all points $\mathbf{r}$ on the surface $z = 0$, denoted by (A).

In Appendix C we give an explicit derivation of the sensitivity kernels $K_\pm^\gamma$ and

$K_\pm^a$. We first compute the sensitivity of the cross-correlation to small local changes in a and γ (eqs. [C.2], [C.3] and [C.4]). We then relate changes in the cross-correlation to changes in travel times, through the weight functions $W_\pm$ (eq. [3.30]). Because of the assumptions that we have made in this example, the kernels can be written in terms of separate one-dimensional integrals over horizontal wavenumber. In Appendix C we show that $K_\pm^a$ are given by

$$
\begin{aligned}
K_\pm^a(\mathbf{1}, \mathbf{2}; \boldsymbol{r}) &= 4\pi \operatorname{Re} \int_0^\infty \mathrm{d}\omega\, W_\pm^*(\mathbf{1}, \mathbf{2}, \omega)\, m^0(\omega) \\
&\quad \times \mathrm{I}^*(\Delta_1, \omega) \mathrm{I}(\Delta_2, \omega),
\end{aligned}
\tag{3.78}
$$

where the integral $\mathrm{I}(d, \omega)$ is a function of a distance d and frequency ω only:

$$
\mathrm{I}(d, \omega) = (2\pi)^3 \int_0^\infty k\, \mathrm{d}k\, J_0(kd) \mathcal{G}^{\Pi}(k, \omega).
\tag{3.79}
$$

In equation (3.78), Δ_1 is the distance from $\mathbf{1}$ to $\boldsymbol{r}$ and Δ_2 is the distance from $\mathbf{2}$ to $\boldsymbol{r}$. The complex integral $\mathrm{I}(d, \omega)/(2\pi)^2$ is the spatial inverse Fourier transform of the Green's function $\mathcal{G}^{\Pi}(\boldsymbol{k}, \omega)$.

As shown in Appendix C, the damping kernels $K_\pm^\gamma$ can also be written as combinations of two one-dimensional integrals, $\mathbb{II}(d, \omega)$ and $\mathbb{III}(d, \omega)$:

$$
\begin{aligned}
K_\pm^\gamma(\mathbf{1}, \mathbf{2}; \boldsymbol{r}) &= 4\pi(\hat{\boldsymbol{\Delta}}_1 \cdot \hat{\boldsymbol{\Delta}}_2) \operatorname{Re} \int_0^\infty \mathrm{d}\omega\, W_\pm^*(\mathbf{1}, \mathbf{2}, \omega) \\
&\quad \times m^0(\omega) \left[\mathbb{II}(\Delta_1, \omega) \mathbb{III}(\Delta_2, \omega) \right. \\
&\quad \left. + \mathbb{II}(\Delta_2, \omega) \mathbb{III}^*(\Delta_1, \omega) \right],
\end{aligned}
\tag{3.80}
$$

where $\hat{\boldsymbol{\Delta}}_1$ is a unit vector in the direction $\boldsymbol{r} - \mathbf{1}$ and $\hat{\boldsymbol{\Delta}}_2$ is a unit vector in the direction $\boldsymbol{r} - \mathbf{2}$. The explicit forms of $\mathbb{II}$ and $\mathbb{III}$ are given in Appendix C. The function $\mathbb{III}$ is complex and involves only one Green's function, $\mathcal{G}^{\Pi}$. The real integral $\mathbb{II}$ involves two Green's functions, G_z and $\mathcal{G}^{\Pi}$, and is related to the scattering process (see Fig. 3.2).

We computed the kernels numerically, with grid spacings of 7×10^{-3} rad Mm^{-1} in k and 10^{-2} mHz in $\omega/2\pi$, which were selected so that the smallest line widths (1.5×10^{-2} rad Mm^{-1}, 1.7×10^{-2} mHz) would be resolved. We ran a second set of
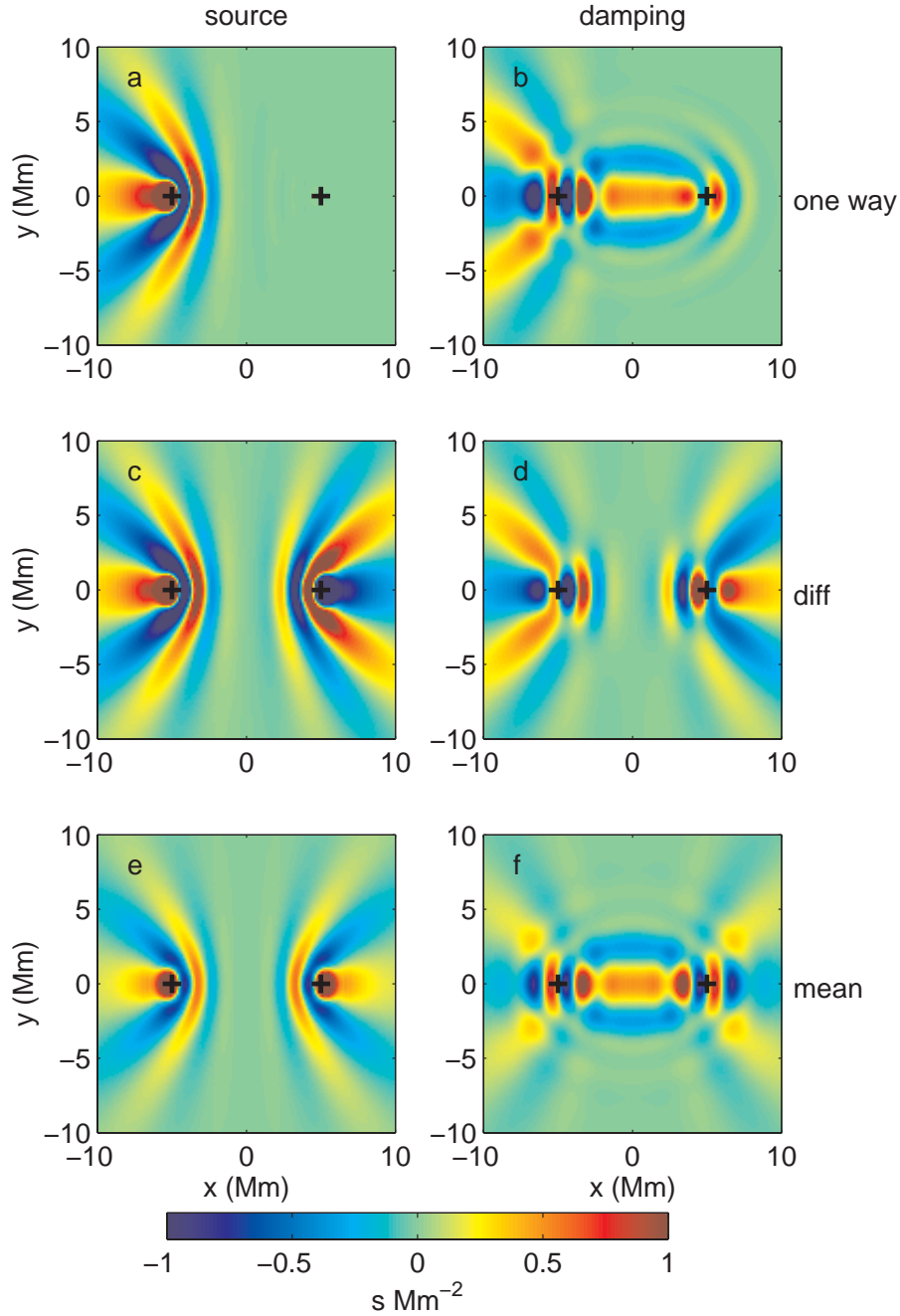
Figure 3.6: Travel-time sensitivity kernels for perturbations in source strength and damping rate as functions of position $r = (x, y)$. The left column displays kernels for source strength, K^a, and the right column displays kernels for damping rate, K^γ. The top row gives the one-way travel-time kernels $K_+^{a,\gamma}$, the middle row gives the travel-time difference kernels $K_{\text{diff}}^{a,\gamma}$, and the bottom row gives the mean travel-time kernels $K_{\text{mean}}^{a,\gamma}$. The observation points **1** and **2** have the coordinates $(x_1, y_1) = (-5, 0)$ Mm and $(x_2, y_2) = (5, 0)$ Mm respectively, and are denoted by the black crosses in each panel. The color scale indicates the local value of the kernel, with blue representing negative value and red positive. The color scale is truncated at ± 1 s Mm^{-2}. The grid spacing is 0.14 Mm.

calculations at twice the above stated resolutions and saw only very minor changes in the resulting kernels.

Figures 3.6a and 3.6b show the kernels $K_+^a(\mathbf{1}, \mathbf{2}; \mathbf{r})$ and $K_+^\gamma(\mathbf{1}, \mathbf{2}; \mathbf{r})$ for the distance $\Delta = 10$ Mm, as a functions of horizontal position $\mathbf{r} = (x, y)$. The observation points $\mathbf{1}$ and $\mathbf{2}$ have coordinates $(x_1, y_1) = (-5, 0)$ Mm and $(x_2, y_2) = (5, 0)$ Mm respectively. An important observation is that the kernels K_+^a and K_+^γ are quite different: one does not simply have the opposite sign of the other. This means that a decrease in source strength is not equivalent to an increase in damping rate, as one might naively expect. In particular, the total integral of the source kernel is zero while the total integral of the damping kernel is positive, with a value of 5.9 s. A uniform increase in source strength results only in a change in the overall amplitude of the power spectrum (and thus in the cross-correlation) and as a result does not affect the travel time. In contrast, a uniform increase in the damping rate affects the shape of the power spectrum, and thus causes a travel-time perturbation $\delta\tau_+$. The kernels $K_+^{a,\gamma}$ have largest amplitude in the vicinity of the observation points $\mathbf{1}$ and $\mathbf{2}$. Both K_+^γ and K_+^a have roughly the same magnitude, of the order a few s Mm^{-2}. Both of the kernels oscillate spatially: this is a finite wavelength effect.

Hyperbola shaped features (with $\Delta_2 - \Delta_1 = $ const) are present in both K_+^γ and K_+^a. As Woodard (1997) noted, all of the sources located along a particular hyperbola (with foci at the observation points) give a similar contribution to the cross-correlation, which explains the appearence of the kernel K_+^a. We emphasize that the kernel $K_+^a(\mathbf{1}, \mathbf{2}; \mathbf{r})$ is for the one-way travel time $\delta\tau_+(\mathbf{1}, \mathbf{2})$ which relates to waves moving from $\mathbf{1}$ to $\mathbf{2}$. As a result only perturbations to the sources which produce waves moving from $\mathbf{1}$ to $\mathbf{2}$ can introduce a perturbation in $\tau_+(\mathbf{1}, \mathbf{2})$. This is clear from Figure 3.6a: the kernel K_+^a is only significant in the region, $x < 0$, which produces waves that arrive at $\mathbf{1}$ before they arrive at $\mathbf{2}$.

The damping kernel K_+^γ is more complicated, as it shows ellipses ($\Delta_2 + \Delta_1 = $ const) in addition to hyperbolas, and results from scattering, unlike the source strength kernel. The ellipses are due to waves that go through $\mathbf{1}$, scatter at $\mathbf{r}$, and are then observed at $\mathbf{2}$. The hyperbolas corresponds to scattered waves which arrive at $\mathbf{1}$ before the direct waves arrive at $\mathbf{2}$. These two distinct processes will be discussed in more detail in Figure 3.10. Note that the damping kernels K^γ change

sign on the circle $\hat{\boldsymbol{\Delta}}_1 \cdot \hat{\boldsymbol{\Delta}}_2 = 0$ which goes through **1** and **2**. This is a result of the details of the scattering of waves by local inhomogeneities in damping rate. The scattered wave depends on the direction of the incoming wave; back-scattered waves are in anti-phase with forward-scattered waves.

In this example, because $C^{\mathrm{ref}} = C^0$ is even in time, $\delta\tau_-(\mathbf{1}, \mathbf{2}) = \delta\tau_+(\mathbf{2}, \mathbf{1})$. As a result the kernels K_-, for the travel-time perturbation $\delta\tau_-$, can be obtained from

$$K_-(\mathbf{1}, \mathbf{2}; \boldsymbol{r}) = K_+(\mathbf{2}, \mathbf{1}; \boldsymbol{r}). \tag{3.81}$$

This is not, however, a general rule, it depends on the choice of reference wavelet. The kernels for the perturbations to the travel-time mean and difference can be easily obtained from the kernels for the one-way travel times:

$$K_{\mathrm{mean}}^{a,\gamma} = \frac{1}{2}(K_+^{a,\gamma} + K_-^{a,\gamma}), \tag{3.82}$$

$$K_{\mathrm{diff}}^{a,\gamma} = K_+^{a,\gamma} - K_-^{a,\gamma}. \tag{3.83}$$

The kernels $K_{\mathrm{mean}}^{a,\gamma}$ and $K_{\mathrm{diff}}^{a,\gamma}$ are plotted in the remaining panels of Figure 3.6.

The kernels for the mean travel time are symmetric on interchange of **1** and **2** and the travel-time difference kernels are antisymmetric on interchange of **1** and **2**. Notice that like the one-way travel time kernels, the kernels $K_{\mathrm{diff}}^{a,\gamma}$ and $K_{\mathrm{mean}}^{a,\gamma}$ are largest near the observation points **1** and **2**. We note that K_{diff}^{a} is roughly of the opposite sign of $K_{\mathrm{diff}}^{\gamma}$, except for inside the circle defined by $\hat{\boldsymbol{\Delta}}_1 \cdot \hat{\boldsymbol{\Delta}}_2 = 0$, where the sign is the same. A localized perturbation to source strength (damping rate) on the line $y = 0$ with $x \lesssim x_1$ gives an increase (decrease) in the travel-time difference.

In order to show the full range of variation of the kernels we plot, in Figure 3.7, cuts of the kernels $K_+^{a,\gamma}$ along the lines $y = 0$ and $x = 0$. Figure 3.7a shows that the source kernel is zero along the line $x = 0$, while the damping kernel is positive and maximum at $y = 0$. The side lobes (the second Fresnel zone) of K_+^{γ} extend out to 3.5 Mm. The slice along the line $y = 0$, Figure 3.7b, shows the complicated behavior of the kernels near the observation points, where they oscillate.

We have studied single-frequency kernels and seen that there is constructive interference between different frequency components along the line $y = 0, -\infty < x < x_2$ for K_+^{γ}, and the line $y = 0, -\infty < x < x_1$ for K_+^{a}. In the limit of infinite
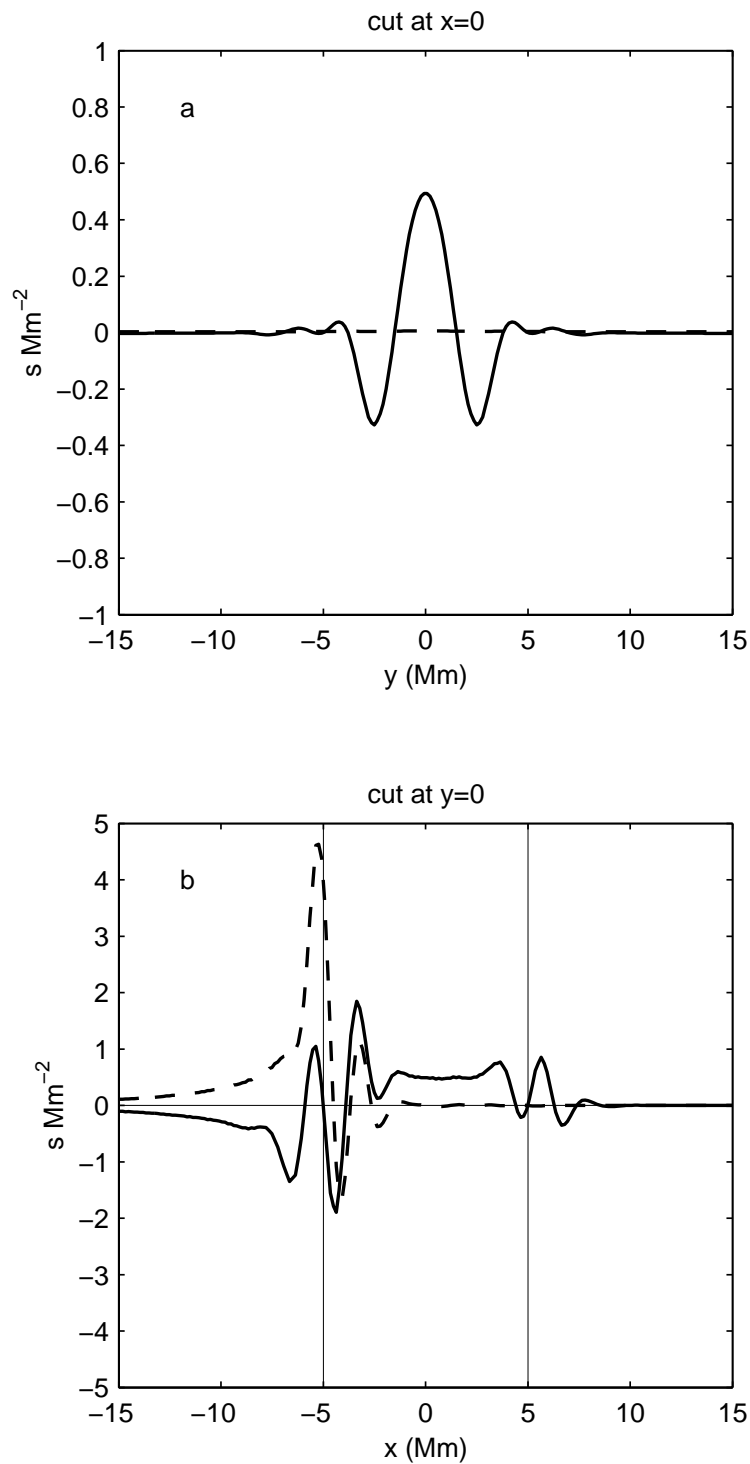
Figure 3.7: Cuts through the source and damping kernels, K_+^a and K_+^γ. Panel (a) shows cuts along the line $x = 0$ and panel (b) shows cuts along the line $y = 0$. The dashed line is for the source kernel K_+^a and the solid line is for the damping kernel K_+^γ.

bandwidth, the kernels K_+^γ and K_+^a reduce to these rays respectively. This is in contrast with conventional ray theory where the ray is restricted to the line segment $y = 0, x_1 < x < x_2$.

In the past, travel-time kernels have been calculated in the "single-source picture" (Birch & Kosovichev, 2000; Jensen et al., 2000). In the following section we test the single-source method by comparing single-source kernels with the kernels calculated using a random distributed source model.

3.3.5   The Single Source Picture

The single-source picture consists of placing a single causal source at **1** and observing the effect of local perturbations on the wavefield observed at **2**. The one-way travel-time perturbation is approximated by the travel time shift,

$$\delta\tau_+^{\rm ss}(\mathbf{1}, \mathbf{2}) = -\frac{\int_{-\infty}^{\infty} {\rm d}t \, \delta\phi(\mathbf{2}, t) \, \dot{\phi}^0(\mathbf{2}, t)}{\int_{-\infty}^{\infty} {\rm d}t \, [\dot{\phi}^0(\mathbf{2}, t)]^2} \,, \tag{3.84}$$

between the unperturbed and perturbed signals at **2** (Birch et al., 2001). This new definition of travel time is necessary: in the single-source picture there is no cross-correlation and thus our earlier definition of travel time can not be used. In equation (3.84), $\phi^0(\mathbf{2})$ and $\delta\phi(\mathbf{2})$ are the unperturbed and perturbed wavefields at **2**. The wavefield is generated by a causal pressure source placed at **1**:

$$\Pi(\mathbf{s}, t_{\rm s}) = \rho \, \Theta(\mathbf{s} - \mathbf{1}, t_{\rm s}) \,. \tag{3.85}$$

The function Θ characterizes the pressure source, and will later be used to tune the source spectrum.

In this section we consider the kernel $K_+^{\gamma, {\rm ss}}$, derived in the single-source picture, which gives the sensitivity of the travel-time perturbation $\delta\tau_+$ to a local fractional perturbation in the damping rate. The single-source picture cannot easily be used to derive a kernel for a source perturbation, which does not involve a scattering process.
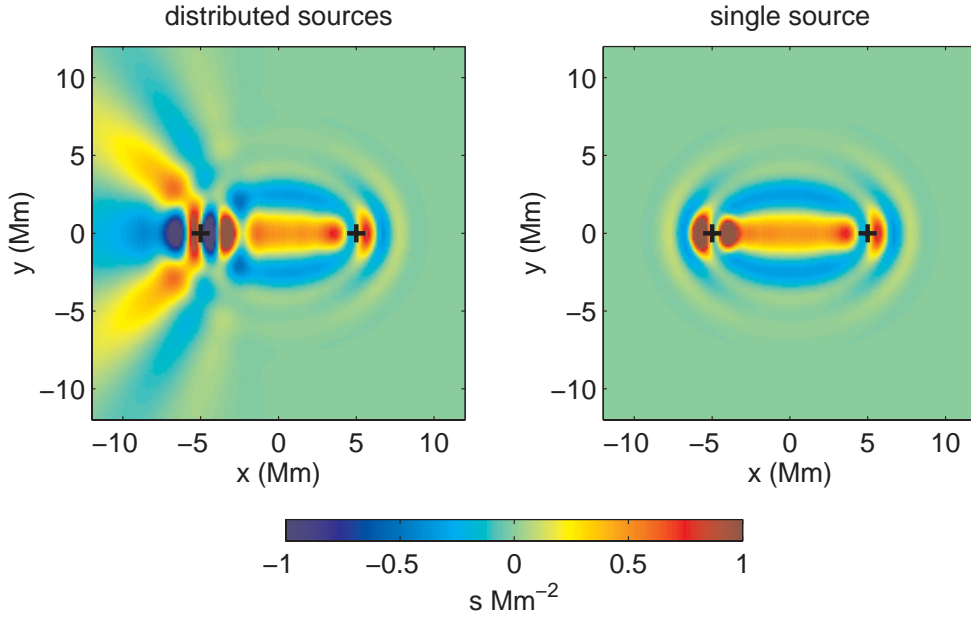
Figure 3.8: A comparison between single and distributed source kernels for damping rate. The left panel shows the distributed source kernel for damping, K_+^γ (also shown in Fig. 3.6b). The right panel is the single source kernel $K_+^{\gamma,\mathrm{ss}}$ discussed in Section 3.3.5 and computed using equations (D.5) and (D.6). For the single source kernel the source is located at **1** with coordinates $(-5, 0)$ Mm. The observation point **2** is located at $(0, 5)$ Mm.

By definition the kernel $K_+^{\gamma,\mathrm{ss}}$, which we derive in Appendix D, satisfies

$$\delta\tau_+^{\mathrm{ss}}(\mathbf{1}, \mathbf{2}) = \int_{(A)} \mathrm{d}\boldsymbol{r}\, \frac{\delta\gamma(\boldsymbol{r})}{\gamma}\, K_+^{\gamma,\mathrm{ss}}(\mathbf{1}, \mathbf{2}; \boldsymbol{r})\,. \tag{3.86}$$

The definition of travel time given in equation (3.84) closely resembles the definition of travel time used in the general theory (eqs [A.6] and [A.8]) if $\phi(\mathbf{2}, t)$ looks like the positive time-lag branch of the zero order cross-correlation from the random source model. This condition implies that the spectrum of the source, $\Theta(\boldsymbol{k}, \omega)$, is given by equation (D.8).

Figure 3.8 is a comparison of the single-source kernel $K_+^{\gamma,\mathrm{ss}}$ with the distributed-source kernel K_+^γ, computed in the previous section. The single-source kernel fails to reproduce the hyperbola shaped features that are seen in the random source kernel, even though the ellipses can be seen in both (with the same order of magnitude and sign). A single causal source at **1** is not sufficient to generate all of the waves which
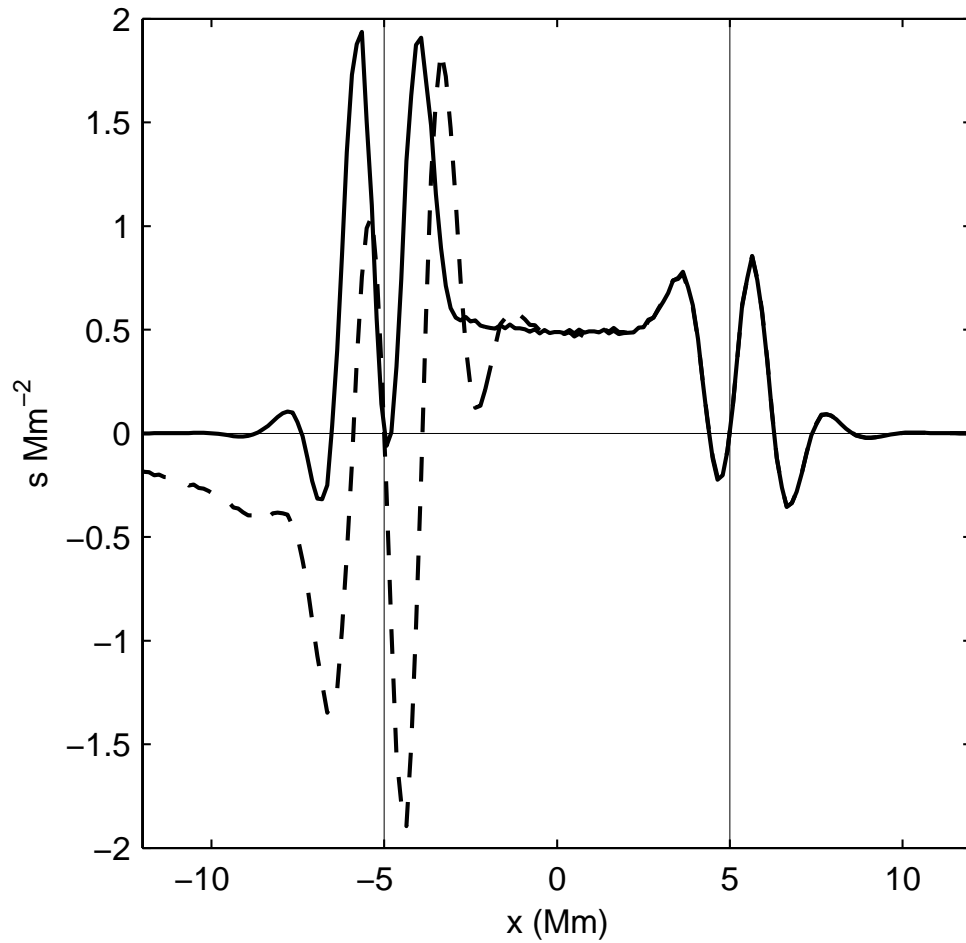
Figure 3.9: Cuts along the line $y = 0$ through the damping kernels K_+^γ and $K_+^{\gamma,\mathrm{ss}}$ shown in Figure 3.8. The dashed line is for the distributed-source kernel and the solid line is for the single-source kernel.

are relevant to the problem of computing travel time kernels (see Fig. 3.10).

Cuts at $y = 0$ through $K_+^{\gamma,\mathrm{ss}}$ and K_+^γ are shown in Figure 3.9, again for the distance $\Delta = 10$ Mm which was used in all previous plots of kernels. The kernels agree well for $x \gtrsim 0$, where the hyperbola shaped features in K_+^γ are absent. For $x \lesssim 0$, the two kernels are quite different, in particular the single-source kernel is nearly zero for $x < -7$ Mm, while K_+^γ has a negative tail there.

In the limit of infinite bandwidth (ray theory), the single-source kernel $K_+^{\gamma,\mathrm{ss}}$ would be restricted to the line segment, $y = 0$, $x_1 < x < x_2$; in contrast with the finding (see § 3.3.4) that the distributed-source kernel K_+^γ would reduce to the ray $y = 0$, $-\infty < x < x_2$.
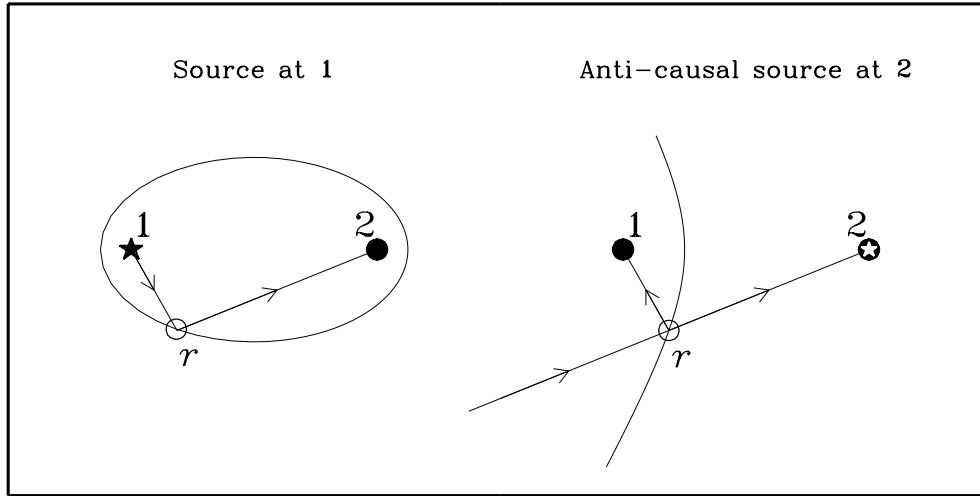
Figure 3.10: A graphical discussion of the single-source picture for computing kernels for the one-way travel time $\delta\tau_+(\mathbf{1}, \mathbf{2})$. The left hand panel is the conventional single-source picture where a causal source is exploded at $\mathbf{1}$ and the scattered wave is observed at $\mathbf{2}$. The scattering point is denoted by $\mathbf{r}$. Perturbations located on curves with constant $\|\mathbf{r} - \mathbf{1}\| + \|\mathbf{2} - \mathbf{r}\|$ contribute to the scattered field with the same geometrical delay in travel time, and as a result ellipse shaped features are seen in the travel-time kernel. A single source at $\mathbf{1}$ does not, however, produce all of the waves which are relevant to computing correct travel-time kernels. The right-hand panel shows an example of a component to the wavefield which is missed in the single-source picture. An anti-causal source at $\mathbf{2}$ causes an incoming wave toward $\mathbf{2}$ which is then scattered at $\mathbf{r}$ and arrives at $\mathbf{1}$. For $\mathbf{r}$ near $\mathbf{1}$ this gives a signal that is first observed at $\mathbf{1}$ and then later at $\mathbf{2}$, i.e. looks like a wave moving from $\mathbf{1}$ to $\mathbf{2}$. Perturbations located on curves with constant $\|\mathbf{r} - \mathbf{1}\| - \|\mathbf{2} - \mathbf{r}\|$, i.e. hyperbolas, contribute to the scattered field with the same geometrical delay in travel time. Were the single-source picture extended to include an anti-causal source at $\mathbf{2}$, hyperbola shaped features would be seen in the travel-time kernels. Note, however, that hyperbolas naturally appear in the distributed-source kernels $K_+^{a,\gamma}$ (Fig. 3.6a and 3.6b). The hyperbolas with $\|\mathbf{r} - \mathbf{1}\| - \|\mathbf{2} - \mathbf{r}\| > 0$ are not seen as they do not affect the positive-time branch of the cross-correlation (the scattered wave arrives at $\mathbf{1}$ after the unperturbed wave arrives at $\mathbf{2}$).

Chapter 4

Global Seismology of Sun-like Stars [1]

4.1 Inclination of Stellar Rotation Axes

4.1.1 Introduction

For an Earth-based observer the rotation axis of the Sun is almost perpendicular to the line of sight. Traditionally, the solar rotation axis has been approximated to be exactly perpendicular to the ecliptic plane for helioseismic investigations of spatially-unresolved oscillation data. An exception concerns the search for oblique rotation of the Sun's core (Goode & Thompson, 1992; Gough et al., 1995). The rotation axes of stars are however randomly distributed in space. Since the visibility of the pulsation modes with various azimuthal orders m is a function of the angle between the rotation axis and the line of sight, i, this angle cannot be ignored in asteroseismology. The presence of random i values not only affects the method to measure oscillation mode parameters, but asteroseismology conversely provides us with the possibility of determining i, a parameter that in general is very poorly determined. Space missions such as COROT of CNES (Baglin et al., 2001) and Eddington of ESA (Favata et al., 2000) are expected to deliver the data necessary to do high-precision asteroseismology on a large number of stars.

The surface rotation rate of a star is one of its fundamental parameters and has been well studied. The standard method of deducing the rotation rate is to consider the widths of spectral lines. This technique only gives $v \sin i$, however, where v is the equatorial rotation velocity at the stellar surface. Asteroseismology can in principle provide measurements of the angular velocity, Ω, and of the inclination angle i. From these three measurements it is possible to determine the stellar radius, another fundamental parameter, without knowledge of stellar structure and evolution.

Knowledge of i is important not just for obtaining improved stellar parameters, but also in order to determine the masses of extra-solar planets. The standard technique used to detect such planets is to look for periodic Doppler shifts in the spectrum of the central star of the extra solar planetary system (Mayor & Queloz, 1995; Noyes et al., 1997; Marcy & Butler, 2000). This technique, however, only returns $M_p \sin i_p$, where M_p is the mass of the orbiting body and i_p is the inclination of the normal to its orbital plane relative to the line of sight. Clearly, the mass estimate obtained in this manner is a lower limit. Since i and i_p are expected to be similar

(see below) a knowledge of i would help to improve the mass estimates of extra solar planets considerably and would distinguish also misidentified brown dwarfs in orbits with small i_{p} from bona fide planets. In the solar system i and i_{p} differ by less than $10°$ for all the planets excluding Pluto. Also, currently favored theories of planetary system formation predict that the orbital plane of planets should nearly coincide with the equatorial plane of the central star (Safronov, 1972; Lissauer, 1993). An alternative technique for detecting planets involves looking for planetary transits in photometric data. So far this technique has uncovered only a couple of such systems (Charbonneau et al., 2000; Henry et al., 2000; Udalski et al., 2002; Konacki et al., 2003; Dreizler et al., 2003), compared to a total of over 100 planets detected using radial velocities. However, missions such as COROT, Eddington, and Kepler aim at discovering many such systems. Since for transiting planets i_{p} is known to high accuracy (Brown et al., 2001), a comparison with the independently measured i of the central stars would allow a direct test of the theoretical prediction that i_{p} and i are very similar. Clearly, there are many reasons to attempt to measure i.

Here we present a technique employing low-degree non-radial oscillations to determine i for sufficiently rapidly rotating stars. The technique makes use of the fact that the ratio of amplitudes of the $m = \pm 1$ and $m = 0$ components of dipole oscillations is a strong function of i. Similarly, the amplitudes of the peaks in quadrupole multiplets exhibit different dependences on i. This technique is thus similar to using the ratios of $\sigma(\Delta M_J = \pm 1)$ to $\pi(\Delta M_J = 0)$ components of Zeeman-split atomic transitions to determine the angle of the magnetic field vector relative to the line-of-sight, a standard procedure in Zeeman magnetometry. By studying solar dipole modes of oscillation, Gough et al. (1995) were able to measure the inclination of the Sun's rotation axis within $5°$ of the true value.

In this chapter we simulate a large number of realizations of oscillation power spectra seen in intensity with known values of the stellar rotation and of the inclination angle. We then fit a parametric model to each power spectrum with a maximum likelihood technique to estimate i, Ω, and other mode parameters. The distribution of the measured values of i indicates how precise a measurement can be. In order to assess the feasibility of the technique we adopt the pessimistic view

that only a single multiplet, $l = 1$ or $l = 2$, is observed. In practice, the information from tens of modes would be combined to better constrain i. Although we are investigating a problem which has not been studied before, we employ many results from helioseismology.

4.1.2 Effect of Rotation on Stellar Oscillations

Stars like the Sun undergo global acoustic oscillations driven by near-surface turbulent convection. The pulsation frequencies ω_{nl} of eigenmodes with radial order n and spherical harmonic degree l are characteristic of the spherically symmetric structure of a star (Brown & Gilliland, 1994). For distant Sun-like stars, observations are mostly sensitive to high-order acoustic modes with $l \leq 2$, i.e. radial, dipole, and quadrupole p modes. Because low-degree frequencies satisfy a relatively simple asymptotic relation (Tassoul, 1980) in which the large separation $\omega_{nl} - \omega_{n-1,l}$ and the small separation $\omega_{n0} - \omega_{n-1,2}$ depend weakly on n, the degree l of a multiplet can in principle be identified without ambiguity in the oscillation power spectrum (Fossat, 1981). A solar oscillation power spectrum for 200 days of observation of the total irradiance (Frohlich et al., 1997) is shown in Figure 4.1. Many attempts have been made to detect p modes on other Sun-like stars. So far they have only been clearly detected on α Cen A (Bouchy & Carrier, 2001; Schou & Buzasi, 2001; Bedding et al., 2002).

Rotation removes the $(2l + 1)$-fold degeneracy of the frequency of oscillation of the mode (n, l). The nonradial modes of a rotating star are thus labeled with a third index, the azimuthal order m, which takes integer values from $-l$ to $+l$. When the angular velocity of the star, Ω, is small, the effect of rotation on mode frequencies can be treated as a small perturbation. In the case of rigid-body rotation, and to a first order of approximation, the frequency of the mode (n, l, m) is given by (Ledoux, 1951):

$$\omega_{nlm} = \omega_{nl} + m\,\Omega\,(1 - C_{nl})\,. \tag{4.1}$$

The kinematic splitting, $m\Omega$, is corrected for the effect of the Coriolis force through the dimensionless quantity $C_{nl} > 0$ whose value depends on the oscillation eigenfunctions of the non-rotating star. High-order low-degree solar oscillations have $C_{nl} < 10^{-2}$; rotational splitting is dominated by advection. We note that the
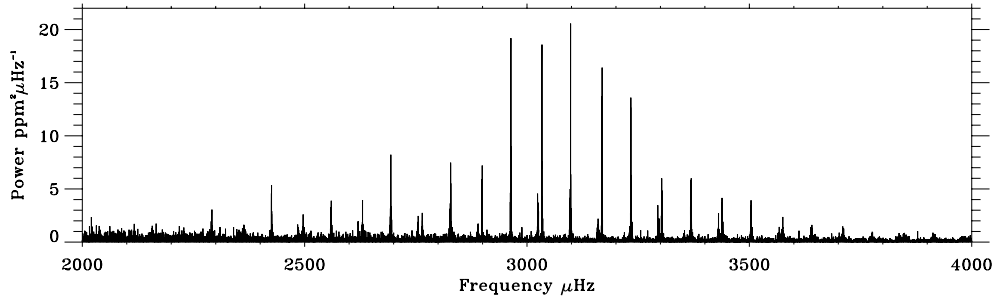
Figure 4.1: Solar oscillation power spectrum for 200 days of observation of the total irradiance (Frohlich et al., 1997). The data are from the VIRGO experiment aboard the ESA/NASA Solar and Heliospheric Observatory (SOHO). The global modes of oscillation are ordered in sequence: $(n-1, l = 2)$, $(n, l = 0)$, and $(n, l = 1)$ with radial order n increasing with frequency. The large frequency separation is $(\omega_{n,l} - \omega_{n-1,l})/2\pi \sim 135$ μHz and the small separation is $(\omega_{n,l=0} - \omega_{n-1,l=2})/2\pi \sim 10$ μHz.

rotation-induced frequency shift would not be linear in m if the angular velocity Ω were to vary with latitude (e.g. Hansen et al., 1977).

To the next order of approximation, centrifugal forces distort the equilibrium structure of the star. This results in an additional frequency perturbation (independent of the sign of m) which scales like the small parameter

$$\frac{\Omega^2 R^3}{\mathcal{G}M} ,\tag{4.2}$$

i.e. the ratio of the centrifugal to the gravitational forces at the stellar surface (Saio, 1981; Gough & Thompson, 1990). Here R denotes the radius of the star, M its mass, and $\mathcal{G}$ the universal constant of gravity. Second-order rotational effects are negligible in the Sun (Dziembowski & Goode, 1992). These effects are however significant for faster rotating Sun-like stars (Kjeldsen et al., 1998). Other perturbations, such as a large-scale magnetic field, may introduce further corrections to the pulsation frequencies (Gough & Thompson, 1990).

Here we only consider first-order rigid rotation, and substitute $\omega_{nl} + m\Omega$ for ω_{nlm}. Our purpose is to assess the feasibility of measuring the basic rotation parameters Ω and i. In an inertial frame $\mathcal{R}'$ with polar axis coincident with the angular velocity vector $\boldsymbol{\Omega}$, scalar eigenfunctions are proportional to a spherical harmonic function $Y_l^m(\theta', \phi')$, where θ' and ϕ' are the co-latitude and longitude defined in

the spherical-polar coordinate system associated with $\mathcal{R}'$. Under the approximation that the intensity fluctuation due to a mode of oscillation is proportional to a scalar eigenfunction measured at the stellar surface (such as the Lagrangian pressure perturbation), the brightness variations due to the free oscillations of a star may be written as a linear combination of eigenmodes:

$$I'(t, \theta', \phi') = \Re \sum_{nl} \sum_{m=-l}^{l} A_{nlm} \, Y_l^m(\theta', \phi') \, e^{i\omega_{nlm} t} , \qquad (4.3)$$

where A_{nlm} are complex amplitudes, t denotes time, and $\Re$ takes the real part of the expression. A more accurate expression for I' requires an explicit relationship between mode displacement and light-flux perturbation (e.g. Toutain & Gouttebroze, 1993).

To obtain the intensity that an Earth-based observer would measure, it is convenient to transform to an inertial frame $\mathcal{R}$ with polar axis pointing toward the observer, inclined by the angle i with respect to $\boldsymbol{\Omega}$. Co-latitude θ and longitude ϕ are spherical-polar coordinates defined in $\mathcal{R}$. For an appropriate choice of longitude origins, spherical harmonics expressed in $\mathcal{R}'$ and $\mathcal{R}$ are related linearly according to (Messiah, 1959):

$$Y_l^m(\theta', \phi') = \sum_{m'=-l}^{l} Y_l^{m'}(\theta, \phi) \, r_{m'm}^{(l)}(i) , \qquad (4.4)$$

where the rotation matrix $\mathbf{r}^{(l)}$ is real and unitary. According to Wigner's formula (see Messiah, 1959) each rotation matrix element can be written explicitly as a homogeneous polynomial of total degree $2l$ in the two variables $\sin(i/2)$ and $\cos(i/2)$. Inserting equation (4.4) into equation (4.3) we obtain intensity variations expressed in the frame with polar axis ($\theta = 0$) pointing toward the observer:

$$I(t, \theta, \phi) = \Re \sum_{nlmm'} A_{nlm} \, Y_l^{m'}(\theta, \phi) \, r_{m'm}^{(l)}(i) \, e^{i\omega_{nlm} t} . \qquad (4.5)$$

The spherical harmonic projection (l, m') is given by a linear combination of eigenmodes (l, m). From the above equation, we derive the observed disk-integrated

intensity signal, $I(t)$:

$$I(t) = \int_0^{2\pi} \mathrm{d}\phi \int_0^{\pi/2} \mathrm{d}\theta\, I(t; \theta, \phi)\, W(\theta) \cos\theta \sin\theta\,, \qquad (4.6)$$

where $W(\theta)$ is the limb-darkening function. Because the function $Y_l^{m'}(\theta, \phi)$ is proportional to $\exp(\mathrm{i}m'\phi)$, components with $m' \neq 0$ vanish upon integration over azimuth, and

$$I(t) = \Re \sum_{nlm} V_l\, A_{nlm}\, r_{0m}^{(l)}(i)\, e^{\mathrm{i}\omega_{nlm}t}\,, \qquad (4.7)$$

with the visibility factor V_l given by

$$V_l = 2\pi \int_0^{\pi/2} Y_l^0(\theta)\, W(\theta) \cos\theta \sin\theta\, \mathrm{d}\theta\,. \qquad (4.8)$$

For each (l,n) there are $2l + 1$ visible peaks in the power spectrum; as is expected for a steady perturbation such as rotation. The quantity V_l^2 is an estimate of the geometrical visibility of the total power in a multiplet (l, n) as a function of l. The solar limb darkening function quoted by Pierce (2000) implies $(V_1/V_0)^2 = 0.50$ and $(V_2/V_0)^2 = 0.17$. These estimates are crude (see Toutain & Gouttebroze, 1993). However, the ratios V_l/V_0 are unimportant to the present study as we are interested in the relative power between azimuthal modes with common values of l and n.

Assuming that there is energy equipartition between modes with different azimuthal order, we write amplitudes A_{nlm} in the form

$$A_{nlm} = |A_{nl}|\, e^{\mathrm{i}\phi_{nlm}}\,, \qquad (4.9)$$

where the magnitude $|A_{nl}|$ is independent of m, and ϕ_{nlm} is an arbitrary phase. Using this assumption, consistent with the solar data, together with equation (4.7), we find that the dependence of mode power on azimuthal order m is given by

$$\mathcal{E}_{lm}(i) = [r_{0m}^{(l)}(i)]^2\,. \qquad (4.10)$$

Matrix elements $r_{0m}^{(l)}(i)$ are explicitly given by Messiah (1959) in terms of associated

Legendre functions, P_l^m:

$$\mathcal{E}_{lm}(i) = \frac{(l - |m|)!}{(l + |m|)!} \left[P_l^{|m|}(\cos i) \right]^2 . \tag{4.11}$$

The above equation links mode visibility to inclination angle i (see also Dziembowski, 1977; Toutain & Gouttebroze, 1993). It provides the basic information required to later extract i from photometric measurements. It is however unknown whether the key assumption, equation (4.9), remains valid for very fast rotators as rotation affects convection and therefore the mechanism by which acoustic modes are excited. For dipole multiplets, $l = 1$, the observed mode power (Eq. [4.11]) is given by

$$\mathcal{E}_{1,0}(i) = \cos^2 i \tag{4.12}$$

$$\mathcal{E}_{1,\pm 1}(i) = \frac{1}{2} \sin^2 i . \tag{4.13}$$

For quadrupole multiplets, $l = 2$, we have

$$\mathcal{E}_{2,0}(i) = \frac{1}{4}(3\cos^2 i - 1)^2 , \tag{4.14}$$

$$\mathcal{E}_{2,\pm 1}(i) = \frac{3}{8} \sin^2(2i) , \tag{4.15}$$

$$\mathcal{E}_{2,\pm 2}(i) = \frac{3}{8} \sin^4 i . \tag{4.16}$$

It is worth noting the symmetries $\mathcal{E}_{lm}(-i) = \mathcal{E}_{lm}(\pi - i) = \mathcal{E}_{lm}(i)$. Knowledge of $\mathcal{E}_{lm}(i)$ is not enough to fully specify the direction and sense of the rotation axis, but only $|i|$ modulo π. When the rotation axis is aligned with the line of sight ($i = 0$ mod π), only the mode $m = 0$ is visible and rotation cannot be inferred. Notice also that $\sum_m \mathcal{E}_{lm}(i) = 1$, so that $\mathcal{E}_{lm}$ represents the relative power in the mode m within a multiplet (n, l).

4.1.3 Modeling Oscillation Power Spectra

In the previous section we studied the intensity variations due to the free oscillations of a star with an arbitrary orientation of the rotation axis. We found that the

brightness variations can be approximated by

$$I(t) = \sum_{m=-l}^{l} \sqrt{\mathcal{E}_{lm}(i)} \, \cos[(\omega_{nl} + m\Omega)t + \phi_m] \,, \qquad (4.17)$$

when considering only the contribution from a single multiplet (n, l). The observed power in the azimuthal component m is given by $\mathcal{E}_{lm}(i)$, and ϕ_m is an arbitrary phase. In Sun-like stars, oscillations are however excited by near-surface turbulent convection. The above model is too simple as it ignores the stochastic nature of stellar pulsations (Woodard, 1984). Oscillations also have a finite lifetime determined by their interaction with convection. In this section we give a more realistic description of the statistical properties of the oscillation signal in Fourier space.

The observed brightness variations of a star are presumed to be given by the function $I(t)$ recorded over a large observation time interval of length T, at a sufficiently high cadence (say less than 1 min). Since pulsations are forced by turbulence, the signal is a random sample drawn from some probability distribution. Neglecting edge effects introduced by the time window, we assume that $I(t)$ is a stationary process. We denote by $I(\omega_j)$ the FFT of $I(t)$ sampled at the angular frequency $\omega_j = 2\pi j/T$. A random variable is fully specified by its expectation value, E, and higher-order moments (in the sense of ensemble averages). Here, $I(\omega_j)$ is complex with zero mean, $\mathrm{E}[I(\omega_j)] = 0$, and stationarity implies that frequency bins are uncorrelated:

$$\mathrm{E}[I^*(\omega_j) \, I(\omega_{j'})] = 0 \quad \text{for } j \neq j' \,. \qquad (4.18)$$

Foglizzo et al. (1998) showed that low-degree modes are essentially uncorrelated. This is a consequence of the fact that there is a very large number of excitation events per damping time. The central limit theorem ensures that mode amplitudes converge to independent Gaussian distributions. The signal $I(\omega_i)$ can thus be modeled by a sum of independent complex Gaussian random variables:

$$I(\omega_j) = \sum_{m} \sigma_m(\omega_j) \, \mathcal{N}_{m,j} + \sigma^{\mathrm{n}} \mathcal{N}_j^{\mathrm{n}} \,. \qquad (4.19)$$

The symbol $\mathcal{N}$ denotes a complex Gaussian random variable with zero mean and unit variance, $\mathrm{E}[\mathcal{N}^*\mathcal{N}] = 1$. The standard deviation of a mode amplitude, denoted

by the function $\sigma_m(\omega)$, is large for ω near the resonant frequency $\omega_{nl} + m\Omega$ (see below). The distributions $\mathcal{N}_{m,j}$ are all independent of each other. The additional term $\sigma^n \mathcal{N}_j^n$ denotes uncorrelated Gaussian noise with standard deviation σ^n. The origin of this noise is both stellar (convection) and instrumental (e.g. photon noise). For simplicity, the noise level, σ^n, is assumed to be frequency independent over a small frequency interval around ω_{nl}.

In order to obtain $\sigma_m(\omega)$ one should in principle solve the inhomogeneous wave equations once a model for wave damping and excitation has been specified. Here, however, we parametrize the variance σ_m^2 in the form

$$\sigma_m^2(\omega) = S \; \mathcal{E}_{lm}(i) \; L_{nl}(\omega - m\Omega) \,. \tag{4.20}$$

The constant S gives the overall amplitude of the power, and the weights $\mathcal{E}_{lm}(i)$ give the m-dependent visibility as a function of inclination angle i (cf. § 4.1.2). The line shape, $L_{nl}(\omega)$, is a real positive function which becomes large for ω near the resonant frequency ω_{nl}. We choose the standard Lorentzian line profile (e.g. Anderson et al., 1990) appropriate for describing an exponentially damped oscillator:

$$L_{nl}(\omega) = \left[1 + \left(\frac{\omega - \omega_{nl}}{\Gamma/2} \right)^2 \right]^{-1} \,, \tag{4.21}$$

where the damping rate Γ represents the full width at half maximum of $L_{nl}(\omega)$. Notice that equation (4.21) only gives the positive-frequency part of the spectrum; the negative-frequency part does not contain extra information and can be deduced from the relation $I(-\omega) = I^*(\omega)$.

Since the sum of independent Gaussian random variables is a Gaussian variable, the Fourier spectrum (Eq. [4.19]) at frequency ω_j can be written in terms of a single complex normal distribution, $\mathcal{N}_j$:

$$I(\omega_j) = \left[S \sum_m \mathcal{E}_{lm}(i) \; L_{nl}(\omega_j - m\Omega) + N \right]^{1/2} \mathcal{N}_j \,. \tag{4.22}$$

We introduced the notation $N = (\sigma^n)^2$. The traditional method to generate a complex Gaussian distribution is called the Box-Muller method. Given a uniform

distribution on $[0, 1]$, U_j, and a uniform distribution on $[0, 2\pi]$, Θ_j, the random variable

$$\mathcal{N}_j \;\; = \;\; \sqrt{-\ln U_j} \; e^{i\Theta_j} \tag{4.23}$$

is complex Gaussian with independent real and imaginary parts and unit variance. From equations (4.22) and (4.23), we see that a realization of the power spectrum is given by

$$P(\omega_j) = |I(\omega_j)|^2 = -\ln(U_j) \; \mathcal{P}(\omega_j) \,, \tag{4.24}$$

where $\mathcal{P}$ is the expectation value of the power spectrum,

$$\mathcal{P}(\omega_j) = S \sum_m \mathcal{E}_{lm}(i) \; L_{nl}(\omega_j - m\Omega) + N \,. \tag{4.25}$$

We now have an expression for generating realizations of a stellar oscillation power spectrum. Because $L_{nl}(\omega_{nl}) = 1$, it makes sense to refer to S/N as the signal-to-noise ratio in the power spectrum. Since $-\ln(U_j)$ is an exponential distribution with unit mean and variance, the probability density function of the random variable $P(\omega_j)$ is given by

$$f(P_j) = \frac{1}{\mathcal{P}(\omega_j)} \exp\left(-\frac{P_j}{\mathcal{P}(\omega_j)}\right) \,, \tag{4.26}$$

where $f(P_j)$ describes the probability that $P(\omega_j)$ takes a particular value P_j (Woodard, 1984; Duvall & Harvey, 1986).

Figure 4.2 shows plots of the expectation value of the power spectrum, $\mathcal{P}(\omega)$, for various values of the inclination angle i. The left panels in Figure 4.2 are for dipole multiplets $l = 1$, and the right panels for quadrupole multiplets $l = 2$. In these plots the parameters are $\Gamma = \Gamma_\odot$ and $\Omega = 6\Omega_\odot$, where $\Gamma_\odot/2\pi = 1 \; \mu$Hz and $\Omega_\odot/2\pi = 0.5 \; \mu$Hz are characteristic solar values for the line width and the angular velocity. For noiseless data, the dependence of the power at different frequencies on i is clearly evident, and it is possible to distinguish between different i values relatively easily.

To illustrate the effect of stochastic excitation, Figure 4.3 shows two realizations, $P(\omega)$, of an $l = 2$ power spectrum for $i = 30°$ and $i = 80°$, together with the expectation values denoted by the thick curves. A solar-like background noise was

prescribed ($S/N = 100$). Although realization noise is important, the two spectra can be distinguished from each other.

In the previous section, we described a simple statistical model for the stellar oscillation power spectrum. This model depends on a minimal set of physical parameters (ω_{nl}, Γ, Ω, i) and the overall signal and noise levels (S,N). In this section, we describe an algorithm which allows to estimate these parameters from a realization of the power spectrum. We use the maximum likelihood method which is commonly used in helioseismology (e.g. Anderson et al., 1990; Schou, 1992; Toutain & Appourchaux, 1994; Appourchaux et al., 1998, 2000).

We consider a section of the spectrum that includes the $2l + 1$ peaks of a given multiplet (l, n). The spherical harmonic degree l is either 1 or 2. We denote by $\boldsymbol{\lambda}$ the set of parameters that we want to estimate:

$$\boldsymbol{\lambda} = \{i, \Omega, \omega_{nl}, \Gamma, S, N\} \, . \tag{4.27}$$

Maximum likelihood estimators involve specifying the joint probability density function for the sample data $\{P_j\}$. For a given frequency ω_j, the probability that the power takes the particular value P_j is given by the probability density function, $f(P_j)$ (see Eq. 4.26). We write $f(P_j|\boldsymbol{\lambda})$ to indicate the dependence on the parameters $\boldsymbol{\lambda}$. Because frequency bins are independent, the joint probability density function is simply the product of $f(P_j|\boldsymbol{\lambda})$ for the index j spanning the frequency interval of interest. The likelihood function $F(\boldsymbol{\lambda})$ is another name for the joint probability function evaluated at the sample data

$$F(\boldsymbol{\lambda}) = \prod_j f(P_j|\boldsymbol{\lambda}) \, . \tag{4.28}$$

The basic idea of maximum likelihood estimation is to choose estimates $\boldsymbol{\lambda}^{\star}$ so as to maximize the likelihood function. In practice, one minimizes

$$\mathcal{L}(\boldsymbol{\lambda}) = -\ln F(\boldsymbol{\lambda}) \, . \tag{4.29}$$

This gives the same result since the logarithm is a monotonic increasing function. The probability of observing the sample values is greatest if the unknown parameters
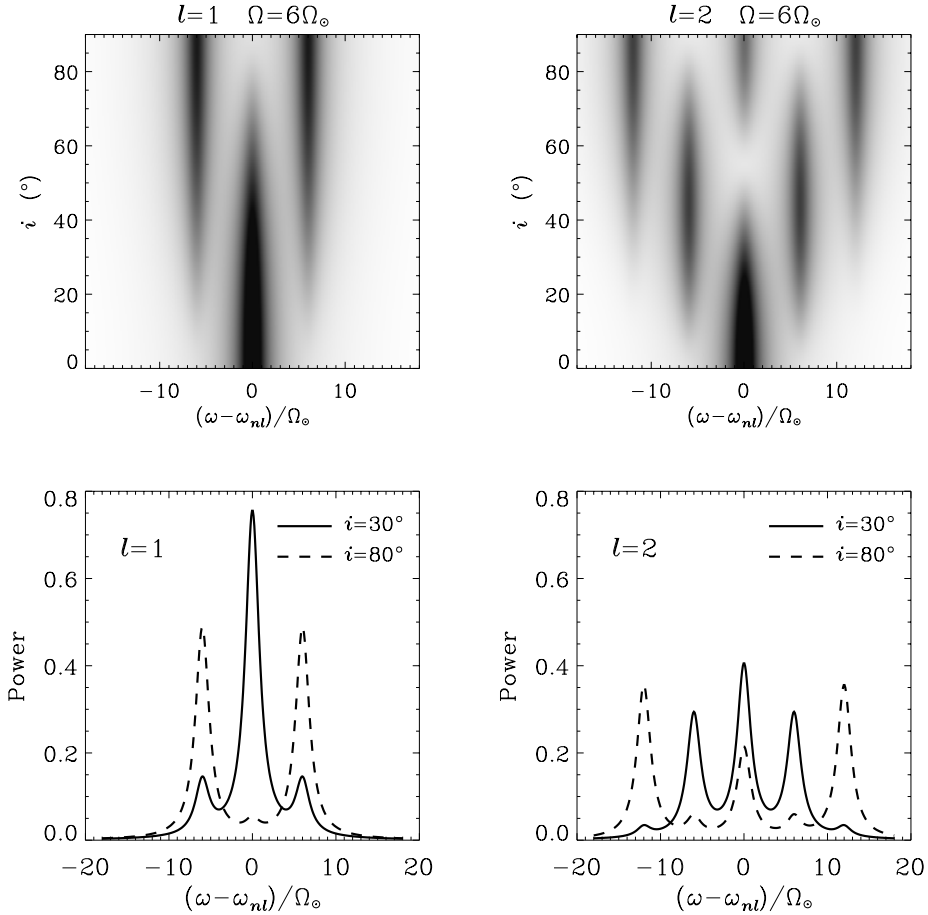
Figure 4.2: Expectation value of the power spectrum, $\mathcal{P}(\omega)$, for dipole and quadrupole multiplets as a function of the inclination angle i. The left panels are for dipole multiplets, $l = 1$, and the right panels are for quadrupole multiplets, $l = 2$. The parameters are $\Gamma = \Gamma_\odot$ and $\Omega = 6\Omega_\odot$, where $\Gamma_\odot/2\pi = 1$ μHz and $\Omega_\odot/2\pi = 0.5$ μHz are characteristic solar values for the line width and the angular velocity. The bottom panels show the power for the specific values $i = 30°$ (solid lines) and $i = 80°$ (dashed lines). There is no background noise in these plots.
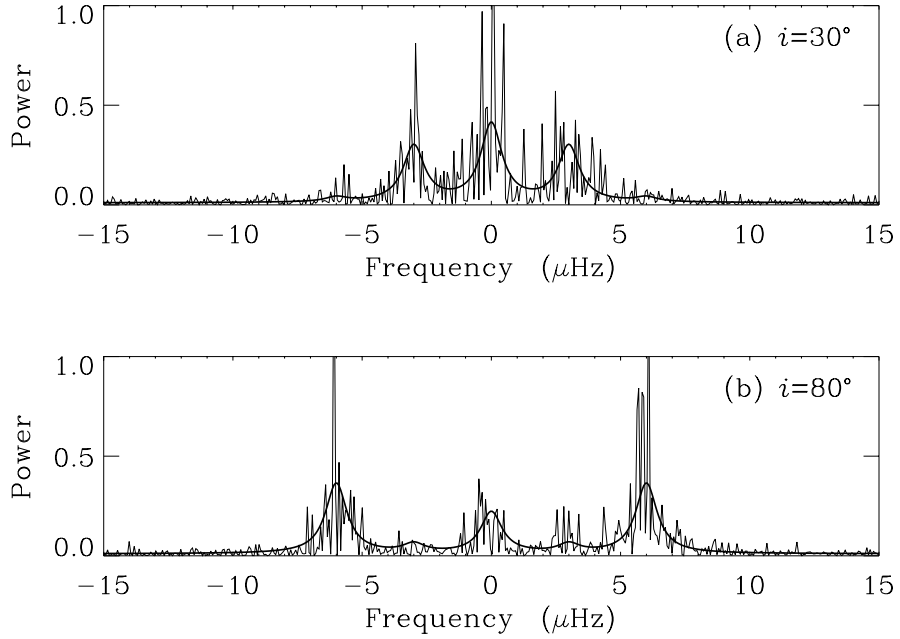
Figure 4.3: Two realizations of the power spectrum of an $l = 2$ multiplet versus centered frequency $(\omega - \omega_{nl})/2\pi$. The stellar rotation is $\Omega = 6\Omega_\odot$ and the mode line width is $\Gamma = \Gamma_\odot$. Panel (a) corresponds to an inclination angle $i = 30°$ and panel (b) is for $i = 80°$. A signal-to-noise ratio S/N=100 has been prescribed and the simulation corresponds to 6 months of uninterrupted observations. The expectation value of the power, $\mathcal{P}$, is overplotted (smooth curves).

are equal to their maximum likelihood estimates:

$$\boldsymbol{\lambda}^\star = \underset{\boldsymbol{\lambda}}{\mathrm{argmin}} \left\{ \mathcal{L}(\boldsymbol{\lambda}) \right\} . \tag{4.30}$$

We use the conjugate gradient method to find the parameters that minimize the function $\mathcal{L}$.

The method of maximum likelihood has many good properties (e.g. Kendall & Stuart, 1967; Rao, 1973). The maximum likelihood estimate $\boldsymbol{\lambda}^\star$ is not biased as the sample size tends to infinity. Moreover, for large sample size, $\boldsymbol{\lambda}^\star$ will have an approximate multi-normal distribution centered on the true parameter value $\boldsymbol{\lambda}$. Maximum likelihood estimators are also minimum variance estimators. Furthermore when the model is misspecified, $\boldsymbol{\lambda}^\star$ will still have a well-defined probability distribution and will be approximately normally distributed. In our case we have a finite sample size, since T is limited to a few months. There is no guarantee that the maximum likelihood estimator will be normally distributed or even unbiased. Note also that the distribution of $i^\star$ has to be periodic since $\mathcal{L}$ only depends on $|i| \bmod \pi$.

In order to derive the correct probability distributions of the likelihood estimates, we run Monte-Carlo simulations (e.g. Toutain & Appourchaux, 1994). The method consists of simulating a large number of realizations of a power spectrum and then fitting each realization to construct the distribution of the measured $\lambda_k^\star$. Monte-Carlo simulations enable us to determine the bias and the precision associated with the measurement of each parameter λ_k. Ideally we would want to run simulations for each relevant point in $\boldsymbol{\lambda}$-space and for varying observation times T. Because Monte-Carlo simulations are time consuming, we decide to keep Γ and S/N fixed to their solar values, varying only Ω and i. For all simulations, the observation time is $T = 6$ months.

4.1.4   Results

In Figure 4.4 we show the results for one set of Monte-Carlo simulations. Plotted are in Figures 4.4a and 4.4c the inclination angle $i^\star$, and in Figures 4.4b and 4.4d the angular velocity in solar units, $\Omega^\star/\Omega_\odot$, returned by the fit versus the inclination angle, i, that entered the computation of each realization. For this set we simulate
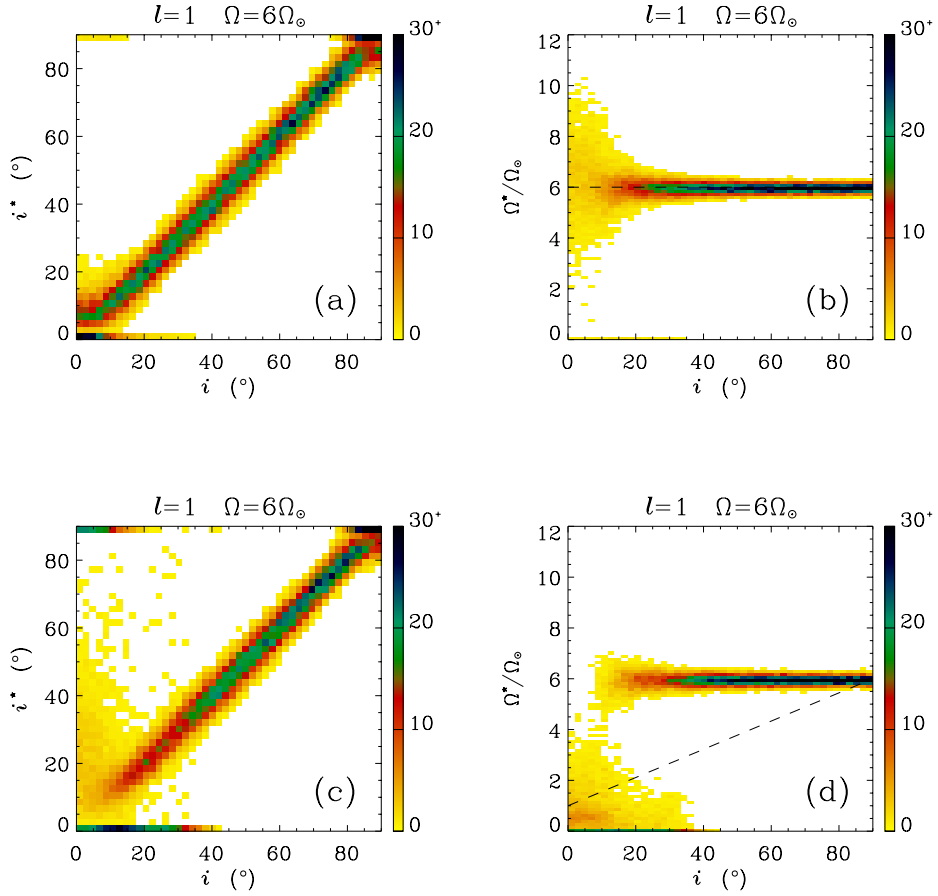
Figure 4.4: Maximum likelihood estimates $i^\star$ and $\Omega^\star$ deduced from an $l = 1$ triplet versus the true i. The true rotation frequency is $\Omega = 6\Omega_\odot$. Plotted are the results of 2000 realizations. Panels (a) and (b) differ from (c) and (d) in the initial guess for the rotation rate (indicated by the dashed lines). The scale indicates the percentage of the points falling into a bin. For (a) and (c) a bin is 2 deg. For (b) and (d) a bin is $0.12\Omega_\odot$.
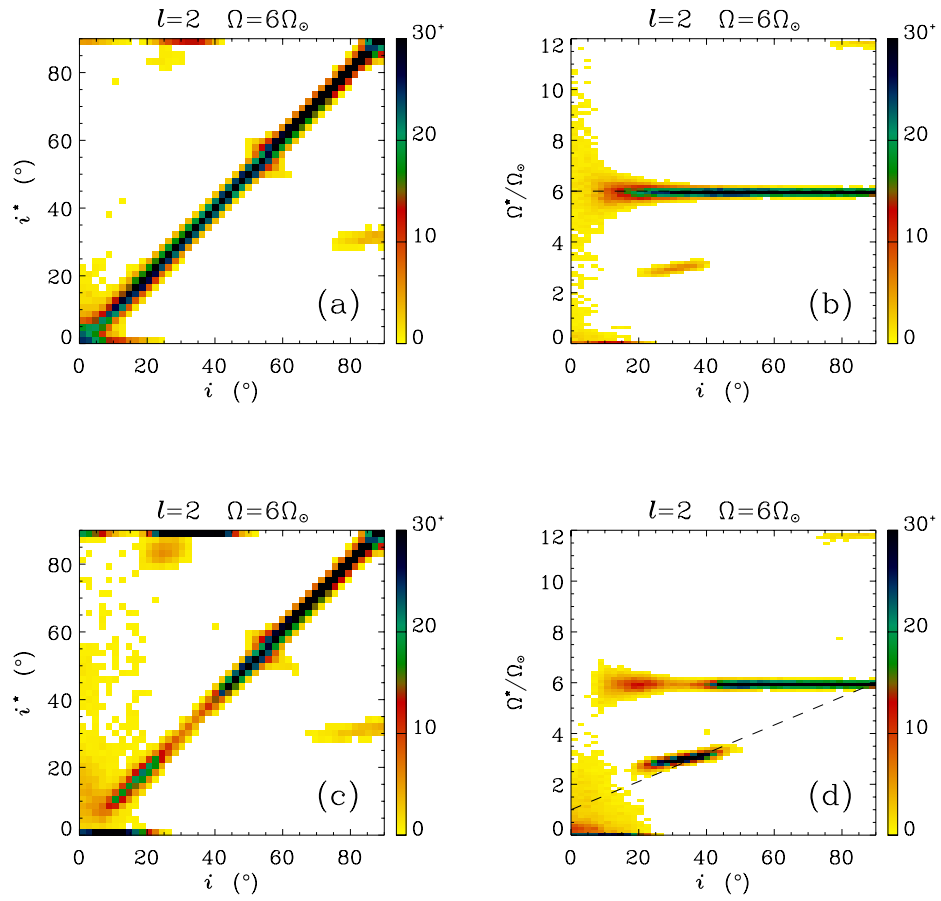
Figure 4.5: The same as Figure 4.4, but for an $l = 2$ multiplet.
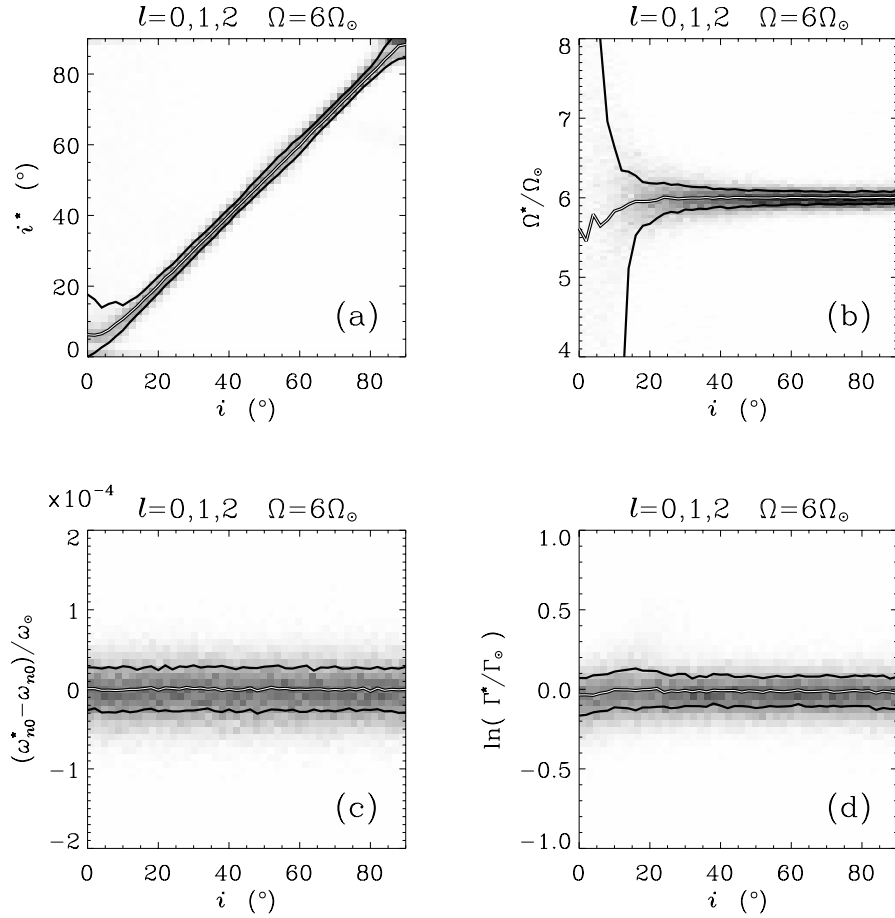
Figure 4.6: Maximum likelihood estimates obtained by fitting three multiplets $l = 0, 1, 2$ simultaneously, for $\Omega = 6\Omega_\odot$. The gray scale shows the distributions of $i^\star$, $\Omega^\star$, the full width at half maximum, $\Gamma^\star$, and the frequency of the $l = 0$ mode, $\omega^\star_{n0}$, versus i. Plotted are the results of 750 realizations. The thin double lines mark the median of the estimated parameters for each i, and 2/3 of the points fall in between the two thick lines.
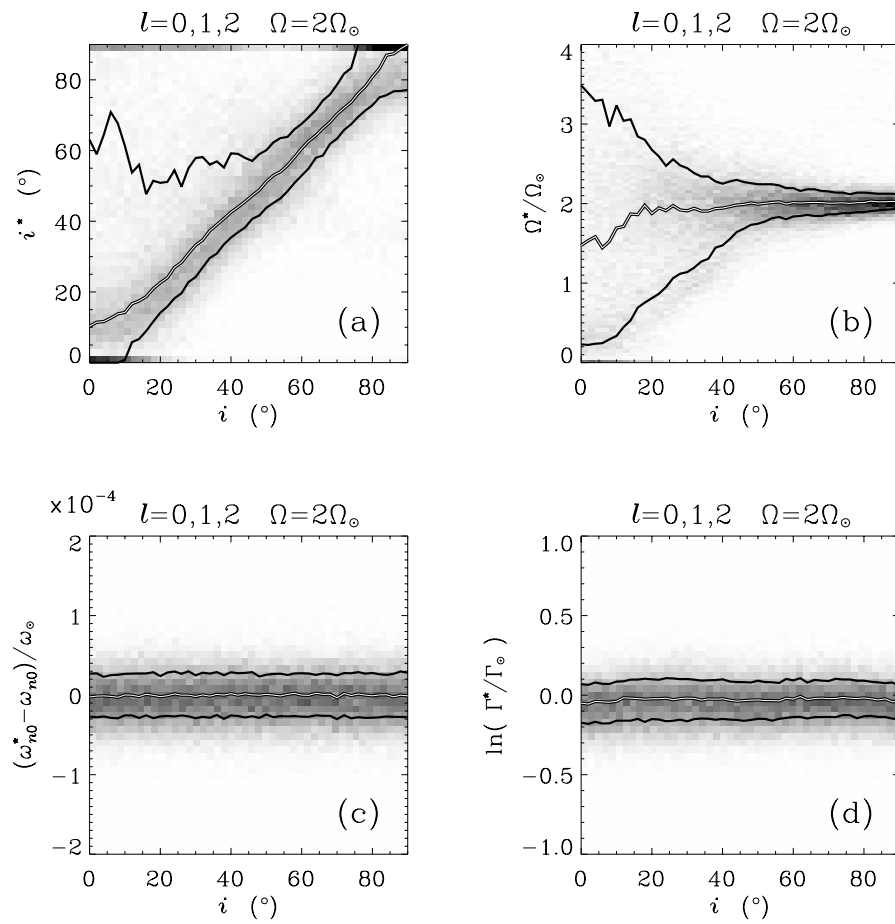
Figure 4.7: Same as Figure 4.6 but for $\Omega = 2\Omega_\odot$

a single $l = 1$ triplet and the rotation frequency is $\Omega = 6\Omega_\odot$. For each value of the inclination angle i ranging from 0 to $90°$, we computed 2000 realizations of the power spectrum. The initial guesses in $\omega_{nl}^\star$, $\Gamma^\star$, $S^\star$, and $N^\star$ for the fits to the simulated spectra are randomly distributed in some interval around the true parameter values. The random initial guess in $i^\star$ is uniformly distributed between 0 and $90°$, whatever the true inclination angle. For $\Omega^\star$, we started with two different initial guesses. The guesses are indicated by the dashed lines in Figure 4.4b (for the results shown in Figures 4.4a and 4.4b) and 4.4d (for Figures 4.4c and 4.4d). The guess for Ω shown in Figure 4.4d is not too dissimilar from an initial guess based on $v \sin i$ measurements.

We note that most $i^\star$ values returned by the fits lie within $\pm 5°$ of the true i. However, the distribution of $i^\star$ is highly non-Gaussian as i tends to either 0 or $90°$. The accuracy is lower for small i values in particular if a wrong initial guess of $\Omega^\star$ is made (Figure 4.4c). In this case the fits tend to either $i^\star = 0$ or $i^\star = 90°$ for $i \lesssim 10°$. The inaccuracies in $\Omega^\star$ are also largest for small i, and systematically too low values are returned if the initial guess is too low (Figure 4.4d).

The reason for this behavior lies in the fact that only the $m = 0$ component is visible at $i \approx 0$ (Figure 2). Hence the oscillation spectrum does not provide any means of distinguishing between a (rapidly) rotating star observed almost pole on and a non-rotating (or very slowly rotating) star with arbitrary i value. In this case the maximum likelihood fit returns the solution closer to the initial guess (compare Figures 4.4b and 4.4d).

In Figure 4.5 we plot the same as Figure 4.4, but for an $l = 2$ mode. On the whole, the results look similar. At most inclination angles the accuracy in the measurements of $i^\star$ and $\Omega^\star$ is higher than for $l = 1$. The major exception is i in the range 20-40°. The fitting procedure cannot decide between $i^\star \approx i$, $\Omega^\star \approx \Omega$ and $i^\star \approx 90°$, $\Omega^\star \approx \Omega/2$. Figure 2 again reveals the cause of this uncertainty. For $i \approx 20$-$40°$ only the $m = 0$ and $m = \pm 1$ components have significant power. The solution with $\Omega^\star \approx \Omega/2$ is achieved if the $m = \pm 1$ components are misidentified as $\Delta m = \pm 2$. This is only possible if simultaneously $i^\star \approx 90°$ is assumed (see Figure 2). Unsurprisingly, this wrong solution is more commonly obtained when the initial guess of $\Omega^\star$ is closer to $\Omega/2$ than to Ω (Figure 4.5d). For $i \gtrsim 80°$ again two

solutions are obtained, the correct one and $\Omega^\star \approx 2\Omega$ combined with $i^\star \approx 30°$. In this case the fitting procedure misidentifies the $m = \pm 2$ peaks as $m = \pm 1$ peaks.

The most reliable result is obtained by fitting dipole and quadrupole modes simultaneously. Figure 4.6 shows likelihood estimates for three multiplets $l = 0, 1, 2$ combined. The ambiguities at $i \approx$ 20-40° and $i \gtrsim 80°$ present in the fits to $l = 2$ alone are removed, while the scatter in $i^\star$ and $\Omega^\star$ is considerably smaller than for fits to $l = 1$ peaks alone. Only the ambiguity at $i \lesssim 10°$ remains. "Medians" and "error bars" are plotted in Figure 4.6. By construction 2/3 of the points lie between error bars. Because the distributions of $i^\star$ and $\Omega^\star$ are definitely not Gaussian these values are only indicative; they are not sufficient to assess the measurement precision. Also plotted in Figures 4.6c and 4.6d are the fitted frequency of the $l = 0$ mode, $\omega^\star_{n0}$, and the line width, $\Gamma^\star$, common to all the modes. The measurement accuracy of these parameters appears to be independent of the inclination angle i. Indeed rotation has no effect on the singlet $l = 0$. Including an $l = 0$ mode in the minimization procedure helps in turn to measure $\Omega^\star$ and $i^\star$ from the dipole and quadrupole modes by reducing the uncertainty on $\Gamma^\star$.

So far we have only considered rapidly rotating stars with rotational splitting considerably larger than the line width. We now turn to the case $\Omega = 2\Omega_\odot$ and repeat the analysis described above for $\Omega = 6\Omega_\odot$. The distribution of $i^\star$ and $\Omega^\star$ obtained by fitting 750 realizations to $l = 0, 1, 2$ combined is shown in Figure 4.7. As expected, the accuracy of the deduced $i^\star$ and $\Omega^\star$ values is considerably lower now than for the more rapidly rotating stars. The individual azimuthal components in a multiplet are not resolved since $\Omega = 2\Gamma$. For $i \gtrsim 45°$ the errors are found to be around $\pm 10°$ for $i^\star$ and 5-15% for $\Omega^\star/\Omega$. At smaller i values the fits tend to overestimate i and the uncertainty for both $i^\star$ and $\Omega^\star$ becomes excessively large for decreasing i, but remains unchanged for $\omega^\star_{n0}$ and $\Gamma^\star$. A comparison with Figure 4.7 reveals that the accuracy of these last two quantities is mostly independent of the rotation rate when $l = 0, 1, 2$ are fit together.

Although extremely useful, Monte-Carlo simulations require long computations. A less reliable but straightforward method to obtain a formal error, σ_k, on the maximum likelihood estimate $\lambda^\star_k$ is to expand $\mathcal{L}$ about the true parameter value λ_k. As mentioned earlier, in the limit of infinite sample size, $\boldsymbol{\lambda}^\star$ tends to a multi-normal

probability distribution which is asymptotically unbiased,

$$\text{E}[\lambda_k^\star] = \lambda_k \,, \tag{4.31}$$

and has minimum variance. An estimate of σ_k is

$$\sigma_k^2 = 1/C_{kk} \,, \tag{4.32}$$

where C_{kk} is the k-th element on the diagonal of the inverse, $\mathbf{C} = \mathbf{H}^{-1}$, of the Hessian matrix given by

$$H_{kk'} = \text{E}\left[\frac{\partial^2 \mathcal{L}}{\partial \lambda_k \partial \lambda_{k'}}(\boldsymbol{\lambda})\right] \,. \tag{4.33}$$

The formal error σ_k, called the Cramer-Rao lower bound, is a lower limit on the error bar associated with the measurement of λ_k (e.g. Kendall & Stuart, 1967). Toutain & Appourchaux (1994) showed that these error bars are useful estimates in helioseismology.

Figure 4.8 shows the errors $\sigma_{\sin i}$ and σ_Ω derived from equation (4.32) for a single $l = 1$ mode, plotted as a function of $\sin i$ and $\Omega/\Omega_\odot$. This calculation is easier to carry out when $\sin i$ is chosen as an independent parameter instead of i. A comparison with Figures 4.6 and 4.7 reveals that the error bars obtained by inverting the Hessian have the correct magnitude. By construction they are symmetric about the true parameter values and they cannot describe the asymmetric distribution of $i^\star$ displayed by the Monte Carlo simulations (Figure 4.7). Of particular interest is the dependence of the error bars on Ω. Figure 4.8 suggests that it is extremely difficult to determine either i or Ω for a star with the solar rotation rate when a single mode $l = 1$ is taken into consideration.

We have also determined error bars from Monte-Carlo simulations for stellar rotation frequencies in the range $1 < \Omega/\Omega_\odot < 10$, although restricted to only $i = 30°$ and $80°$. Medians and error bars are plotted in Figure 4.9 for a simultaneous fit to three multiplets, $l = 0, 1, 2$. This figure shows that it is realistic to apply asteroseismic techniques for $\Omega \gtrsim 2\Omega_\odot$, with the results being more reliable for $i = 80°$ than $i = 30°$. When azimuthal modes are fully resolved (say $\Omega > 3\Omega_\odot$), error bars are fairly independent of the rotation rate. Note that for $i = 30°$ and
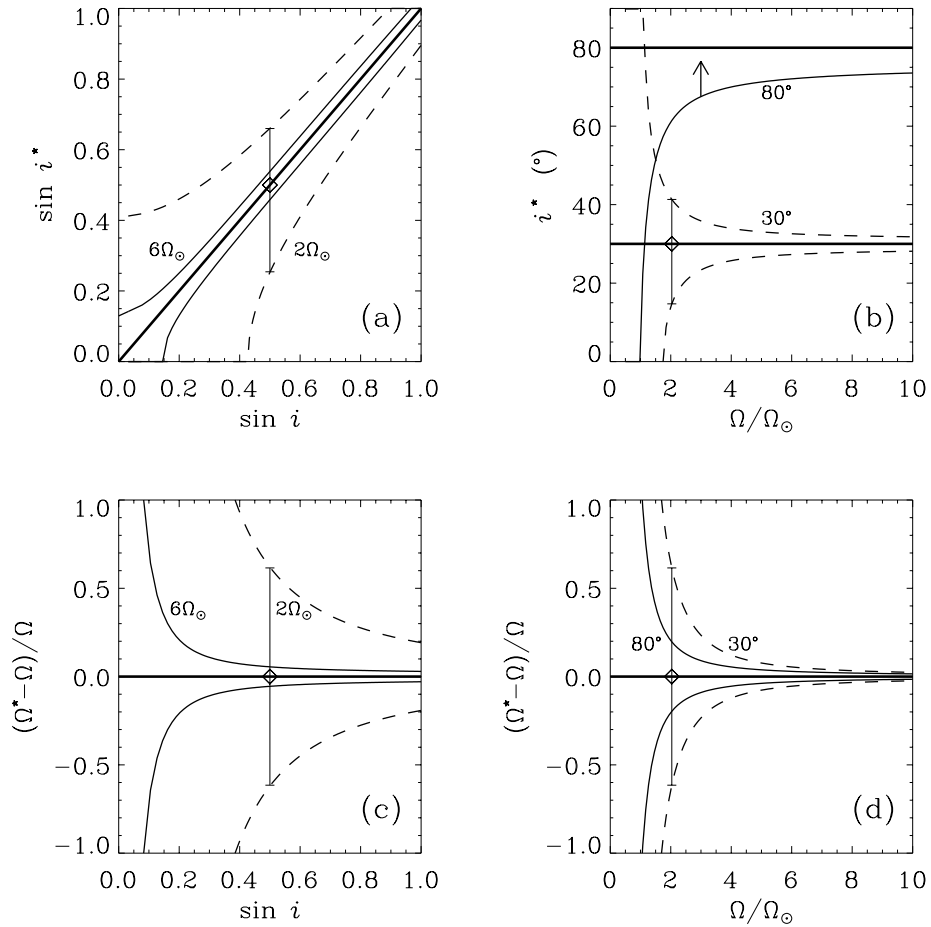
Figure 4.8: Formal error bars obtained by inverting the Hessian for an $l = 1$ multiplet. In panels (a) and (c) the error bars on $i^\star$ and $\Omega^\star$ versus $\sin i$ are given for two rotation rates, $\Omega = 2\Omega_\odot$ (dashed curves) and $\Omega = 6\Omega_\odot$ (solid). In panels (b) and (d) error bars for $i = 30°$ (dashed) and $i = 80°$ (solid) are plotted versus $\Omega/\Omega_\odot$. A sample error bar for $\Omega = 2\Omega_\odot$ and $i = 30°$ is explicitly plotted. Other parameters are $\Gamma = \Gamma_\odot$, $S/N = 100$, and $T = 6$ months.
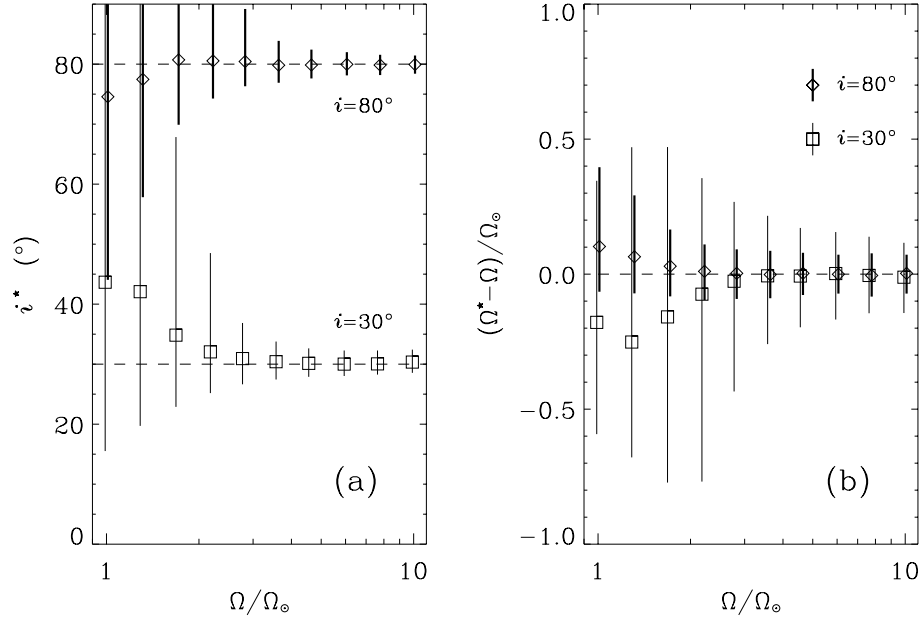
Figure 4.9: Median and error bars for maximum likelihood estimates $i^\star$ and $(\Omega^\star - \Omega)/\Omega_\odot$ deduced from Monte Carlo simulations as a function of rotation rate. Results are shown for two input inclinations, $i = 30°$ (squares and thin error bars) and $i = 80°$ (diamonds and thick error bars). Three multiplets $l = 0, 1, 2$ are fit together. $\Gamma = \Gamma_\odot$, $S/N = 100$, and $T = 6$ months.

$\Omega < 2\Omega_\odot$, the error bars on Ω (Figure 4.9b) appear to be decreasing for decreasing Ω. This is an artifact: we simply do not have enough realizations to describe the broad distribution of $\Omega^\star$ in this range. Also, likelihood estimates $i^\star$ and $\Omega^\star$ appear to be biased when $\Omega \lesssim 2\Omega_\odot$. This is likely to be due to our definition of the median (we do not take into account the periodic nature of the distributions).

4.2   Stellar Asphericity

4.2.1   Introduction

Magnetic activity affects the structure of the Sun. These changes are reflected in the observed shifts of the eigenfrequencies of the global modes of solar oscillations (Woodard & Noyes, 1985). Mode frequencies increase with magnetic activity: over the period of the 11-year solar cycle, low-degree modes show fractional frequency shifts of the order of 10^{-4}. Acoustic wave propagation may be affected directly by the magnetic field and/or indirectly through thermal and density changes. The study of high-degree modes has revealed that frequency shifts are caused by structural perturbations confined to the near solar surface and localized in latitude (Libbrecht & Woodard, 1990). The latitudinal dependence can be inferred from the observation that modes with different azimuthal orders, m, are shifted by different amounts. Sound-speed asphericity inversions of high-precision helioseismic data show latitudinal variations that match the butterfly diagram (Antia et al., 2001).

Thanks to Doppler imaging (e.g. Rice, 2002) the spatial distribution of starspots on a rapidly rotating star can be recovered from a series of high-resolution spectral line profiles. Many stars are found to exhibit large polar cap features. Theoretical work by Schüssler & Solanki (1992) indicates that magnetic flux should emerge at high latitudes for fast rotators. However, axisymmetric features such as polar spots do not introduce wavelength variability in the line profiles. For this reason, doubts have been raised about their reality.

Can we learn about the surface distribution of magnetic activity on a star other than the Sun by studying the frequencies of its global modes of oscillation? For distant stars, only modes with spherical harmonic degrees $l \leq 3$ can be observed. As a result wave-speed asphericity inversions will have poor resolution in latitude. In this section we ask whether it might be possible to discriminate between two simple activity configurations: an equatorial band and a polar cap. Asteroseismology will heavily rely on the long and continuous observations provided by the future European space missions COROT and Eddington.

4.2.2 Asphericities

We consider a rotating Sun-like star subject to near-surface structural perturbations introduced by magnetic activity. For perturbations that are steady in an inertial frame, the frequencies of oscillations may be written as

$$\omega_{nlm} = \omega_{nl} + \delta\omega_{nlm}^{(\text{rot})} + \delta\omega_{nlm}^{(\text{AR})} \; . \tag{4.34}$$

Here the central frequency ω_{nl} includes all spherically symmetric distortions. The rotation-induced frequency splitting is denoted by $\delta\omega_{nlm}^{(\text{rot})}$, and the frequency perturbation due to near-surface magnetic activity is $\delta\omega_{nlm}^{(\text{AR})}$. The activity perturbations have to be azimuthally symmetric with respect to the rotation axis.

In the case of a rigidly rotating star with angular velocity Ω, and up to a second order of approximation, the m-dependent rotational frequency perturbation is approximated by (Dziembowski & Goode, 1992; Kjeldsen et al., 1998):

$$\delta\omega_{nlm}^{(\text{rot})} = m(1 - C_{nl})\Omega + \frac{\Omega^2 R^3}{\mathcal{G}M}\omega_{nl}Q_{lm} \; , \tag{4.35}$$

where R is the stellar radius, M is the stellar mass, $\mathcal{G}$ is the universal constant of gravity, and C_{nl} is the Ledoux constant whose value depends on the oscillation eigenfunctions of the non-rotating star. The second term in Eq. (4.35) describes the P_2-distortion of the stellar surface due to centrifugal forces, with Q_{lm} given by (Kjeldsen et al., 1998):

$$Q_{lm} \simeq \frac{2/3 \int_{-1}^{1} P_2(x)[P_l^m(x)]^2 \; \mathrm{d}x}{\int_{-1}^{1}[P_l^m(x)]^2 \; \mathrm{d}x} \; . \tag{4.36}$$

The P_l^m are associated Legendre functions and P_2 is a second-order Legendre polynomial.

There is no definitive theory for estimating the frequency shifts introduced by near-surface magnetic activity. Here, we separate the physics from the geometry, and parameterize the frequency perturbation in the form

$$\delta\omega_{nlm}^{(\text{AR})} \simeq \omega_{nl}\,\epsilon_{nl}\,G_{lm} \; . \tag{4.37}$$

In this expression, ϵ_{nl} gives the overall (unspecified) amplitude of the fractional frequency shifts. In the Sun, $\epsilon \simeq 10^{-4}$. The m-dependent coefficient G_{lm} is a geometrical weight factor that depends on the latitudinal distribution of surface activity:

$$G_{lm} = \int_{\mathrm{AR}} |Y_l^m(\theta, \phi)|^2 \, \sin\theta \, \mathrm{d}\theta \, \mathrm{d}\phi \, , \tag{4.38}$$

where AR refers to the axisymmetric area covered by magnetic "active regions". The Y_l^m are normalized spherical harmonics, and θ and ϕ are spherical-polar coordinates defined in the inertial frame with polar axis pointing in the direction of the rotation axis.

For a given multiplet (l, n), the mode frequencies ω_{nlm} can be expressed in terms of a unique set of $2l + 1$ so-called a-coefficients:

$$\omega_{nlm} = \sum_{j=1}^{2l+1} a_j(n, l) \, \mathcal{P}_j^{(l)}(m) \, , \tag{4.39}$$

where the polynomials $\mathcal{P}_j^{(l)}(m)$ form an orthogonal set. The standard polynomials used in this expansion are describe by Schou et al. (1994). For quadrupole multiplets, the expansion up to a_2 is:

$$\omega_{n2m} = \omega_{n2} + m \, a_1(n, 2) + (m^2 - 2) \, a_2(n, 2) + \cdots \tag{4.40}$$

The coefficient a_1 relates to the first-order effect of rotation, with $a_1 \simeq \Omega$ in the case of rigid-body rotation. The coefficient a_2 is a measure of asphericity and includes magnetic and second-order rotational effects. Rotational oblateness implies $a_2 < 0$. Because wave-speed is increased in active regions, an equatorial band of activity would tend to reduce the effective oblateness, i.e. to increase a_2. Polar activity, on the other hand, decreases the value of a_2. In the Sun, activity migrates equatorward as the cycle develops and the coefficient a_2 is about 35 nHz higher at solar maximum than at minimum (Appourchaux, 2002).
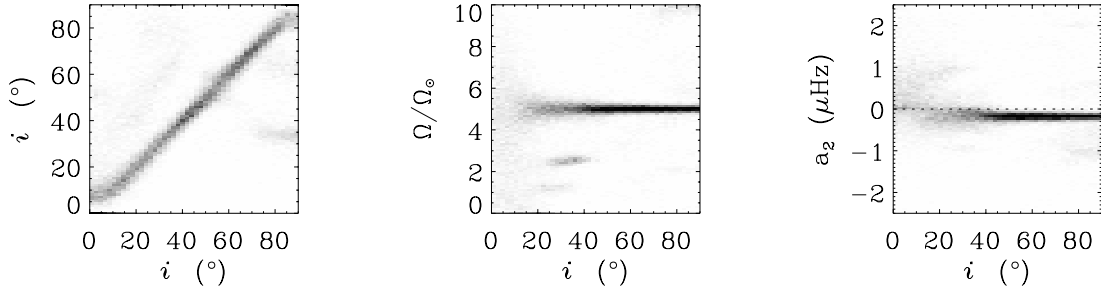
Figure 4.10: Maximum likelihood estimates of i, Ω and a_2 deduced from an $l = 2$ multiplet versus the true inclination angle. The star is solar-like with angular velocity $\Omega = 5\Omega_\odot$. The negative value of a_2 is entirely due to rotational oblateness (no magnetic perturbation was introduced). Observation time $T = 6$ months.

4.2.3 Equatorial Band vs. Polar Cap

The precision of the measurement of the asphericity parameter a_2 depends on the input stellar parameters and is limited by realization noise (stellar pulsations are forced by turbulence). Like before we simulate a large number of realizations of an oscillation power spectrum for a given stellar configuration, then extract oscillation parameters using a maximum likelihood technique, and derive the distribution of the measured values of a_2.

For this preliminary study we consider a solar-like star with solar mass and radius and uniform angular velocity $\Omega = 5\Omega_\odot$, where $\Omega_\odot = 0.5~\mu$Hz. Mode visibility is a function of the inclination angle, i, between the line of sight and the stellar rotation axis. Ignoring activity-related changes in the mode eigenfunctions, the observed power in individual m-components is given by:

$$\mathcal{E}_{lm}(i) = \frac{(l - |m|)!}{(l + |m|)!} \left[P_l^m(\cos i)\right]^2 ~. \tag{4.41}$$

Each mode is assumed to have a Lorentz profile with full width at half maximum $\Gamma = 1~\mu$Hz, and the signal-to-noise ratio in the power spectrum is $S/N = 20$, i.e. one fifth of the solar value. The observation time interval is $T = 6$ months. As mentioned earlier we restrict our attention to two basic configurations: a polar cap $45° < \lambda < 90°$ and an equatorial band $-8.4° < \lambda < 8.4°$, where $\lambda = \pi/2 - \theta$ is the latitude. Activity covers the same area in both cases. The amplitude of the magnetic perturbation, ϵ, remains a variable parameter with values up to 10^{-3}. For
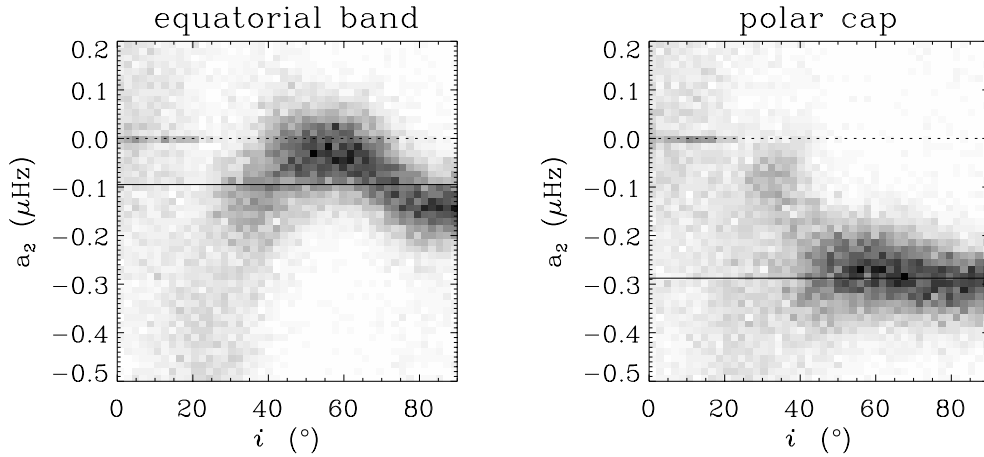
Figure 4.11: Maximum likelihood estimates of the asphericity parameter a_2 versus inclination angle for an $l = 2$ multiplet. In the left panel, activity is restricted to an equatorial band, and in the right panel to a polar cap. The activity-related fractional frequency shift is $\epsilon = 5 \times 10^{-4}$. Solid lines refer to the true a_2.

each inclination angle, we simulate 1000 realizations of the power spectrum for a single $l = 2$ multiplet.

Using a maximum likelihood technique (e.g. Toutain & Appourchaux (1994)), we fit a parametric model to each simulated power spectrum, which depends on ω_{n2}, Ω, a_2, Γ, i and the overall signal and noise levels. Figure 4.10 shows, for $\epsilon = 0$, the distributions of the estimates of i, Ω, and a_2 returned by the fit, as a function of the true inclination angle i. The fit works reasonably well for $i > 40°$. For $i < 20°$ rotation cannot be inferred with sufficient precision. In the range $20° < i < 40°$, the $m = \pm 1$ modes are sometimes misidentified as $m = \pm 2$ modes. Rotational oblateness can be retrieved for $i > 40°$.

Figure 4.11 shows the values of a_2 returned by the fit when the activity perturbation is switched on. For $\epsilon = 5 \times 10^{-4}$ and $i > 40°$, it is possible to distinguish a polar cap of activity from an equatorial band of activity. Note that the estimate of a_2 may be significantly biased. There are two reasons for this bias: (1) all 5 modes are not visible simultaneously and (2) the model of the power spectrum is misspecified (we do not fit for a_4). Figure 4.12 shows that for $i = 60°$ the parameter a_2 can be measured from a single $l = 2$ multiplet with a precision of ± 50 nHz. The distinction between the two configurations can only be made if $\epsilon > 5 \times 10^{-4}$.
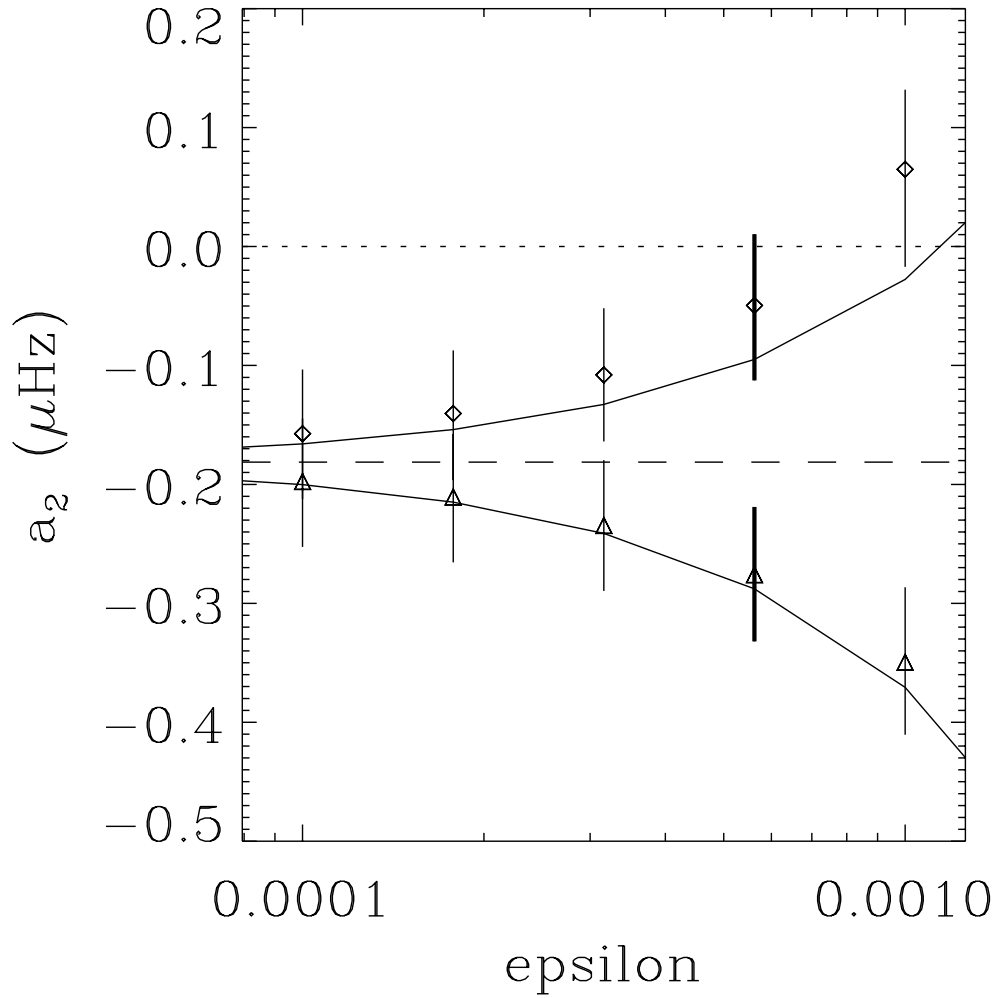
Figure 4.12: Mean and standard deviation of measured a_2 versus ϵ at inclination angle $i = 60°$ and for $l = 2$. Equatorial band of activity (diamonds) and polar cap (triangles). Solid lines refer to the true a_2. The dashed line is the rotational oblateness value ($\epsilon = 0$).

We have seen that stellar oscillations may contain measurable information about the latitudinal distribution of stellar activity. Stellar rotation must be large enough (individual m-components must be resolved), stellar activity must be strong enough (say $\epsilon > 5\epsilon_\odot$), and the inclination angle of the star must be large enough (say $i > 40°$).

Both rotational oblateness and aspherical magnetic perturbations contribute to the value of the parameter a_2. In order to detect the asphericity due to activity alone, it is necessary to remove the oblateness due to rotation. To do so, one must estimate $\Omega^2 R^3/\mathcal{G}M$. Hopefully, Ω can be measured from the frequency splittings and the mean stellar density M/R^3 can be deduced from the large frequency separation $\omega_{nl} - \omega_{n-1,l} \propto \sqrt{R^3/M}$ (Brown & Gilliland, 1994).

The present study is however not appropriate for a long-lived patch of activity that would be localized in longitude, because such a perturbation is unsteady in the inertial frame of the observer. The signature of an unsteady magnetic perturbation in oscillation power spectra is rather complicated. An example for the Sun is provided by Gizon (1998) who studied the perturbation arising from the presence of a large rotating "sunspot". In this case the power spectrum of a given multiplet (l,n) displays $(l+1)(2l+1)$ peaks, most of which cannot be resolved.

Chapter 5

Concluding Remarks

5.1 Solar Near-Surface Flows

Supergranulation has wavelike properties. The spectrum of the horizontal divergence of the supergranular flows is consistent with a spectrum of traveling waves with a dispersion relation $\nu \simeq 1.65(l/100)^{0.45}$ μHz. The distribution of wave power is anisotropic with increased power in the direction of rotation and toward the equator, explaining the anomalous motion of the pattern measured by correlation tracking (e.g. super-rotation, see Fig 5.1). The spectrum of supergranulation is Doppler shifted by flows and can be used as a diagnostic tool to probe rotation and meridional circulation in the upper layers of the convection zone. We have shown that the rotation of the plasma through which the pattern propagates is consistent with the rotation of the magnetic network. It is important to note that the main conclusions presented here (Gizon et al., 2003) have recently been confirmed by Schou (2003) with direct Doppler data. Realistic numerical modeling is required to understand supergranulation. Unfortunately the solar convection zone is so highly turbulent and stratified that modeling of the supergranular scales has remained elusive — the most promising calculations are due to DeRosa (2001) and Rieutord et al. (2001).
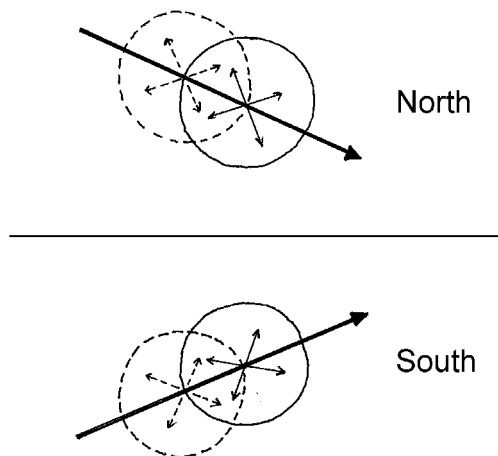

Figure 5.1: Propagation of the supergranules with respect to the local flow. After about 3 days the divergence pattern (solid) is anti-correlated with the initial pattern (dashed). The direction of propagation is prograde and toward the equator in both hemispheres.

Supergranular flows have a net kinetic helicity. We showed that the vertical vorticity of the supergranular flows (curl) is anti-correlated with the horizontal divergence (div) in the northern hemisphere, and that the latitudinal variation of $\langle \text{div}\,\text{curl}\rangle$ can be explained by the effect of the Coriolis force on convection (Gizon & Duvall, 2003). Parker (1955) proposed that the magnetic field can grow in a moving medium with a net kinetic helicity, $\mathcal{H}_{\text{kin}} = \langle \boldsymbol{v} \cdot \boldsymbol{\nabla} \times \boldsymbol{v}\rangle \neq 0$. Cyclonic convection is also invoked as an important mechanism for generating a large-scale poloidal field from an initial toroidal field. Although we only observe the two horizontal components of velocity, we may use a proxy for the average kinetic helicity (Rüdiger et al., 1999): $\mathcal{H}_{\text{kin}} \sim H_{\text{m}} \langle \text{div}\,\text{curl}\rangle$, where $H_{\text{m}} = -\langle \partial_z \ln|\rho v_z|\rangle^{-1}$ is the average vertical momentum scale height, expected to be positive. Hence, our measurements would suggest a negative kinetic helicity in the north for supergranulation. However, turbulence may also be driven by magnetic buoyancy (Brandenburg & Schmitt, 1998; Rüdiger et al., 2001) and it may be of interest to search for solar cycle variations in the quantity $\langle \text{div}\,\text{curl}\rangle$. Our observations give hope for a direct measurement of the kinetic helicity in the upper convection zone that would perhaps constrain models of the solar dynamo.

Local flows associated with magnetic active regions. Yoshimura (1971) suggested a long time ago that the longitudinal ordering of solar magnetic fields may be explained by the existence of large convective patterns. Earlier attempts at detecting such flows in direct Doppler data proved difficult (e.g. Scherrer et al., 1986). The observations presented in section 2.4 provide reliable evidence for extended surface flows converging toward active regions with an amplitude of 50 m/s at most (Gizon et al., 2001b, , see Fig. 5.2). The time-distance results agree with the ring analysis (Hindman et al., 2003) and are consistent with claims by Howard (1996) that plages drift toward the mean latitude of activity. Perhaps the observed flows favor the formation of active regions at particular sites on the solar surface; but these flows may also be a secondary consequence of the emergence of the magnetic flux. On a larger scale, Beck et al. (1998) and Ulrich (2001) have found evidence for long-lived giant velocity patterns, with no obvious connection to patterns of magnetic activity.
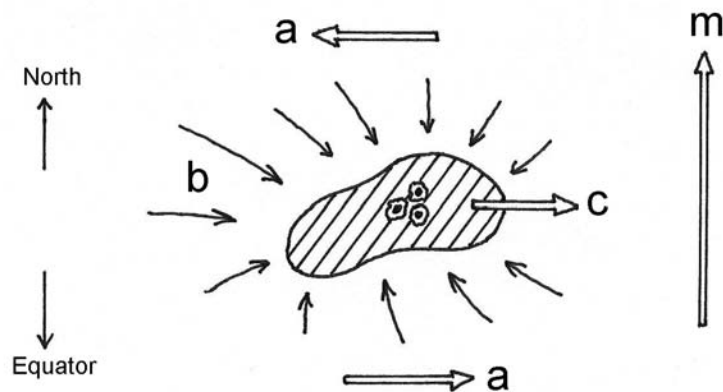
Figure 5.2: Sketch of horizontal flows around an active region, measured 1 Mm below the surface with time-distance helioseismology. (b) Active regions are surrounded by a $\sim$ 50 m/s converging flow. (a) Zonal flows switch sign near active latitudes (± 5 m/s). (m) Poleward 20 m/s meridional flow. (c) The magnetized plasma rotates a little faster than the quiet Sun.

Solar-cycle variability of the meridional circulation and differential rotation. At the surface the flows associated with complexes of magnetic activity are superimposed on the "torsional oscillations" that migrate equatorward with an eleven year period and an amplitude of the order of 5 m/s. It has been suggested that the "torsional oscillations" may be driven by the Lorentz force due to a migrating dynamo wave (Schüssler, 1981) or caused by a thermal effect due to surface magnetic fields (Spruit, 2003). We have shown that the "torsional oscillations" have both an east-west and a north-south component (Beck et al., 2002). The east-west component of the torsional oscillation shows a shear around the latitude of mean activity with the same sign at the surface and deeper in the convection zone. The p-mode travel times reveal residual flows in the meridional plane that diverge from the mean latitude of activity, tens of megameters below the surface. On the other hand, flows that converge toward the latitude of mean activity are seen near the surface. This suggests the existence of two rolls with helical streamlines of opposite handedness on each side of the latitude of mean activity. Figure 5.3 reviews the observations and displays the proposed flow geometry of the "torsional oscillations".
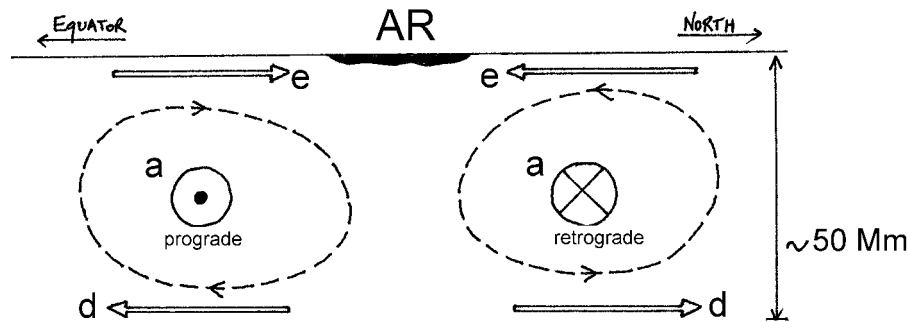
Figure 5.3: Meridional cut in the northern hemisphere showing longitudinal averages of the residual flows (with respect to smooth fits to the rotation and meridional circulation) around the mean latitude of activity (AR). (e) 5 m/s inflow near the surface (f modes). (d) Outflow as deep as 65 Mm below the surface (p modes). (a) ± 5 m/s sheared zonal flow throughout the upper convection zone. Observations are consistent with the existence of two counter-rotating meridional cells centered about the mean latitude of activity (dashed), superimposed on the 20 m/s large-scale meridional circulation.
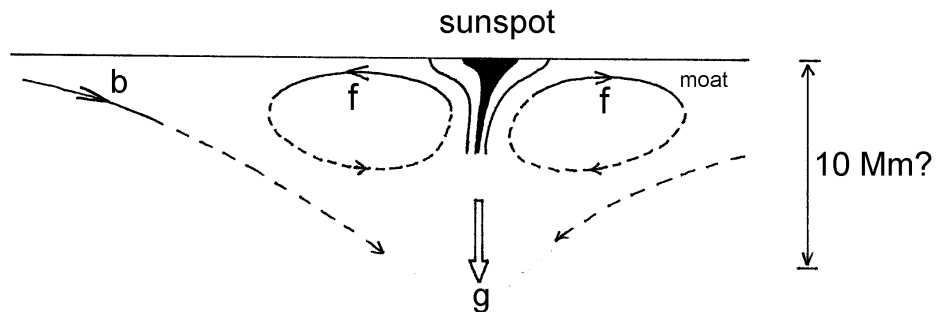
Figure 5.4: Tentative sketch of flows under sunspots. (f) Near-surface horizontal outflow with values up to 1 km/s, called the moat. The horizontal extent of the moat flow is ~ 30 Mm from the center of the sunspot. (b) Well beyond the moat is a large-scale ~ 50 m/s inflow, as shown in Fig. 5.2. (g) Under the sunspot is a ~ 1 km/s downflow (Duvall et al., 1996; Zhao et al., 2001). The dashed lines are proposed model streamlines consistent with (most) observations. The vertical scale is uncertain.

Sunspot flows. As mentioned in the introduction, Gizon et al. (2000) have studied near-surface flows around sunspots. Wave-based sensitivity kernels for horizontal flows were used in an iterative deconvolution of f-mode travel times (high-resolution MDI data). Because these results are still preliminary, we shall only mention that the horizontal outflow around a sunspot, called the moat (e.g. Solanki, 2003), was detected. This outflow was detected earlier by Lindsey et al. (1996), deeper inside the Sun. Figure 5.5 shows a map of the horizontal flows near the surface for one sunspot observed on Dec 6, 1998 (the horizontal spatial resolution is 3 Mm). The internal structure of flows under sunspots is still largely unknown. Duvall et al. (1996) and Zhao et al. (2001) have detected downflows below sunspots and Braun & Lindsey (2003) observe the moat outflow down to a depth of 3 Mm. Fig. 5.4 is an attempt to show how the flows measured with f-mode time-distance helioseismology *may* fit into a consistent picture.
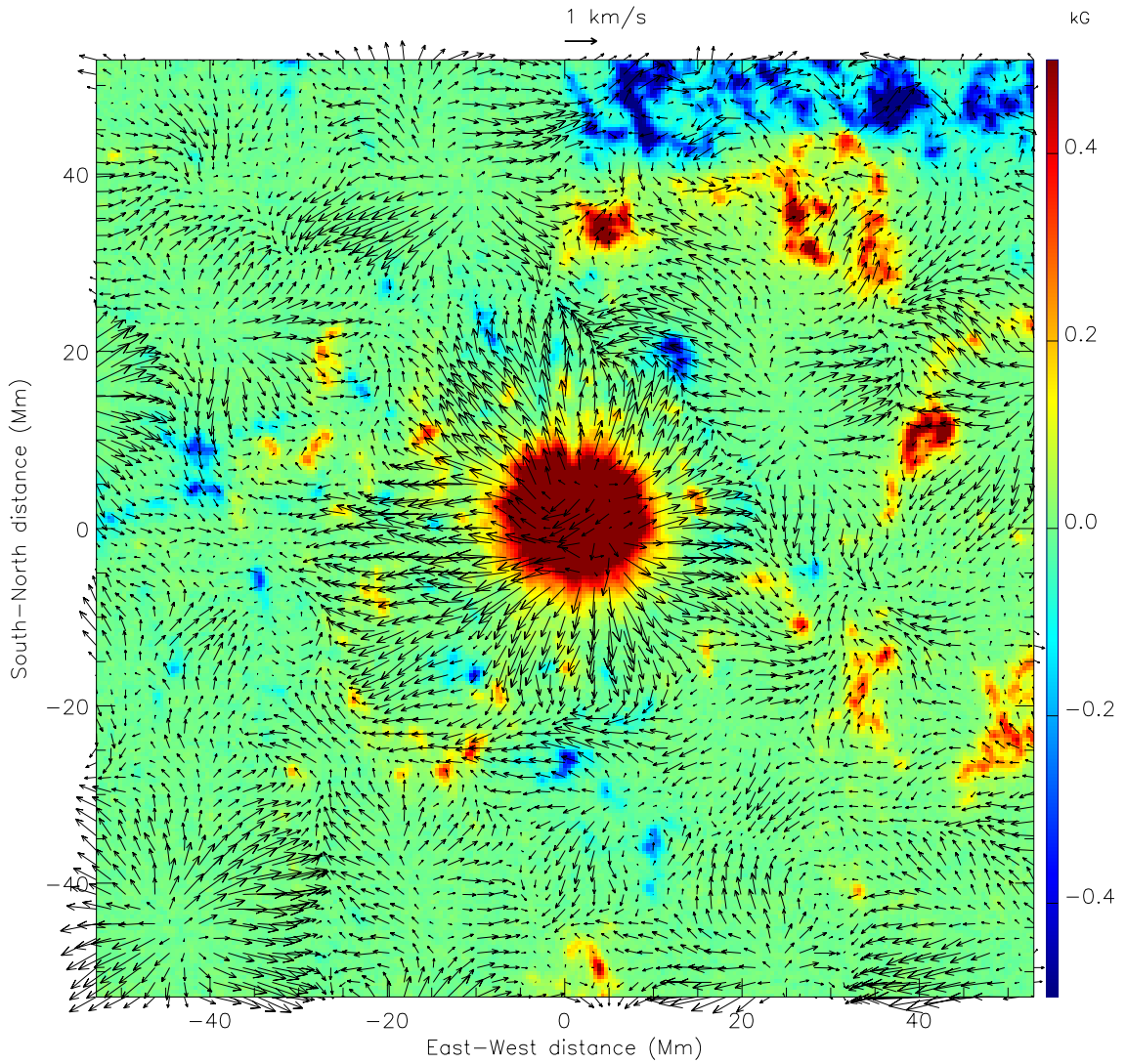
Figure 5.5: Horizontal flows around a sunspot on Dec 6, 1998, obtained with f-mode time-distance helioseismology (Gizon et al., 2000). Overplotted is the line-of-sight magnetic field (MDI high resolution) truncated at ±0.5 kG. The moat flow beyond the penumbra (red) is clearly visible.

5.2   Toward Travel-Time Sensivity Kernels

We now have a general recipe (§ 3.2) for solving the linear forward problem, i.e. computing travel-time sensitivity kernels. This recipe is based on a physical description of the observed wave field. The kernels give the linear dependence of travel-time perturbations on perturbations to a solar model and they take account of the details of the measurement procedure. The sensitivity kernels depend on the background solar model, on the filtering and fitting of the data, and on position on the solar disk (through the line of sight).

In section 3.3 we have shown how to compute the 2D sensitivity of travel-time perturbations to source and damping inhomogeneities for surface gravity waves. This example was important as it shows that kernels can be obtained, using our recipe, once the physics of the model is fully specified. In particular the source spectrum and the details of the observation procedure need to be specified at the start of the problem and appear explicitly in the expression for the travel-time kernels.

The model with random excitation sources reveals some important details in the sensitivity kernels that are not accounted for in the single source model. In particular, the single-source kernels show only ellipse shaped features, while the distributed-source kernels show both hyperbola and ellipse shaped features. Computations of kernels in the single-source picture are as difficult, both analytically and numerically, as kernels in the distributed-source picture.

The example we have presented is a simplified model for the solar f mode. Improvements to the model would include stratification, spherical geometry, compressibility, and a physical model of excitation and damping. In particular, in a compressible medium the effect of the conversion of p modes into f modes by scattering could be computed. Despite these limitations, we believe that our 2D example kernels can be useful in studying solar problems using time-distance helioseismology. The kernels may be interpreted as depth averages over the first few Mm below the photosphere of the three-dimensional solar kernels (Duvall & Gizon, 2000).

Woodard (1997) performed an analysis of the effect of localized damping on travel times for acoustic waves; this analysis showed that for a model sunspot, with radius 10 Mm, the travel-time difference is of order -1 minute, in the case where **1**

is located at the center of the sunspot and **2** is a distance 10 Mm away. For the same geometry the kernel K^γ_{diff}, which we have computed, predicts a positive travel-time difference of 1 s for a 50% increase in damping rate. These two apparently conflicting results are, however, for different types of waves and quite different models for the effect of damping inhomogeneities. The damping perturbation employed by Woodard (1997) can be understood in terms of a reduction in source strength for sources located behind the sunspot from the observation points, as scattering by the damping inhomogeneties was neglected. There remains work to be done on this subject. For example, it is known that absorption by magnetic structures is a strong function of frequency (Braun et al., 1988; Bogdan et al., 1993). This effect could be modeled by writing kernels for local changes to the exponent β in equation (3.57) for the damping rate. We plan to do a quantitative analysis of this problem in the future. Note that perturbations in sunspots are strong and that linear theory may not be accurate in this case (e.g. Cally & Bogdan, 1997)

The most significant obstacle to the computation of accurate travel-time kernels is our lack of a detailed understanding of turbulent convection. The excitation and damping of solar oscillations is due to convection and is thus extremely difficult to account for in the background model: approximations must be introduced. In chapter 3 we employed a phenomenological model based on observed properties of solar convection. An important constraint on the zero-order solar model is that it must produce a k-ω diagram compatible with observations. A further complication introduced by turbulence is that, in principle, it demands a theory for wave propagation through random media, i.e. a treatment of perturbations that vary on short temporal and spatial scales.

We have not addressed the computation of three dimensional travel time kernels in a spherical solar model. Preliminary efforts have shown that such a computation is feasible, but is demanding (Birch & Kosovichev, 2000). There are a number of less fundamental issues relating to the interpretation of travel times. We emphasize that the filter $\mathcal{F}$ includes the point spread function of the instrument, which is not always well known. It is unclear how an inaccurate estimate of the point spread function affects the interpretation of travel-time measurements. A straightforward issue is that cross-correlations are typically averaged over annuli or sectors of annuli

(Duvall et al., 1997); this can easily be accounted for by averaging the point-to-point kernels described in chapter 3.

The inverse problem, using measured travel times to learn about how the Sun differs from a model, is an entirely separate issue and beyond the scope of this thesis. We wish to note, however, that techniques for the 3D inversion of time-distance data have already been developed (Kosovichev, 1996; Jensen et al., 1998). The errors in the travel-time measurements, which are essential to solving the inverse problem, are mainly due to realization noise. The formalism presented in this thesis will be helpful in estimating these errors.

5.3 Prospects for Asteroseismology

We have shown that the inclination angle, i, of the axis of rotation of a Sun-like star can in principle be determined with great precision using the techniques of asteroseismology. The observational requirement is a long nearly-continuous time series sampled at a high cadence. The missions COROT and Eddington will provide such data for a large number of stars, with continuous observation for up to 5 and 36 months, respectively. The Danish project MONS (Kjeldsen & Bedding, 1998) aims at targeting individual stars for up to 2 months with a high duty cycle. We have found that it is difficult to estimate the inclination angle for stars with $i < 30°$, whereby this limit is lower for more rapidly rotating stars. Note however that, statistically, more than 85% of the stars have $i > 30°$.

Gough et al. (1995) applied essentially the same method to estimate the inclination angle of the Sun. Solar p modes were observed continuously in irradiance for 160 days in 1988 by the IPHIR experiment (PHOBOS mission). Gough et al. (1995) found the ratio between the power in $(l = 1, m = 0)$ modes and $(l = 1, m = \pm 1)$ modes to be less then 0.0009, i.e. $i > 89.96°$. They pointed out that at the time of the observations the mean inclination of the rotation axis of the solar surface was $i = 85°$, corresponding to an expected ratio of 0.015. Although this discrepancy could be interpreted as a depth dependence in the direction of the solar rotation axis, it is more likely that it is due to a measurement bias. Examination of Figure 4.4a reveals that the fitting procedure preferentially returns values $i^\star \approx 90°$

for inclination angles in the range $80° < i < 90°$. Besides, the hypothesis of solar rotation about a unique axis is consistent with spatially-resolved LOI data (Gizon et al., 1998). From an astronomer's point of view, it should be clear that Gough et al. (1995) were successful in measuring i with a good precision. We also note that Paunzen et al. (1998) used a somewhat similar diagnostic, i.e. the amplitude ratio of $m = \pm 1$ and $m = 0$ dipole gravity modes, to estimate the inclination of an oscillating pre-white dwarf star (although their formulas appear to be incorrect).

The precision that can be achieved on the measurement of i depends on each individual star. First of all, acoustic modes must be excited to a sufficiently high amplitude. In Sect 4.1 we fixed luminosity amplitudes at their solar value with respect to the background noise. Houdek et al. (1999) presented estimates of oscillation amplitudes in main-sequence stars derived from model calculations of stellar convection. They found that velocity amplitudes essentially scale like the mass-to-light ratio of the star, in agreement with an earlier prediction by Kjeldsen & Bedding (1995). The noise background may also vary. Here we took $S/N = 100$, but it has been shown that a useful estimate of i can be obtained when the signal-to-noise ratio is as low as $S/N = 20$ (Gizon, 2002).

Another condition for determining i is a sufficiently large stellar rotation rate, in order to resolve azimuthal modes split by rotation. This condition is met when the angular velocity of the star, Ω, is at least twice larger than the linewidth, Γ, of the modes of oscillation. Since Γ is a decreasing function of frequency, the analysis of low-frequency multiplets may be crucial in order to measure the inclination angle of slowly rotating stars. We refer the reader to the work of Houdek et al. (1999) for a study of the variation of mode damping with frequency and stellar parameters.

A single realization of the power spectrum will be available for a particular star. How will we know when a measurement of i is meaningful? A large set of Monte-Carlo simulations will be essential in assessing the reliability of a measurement. As we saw in this study, the answer is likely to be very reliable for several outcomes of the minimization procedure (e.g. large $\Omega^\star$ and large $i^\star$). In general the fit also returns an error bar on each estimated parameter which could be used to further increase the confidence in a measurement. Finally we repeat that the precision on i can be improved by considering more than one multiplet in the power spectrum. As

a rough estimate, the error on i goes like $n^{-1/2}$, where n is the number of multiplets. The exact number of potentially usable modes depends on the oscillation amplitudes for a particular star. For the Sun, tens of modes can be employed (Fig. 4.1).

The technique that we have described also provides accurate measurements of the angular velocity, Ω (Fig. 4.9). For active Sun-like stars Ω may also be determined by following surface tracers (photometry). By comparing the Ω determined from oscillations with the angular velocity from tracers, inferences can be made on the stellar differential rotation. A knowledge of this quantity, particularly for more rapidly rotating stars, would be of great interest (e.g., for dynamo theories). Alternatively, for those stars for which accurate astrometrically determined parallaxes are known and from which radii $R_\star$ have been determined, a comparison of $\Omega R_\star \sin i$ obtained from asteroseismology with $v \sin i$ determined spectroscopically could set limits on the differential rotation. Differential rotation could also be determined seismically by measuring the rotational splitting frequencies of the quadrupole modes with $m = \pm 1$ and $m = \pm 2$ (when i is such that these modes are visible).

Appendix A

Definition of Travel Time

According to equation (3.5) the travel times $\tau_+(\mathbf{1}, \mathbf{2})$ and $\tau_-(\mathbf{1}, \mathbf{2})$ are the time lags which minimize the functions

$$X_\pm(\mathbf{1}, \mathbf{2}, t) = \int_{-\infty}^{\infty} \mathrm{d}t' \ f(\pm t') \left[C(\mathbf{1}, \mathbf{2}, t') - C^{\mathrm{ref}}(\mathbf{1}, \mathbf{2}, t' \mp t) \right]^2 . \qquad \text{(A.1)}$$

As a result the time derivatives of $X_\pm$ evaluated at $\tau_\pm$ are zero:

$$\dot{X}_\pm(\mathbf{1}, \mathbf{2}, \tau_\pm) = 0 . \qquad \text{(A.2)}$$

Notice that $\dot{X}$ does not involve a time derivative of the observed cross-correlation C. In order to obtain the travel-time perturbations $\delta\tau_\pm$ we need to linearize around the zero-order travel times $\tau_\pm^0$, which are defined by

$$\tau_\pm^0(\mathbf{1}, \mathbf{2}) = \operatorname*{argmin}_{t} \{ \ X_\pm^0(\mathbf{1}, \mathbf{2}, t) \ \} . \qquad \text{(A.3)}$$

The functions $X_\pm^0$ refer to equation (A.1) evaluated for $C = C^0$, where C^0 is the zero-order cross-correlation in the reference model. Linearizing equation (A.2) about $\tau_\pm = \tau_\pm^0$ gives

$$\delta\tau_\pm(\mathbf{1}, \mathbf{2}) = -\frac{\delta\dot{X}_\pm(\mathbf{1}, \mathbf{2}, \tau_\pm^0)}{\ddot{X}_\pm^0(\mathbf{1}, \mathbf{2}, \tau_\pm^0)} . \qquad \text{(A.4)}$$

157

The functions $\delta\dot{X}_\pm$ are given by

$$\delta\dot{X}_\pm(\mathbf{1},\mathbf{2},t) = \pm 2 \int_{-\infty}^{\infty} dt' \ f(\pm t')\dot{C}^{\mathrm{ref}}(\mathbf{1},\mathbf{2},t' \mp t)\delta C(\mathbf{1},\mathbf{2},t') \,. \qquad (A.5)$$

We can then compute $\ddot{X}^0(\tau_\pm^0)$ by straigtforward differentiation of equation (A.1). The result for $\delta\tau_\pm(\mathbf{1},\mathbf{2})$ is thus

$$\delta\tau_\pm(\mathbf{1},\mathbf{2}) = \int_{-\infty}^{\infty} dt \ W_\pm(\mathbf{1},\mathbf{2},t)\delta C(\mathbf{1},\mathbf{2},t) \,, \qquad (A.6)$$

with

$$W_\pm(t) = \frac{\pm f(\pm t)\dot{C}^{\mathrm{ref}}(t \mp \tau_\pm^0)}{\int_{-\infty}^{\infty} dt' \ \left[f(\pm t')C^0(t')\ddot{C}^{\mathrm{ref}}(t' \mp \tau_\pm^0) \pm \dot{f}(\pm t')C^{\mathrm{ref}}(t' \mp \tau_\pm^0)\dot{C}^{\mathrm{ref}}(t' \mp \tau_\pm^0)\right]} \,. \qquad (A.7)$$

We have supressed the spatial arguments $\mathbf{1}$ and $\mathbf{2}$ in the above equation for the sake of readability. This is the general linearized result for arbitrary C^{ref} and f. The only assumption is that the perturbation to the cross-correlation is small compared to the zero-order cross-correlation. Note that we have not written an explicit expression for $\tau_\pm^0$, which needs to be computed numerically by minimizing $X_\pm^0(t)$ (eq. [A.3]).

In the case where C^{ref} and C^0 are even in time, $\tau_+^0 = \tau_-^0$. For the choice $C^{\mathrm{ref}} = C^0$, the zero-order travel times are both zero, $\tau_\pm^0 = 0$. This choice is recommended if a theoretical model is available to the observer. With $C^{\mathrm{ref}} = C^0$ the weight functions $W_\pm$ simplify to:

$$W_\pm(\mathbf{1},\mathbf{2},t) = \frac{\mp f(\pm t)\dot{C}^0(\mathbf{1},\mathbf{2},t)}{\int_{-\infty}^{\infty} dt' \ f(\pm t')[\dot{C}^0(\mathbf{1},\mathbf{2},t')]^2} \,. \qquad (A.8)$$

In the example presented in Section 3.3 we choose $C^{\mathrm{ref}} = C^0$ and $f(t) = \mathrm{Hea}(t)$.

Appendix B

Fourier Convention

Given a function $q(\boldsymbol{x}, t)$, of horizontal position $\boldsymbol{x}$ and time t, we employ the convention that the function $q(\boldsymbol{x}, t)$ and its Fourier transform $\check{q}(\boldsymbol{k}, \omega)$ are related by

$$q(\boldsymbol{x}, t) = \iint_{-\infty}^{\infty} \mathrm{d}\boldsymbol{k} \int_{-\infty}^{\infty} \mathrm{d}\omega \; e^{\mathrm{i}\boldsymbol{k}\cdot\boldsymbol{x} - \mathrm{i}\omega t} \, \check{q}(\boldsymbol{k}, \omega) \,, \tag{B.1}$$

$$\check{q}(\boldsymbol{k}, \omega) = \frac{1}{(2\pi)^3} \iint_{-\infty}^{\infty} \mathrm{d}\boldsymbol{x} \int_{-\infty}^{\infty} \mathrm{d}t \; e^{-\mathrm{i}\boldsymbol{k}\cdot\boldsymbol{x} + \mathrm{i}\omega t} \, q(\boldsymbol{x}, t) \,, \tag{B.2}$$

where $\boldsymbol{k}$ is a two-dimensional horizontal wave vector and ω is the angular frequency. We commonly use the same symbol for q and $\check{q}$: the arguments make clear whether the function or its transform is intended. We use the notation $q(k, \omega)$ when $q(\boldsymbol{k}, \omega)$ only depends on the magnitude of $\boldsymbol{k}$, not its direction, for example in the filter function $F(k, \omega)$. We note that for functions $q(\boldsymbol{x}, t)$ which do not vanish at large $\|\boldsymbol{x}\|$ or $|t|$ the Fourier transform is not defined. In particular there is a problem for the case when the observable is not windowed in space or time. In such a case, $q(\boldsymbol{k}, \omega)$ is intended to mean the Fourier transform of the function $q(\boldsymbol{x}, t)$ truncated to zero for $|t| > T/2$ and $\|\boldsymbol{x}\| > \sqrt{A/\pi}$, where the time interval T and the area A are both large and finite. This modification enables us to refer to the Fourier transform of a stationary/homogeneous random function (cf. Yaglom, 1962, for a rigorous formalism).

When a function of four arguments, $Q(\boldsymbol{x}, t; \boldsymbol{x}', t')$, depends only on the separations $\boldsymbol{x} - \boldsymbol{x}'$ and $t - t'$ (translation invariance), we use the following conventions:

$$Q(\boldsymbol{x} - \boldsymbol{x}', t - t') = Q(\boldsymbol{x}, t; \boldsymbol{x}', t'), \tag{B.3}$$

$$Q(\boldsymbol{k}, \omega) = \frac{1}{(2\pi)^3} \iint_{-\infty}^{\infty} \mathrm{d}\boldsymbol{x} \int_{-\infty}^{\infty} \mathrm{d}t \, e^{-\mathrm{i}\boldsymbol{k}\cdot\boldsymbol{x} + \mathrm{i}\omega t} \, Q(\boldsymbol{x}, t). \tag{B.4}$$

The above conventions are employed, in our example, for the functions $m^0(k, \omega)$, $\boldsymbol{G}(\boldsymbol{k}, \omega; z)$, and $\mathcal{G}(k, \omega)$.

Finally, we recall the relations

$$\int_{-\infty}^{\infty} \mathrm{d}t \, e^{\mathrm{i}\omega t} = 2\pi \, \delta_{\mathrm{D}}(\omega), \tag{B.5}$$

$$\iint_{-\infty}^{\infty} \mathrm{d}\boldsymbol{x} \, e^{-\mathrm{i}\boldsymbol{k}\cdot\boldsymbol{x}} = (2\pi)^2 \, \delta_{\mathrm{D}}(\boldsymbol{k}), \tag{B.6}$$

which are very useful in rewriting the kernels in Fourier space (Appendix C).

Appendix C

Travel Time Sensitivity Kernels for the Example

In this Appendix we derive surface gravity wave travel time kernels, $K_\pm^a$ and $K_\pm^\gamma$, for perturbations to local source strength and damping rate respectively. These kernels connect travel times perturbations, $\delta\tau_\pm$, to perturbations to the model:

$$\delta\tau_\pm(\mathbf{1}, \mathbf{2}) = \int_{(A)} \mathrm{d}\mathbf{r} \, \frac{\delta a(\mathbf{r})}{a} \, K_\pm^a(\mathbf{1}, \mathbf{2}; \mathbf{r}) + \int_{(A)} \mathrm{d}\mathbf{r} \, \frac{\delta\gamma(\mathbf{r})}{\gamma} \, K_\pm^\gamma(\mathbf{1}, \mathbf{2}; \mathbf{r}) \,. \qquad (C.1)$$

Here $\delta a(\mathbf{r})/a$ is the local fractional change in the source strength and $\delta\gamma(\mathbf{r})/\gamma$ the local fractional change in damping rate. The spatial integral $\int_{(A)} \mathrm{d}\mathbf{r}$ is a two-dimensional integral taken over all points $\mathbf{r}$ on the surface $z = 0$. From the theory part of this paper (§ 3.2) we know that in order to compute kernels we first need to write the perturbation to the cross-correlation in terms of the functions $\mathcal{C}^a$ and $\mathcal{C}^\gamma$ (see eq. [3.29]):

$$\delta C(\mathbf{1}, \mathbf{2}, t) = \int_{(A)} \mathrm{d}\mathbf{r} \, \frac{\delta a(\mathbf{r})}{a} \, \mathcal{C}^a(\mathbf{1}, \mathbf{2}, t; \mathbf{r}) + \int_{(A)} \mathrm{d}\mathbf{r} \, \frac{\delta\gamma(\mathbf{r})}{\gamma} \, \mathcal{C}^\gamma(\mathbf{1}, \mathbf{2}, t; \mathbf{r}) \,. \qquad (C.2)$$

The general expression for $\delta C(\mathbf{1}, \mathbf{2}, t)$ is given by equations (3.25), (3.26), and (3.27). In our example, however, the superscripts on the Green's function can be dropped as the source S is scalar. To obtain $\mathcal{C}^a$, we use equation (3.27) for $\mathcal{C}_S$ and the definition of the source perturbation δM (eqs. [3.49] and [3.53]). After integrations by parts

on the source variables in the right-hand side of equation (3.27) and the change of variables $\boldsymbol{r} = (\boldsymbol{s} + \boldsymbol{s}')/2$ and $\boldsymbol{u} = \boldsymbol{s} - \boldsymbol{s}'$, we obtain

$$
\begin{aligned}
\mathcal{C}^a(\mathbf{1}, \mathbf{2}, t; \boldsymbol{r}) \;=\; & \frac{1}{T} \int \mathrm{d}t' \, \mathrm{d}t_{\mathrm{s}} \, \mathrm{d}t'_{\mathrm{s}} \, \mathrm{d}\boldsymbol{u} \; m^0(\boldsymbol{u}, t_{\mathrm{s}} - t'_{\mathrm{s}}) \\
& \times \mathcal{G}^{\boldsymbol{\Pi}}(\mathbf{1} - \boldsymbol{r} - \boldsymbol{u}/2, t' - t_{\mathrm{s}}) \, \mathcal{G}^{\boldsymbol{\Pi}}(\mathbf{2} - \boldsymbol{r} + \boldsymbol{u}/2, t' - t'_{\mathrm{s}} + t) \, . \quad \text{(C.3)}
\end{aligned}
$$

The function $\mathcal{C}^\gamma$ is obtained from equation (3.26) with $\delta\mathcal{L}$ defined by equations (3.46) and (3.58). After integrations by parts on the source variables, and a partial integration on the variable $\boldsymbol{r}$, the result is:

$$
\begin{aligned}
\mathcal{C}^\gamma(\mathbf{1}, \mathbf{2}, t; \boldsymbol{r}) \;=\; & \frac{1}{2\pi T} \int \mathrm{d}t' \, \mathrm{d}t'' \, \mathrm{d}\boldsymbol{s} \, \mathrm{d}t_{\mathrm{s}} \, \mathrm{d}\boldsymbol{s}' \, \mathrm{d}t'_{\mathrm{s}} \, \mathrm{d}\bar{t} \, \Gamma^0(t'' - \bar{t}) \, m^0(\boldsymbol{s} - \boldsymbol{s}', t_{\mathrm{s}} - t'_{\mathrm{s}}) \\
& \times \boldsymbol{\nabla}_{\mathrm{h}}^2 \dot{\boldsymbol{G}}_{\mathrm{h}}(\boldsymbol{r} - \boldsymbol{s}, \bar{t} - t_{\mathrm{s}}) \cdot \Big[\mathcal{G}^{\boldsymbol{\Pi}}(\mathbf{1} - \boldsymbol{s}', t' - t'_{\mathrm{s}}) \, \boldsymbol{\nabla}_{\mathrm{h}} \dot{\mathcal{G}}(\mathbf{2} - \boldsymbol{r}, t' + t - t'') \\
& + \mathcal{G}^{\boldsymbol{\Pi}}(\mathbf{2} - \boldsymbol{s}', t' + t - t'_{\mathrm{s}}) \, \boldsymbol{\nabla}_{\mathrm{h}} \dot{\mathcal{G}}(\mathbf{1} - \boldsymbol{r}, t' - t'') \Big] \, , \quad \text{(C.4)}
\end{aligned}
$$

where $\boldsymbol{G}_{\mathrm{h}}$ denotes the two horizontal components of the vector $\boldsymbol{G}$. In the space-time domain these integrals are quite complicated to compute. They, however, are greatly simplified when written in terms of the Fourier transforms of the various functions:

$$
\begin{aligned}
\mathcal{C}^a(\mathbf{1}, \mathbf{2}, t; \boldsymbol{r}) \;=\; & (2\pi)^4 \int \mathrm{d}\omega \, \mathrm{d}\boldsymbol{k} \, \mathrm{d}\boldsymbol{k}' \, e^{i\boldsymbol{k}\cdot\boldsymbol{\Delta}_1 - i\boldsymbol{k}'\cdot\boldsymbol{\Delta}_2 - i\omega t} \, m^{0*}[(\boldsymbol{k} + \boldsymbol{k}')/2, \omega] \\
& \times \mathcal{G}^{\boldsymbol{\Pi}*}(\boldsymbol{k}, \omega) \, \mathcal{G}^{\boldsymbol{\Pi}}(\boldsymbol{k}', \omega) \, , \quad \text{(C.5)} \\
\mathcal{C}^\gamma(\mathbf{1}, \mathbf{2}, t; \boldsymbol{r}) \;=\; & (2\pi)^7 \int \mathrm{d}\omega \, \mathrm{d}\boldsymbol{k} \, \mathrm{d}\boldsymbol{k}' \, \Big(e^{i\boldsymbol{k}\cdot\boldsymbol{\Delta}_1 - i\boldsymbol{k}'\cdot\boldsymbol{\Delta}_2 - i\omega t} + e^{i\boldsymbol{k}\cdot\boldsymbol{\Delta}_2 - i\boldsymbol{k}'\cdot\boldsymbol{\Delta}_1 + i\omega t} \Big) \\
& \times \Gamma^0(\omega) m^0(\boldsymbol{k}, \omega) G^{\boldsymbol{\Pi}}(\boldsymbol{k}, \omega) \mathcal{G}^{\boldsymbol{\Pi}*}(\boldsymbol{k}, \omega) \, \hat{\boldsymbol{k}} \cdot \hat{\boldsymbol{k}}' \, \mathcal{G}^{\boldsymbol{\Pi}}(\boldsymbol{k}', \omega)/k' \, . \quad \text{(C.6)}
\end{aligned}
$$

We have used the definitions

$$
\begin{aligned}
\mathcal{G}^{\boldsymbol{\Pi}}(\boldsymbol{k}, \omega) \;&=\; F(\boldsymbol{k}, \omega) G^{\boldsymbol{\Pi}}(\boldsymbol{k}, \omega) \, , & \text{(C.7)} \\
G^{\boldsymbol{\Pi}}(\boldsymbol{k}, \omega) \;&=\; i\omega k^2 G_z(\boldsymbol{k}, \omega; z = 0) \, , & \text{(C.8)}
\end{aligned}
$$

and the identity $\boldsymbol{G}_{\mathrm{h}}(\boldsymbol{k}, \omega) = i\hat{\boldsymbol{k}} G_z(\boldsymbol{k}, \omega)$ resulting from equation (3.70). The Green's function $G_z(k, \omega)$ is the $\hat{\boldsymbol{z}}$ component of $\boldsymbol{G}$, given by equation (3.70).

With the assumption that m^0 is independent of $\boldsymbol{k}$, the above expressions can be

simplified to

$$
\mathcal{C}^a(\mathbf{1}, \mathbf{2}, \omega; \boldsymbol{r}) \;=\; m^0(\omega)\, \mathrm{I}^*(\Delta_1, \omega)\, \mathrm{I}(\Delta_2, \omega)\,, \tag{C.9}
$$

$$
\mathcal{C}^\gamma(\mathbf{1}, \mathbf{2}, \omega; \boldsymbol{r}) \;=\; m^0(\omega)\, \hat{\boldsymbol{\Delta}}_1 \cdot \hat{\boldsymbol{\Delta}}_2
$$
$$
\times\, \left[\mathbb{II}(\Delta_1, \omega)\, \mathbb{III}(\Delta_2, \omega) + \mathbb{II}(\Delta_2, \omega)\, \mathbb{III}^*(\Delta_1, \omega)\right]. \tag{C.10}
$$

The integrals I, $\mathbb{II}$, and $\mathbb{III}$ are given by

$$
\mathrm{I}(d, \omega) \;=\; (2\pi)^3 \int_0^\infty k\mathrm{d}k\; J_0(kd)\mathcal{G}^{\boldsymbol{\Pi}}(k, \omega)\,, \tag{C.11}
$$

$$
\mathbb{II}(d, \omega) \;=\; (2\pi)^6\, \Gamma^0(\omega) \int_0^\infty k\mathrm{d}k\; J_1(kd) G^{\boldsymbol{\Pi}}(k, \omega)\mathcal{G}^{\boldsymbol{\Pi}*}(k, \omega)\,, \tag{C.12}
$$

$$
\mathbb{III}(d, \omega) \;=\; (2\pi)^3 \int_0^\infty \mathrm{d}k\; J_1(kd)\mathcal{G}^{\boldsymbol{\Pi}}(k, \omega)\,. \tag{C.13}
$$

The kernels for source strength and damping are then obtained from

$$
K_\pm^{a,\gamma}(\mathbf{1}, \mathbf{2}, \boldsymbol{r}) = 4\pi\mathrm{Re} \int_0^\infty \mathrm{d}\omega\; W_\pm^*(\mathbf{1}, \mathbf{2}, \omega)\mathcal{C}^{a,\gamma}(\mathbf{1}, \mathbf{2}, \omega; \boldsymbol{r}) \tag{C.14}
$$

with $W_\pm^*(\mathbf{1}, \mathbf{2}, \omega)$ given equation 3.66. The kernels, in terms of the integrals I, $\mathbb{II}$, and $\mathbb{III}$, are reported in the main body of the text (eqs. [3.78] and [3.80]).

Appendix D

Single-Source Kernels for the Damping Rate

In the single-source picture, we seek an expression for the kernel $K_+^{\gamma,\mathrm{ss}}$ which provides an integral relationship between the one-way travel time $\delta\tau_+^{\mathrm{ss}}$ (eq. [3.84]) and the local damping perturbation $\delta\gamma(\boldsymbol{r})/\gamma$, i.e.

$$\delta\tau_+^{\mathrm{ss}}(\boldsymbol{1},\boldsymbol{2}) = \int_{(A)} \mathrm{d}\boldsymbol{r} \, \frac{\delta\gamma(\boldsymbol{r})}{\gamma} \, K_+^{\gamma,\mathrm{ss}}(\boldsymbol{1},\boldsymbol{2};\boldsymbol{r}) \,. \tag{D.1}$$

We first rewrite the single-source definition of travel time (eq. [3.84]) in terms of the temporal Fourier transform of the signal observed at point $\boldsymbol{2}$:

$$\delta\tau_+^{\mathrm{ss}}(\boldsymbol{1},\boldsymbol{2}) = -\frac{\mathrm{Re}\int_0^\infty \mathrm{d}\omega \, \mathrm{i}\omega \, \phi^{0*}(\boldsymbol{2},\omega) \, \delta\phi(\boldsymbol{2},\omega)}{\int_0^\infty \mathrm{d}\omega \, \omega^2 \, |\phi^0(\boldsymbol{2},\omega)|^2} \,. \tag{D.2}$$

Given the pressure source $\rho\Theta$, located at point $\boldsymbol{1}$, and defined by equation (3.85), the zero- and first-order signals observed at $\boldsymbol{2}$ are

$$\phi^0(\boldsymbol{2},\omega) = (2\pi)^4 \int_0^\infty k\mathrm{d}k \, J_0(k\Delta)\mathcal{G}^{\Pi}(k,\omega)\Theta(k,\omega) \,, \tag{D.3}$$

$$\begin{aligned}
\delta\phi(\boldsymbol{2},\omega) = {} & (2\pi)^4 \, \Gamma^0(\omega) \int_{(A)} \mathrm{d}\boldsymbol{r} \, \frac{\delta\gamma(\boldsymbol{r})}{\gamma} \int \mathrm{d}\boldsymbol{k}\,\mathrm{d}\boldsymbol{k}' \, e^{\mathrm{i}\boldsymbol{k}\cdot\boldsymbol{\Delta}_1 - \mathrm{i}\boldsymbol{k}'\cdot\boldsymbol{\Delta}_2} \\
& \times G^{\Pi}(\boldsymbol{k},\omega)\Theta(\boldsymbol{k},\omega) \, \hat{\boldsymbol{k}}\cdot\hat{\boldsymbol{k}}' \, \mathcal{G}^{\Pi}(\boldsymbol{k}',\omega)/k' \,.
\end{aligned} \tag{D.4}$$

Using equation (D.2) we obtain the damping kernel $K_+^{\gamma,\mathrm{ss}}$ in the form

$$K_+^{\gamma,\mathrm{ss}}(\mathbf{1},\mathbf{2};\boldsymbol{r}) = \frac{\int_0^\infty \mathrm{d}\omega\ \omega^2 |\phi^0(\mathbf{2},\omega)|^2\ \mathcal{K}_+^{\gamma,\mathrm{ss}}(\mathbf{1},\mathbf{2};\boldsymbol{r};\omega)}{\int_0^\infty \mathrm{d}\omega\ \omega^2 |\phi^0(\mathbf{2},\omega)|^2}\ , \tag{D.5}$$

with the function $\mathcal{K}_+^{\gamma,\mathrm{ss}}$ (single-frequency kernel) defined by

$$\mathcal{K}_+^{\gamma,\mathrm{ss}}(\mathbf{1},\mathbf{2};\boldsymbol{r};\omega) = \hat{\boldsymbol{\Delta}}_1 \cdot \hat{\boldsymbol{\Delta}}_2\ \mathrm{Im}\left[\frac{\mathrm{IV}(\Delta_1,\omega)\ \mathrm{III}(\Delta_2,\omega)}{\omega\ \phi^0(\mathbf{2},\omega)}\right]\ . \tag{D.6}$$

In the above equation, the function IV is a one-dimensional integral given by

$$\mathrm{IV}(d,\omega) = (2\pi)^3\ \Gamma^0(\omega) \int_0^\infty k\mathrm{d}k\ J_1(kd)G^{\mathbf{\Pi}}(k,\omega)\Theta(k,\omega)\ , \tag{D.7}$$

and the function III denotes the integral already defined by equation (C.13). Notice from equation (D.5) that the kernel $K_+^{\gamma,\mathrm{ss}}$ is a frequency average of $\mathcal{K}_+^{\gamma,\mathrm{ss}}$ weighted by $\omega^2 |\phi^0(\mathbf{2},\omega)|^2$.

In order to compute the kernel we have to make a choice for the source spectrum, $\Theta(k,\omega)$. In general, this is difficult without a priori knowledge of the zero-order cross-correlation. When comparing the definition of travel time of Appendix A with the single-source definition (eq. [3.84]), we find that a good match between the two definitions is obtained when $\phi^0(\mathbf{2},t)$ looks like $\mathrm{Hea}(t)C^0(\mathbf{1},\mathbf{2},t)$. This condition is best met when

$$\Theta(k,\omega) = -\frac{k\,F(k,\omega)\,m^0(k,\omega)}{2\Gamma^0(\omega)}\ . \tag{D.8}$$

Note that the filter function $F(k,\omega)$ appears in equation (D.8). The kernel $K_+^{\gamma,\mathrm{ss}}$, shown in Figure 3.8, was computed using this choice.

Appendix E

Constraints on Oblique Rotation of the Solar Core

The axis of rotation of the Sun's surface is inclined from the normal to the ecliptic by 7°.25. Is that true also of the rotation of the rest of the Sun? Knowledge of the direction of the angular momentum is pertinent to studies of the formation of the solar system. Moreover, Bai & Sturrock (1993) have recently interpreted temporal variations in the spatial distribution of solar flares as the outcome of the interaction of the Sun's envelope with an obliquely rotating core. We report here an attempt to determine the principal seismic axes of oscillation of the dipole and quadrupole p modes from LOI data obtained as a component of the VIRGO investigation on the spacecraft SOHO. We find that formally their most likely orientation is somewhat closer to being normal to the ecliptic than is the axis of the surface rotation. However, the uncertainty in the determination well encompasses the possibility of them being parallel to the surface rotation axis, yet it does not reject (at a level marginally greater than one standard deviation) the possibility that the Sun's angular momentum is parallel to that of the rest of the solar system.

Rotation splits the degeneracy of oscillation modes in a multiplet (having like radial order n and degree l). If angular velocity is constant on spheres, a scalar p-mode eigenfunction is approximately proportional to $\Re[Y_l^m(\theta, \phi) \exp(-\mathrm{i}\omega_m t)]$ with respect to spherical polar coordinates (r, θ, ϕ) about an appropriate axis $\mathbf{P}$. The index m denotes the azimuthal order, and Y_l^m is a spherical harmonic function. If

rotation is about a unique axis $\mathbf{R}$, then $\mathbf{P}$ coincides with $\mathbf{R}$. But if $\mathbf{R}$ varies with r, $\mathbf{P}$ is a vector average of $\mathbf{R}(r)$, weighted with the rotational splitting kernel K of the mode (Gough & Kosovichev, 1993). When the magnitude Ω of the angular velocity varies with latitude (defined relative to $\mathbf{R}(r)$), K depends on m and, except in the case $l = 1$, the pulsation axis of the multiplet is not well defined. In the case of the Sun, the latitudinal variation of Ω is small: in the data analysis of quadrupole modes we report below, we assume that there exists a frame in which each azimuthal component can still be described geometrically in terms of a single spherical harmonic, and that the m dependence of the splitting is negligible. If the oscillation axis $\mathbf{P}$ is not coincident with the surface rotation axis $\mathbf{S}$ with respect to which one imagines solar oscillations are analysed, each harmonic projection (l, m') with respect to $\mathbf{S}$ is actually a linear combination of normal modes, and will exhibit all the rotationally split frequencies ω_m (where m is the true azimuthal order, with respect to $\mathbf{P}$). The orientation of $\mathbf{P}$ cannot be determined from frequencies alone, however – the frequencies of an (aspherical) object are independent of the direction from which that object is viewed. To determine $\mathbf{P}$ it is necessary to measure the eigenfunctions. A first attempt at that (Gough et al., 1995), made by estimating in the IPHIR data the amplitudes of whole-disc projections of blended components of $l = 1$ multiplets, suggested that $\mathbf{P}$ might be closer to the normal $\mathbf{n}$ to the ecliptic than is $\mathbf{S}$, but the significance of the measurement is difficult to assess. Here we report a more sophisticated analysis of modes with $l = 1$ and $l = 2$ observed with the LOI (Appourchaux et al., 1997).

The LOI measures radiant intensity $s_p(t)$ integrated over a set of 12 pixels p. The nominal attitude of SOHO is such that the projection of $\mathbf{S}$ onto the detector should coincide with a principal axis of symmetry $\mathbf{d}$ of the detector at all times. A multiplet (l, n) is presumed to be composed of $2l+1$ independently randomly excited modes m, each producing a disturbance of the form $x_m(\theta, \phi, t) \equiv f_m(t; \omega_m)Y_l^m(\theta, \phi)$ about a pulsation axis $\mathbf{P}$. We denote by $\beta_d(t)$ the inclination of the axis $\mathbf{P}$ with respect to $\mathbf{d}$, and by $\alpha_d(t)$ the azimuth of $\mathbf{P}$ relative to the line of sight. During the short selected interval of observation, the variation of $\alpha_d(t)$ and $\beta_d(t)$ is small, and accordingly we ignore it, replacing $\alpha_d(t)$ and $\beta_d(t)$ by their averages $\overline{\alpha}_d$ and $\overline{\beta}_d$. This approximation implies that we neglect the hyperfine structure that results

mode set	$\overline{\alpha}_d$	$\overline{\beta}_d$
$l = 1$ and $15 \leq n \leq 24$	$5° \pm 10°$	$4°.9 \pm 2°.5$
$l = 2$ and $14 \leq n \leq 24$	$10° \pm 10°$	$5°.7 \pm 1°.6$
all	$8° \pm 7°$	$5°.5 \pm 1°.4$

Table E.1: Euler angles $\overline{\alpha}_d$ and $\overline{\beta}_d$ which define the directions of the pulsation axes **P** with respect to **d**.

from SOHO's orbit about **n** (see Goode & Thompson, 1992). The sensitivity of a pixel p to a mode m can thus be expressed in terms of the Euler angles $\overline{\alpha}_d$ and $\overline{\beta}_d$ by integrating over the pixel the Fourier amplitude $\hat{x}_m(\theta, \phi, \omega)$ of x_m weighted with the limb-darkening function. Now consider a small frequency range, and construct $2l + 1$ linear combinations $\hat{y}_M(\omega)$, $-l \leq M \leq l$, of the 12 Fourier transforms $\hat{s}_p(\omega)$ in order to isolate each component m. Using a maximum likelihood technique, we fit a parametric model to the $2l+1$ complex spectra $\hat{y}_M(\omega)$. For each discrete frequency ω, $\hat{f}_m(\omega; \omega_m)$ is presumed to be (a realization of) a centred complex Gaussian random variable whose variance is Lorentzian with amplitude A_m, linewidth Γ, and central frequency $\omega_0 + m\,a_1$, where a_1 is the mean rotational splitting. The $\hat{f}_m$ are assumed to be independent random variables. We add independent Gaussian noise to each pixel with location-dependent variance depending on three undetermined parameters N_j. The parameters $(\overline{\alpha}_d, \overline{\beta}_d, \omega_0, a_1, \Gamma, A_m, N_j)$ are chosen such that they maximize the joint probability density function over some frequency interval (frequency bins are assumed to be independent of each other). Realistic Monte Carlo simulations have been performed which demonstrate that the estimators are essentially unbiased.

Observations were taken over the four-month interval 1996, July 10 – Nov. 6, centred about Sept. 8 when the inclination $B_0(t)$ of **S** from the axis **d** was the greatest (on average, $\overline{B}_0 = 6°.06$). During this interval the average position of **n** is coincident with **d**. The angles $\overline{\alpha}_d$ and $\overline{\beta}_d$ where determined for each multiplet separately. Means and standard deviations are listed in Table E. From the knowledge of the satellite's orbit it is also possible to deduce constraints on the fixed azimuth α and inclination β of **P** with respect to the ecliptic normal **n** (Fig. E.1). The results are not inconsistent with **P** being coincident with **S**.

We adopt a simple two-zone model. The outer zone, $r_c < r \leq R_\odot$ is assumed to

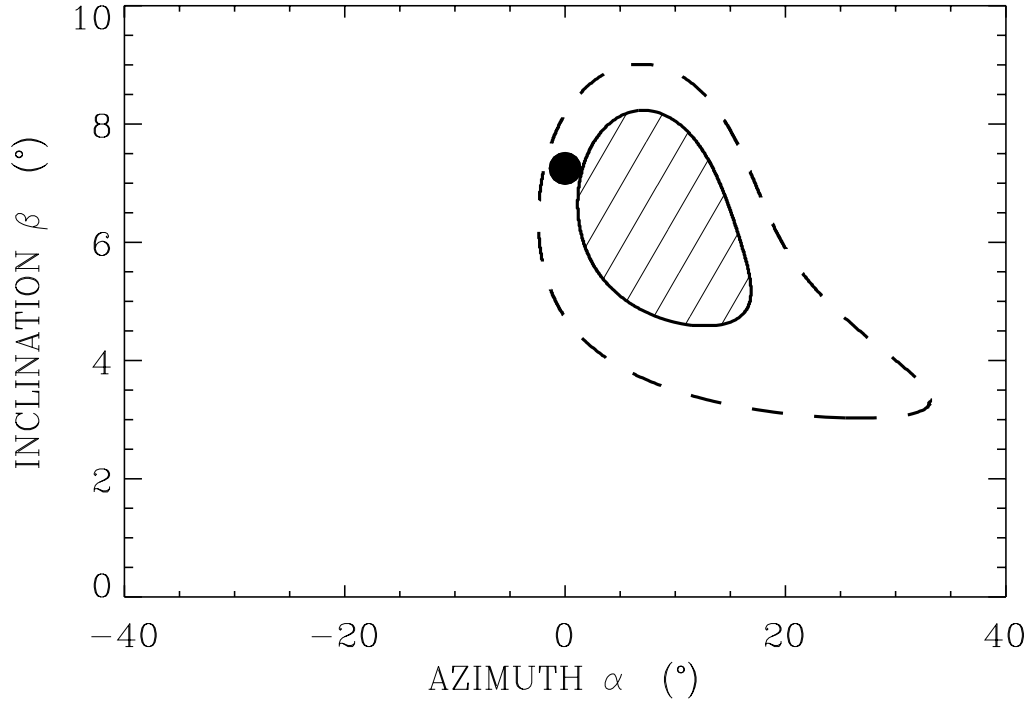Figure E.1: Permitted orientations (α, β) of the mean pulsation axis $\mathbf{P}$ with respect to the normal $\mathbf{n}$ to the ecliptic. The hatched area and the dashed boundary refer to the 1-σ and 1.5-σ confidence levels respectively, computed under the assumption that the uncertainties in $\overline{\alpha}_d$ and $\overline{\beta}_d$ are independent. The filled circle indicates the direction of $\mathbf{S}$.

rotate about $\mathbf{S}$ with angular velocity determined from higher-degree modes (Kosovichev et al., 1997); beneath the convection zone a uniform rate of 435 nHz was adopted. The inner zone, $0 \leq r \leq r_c$, was assumed to rotate uniformly with angular velocity Ω_c about an axis $\mathbf{C}$. The constraints on (α, β) can then be used to constrain the obliquity β_c of $\mathbf{C}$ with respect to $\mathbf{S}$ for each value of r_c. In this way one can test, for example, the model of Bai & Sturrock (1993) in which the core rotates at a rate $\Omega_c/2\pi = 454$ nHz inclined by $\beta_c = 40°$. In this model, we find that the core radius r_c has to be less than $0.24 R_\odot$ in order to be consistent with LOI data.

Subject to the same two-zone model, we can also constrain the orientation (α_L, β_L) of the axis $\mathbf{L}$ of the Sun's angular momentum with respect to the normal $\mathbf{n}$. In Figure E.2, the hatched region in the (β_c, β_L) plane is the permitted region if α, β and a_1 are all within one standard deviation of their seismically determined values. We measured the averaged rotational splitting over the same set of modes to be $a_1 = 440 \pm 7$ nHz from one year of data. It is evident that at a level of significance
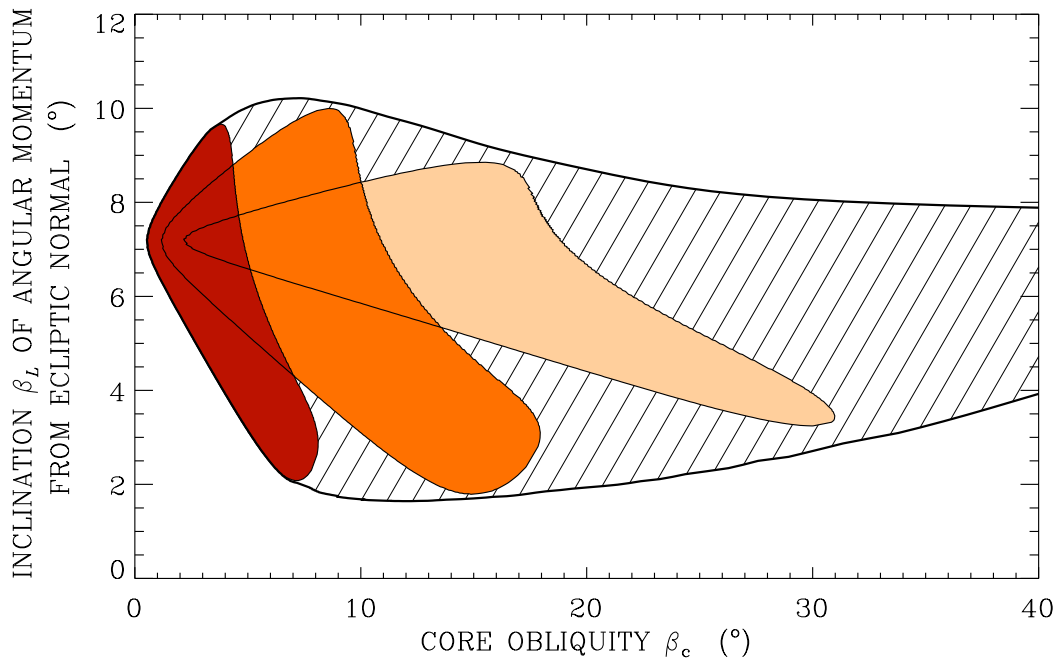
Figure E.2: Permitted inclinations β_L of the solar angular momentum when $a_1 = 440$ nHz, for $r_c/R_\odot = 0.25$ (light orange), 0.4 (orange) and 0.7 (red). The hatched area is the permitted region for $r_c < 0.7R_\odot$ and 433 nHz $< a_1 <$ 447 nHz.

only slightly above one standard deviation the possibility of **L** being perpendicular to the plane of the ecliptic is not ruled out.

Bibliography

Anderson, E. R., Duvall, T. L., & Jefferies, S. M. 1990, Astrophys. J., 364, 699

Antia, H. M., Basu, S., Hill, F., Howe, R., Komm, R. W., & Schou, J. 2001, MNRAS, 327, 1029

Appourchaux, T. 2002, private communication

Appourchaux, T., Andersen, B., Frohlich, C., Jimenez, A., Telljohann, U., & Wehrli, C. 1997, Solar Phys., 170, 27

Appourchaux, T., Chang, H.-Y., Gough, D. O., & Sekii, T. 2000, MNRAS, 319, 365

Appourchaux, T., Gizon, L., & Rabello-Soares, M.-C. 1998, Astron. Astrophys. Suppl., 132, 107

Baglin, A., Auvergne, M., Catala, C., Michel, E., & COROT Team. 2001, Proc. SOHO 10: Helio- and asteroseismology at the dawn of the millennium, Edited by A. Wilson, ESA SP-464, Noordwijk: ESA, 395

Bai, T., & Sturrock, P. A. 1993, Astrophys. J., 409, 476

Beck, J. G. 1997, PhD thesis, Univ. California at Los Angeles

Beck, J. G. 2000, Solar Phys., 191, 47

Beck, J. G., & Duvall, T. L. 2001, Proc. SOHO 10: Helio- and asteroseismology at the dawn of the millennium, Edited by A. Wilson, ESA SP-464, Noordwijk: ESA, 577

Beck, J. G., Duvall, T. L., & Scherrer, P. H. 1998, Nature, 394, 653

Beck, J. G., Gizon, L., & Duvall, T. L. 2002, Astrophys. J., 575, L47

Beck, J. G., & Schou, J. 2000, Solar Phys., 193, 333

Bedding, T. R., Butler, R. P., McCarthy, C., Kjeldsen, H., Marcy, G. W., O'Toole, S. J., Tinney, C. G., & Wright, J. 2002, Asteroseismology Across the HR Diagram. Edited by M. Thompson, M. Cunha and M. Monteiro (Kluwer)

Berrilli, F., Ermolli, I., Florio, A., & Pietropaolo, E. 1999, Astron. Astrophys., 344, 965

Birch, A. C. 2002, PhD thesis, Stanford University

Birch, A. C., & Kosovichev, A. G. 2000, Solar Phys., 192, 193

Birch, A. C., Kosovichev, A. G., Price, G. H., & Schlottmann, R. B. 2001, Astrophys. J., 561, L229

Bogdan, T. J. 1997, Astrophys. J., 477, 475

—. 2000, Solar Phys., 192, 373

Bogdan, T. J., Braun, D. C., & & Lites, B. W. 1998, Astrophys. J., 492, 379

Bogdan, T. J., M., B. T., Lites, B. W., & Thomas, J. H. 1993, Astrophys. J., 406, 723

Bouchy, F., & Carrier, F. 2001, Astron. Astrophys., 374, L5

Brandenburg, A., & Schmitt, D. 1998, Astron. Astrophys., 338, L55

Braun, D. C., Duvall, Jr., T. L., & LaBonte, B. J. 1988, Astrophys. J., 335, 1015

Braun, D. C., & Lindsey, C. 2003, Proc. SOHO 12, ESA SP-517, 15

Brown, T. M., Charbonneau, D., Gilliland, R. L., Noyes, R. W., & Burrows, A. 2001, Astrophys. J., 552, 699

Brown, T. M., & Gilliland, R. L. 1994, Ann. Rev. Astron. Astrophys., 32, 37

Brummell, N. H., Hurlburt, N. E., & Toomre, J. 1996, Astrophys. J., 473, 494

Cally, P. S., & Bogdan, T. J. 1997, Astrophys. J., 486, L67

Charbonneau, D., Brown, T. M., Latham, D. W., & Mayor, M. 2000, Astrophys. J., 529, L45

Chou, D. 2000, Solar Phys., 192, 241

Chou, D., & Dai, D. 2001, Astrophys. J., 559, L175

Chou, D.-Y., Labonte, B. J., Braun, D. C., & Duvall, T. L. 1991, Astrophys. J., 372, 314

Christensen-Dalsgaard, J., Proffitt, C. R., & Thompson, M. J. 1993, Astrophys. J., 403, L75

Corbard, T., & Thompson, M. J. 2002, Solar Phys., 205, 211

Dahlen, F. A., & Tromp, J. 1998, Theoretical Global Seismology (Princeton: Princeton Univ. Press)

DeRosa, M. L. 2001, PhD thesis, Univ. Colorado at Boulder

DeRosa, M. L., Duvall, Jr., T. L., & Toomre, J. 2000, Solar Phys., 192, 351

Deubner, F.-L. 1975, Astron. Astrophys., 44, 371

Dreizler, S., Hauschildt, P. H., Kley, W., Rauch, T., Schuh, S. L., Werner, K., & Wolff, B. 2003, Astron. Astrophys., in press

D'Silva, S., Duvall, T. L., Jefferies, S. M., & Harvey, J. W. 1996, Astrophys. J., 471, 1030

Duvall, T. L. 1979, Solar Phys., 63, 3

—. 1980, Solar Phys., 66, 213

Duvall, T. L. 1995, in ASP Conf. Ser. 76: GONG 1994. Helio- and Astro-Seismology from the Earth and Space, 465

Duvall, T. L. 1998, in Structure and Dynamics of the Interior of the Sun and Sun-like Stars SOHO 6/GONG 98 Workshop, Vol. 2, p. 581

Duvall, T. L., D'Silva, S., Jefferies, S. M., Harvey, J. W., & Schou, J. 1996, Nature, 379, 235

Duvall, T. L., & Gizon, L. 2000, Solar Phys., 192, 177

Duvall, T. L., & Harvey, J. W. 1986, NATO ASI Series C: Mathematical and Physical Sciences, Vol. 169, Seismology of the Sun and the Distant Stars, ed. D. O. Gough (Dordrecht: Reidel), 105

Duvall, T. L., Jefferies, S. M., Harvey, J. W., Osaki, Y., & Pomerantz, M. A. 1993a, Astrophys. J., 410, 829

Duvall, T. L., Jefferies, S. M., Harvey, J. W., & Pomerantz, M. A. 1993b, Nature, 362, 430

Duvall, T. L., Kosovichev, A. G., & Murawski, K. 1998, Astrophys. J., 505, L55

Duvall, T. L., Kosovichev, A. G., Scherrer, P. H., Bogart, R. S., Bush, R. I., de Forest, C., Hoeksema, J. T., Schou, J., Saba, J. L. R., Tarbell, T. D., Title, A. M., Wolfson, C. J., & Milford, P. N. 1997, Solar Phys., 170, 63

Dziembowski, W. 1977, Acta Astronomica, 27, 203

Dziembowski, W. A., & Goode, P. R. 1992, Astrophys. J., 394, 670

Favata, F., Roxburgh, I., & Christensen-Dalsgaard, J. 2000, in The Third MONS Workshop: Science Preparation and Target Selection, 49

Foglizzo, T., Garcia, R. A., Boumier, P., Charra, J., Gabriel, A. H., Grec, G., Robillot, J. M., Roca Cortes, T., Turck-Chieze, S., & Ulrich, R. K. 1998, Astron. Astrophys., 330, 341

Fossat, E. 1981, in NATO ASIC Proc. 68: Solar Phenomena in Stars and Stellar Systems, 75

Foukal, P. 1972, Astrophys. J., 173, 439

Frohlich, C., Andersen, B., Appourchaux, T., Berthomieu, G., Crommelynck, D. A., Domingo, V., Fichot, A., Finsterle, W., Gomez, M. F., Gough, D., Jimenez, A.,

Leifsen, T., Lombaerts, M., Pap, J. M., Provost, J., Cortes, T. R., Romero, J., Roth, H., Sekii, T., Telljohann, U., Toutain, T., & Wehrli, C. 1997, Solar Phys., 170, 1

Galloway, D. J., Proctor, M. R. E., & Weiss, N. O. 1977, Nature, 266, 686

Galloway, D. J., & Weiss, N. O. 1981, Astrophys. J., 243, 945

Giles, P. M. 2000, PhD thesis, Stanford University

Giles, P. M., Duvall, Jr., T. L., Scherrer, P. H., & Bogart, R. S. 1997, Nature, 390, 52

Giovanelli, R. G. 1980, Solar Phys., 67, 211

Gizon, L. 1998, in IAU Symp. 185, 173

Gizon, L. 2002, Astron. Nachr., 323, 251

Gizon, L., Appourchaux, T., & Gough, D. O. 1998, in IAU Symp. 185, 37

Gizon, L., & Birch, A. C. 2001, in First Solar Orbiter Workshop, ed. B. Battrick & H. Sawaya-Lacoste (Noordwijk: ESA SP-493), 233

Gizon, L., & Birch, A. C. 2002, Astrophys. J., 571, 966

Gizon, L., Birch, A. C., Bush, R. I., Duvall, T. L., Kosovichev, A. G., Scherrer, P. H., & Zhao, J. 2001a, in First Solar Orbiter Workshop, ed. B. Battrick & H. Sawaya-Lacoste (Noordwijk: ESA SP-493), 227

Gizon, L., & Duvall, T. L. 2003, in Proc. SOHO 12, ESA SP-517, 43

Gizon, L., Duvall, T. L., & Larsen, R. M. 2000, J. Astrophys. Astron., 21, 339

Gizon, L., Duvall, T. L., & Larsen, R. M. 2001b, in IAU Symp. 203, 189

Gizon, L., Duvall, T. L., & Schou, J. 2003, Nature, 421, 43 (erratum: Nature, 421, 764)

Gizon, L., & Solanki, S. K. 2003, Astrophys. J., in press

Goode, P. R., & Thompson, M. J. 1992, Astrophys. J., 395, 307

Gough, D. O. 1993, in Les Houches Session LXVII, Astrophysical Fluid Dynamics, ed. J.-P. Zahn & J. Zinn-Justin (Amsterdam: Elsevier), 399

Gough, D. O., & Kosovichev, A. G. 1993, in ASP Conf. Ser. 40: Inside the Stars, 566

Gough, D. O., Kosovichev, A. G., & Toutain, T. 1995, in ASP Conf. Ser. 76: GONG 1994. Helio- and Astro-Seismology from the Earth and Space, 55

Gough, D. O., & Thompson, M. J. 1990, MNRAS, 242, 25

Haber, D. A., Hindman, B. W., Toomre, J., Bogart, R. S., Larsen, R. M., & Hill, F. 2002, Astrophys. J., 570, 855

Haber, D. A., Hindman, B. W., Toomre, J., Bogart, R. S., Thompson, M. J., & Hill, F. 2000, Solar Phys., 192, 335

Hagenaar, H. J., Schrijver, C. J., & Title, A. M. 1997, Astrophys. J., 481, 988

Hansen, C. J., Cox, J. P., & van Horn, H. M. 1977, Astrophys. J., 217, 151

Hart, A. B. 1954, MNRAS, 114, 17

—. 1956, MNRAS, 116, 38

Harvey, J. 1985, in Future Missions in Solar, Heliospheric and Space Plasma Physics, ed. E. Rolfe & B. Battrick (Noordwijk: ESA), 199

Hathaway, D., Gilman, P., Harvey, J. W., Hill, F., Howard, R. B., Jones, H. P., Kasher, J., Leibacher, J. B., Pintar, J., & Simon, G. W. 1996, Science, 272, 1306

Hathaway, D. H. 1982, Solar Phys., 77, 341

Hathaway, D. H. 1992, Solar Phys., 137, 15

Hathaway, D. H. 1996, Astrophys. J., 460, 1027

Hathaway, D. H., Beck, J. G., Bogart, R. S., Bachmann, K. T., Khatri, G., Petitto, J. M., Han, S., & Raymond, J. 2000, Solar Phys., 193, 299

Hathaway, D. H., Beck, J. G., Han, S., & Raymond, J. 2002, Solar Phys., 205, 25

Henry, G. W., Marcy, G. W., Butler, R. P., & Vogt, S. S. 2000, Astrophys. J., 529, L41

Hill, F. 1988, Astrophys. J., 333, 996

Hindman, B., Gizon, L., Haber, D., Duvall, T., & Toomre, J. 2003, in Proc. SOHO 12, ESA SP-517, 299

Houdek, G., Balmforth, N. J., Christensen-Dalsgaard, J., & Gough, D. O. 1999, Astron. Astrophys., 351, 582

Howard, R., & LaBonte, B. 1980, Astrophys. J., 239, L33

Howard, R. F. 1996, Ann. Rev. Astron. Astrophys., 34, 75

Howe, R., Christensen-Dalsgaard, J., Hill, F., Komm, R. W., Larsen, R. M., Schou, J., Thompson, M. J., & Toomre, J. 2000, Astrophys. J., 533, L163

Hung, S.-H., Dahlen, F. A., & Nolet, G. 2000, Geophys. J. Int., 141, 175

Hurlburt, N. E., Matthews, P. C., & Proctor, M. R. E. 1996, Astrophys. J., 457, 933

Jensen, J. M., Jacobsen, B., & Christensen-Dalsgaard, J. . 2000, Solar Phys., 192, 231

Jensen, J. M., Jacobsen, B. H., & Christensen–Dalsgaard, J. 1998, in Structure and Dynamics of the Interior of the Sun and Sun-like Stars, Vol. 2 (Noordwijk: ESA), 635

Julien, K., Legg, S., McWilliams, J., & Werne, W. 1996, J. Fluid Mech., 322, 243

Kendall, M. G., & Stuart, A. 1967, The Advanced Theory of Astrophysics: Inference and Relationship, Vol. 2, 2nd ed. (London: Butler & Tanner)

Kjeldsen, H., Arentoft, T., Bedding, T., Christensen-Dalsgaard, J., Frandsen, S., & Thompson, M. J. 1998, in Structure and Dynamics of the Interior of the Sun and Sun-like Stars SOHO 6/GONG 98 Workshop, p. 385

Kjeldsen, H., & Bedding, T. R. 1995, Astron. Astrophys., 293, 87

Kjeldsen, H., & Bedding, T. R. 1998, in The First MONS Workshop: Science with a Small Space Telescope, Eds.: H. Kjeldsen, T.R. Bedding, Aarhus Universitet, p. 1.

Komm, R. W., Howard, R. F., & Harvey, J. W. 1993a, Solar Phys., 143, 19

—. 1993b, Solar Phys., 145, 1

—. 1993c, Solar Phys., 147, 207

Konacki, M., Torres, G., Jha, S., & Sasselov, D. 2003, Nature, 421, 507

Kosovichev, A. G. 1996, Astrophys. J., 461, L55

Kosovichev, A. G., & Duvall, T. L. 1997, in ASSL Vol. 225: SCORe'96 : Solar Convection and Oscillations and their Relationship, ed. F. P. Pijpers, J. Christensen-Dalsgaard, & C. S. Rosenthal (Dordrecht: Kluwer), 241–260

Kosovichev, A. G., Duvall, T. L., Birch, A. C., Gizon, L., Scherrer, P. H., & Zhao, J. 2002, Advances in Space Research, 29, 1899

Kosovichev, A. G., Duvall, T. L. . J., & Scherrer, P. H. 2000, Solar Phys., 192, 159

Kosovichev, A. G., Schou, J., Scherrer, P. H., Bogart, R. S., Bush, R. I., Hoeksema, J. T., Aloise, J., Bacon, L., Burnette, A., de Forest, C., Giles, P. M., Leibrand, K., Nigam, R., Rubin, M., Scott, K., Williams, S. D., Basu, S., Christensen-Dalsgaard, J., Dappen, W., Rhodes, E. J., Duvall, T. L., Howe, R., Thompson, M. J., Gough, D. O., Sekii, T., Toomre, J., Tarbell, T. D., Title, A. M., Mathur, D., Morrison, M., Saba, J. L. R., Wolfson, C. J., Zayer, I., & Milford, P. N. 1997, Solar Phys., 170, 43

Kubičela, A. 1973, in Solar Activity and Related Interplanetary and Terrestrial Phenomena, ed. J. Xanthakis (Berlin: Springer-Verlag), 123

Kuhn, J. R., Armstrong, J. D., Bush, R. I., & Scherrer, P. 2000, Nature, 405, 544

Kumar, P., & Basu, S. 2000, Astrophys. J., 545, L65

LaBonte, B., & Howard, R. 1982, Solar Phys., 63, 373

Lamb, H. 1932, Hydrodynamics, 6th ed. (New York: Dover)

Ledoux, P. 1951, Astrophys. J., 114, 373

Leighton, R. B., Noyes, R. W., & Simon, G. W. 1962, Astrophys. J., 135, 474

Libbrecht, K. G., & Woodard, M. F. 1990, Nature, 345, 779

Lin, H., & Kuhn, J. R. 1992, Solar Phys., 141, 1

Lindsey, C., & Braun, D. C. 2000, Solar Phys., 192, 261

Lindsey, C., Braun, D. C., Jefferies, S. M., Woodard, M. F., Fan, Y., Gu, Y., &
    Redfield, S. 1996, Astrophys. J., 470, 636

Lindsey, C., Braun, D. C., Jefferies, S. M., Woodard, M. F., Fan, Y., Gu, Y., &
    Redfield, S. 1996, Astrophys. J., 470, 636

Lissauer, J. J. 1993, Ann. Rev. Astron. Astrophys., 31, 129

Lynden-Bell, D., & Ostriker, J. P. 1967, MNRAS, 136, 293

Marcy, G. W., & Butler, R. P. 2000, Pub. Astron. Soc. Pacific, 112, 137

Marquering, H., Dahlen, F. A., & Nolet, G. 1999, Geophys. J. Int., 137, 805

Mayor, M., & Queloz, D. 1995, Nature, 378, 355

Messiah, A. 1959, Mécanique quantique, Tome 2 (Paris: Dunod)

Meunier, N. 1999, Astrophys. J., 527, 967

Miesch, M. S., Elliott, J. R., Toomre, J., Clune, T. L., Glatzmaier, G. A., & Gilman,
    P. A. 2000, Astrophys. J., 532, 593

Miller, P., Foukal, P., & Keil, S. 1984, Solar Phys., 92, 33

Murawski, K., & Roberts, B. 1993, Astron. Astrophys., 272, 595

Nesme-Ribes, E., Meunier, N., & Vince, I. 1997, Astron. Astrophys., 321, 323

Nigam, R., & Kosovichev, A. G. 1999, Astrophys. J., 514, L53

November, L. J. 1989, Astrophys. J., 344, 494

Noyes, R. W., Jha, S., Korzennik, S. G., Krockenberger, M., Nisenson, P., Brown, T. M., Kennelly, E. J., & Horner, S. D. 1997, Astrophys. J., 483, L111

Parker, E. N. 1955, Astrophys. J., 122, 293

—. 1963, Astrophys. J., 138, 552

—. 1973, Astrophys. J., 186, 643

—. 1979, Astrophys. J., 230, 905

Paunzen, E., Konig, M., & Dreizler, S. 1998, Astron. Astrophys., 331, 162

Pearson, F. 1990, Map Projection: Theory and Applications (Boca Raton: CRC Press)

Pierce, K. 2000, Allen's Astrophysical Quantities, ed. A. N. Cox (4th ed.; New York: Springer-Verlag)

Ploner, S. R. O., Solanki, S. K., & Gadun, A. S. 2000, Astron. Astrophys., 356, 1050

Rüdiger, G., Brandenburg, A., & Pipin, V. V. 1999, Astronomische Nachrichten, 320, 135

Rüdiger, G., Pipin, V. V., & Belvedère, G. 2001, Solar Phys., 198, 241

Rao, C. R. 1973, Linear Statistical Inference and Its Applications (2nd ed., Wiley)

Rast, M. P. 1997, in ASSL Vol. 225: SCORe'96 : Solar Convection and Oscillations and their Relationship, 135

Rast, M. P. 2003, in Proc. SOHO 12, ESA SP-517, 163

Rice, J. B. 2002, Astron. Nachr., 323, 220-235 (2002), 323, 220

Rieutord, M., Ludwig, H.-G., Roudier, T., Nordlund, A., & Stein, R. 2001, Il Nuovo Cimento C, in press

Rieutord, M., Roudier, T., Malherbe, J. M., & Rincon, F. 2000, Astron. Astrophys., 357, 1063

Rimmele, T., & Schroeter, E. H. 1989, Astron. Astrophys., 221, 137

Rogers, E. H. 1970, Solar Phys., 13, 57

Saff, E. B., & Snider, A. D. 1993, Fundamentals of Complex Analysis for Mathematics, Science, and Engineering, 2nd ed. (Upper Saddle River: Prentice Hall), sect. 8.5, p. 423

Safronov, V. S. 1972, Evolution of the Protoplanetary Cloud and formation of the Earth and the Planets, Israel Program for Scientific Translation, Jerusalem

Saio, H. 1981, Astrophys. J., 244, 299

Sakurai, J. J. 1995, Modern Quantum Mechanics (Reading, MA: Addison-Wesley)

Scherrer, P. H., Bogart, R., Hoeksema, J. T., & Yoshimura, H. 1986, in NATO ASIC Proc. 169: Seismology of the Sun and the Distant Stars, 93

Scherrer, P. H., Bogart, R. S., Bush, R. I., Hoeksema, J. T., Kosovichev, A. G., Schou, J., Rosenberg, W., Springer, L., Tarbell, T. D., Title, A., Wolfson, C. J., Zayer, I., & The MDI Engineering Team. 1995, Solar Phys., 162, 129

Schlichenmaier, R., Jahn, K., & Schmidt, H. U. 1998, Astron. Astrophys., 337, 897

Schou, J. 1992, PhD thesis, Aarhus University

—. 1999, Astrophys. J., 523, L181

—. 2003, in Proc. SOHO 12, ESA SP-517, 381

Schou, J., & Bogart, R. S. 1998, Astrophys. J., 504, L131

Schou, J., & Buzasi, D. L. 2001, Proc. SOHO 10/GONG 2000 Workshop: Helio- and asteroseismology at the dawn of the millennium, ESA SP-464, p. 391, 464, 391

Schou, J., Christensen-Dalsgaard, J., & Thompson, M. J. 1994, Astrophys. J., 433, 389

Schrijver, C. J., Hagenaar, H. J., & Title, A. M. 1997, Astrophys. J., 475, 328

Schüssler, M. 1981, Astron. Astrophys., 94, L17

Schüssler, M., & Solanki, S. K. 1992, Astron. Astrophys., 264, L13

Shine, R. A., Simon, G. W., & Hurlburt, N. E. 2000, Solar Phys., 193, 313

Simon, G. W., & Leighton, R. B. 1964, Astrophys. J., 140, 1120

Simon, G. W., & Weiss, N. O. 1968, Z. Astrophys., 69, 435

Snodgrass, H. B. 1984, Solar Phys., 94, 13

Snodgrass, H. B., & Ulrich, R. K. 1990, Astrophys. J. Suppl., 351, 309

Solanki, S. K. 2003, Astron. Astrophys. Rev., 11, 153

Spruit, H. C. 2003, Solar Phys., 213, 1

Stein, R. F. 1967, Solar Phys., 2, 385

Stein, R. F., & Nordlund, Å. 2000, Solar Phys., 192, 91

—. 2001, Astrophys. J., 546, 585

Strous, L. H., Goode, P. R., & Rimmele, T. R. 2000, Astrophys. J., 535, 1000

Tarbell, T. D., Acton, D. S., & A., F. Z. 1997, in Adaptative Optics, Vol. 13, ed. D. Hennage (Washington, DC: OSA), 96

Tassoul, M. 1980, Astrophys. J. Supp. Ser., 43, 469

Thompson, M. J., Toomre, J., Anderson, E., Antia, H. M., Berthomieu, G., Burtonclay, D., Chitre, S. M., Christensen-Dalsgaard, J., Corbard, T., Derosa, M., Genovese, C. R., Gough, D. O., Haber, D. A., Harvey, J. W., Hill, F., Howe, R., Korzennik, S. G., Kosovichev, A. G., Leibacher, J. W., Pijpers, F. P., Provost, J., Rhodes, E. J., Schou, J., Sekii, T., Stark, P. B., & Wilson, P. 1996, Science, 272, 1300

Title, A. M., Tarbell, T. D., Topka, K. P., Ferguson, S. H., Shine, R. A., & SOUP Team. 1989, Astrophys. J., 336, 475

Toner. 2001, private communication

Tong, J., Dahlen, F. A., Nolet, G., & Marquering, H. 1998, Geophys. Res. Lett., 25, 1983

Toutain, T., & Appourchaux, T. 1994, Astron. Astrophys., 289, 649

Toutain, T., & Gouttebroze, P. 1993, Astron. Astrophys., 268, 309

Udalski, A., Zebrun, K., Szymanski, M., Kubiak, M., Soszynski, I., Szewczyk, O., Wyrzykowski, L., & Pietrzynski, G. 2002, Acta Astronomica, 52, 115

Ulrich, R. K. 1970, Astrophys. J., 162, 993

Ulrich, R. K. 1988, Solar Phys., 117, 291

Ulrich, R. K. 2001, Astrophys. J., 560, 466

Vernazza, J. E., Avrett, E. H., & Loeser, R. 1981, Astrophys. J. Suppl., 45, 635

Veronis, G. 1959, J. Fluid Mech., 5, 401

Wang, H., & Zirin, H. 1989, Solar Phys., 120, 1

Woodard, M. F. 1984, PhD thesis, Univ. California at San Diego

—. 1997, Astrophys. J., 485, 890

Woodard, M. F., & Noyes, R. W. 1985, Nature, 318, 449

Worden, S. P., & Simon, G. W. 1976, Solar Phys., 46, 73

Yaglom, A. M. 1962, An Introduction to the Theory of Stationary Random Functions (Englewood Cliffs: Prentice Hall)

Yoshimura, H. 1971, Solar Phys., 18, 417

Zhao, J. 2003, in Proc. SOHO 12, ESA SP-517, 417

Zhao, J., Kosovichev, A. G., & Duvall, T. L. 2001, Astrophys. J., 557, 384

Zhao, L., & Jordan, T. H. 1998, Geophys. J. Int., 133, 683